

## Experimental Study and Numerical Simulation of the Reaction Process and Microstructure Formation of Alkali-Activated Materials

Zuo, Yibing

### DOI

[10.4233/uuid:193a4016-5fc7-401b-babe-722ff6a95a6c](https://doi.org/10.4233/uuid:193a4016-5fc7-401b-babe-722ff6a95a6c)

### Publication date

2019

### Document Version

Final published version

### Citation (APA)

Zuo, Y. (2019). *Experimental Study and Numerical Simulation of the Reaction Process and Microstructure Formation of Alkali-Activated Materials* (1 ed.). [Dissertation (TU Delft), Delft University of Technology]. Delft University of Technology. <https://doi.org/10.4233/uuid:193a4016-5fc7-401b-babe-722ff6a95a6c>

### Important note

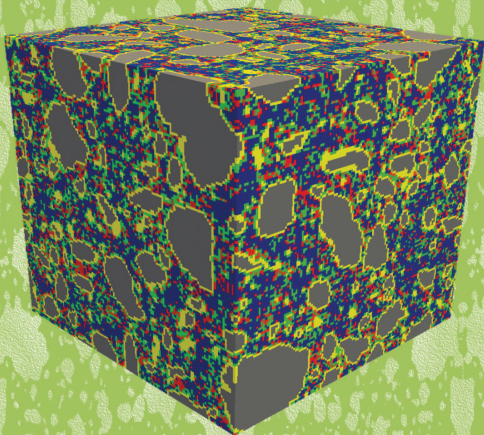
To cite this publication, please use the final published version (if applicable).  
Please check the document version above.

### Copyright

Other than for strictly personal use, it is not permitted to download, forward or distribute the text or part of it, without the consent of the author(s) and/or copyright holder(s), unless the work is under an open content license such as Creative Commons.

### Takedown policy

Please contact us and provide details if you believe this document breaches copyrights.  
We will remove access to the work immediately and investigate your claim.



# Experimental Study and Numerical Simulation of the Reaction Process and Microstructure Formation of Alkali-Activated Materials

Yibing ZUO





# **Experimental Study and Numerical Simulation of the Reaction Process and Microstructure Formation of Alkali-Activated Materials**



# **Experimental Study and Numerical Simulation of the Reaction Process and Microstructure Formation of Alkali-Activated Materials**

## **Dissertation**

For the purpose of obtaining the degree of doctor  
at Delft University of Technology  
by the authority of the Rector Magnificus Prof.dr.ir. T.H.J.J. van der Hagen  
chair of the Board for Doctorates  
to be defended publicly on  
Monday 23 September 2019 at 10:00 o'clock

By

**Yibing ZUO**

Master of Science in Structural Engineering  
Huazhong University of Science and Technology, P.R. China  
Born in Xiaogan, Hubei Province, P.R. China

The dissertation has been approved by the promotor:

Promotor: Prof. K. van Breugel

Promotor: Dr. G. Ye

Composition of the doctoral committee:

Rector Magnificus	chairperson
Prof. K. van Breugel	Delft University of Technology, promotor
Dr. G. Ye	Delft University of Technology, promotor

*Independent members:*

Prof. S.J. Picken	Delft University of Technology
Prof. P. Krivenko	Kyiv National University of Construction and Architecture, Ukraine
Prof. J.L. Provis	University of Sheffield, UK
Dr. H.W. Nugteren	Delft University of Technology
Prof. E. Schlangen	Delft University of Technology, reserve member

*Other member:*

Prof. X. Wei	Huazhong University of Science and Technology, P.R. China
--------------	---

*Keywords:* alkali-activated materials, slag, fly ash, pore solution composition, reaction kinetics, heat release, microstructure formation, numerical simulation, initial particle packing structure, spherical harmonics, dissolution, lattice Boltzmann method, thermodynamic modelling, nucleation and growth, GeoMicro3D

*Printed by:* Ipskamp Printing, The Netherlands

*Thesis format by:* Yibing Zuo

*Cover design by:* Yibing Zuo and Xujia He

Copyright © 2019 by Yibing Zuo

All rights reserved. No part of the material protected by this copyright notice may be reproduced or utilized in any form or by any means, electronic or mechanical, including photocopying, recording or by any information storage and retrieval system, without written consent from the author.

ISBN 978-94-6384-062-0

An electrical version of this dissertation is available at:

<http://repository.tudelft.nl/>.



*To my family*





# Acknowledgements

---

The research work presented in this thesis was sponsored by Chinese Scholarship Council (CSC) and Delft University of Technology (TU Delft). These institutes deserve the greatest acknowledgement and appreciation. Besides the institutes many people have been supporting me in this research work and for that they should be recognized here with my deepest gratitude.

I would like to express my deepest appreciation to my promotor Prof. Klaas van Breugel for providing me the opportunity to realize this research work in Microlab at TU Delft. His tireless efforts and constructive comments on this dissertation are highly appreciated. I also would like to sincerely thank my promotor Dr. Guang Ye for his encouragement and persistent support through the whole course of this research work. Inspiring discussions with him helped me to walk out of problems that came across on the way. Many thanks also go to him for his invitation and warm reception during the New Year Party for every year since I came to the Netherlands. Without the guidance, suggestions and help from my two promotors I would not accomplish this research work.

All my committee members are greatly acknowledged for spending their time on reviewing my thesis, giving their comments and being willing to attend my PhD defence. Particular gratitude must go to Prof. John L. Provis at University of Sheffield, for one of his very impressive lectures from which I got to know “geopolymer” and for his kind encouragement and advice thereafter in the communications about “geopolymer”.

I would like to take a moment to express my deepest gratitude to Prof. Xiaosheng Wei at Huazhong University of Science and Technology, who brought me into the research field of cementitious materials, recommended me to pursue a PhD study at TU Delft and always encourages me to destine for a scientific researcher. I have learned a lot from him about scientific research and presenting. Without his persistent encouragement and guidance I would not go so far now in the research of cementitious materials. Sincere thanks also go to Dr. Yishun Liao at Wuhan University of Science and Technology, for being my guarantor in my CSC scholarship application. I also want to deliver my special gratitude to Prof. Lianzhen Xiao at Wuhan Institute of Technology, for her care and support in my career development as a scientific researcher.

A special note of appreciation goes to Prof. Edward Garboczi at National Institute of Standards and Technology (NIST) for providing me the spherical harmonic databases of slag and fly ash, reviewing and commenting the conference/journal papers that we are authored. My gratitude also goes to Dr. Zhiwei Qian who assisted me with extending the

Anm model and helped me a lot in the daily life. I am also thankful to Dr. Rupert Myers at The University of Edinburg for his valuable suggestions and help with performing thermodynamic calculations using GEMs. My appreciation should be also delivered to Jiayi Chen (Dr. Wenqin Shi) who kindly shared his opinions and experience about lattice Boltzmann method. The discussions with Dr. Zhiwei Qian, Dr. Rupert Myers and Jiayi Chen inspired me very much in the modelling work. Particularly I would like to express my sincere thanks to PSI and Empa for providing GEMS based on which the thermodynamic module of GeoMicro3D was developed.

I am very thankful to the technicians in Microlab at TU Delft. Thanks go to Arjan Thijssen, Ton Blom, Ron Penners and John van den Berg for their help with my experimental work. Special thanks go to Maiko van Leeuwen not only for his kind help with the experiments but also for checking my Dutch translation of the summary. I also owe my gratitude to our secretaries at TU Delft, Nynke Verhulst for assisting me to prepare the administration documents before and after I arrived in the Netherlands, Claire de Bruin, Iris Batterham and Jacqueline van Unen-Bergenhengouwen for helping me a lot with various daily issues. In particular I would like to thank Cees Timmers at the Center for International Cooperation and Appropriate Technology (CICAT) of TU Delft for his kind help and support during the application of my PhD study at TU Delft. I also want to express my thanks to the scientific staff in Microlab, Dr. Henk Jonkers, Dr. Dessi Koleva, Dr. Marc Ottele and Dr. Oguzhan Copuroglu.

I want to thank Dr. Xiaowei Ouyang (Cui Wei) for his very kind help and encouragement in my research and life, Dr. Marija Nedeljkovic and Dr. Kamel Arbi for their support and helpful advice in my research work, Dr. Peng Gao for his assistance in performing simulations using HYMOSTRUC3D-E, Dr. Haoliang Huang for his helpful comments on the use of CHESS, Dr. Virginie Wiktor for answering my questions about ICP-OES, Dr. Branko Savija for this help with the chloride ingress test, Dr. Yang Lu for his assistance in the calorimetry test at Ghent University, Balqis MD Yunus for sharing her pipet for the ICP-OES test, Dr. Hua Dong and Dr. Tianshi Lu for giving me a lift several times, Shizhe Zhang for his help with the FTIR test, Boyu Chen for her kind assistance during my job interview, Xuliang Hou (Dr. Yin Yang) and Dr. Xu Ma for leading me around after my arrival in the Netherlands, Hao Huang for showing me the nitrogen adsorption test, Dr. Yong Zhang for his insightful comments on the use of PDC-MIP, and Yidong Gan for his help with nanoindentation test. Special thanks also go out to the anonymous reviewers for their helpful and constructive comments on the journal/conference papers that are related to this research work.

It is my pleasure to express my sincere acknowledgements to my current and former colleagues at TU Delft for their friendship, support and interesting discussions over the years. They are Dr. Zhuqing Yu, Dr. Zhengxian Yang, Dr. Senot Sangadji, Dr. Fuhai Li, Prof. Jiangxiong Wei, Dr. Yun Huang, Prof. Yingzi Yang, Bei Wu, Zhenming Li, Agus Susanto, Dr. Farhad Pargar, Dr. Bahman Ghiassi, Dr. Damian Palin, Dr. Mladena Lukovic, Dr. Zichao Pan, Zhipei Chen, Dr. Leyang Lu, Dr. Eirini Tziviloglou, Vladislav Omelchuk, Stefan Chaves Figueiredo, Claudia Romero, Ze Chang, Yu Chen,, Gabriel Hoder, Clarissa

Justino de Lima, Albina Kostiuchenko, Yask Kulshreshtha, Jeannette van den Bos, Xuhui Liang, Jiahua Liu, Yun Chen, Zhiyuan Xu, Wenjuan Lyu, Renee Mors, Shi Xu, Yading Xu, Hongzhi Zhang, Dr. Caglar Yalcinkaya, Bart Hendrix, Luiz Lima, Mohammad Sadeghi, Fernando Franca, Wenhao Guo and Bo Li etc. I am grateful to all the friends that I met outside the Microlab. Their friendships accompanied me and made my life more colorful. They are Dr. Zhiyong Wang, Dr. Yong Guo, Dr. Ye Zhang, Dr. Shuai Yuan, Dr. Meixia Shan, Dr. Chunsen Shi, Dr. Xing Chang, Dr. Xiaoya Ma and Dr. Jian Fang etc.

I want to express my greatest appreciation to my parents for bringing me up and endlessly supporting me. Their love always surrounds me and replace my longlines with happiness in the land that is far away from my hometown. My heartfelt gratitude also goes to my grandmother who is always there to encourage me for pursuit of knowledge and support me by her best. Special thanks go out to my older brother and his family who always support me and take care of our parents and grandmother. Without their unconditional love, support, sacrifices and endless encouragement I would never have accomplished this research work and had this colorful and enjoyable life.

Last but not the least, I would like to express my deepest gratitude to my beloved wife (Xujia He) and parents-in-law. My parents-in-law always support me and provide me a relaxed atmosphere. Although my wife works in China, her unconditional love always surrounds me and it seems like she is just around me. It is her accompany, support and encouragement that give me strength to move on my research work and that make my life filled with happiness. I am heartily grateful for having her with me until white-headed.



Yibing Zuo

Delft, August 2019



# Table of Contents

---

Table of Contents .....	i
List of Symbols .....	vii
List of Abbreviations .....	xiii

---

## PART I: INTRODUCTION

---

<b>Chapter 1 General introduction.....</b>	<b>1</b>
1.1 Background of this research .....	2
1.2 Objectives of this research.....	3
1.3 Scope of this research .....	4
1.4 Strategy of this research.....	4
1.5 Outline of this research.....	5
<b>Chapter 2 Literature review.....</b>	<b>7</b>
2.1 Introduction.....	8
2.2 Experimental studies of AAMs .....	8
2.2.1 Dissolution and pore solution chemistry of AAMs .....	8
2.2.2 Reaction kinetics of AAMs.....	10
2.2.3 Reaction products of AAMs .....	13
2.2.4 Microstructure formation of AAMs.....	15
2.3 Thermodynamics of AAMs .....	16
2.4 Numerical studies of AAMs .....	17
2.4.1 Numerical studies of alkali-activated slag .....	17
2.4.2 Numerical studies of alkali-activated fly ash.....	18
2.5 Summary of the literature study .....	21
2.6 Motivation of this research .....	21

---

## PART II: EXPERIMENTAL STUDY

---

<b>Chapter 3 Pore solution composition of alkali-activated materials.....</b>	<b>23</b>
3.1 Introduction.....	24

3.2 Materials and methods .....	25
3.2.1 Materials .....	25
3.2.2 Mixtures .....	27
3.2.3 Pore solution analysis via ICP-OES .....	28
3.3 Results and discussion .....	30
3.3.1 Pore solution composition of alkali-activated slag paste .....	30
3.3.2 Pore solution composition of alkali-activated fly ash paste.....	33
3.3.3 Pore solution composition of alkali-activated slag/fly ash paste .....	38
3.4 Conclusions.....	39
<b>Chapter 4 Reaction kinetics of alkali-activated materials.....</b>	<b>41</b>
4.1 Introduction.....	42
4.2 Materials and methods.....	43
4.2.1 Materials and mixtures.....	43
4.2.2 Isothermal calorimetry test.....	43
4.2.3 Determination of degree of reaction .....	43
4.3 Results and discussion .....	44
4.3.1 Isothermal calorimetry study of the reaction kinetics of alkali-activated slag and fly ash .....	44
4.3.2 Assessments of the calorimetric differences caused by aluminosilicate precursors and alkaline activators.....	49
4.3.3 Degree of reaction.....	55
4.4 Conclusions.....	57
<b>Chapter 5 Microstructure analysis of alkali-activated materials.....</b>	<b>61</b>
5.1 Introduction.....	62
5.2 Materials and methods.....	63
5.2.1 Materials and mixtures.....	63
5.2.2 Scanning electron microscopy (SEM) .....	63
5.2.3 Mercury intrusion porosimetry (MIP) .....	63
5.2.4 SEM-image analysis .....	64
5.3 Results.....	67
5.3.1 Morphology and degree of reaction of hardened alkali-activated slag paste.....	67
5.3.2 Morphology and degree of reaction of hardened alkali-activated fly ash paste .....	69
5.3.3 Morphology and degree of reaction of hardened alkali-activated slag/fly ash paste .....	73



5.3.4 Pore structure of alkali-activated slag paste.....	74
5.3.5 Pore structure of alkali-activated fly ash paste .....	79
5.3.6 Pore structure of alkali-activated slag/fly ash paste.....	85
5.4 Discussion.....	87
5.4.1 Comparison of the results from MIP and SEM-image analysis.....	87
5.4.2 Microstructure formation of alkali-activated materials .....	88
5.5 Conclusions.....	92

---

### **PART III: NUMERICAL SIMULATION AND VALIDATION**

---

<b>Chapter 6 Simulation of the initial particle parking structure of alkali-activated materials.....</b>	<b>95</b>
6.1 Introduction.....	96
6.2 Methodology.....	97
6.2.1 Extended Anm material model .....	97
6.2.2 Characterization of the initial particle parking structure .....	101
6.3 Simulation parameters .....	102
6.4 Results and discussion .....	102
6.4.1 Simulated initial particle parking structures of alkali-activated materials.....	102
6.4.2 Evaluation of the simulated initial particle parking structure .....	106
6.4.3 Computation efficiency of the simulations .....	111
6.5 Conclusions.....	111
<b>Chapter 7 Simulation of the dissolution of slag and fly ash in alkaline solution.....</b>	<b>113</b>
7.1 Introduction.....	114
7.2 Methodology.....	115
7.2.1 Initial particle parking structure.....	115
7.2.2 Dissolution rate .....	116
7.2.3 Transport of aqueous ions .....	121
7.2.4 Dissolution front .....	122
7.2.5 Influence of temperature .....	124
7.3 Three affecting factors.....	125
7.3.1 Depression of dissolution rate by aqueous aluminum species.....	125
7.3.2 Factor of the solution-volume to precursor-surface-area ratio.....	126
7.3.3 Factor of non-steady dissolution .....	126
7.4 Implementation of the numerical model.....	127

7.4.1 Simulation parameters.....	127
7.4.2 Simulation of the dissolution of slag in alkaline solution.....	128
7.4.3 Simulation of the dissolution of fly ash in alkaline solution .....	129
7.5 Conclusions.....	130
<b>Chapter 8 Thermodynamic modelling of the reactions in alkali-activated materials...</b>	<b>131</b>
8.1 Introduction.....	132
8.2 Methods .....	133
8.2.1 Thermodynamics, thermodynamic database and thermodynamic modelling.....	133
8.2.2 Thermodynamic models for the C-(N-)A-S-H gel and hydrotalcite-like phase in alkali- activated slag.....	134
8.2.3 Thermodynamic model for the N-A-S-H gel in alkali-activated fly ash .....	135
8.2.4 Other solid phases .....	138
8.2.5 Modelling approach .....	139
8.3 Thermodynamic modelling of the reactions in alkali-activated slag.....	139
8.4 Thermodynamic modelling of the reactions in alkali-activated fly ash .....	141
8.4.1 Element composition of the N-A-S-H gel .....	141
8.4.2 Aqueous phase composition of alkali-activated fly ash.....	142
8.4.3 Simulated solid phase evolution of alkali-activated fly ash.....	143
8.5 Thermodynamic modelling of the reactions in alkali-activated slag/fly ash.....	145
8.6 Conclusions.....	146
<b>Chapter 9 Simulation of the reaction process and microstructure formation of alkali-activated materials.....</b>	<b>147</b>
9.1 Introduction.....	148
9.2 Simulation of the nucleation and growth of reaction products.....	149
9.3 Diffusivity of ions through lattice nodes .....	151
9.4 GeoMicro3D: the overall flowchart.....	154
9.5 Implementation – a case study of the alkali-activated slag systems.....	155
9.5.1 Water retention of the C-(N-)A-S-H gel .....	155
9.5.2 Simulation parameters.....	156
9.5.3 Degree of reaction.....	158
9.5.4 Pore solution chemistry.....	158
9.5.5 Microstructure development .....	161
9.5.6 Volume evolution of phases.....	166

9.5.7 Porosity and pore size distribution.....	168
9.5.8 Simulation results of sample BFS_N4S0 at an age of 28 days.....	169
9.6 Discussion.....	170
9.6.1 Computation efficiency.....	170
9.6.2 Comparison of the simulation results from GeoMicro3D and the experimental results from MIP and SEM-image analysis .....	170
9.7 Conclusions.....	171
 <b>PART IV: CONCLUSIONS AND OUTLOOKS</b>	
<b>Chapter 10 Retrospection, conclusions and outlooks .....</b>	<b>173</b>
10.1 Retrospection .....	174
10.2 Contributions of this research.....	176
10.3 Conclusions and observations.....	177
10.4 Outlooks.....	179
10.4.1 Potentials of GeoMicro3D .....	179
10.4.2 Recommendations for future research .....	181
Summary.....	183
Samenvatting.....	185
Appendix A Determination of the log forward dissolution rates of Ca and Si .....	189
Appendix B Thermodynamic properties of the phases used for thermodynamic modelling in this work .....	199
Appendix C Additional simulation results for samples BFS_N6S0 and BFS_N6S5.4 .....	203
References .....	213
Propositions.....	225
List of Publications.....	227
Curriculum Vitae.....	231



# List of Symbols

---

## Roman lower case letters

$\bar{a}$	Average ion size	[m]
$a_i$	Size range bounds for slag where $a_1 > a_2 > \dots > a_i$	[ $\mu\text{m}$ ]
$a_{nm}$	Spherical harmonic expansion coefficients	
$b$	A constant	
$b^{sc}$	Neutron scattering lengths	[m]
$b_i$	Size range bounds for fly ash, where $b_1 > b_2 > \dots > b_i$	[ $\mu\text{m}$ ]
$b_\gamma$	A parameter for common short-range interactions of the charged species	
$c$	Shape factor for nucleation	
$c^*$	Molar solubility	mol/L
$d$	Pore diameter	[ $\mu\text{m}$ ]
$e_j$	Microscopic velocity at location $x$ at time $t$ and in velocity direction $j$	
$f_{\text{dissolving-area}}$	Fraction of the interface area that is dissolving	
$f_i$	Size range fraction, where $f_1 + f_2 + \dots + f_i = 1$	
$f_j, f_j^{eq}$	Non-equilibrium and equilibrium particle distribution function at location $x$ at time $t$ and in the direction of the velocity $j$ ( $j = 0, 1, 2, 3, 4, 5, 6$ )	
$f_{Fe}, f_{Al}$	Parameters that specify the molar fractions of $\text{Fe}_2\text{O}_3$ and $\text{Al}_2\text{O}_3$ acting as framework modifier	
$f_{Mg}, f_{Na}, f_K, f_S$	ratios of the dissolution rate of Mg, Na, K and S relative to the dissolution rate of Ca, respectively	
$k$	A parameter	
$k_B$	Boltzmann constant	
$n$	Index	
$\Delta n_{X,i}$	Dissolved amount of element $X$ at interface $i$ at one lattice Boltzmann time step. Element $X$ can be Si, Al, Ca, Mg, S or K	[mol]
$l_0$	Side length of lattice node	[m]
$m$	Index	

$p$	Pressure	[MPa]
$r$	Overall dissolution rate	[mol·m <sup>-2</sup> s <sup>-1</sup> ]
$r_+$	Forward dissolution rate	[mol·m <sup>-2</sup> s <sup>-1</sup> ]
$r_{new}, r_{ref}$	Rates of dissolution at the Kelvin temperatures $T_{new}$ and $T_{ref}$ , respectively	[mol·m <sup>-2</sup> s <sup>-1</sup> ]
$r_{X,i}$	Dissolution rate of element X at the interface $i$	[mol·m <sup>-2</sup> s <sup>-1</sup> ]
$r(\theta, \varphi)$	Radial distance	[m]
$t_0$	Lattice Boltzmann step time	[s]
$t_l$	time in lattice unit	
$t_p$	time in physical unit	[s]
$v$	Molecular volume	[m <sup>3</sup> ]
$v_{Si}, v_{Al}, v_{Ca}, v_{Mg}, v_S, v_K, v_{Na}$	Molar fraction of Si, Al, Ca, Mg, S, K and Na in aluminosilicate precursor, respectively	
$w_j$	Weighting factor in the velocity direction $j$	
$x_l$	Length in lattice unit	
$x_{jw}$	Mole quantity of water	[mol]
$x_p$	Length in physical unit	[m]
$z_j$	Charge of the aqueous species $j$	

### Roman capital letters

$A$	Kinetic parameter	m <sup>-3</sup> s <sup>-1</sup>
$A^*$	Chemical affinity	[J/mol]
$A_\gamma$	Electrostatic parameter	
$B$	Thermodynamic parameter	
$B_\gamma$	Electrostatic parameter	
$C_{Al}$	Concentration of aqueous Al	[mol/L]
$\Delta C$	Element concentration change	[mol/L]
$C_p^0$	Standard heat capacity	[J·mol <sup>-1</sup> K <sup>-1</sup> ]
$D$	Particle size	[μm]
$D_A, D_B, D_{BC}$	Diffusivity of phase A, phase B and phase BC, respectively	[m <sup>2</sup> /s]
$D_{medium}$	Diffusivity of a medium	[m <sup>2</sup> /s]
$D_{new}, D_{ref}$	Diffusion coefficients at the Kelvin temperatures $T_{new}$ and $T_{ref}$ , respectively	[m <sup>2</sup> /s]



$D_p$	ion diffusivity in physical unit	[m <sup>2</sup> /s]
$D_{LB}$	ion diffusivity in Lattice Boltzmann simulation	
$E_a$	Activation energy of the dissolving element	[J/mol]
$E_{diff}$	Activation energy of diffusion	[J/mol]
$F$	Ion concentration in a lattice node	[mol/L]
$F_0$	Volume fraction of slag or fly ash in the mixture	
$F_{ac}$	Pre-factor	
$F_{non-steady}$	Non-steady factor	
$F_t$	Volume fraction of slag or fly ash at time $t$	
$F_{V-S}$	A factor of the solution-volume to precursor-surface-area ratio	
$\Delta G_{crit}$	Activation energy of step retreat at pre-existing roughness	[J/mol]
$\Delta G_{crit}^n$	Activation energy of etch pit formation at dislocations	[J/mol]
$\Delta_f G^0$	Standard molar Gibbs free energy	[kJ/mol]
$\Delta_f H^0$	Standard enthalpy	[kJ/mol]
$I$	Ionic strength	[mol/kg]
$IAP$	Ion activity product	
$J$	Nucleation rate	m <sup>3</sup> /s
$K_{sp}$	Solubility product	
$L_0$	Conversion factor for length	[m]
$M_0$	Conversion factor for mass	[g]
$M_s$	Activator modulus	
$MW_{N(C)ASH}$	Molecular weight of a N-(C-)A-S-H solid solution member	[g]
$NBO/T$	Ratio of the non-bridging oxygen atoms to oxygen atoms in tetragonal coordination	
$N_a$	Avogadro's number	
$N_p, N_s$	Number of primary reaction products and secondary reaction products that are predicted to nucleate, respectively	
$\Delta N_X$	Dissolved amount of element $X$ at six interfaces at one lattice Boltzmann time step. Element $X$ can be Si, Al, Ca, Mg, S or K	[mol]
$P_{nm}(\cos \theta)$	Legendre polynomial	
$P_{random}$	Random probability	
$P_A, P_B, P_C$	Nucleation probabilities for secondary reaction products	
$P_X, P_Y, P_Z$	Nucleation probabilities for primary reaction products	
$P(\Delta t)$	Nucleation probability at the time interval $\Delta t$	

$Q(t)$	Cumulative heat release at time $t$	[J/g]
$Q_{\max}$	Maximum heat release	[J/g]
$R$	Gas constant	[J·mol <sup>-1</sup> K <sup>-1</sup> ]
$R_c$	Critical radius	[μm]
$S$	Source term	
$SA$	Surface area	[m <sup>2</sup> ]
$SSA$	Specific surface area	[μm <sup>-1</sup> ]
$S^0$	Standard entropy	[J·mol <sup>-1</sup> K <sup>-1</sup> ]
$T$	Absolute temperature	[K]
$T_0$	Conversion factors for time	[s]
$V$	Solution volume	[m <sup>3</sup> ]
$V_a$	Apparent volume of fly ash	[cm <sup>3</sup> ]
$V_v$	Volume of voids in fly ash particle	[cm <sup>3</sup> ]
$X_w$	Total mole amount of the aqueous phase	[mol]
$Y_{nm}(\theta, \varphi)$	Spherical harmonic function	

### Greek letters

$\alpha(t)$	Degree of reaction at time $t$	
$\beta$	Shape parameter	
$\beta_N$	Numerical factor	
$\gamma$	Interfacial energy	J/m <sup>2</sup>
$\gamma_{ef}$	Effective interfacial energy	J/m <sup>2</sup>
$\gamma_m$	Surface tension of mercury	[N/m]
$\gamma_j$	Activity coefficient of the aqueous species $j$	
$\delta_t$	Time step	[s]
$\theta$	Polar angle	
$\theta_{Al}$	Fraction of the quartz surface that is passivated	
$\theta_{Al,max}$	Maximum fraction of the quartz surface that is passivated	
$\lambda$	Time parameter	
$\rho_a$	Apparent density of fly ash	[g/cm <sup>3</sup> ]
$\rho_l$	mass in lattice unit	
$\rho_p$	mass in physical unit	[g]
$\rho_r$	Real density of fly ash	[g/cm <sup>3</sup> ]

$\rho_{N(C)ASH}^{sc}$	Scattering length density	$[\text{m}^{-2}]$
$\rho'_{N(C)ASH}$	Predicted density of a N-(C-)A-S-H solid solution member	$[\text{g}/\text{cm}^3]$
$\sigma$	Ratio of the rate of dissolution of the activated complex relative to the overall reaction rate	
$\tau$	Relaxation time	
$\varphi$	Azimuthal angle	
$\varphi_B, \varphi_C, \varphi_{BC}$	Volume fraction of phase B, phase C and phase BC in the medium, respectively	
$\Phi^\theta$	Denotes the standard heat capacity ( $C_p^\theta$ ) or entropy ( $S^\theta$ )	
$\psi$	Activity factor	
$\omega$	Contact angle between mercury and sample surface	



# List of Abbreviations

---

AABFS	Alkali-activated blast furnace slag
AAMs	Alkali-activated materials
AAFA	Alkali-activated fly ash
AF <sub>m</sub>	Monosulfate aluminate hydrate
AF <sub>t</sub>	Ettringite
A <sub>nm</sub>	a geometrical model
BCI, TU, CB, IC, IW, BT	Sublattice sites in the C-(N-)A-S-H gel structure, where BCI=BT+CB+IC
BFS	Blast furnace slag
C <sub>3</sub> AH <sub>6</sub>	Katoite
C <sub>2</sub> ASH <sub>8</sub>	Strätlingite
CH	Portlandite
CNASH <sub>ss</sub>	C-(N-)A-S-H solid solution model
CSTM	Cross-linked substituted tobermorite model
C, S, A, N, H, F, c	Represent CaO, SiO <sub>2</sub> , Al <sub>2</sub> O <sub>3</sub> , Na <sub>2</sub> O, H <sub>2</sub> O, Fe <sub>2</sub> O <sub>3</sub> and CO <sub>2</sub> in the stoichiometry notations, respectively
C-(N-)A-S-H	Alkali (sodium) calcium-aluminosilicate hydrate
C-S-H	Calcium silicate hydrate
DFT/CGMC	Density functional theory/coarse-grained Monte Carlo
EDS	Energy dispersive spectroscopy
ESEM	Environmental scanning electron microscopy
FA	Fly ash
FTIR	Fourier transform infrared spectroscopy
GEMS	Gibbs energy minimization software
HYMOSTRUC3D	Hydration, morphology and structure (3 dimension) model for simulating cement hydration and microstructure formation
ICP-OES	Inductively coupled plasma optical emission spectroscopy
INFCN	A C-N-S-H end-member
IW*	A fixed interlayer water site

---

MA-OH-LDH	Hydrotalcite-like phase
MIP	Mercury intrusion porosimetry
N-A-S-H	Sodium aluminosilicate hydrate
N(C)ASH <sub>ss</sub>	N-(C-)A-S-H solid solution model
NMR	Nuclear magnetic resonance
OPC	Ordinary Portland cement
PSD	Particle size distribution
T2C*, T5C*, TobH*	Three C-S-H end-members
VRML	Virtual reality modeling language
XRF	X-ray fluorescence
XRD	X-ray diffraction
5CA, INFCA	Two C-A-S-H end-members
5CNA, INFCNA	Two C-N-A-S-H end-members



# PART I

---

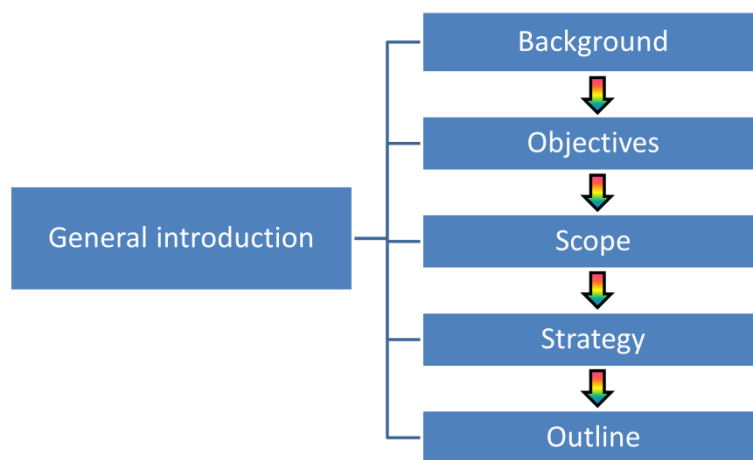
## INTRODUCTION



# Chapter 1

---

## General Introduction



This chapter gives a general introduction of this research. Firstly, the background of this research is introduced. Then, the objectives, scope and strategy of this research are given. Finally, the outline of this research is presented.

## 1.1 Background of this research

Alkali-activated materials (AAMs) are a new class of materials. They are obtained by the chemical reaction of a powdered aluminosilicate precursor (most commonly slag and/or fly ash) with an alkaline activator (usually a solution of sodium hydroxide and/or sodium silicate) at ambient or slightly elevated temperature. Due to their ability to valorize high volumes of industrial by-products as the powdered aluminosilicate precursors, AAMs can deliver an 80 % or greater reduction of CO<sub>2</sub> emission compared to ordinary Portland cement (OPC) based materials [1, 2]. Besides, AAMs release a lower amount of heat [3], and provide comparable or even superior mechanical properties and durability performance in comparison with the OPC-based materials under the similar testing conditions [1, 4-7]. AAMs have been applied in precast products, such as railroad sleepers, precast box culverts, sewer pipes and fire resistant wall panels [8-10]. In particular, AAMs show very promising potential for use in aggressive environments due to their outstanding resistance to chemical attack [10].

AAMs, same as any OPC based materials, are porous materials. The influence of the pore structure on their performance can be viewed from two aspects. First, the pore structure has a significant influence on the mechanical properties of AAMs, such as strength, fracture energy, toughness and elastic properties. Second, the pore structure significantly affects the transport properties of AAMs, such as permeability and diffusivity. Those two aspects determine the durability and service life of AAMs. From the engineering point of view, AAMs, if utilized as building materials, must have high durability and a long service life. To meet these conditions, a homogeneous and dense microstructure is required.

Blast furnace slag and fly ash, as industrial by-products, are the most used aluminosilicate precursors in AAMs. In this research, AAMs are mostly made of alkali-activated slag or fly ash. The reaction of AAMs starts with the dissolution of slag or fly ash, and subsequently a set of reactions commence, resulting in the formation of various solid reaction products. In this way, the microstructure of AAMs is formed.

The pore solution is an essential component of AAMs. It is in this medium where slag or fly ash dissolves and reactions take place to produce solid reaction products. The pore solution composition determines the dissolution kinetics, reflects the ongoing reaction process, and plays a very important role on the durability [11]. The dissolution kinetics determines the degree of reaction, and thus controls the amount of reaction products that are produced with time. Besides the dissolution kinetics, the reaction kinetics also has a large influence on the microstructure formation of alkali-activated materials [12].

The time-dependent microstructure formation is closely associated with the continuous production of reaction products in AAMs. Thermodynamics is essential for understanding the chemical reactions. The thermodynamic modelling has been extensively and successfully used in the research of OPC based materials to describe the reactions and quantify the reaction products [13, 14]. However, thermodynamic modelling is seldom applied in the research of AAMs. Moreover, the studies coupling thermodynamic modelling and kinetics modelling are scant in the research of AAMs. The limited utilization of thermodynamic modelling is mainly due to insufficient data of the solubility products of the solid reaction products in AAMs.

Previous literature shows that the type of alkaline activator leads to a large influence on the reaction kinetics and microstructure formation of AAMs [15-17]. In alkali-activated blast furnace slag, if activated with sodium silicate solution, the rapidly formed rims of reaction products around the slag grains slow down the reaction kinetics. This leaves ample time for

the gels to form evenly and thus results in a well distributed porosity [15]. If activated with sodium hydroxide solution, two layers of reaction products are formed around the slag grains. The outer layer of reaction products are due to a fast precipitation of relatively dense products [15]. Further reactions develop almost entirely in the place of the original slag grains with very little formation in the empty pore space, which results in an inner layer of products [15]. In alkali-activated fly ash, if activated with sodium silicate solution, the reaction products are distributed homogenously throughout the sample – on the surface of fly ash grains and also relatively far away in the interstitial space [16, 17]. But if activated with sodium hydroxide solution, the reaction products are formed predominantly on the surface of fly ash grains rather than in the empty pore space.

To sum up, there are at least four categories of factors that affect the reaction process and microstructure formation of AAMs:

- Reactivity and particle size distribution of raw aluminosilicate precursors.
- Chemical composition of raw aluminosilicate precursors and activators.
- Mixture design (water-to-powder ratio, activator nature and concentration).
- Curing condition (temperature, relative humidity and time).

These parameters determine the microstructure of AAMs. The microstructure controls the general properties including mechanical properties, transport properties and durability.

So far, no computer-based simulation models have been developed to simulate the microstructure formation, particularly the pore structure in hardening AAMs. It is still a big issue and challenge today to numerically obtain the microstructure of AAMs. A robust model or simulation technique will not only help to clarify the conversion process of AAMs from aluminosilicate precursors to binding phases, but also enable to design the applications of AAMs. Based on the knowledge acquired from the experimental study, this research will develop a numerical model to simulate the reaction process and microstructure development of AAMs.

## 1.2 Objectives of this research

The main aim of this research is to develop the numerical model – GeoMicro3D, abbreviated from Geopolymer Microstructure 3 Dimensions. By using this model, the evolution of microstructure can be simulated and the mixtures of AAMs can be properly designed. For these purposes, this study contains the following objectives:

- To experimentally investigate the pore solution composition and reaction kinetics of alkali-activated slag or fly ash paste in various alkaline activation conditions.
- To experimentally study the microstructure development of alkali-activated slag or fly ash paste in various alkaline activation conditions.
- To supplement and improve the thermodynamic database, and quantify the reaction products as a function of time.

- To develop simulation modules, with which it is possible to simulate the initial particle parking structure of slag or fly ash in alkaline activator, dissolution of slag or fly ash, chemical reactions and growth of reaction products.

### 1.3 Scope of this research

In this research, alkali-activated slag paste, alkali-activated fly ash paste and alkali-activated slag blended with fly ash paste were studied. Experimental studies on the reaction process and microstructure development of alkali-activated slag or fly ash paste will be carried out, based on which a numerical model is developed. The specifications can be outlined as follows:

- Two kinds of aluminosilicate precursors: blast furnace slag (BFS), and fly ash (FA).
- Two kinds of alkaline solution: sodium hydroxide, and sodium silicate.
- Water-to-binder ratio: 0.40 for alkali-activated blast furnace slag paste (AABFS) and alkali-activated blend of slag and fly ash paste (AABFS/FA), and 0.35 for alkali-activated fly ash paste (AAFA).
- Curing regime: ambient temperature with sealed curing for AABFS and AABFS/FA, and sealed curing at elevated temperature for AAFA.
- Curing time: up to 28 days.
- No admixtures were used.
- The numerical model is mainly developed for alkali-activated slag or fly ash paste.
- Irregular shape particles were used to represent the particle shapes of BFS and FA.

### 1.4 Strategy of this research

According to the objectives of this research, two aspects are focused on:

- Experimental study of the pore solution composition, reaction kinetics, and microstructure development of alkali-activated slag or fly ash paste in various alkaline activation conditions.
- Numerical simulation of the reaction process and microstructure development of alkali-activated slag or fly ash paste.

Regarding the experiments: inductively coupled plasma optical emission spectroscopy (ICP-OES) analysis technique was used to determine the pore solution composition as a function of time; an isothermal conduction calorimeter was used to measure the heat evolution with time; mercury intrusion porosimetry (MIP) and environmental scanning electron microscopy (ESEM) were used to determine the pore volume and pore size distribution.

Regarding the numerical simulation; the *Anm material model*<sup>1</sup> [18] was extended and used to simulate the initial particle parking<sup>2</sup> structure; a transition state theory<sup>3</sup> based function was employed to describe the dissolution rate; lattice Boltzmann method was used to describe the transport of ions; a thermodynamic tool – *GEMS*<sup>4</sup> [19, 20] was employed to describe the reactions and calculate the amount of reaction products; a nucleation probability theory [21] was applied to quantitatively describe the spatial distribution of reaction products.

## 1.5 Outline of this research

This research is subdivided into four parts.

- Part I: Introduction (Chapters 1 - 2).
- Part II: Experimental study (Chapters 3 - 5).
- Part III: Numerical simulation and validation (Chapters 6 - 9).
- Part IV: Conclusions (Chapter 10).

The structure of this thesis is shown in Figure 1.1. In the first part of this research, a general introduction is presented (Chapter 1). In Chapter 2, a literature survey is given on AAMs, from the dissolution of aluminosilicate precursor to the microstructure formation. A couple of numerical simulation models for AAMs are also briefly described.

In the second part of this research (Chapters 3 - 5), the experimental methods and experimental results are presented in detail. In Chapter 3, the changes in the pore solution composition were measured by using ICP-OES analysis technique. In Chapter 4, the heat release of alkali-activated slag or fly ash paste was measured with an isothermal conduction calorimeter. In Chapter 5, the microstructure analysis of alkali-activated slag or fly ash paste was performed by MIP and SEM-image analysis. All the experimental results will give insights into formulating the numerical model and validating the models in part III.

In the third part of this research (Chapters 6 - 9), the numerical model developed in this research is described in detail. In Chapter 6, the *Anm material model* was extended and used to simulate the initial particle parking structure of alkali-activated slag or fly ash paste using real-shape particles. In Chapter 7, the dissolution of slag and fly ash in alkaline solution was simulated using the lattice Boltzmann method coupled with thermodynamics. In Chapter 8, the existing thermodynamic database for AABFS was presented, and the thermodynamic database for AAFA was established. In Chapter 9, *GEMS* was utilized to describe the reactions and quantify the reaction products. A nucleation probability theory was presented

---

<sup>1</sup> *Anm material model* is a geometrical model, in which a set of spherical harmonic coefficients (anm) are used to describe the irregular particle shape [18]. More detailed information will be given in Chapter 6.

<sup>2</sup> In this research work we used “parking” instead of “packing”. The term “packing” in practice usually means the use of “vibration” to compact the composites. In the simulation, the composite structure after the vibration is simulated. In this process, however, particles are placed one by one without “vibration”.

<sup>3</sup> Transition state theory is the theory that explains the reaction rate of elementary chemical reactions. ([https://en.wikipedia.org/wiki/Transition\\_state\\_theory](https://en.wikipedia.org/wiki/Transition_state_theory))

<sup>4</sup> *GEMS* is a thermodynamic tool. It is abbreviated from Gibbs Energy Minimization Software (<http://gems.web.psi.ch/>).

and applied to describe the nucleation and growth of reaction products. In this way, the numerical model – GeoMicro3D, covering the whole range from the initial particle parking structure to the microstructure formation, was developed for alkali-activated slag or fly ash paste. As a case study, GeoMicro3D was implemented to simulate the reaction process and microstructure formation of alkali-activated slag systems with different alkaline activators.

The last part consists of conclusions of this research. Some remarks and recommendations for future research were presented.

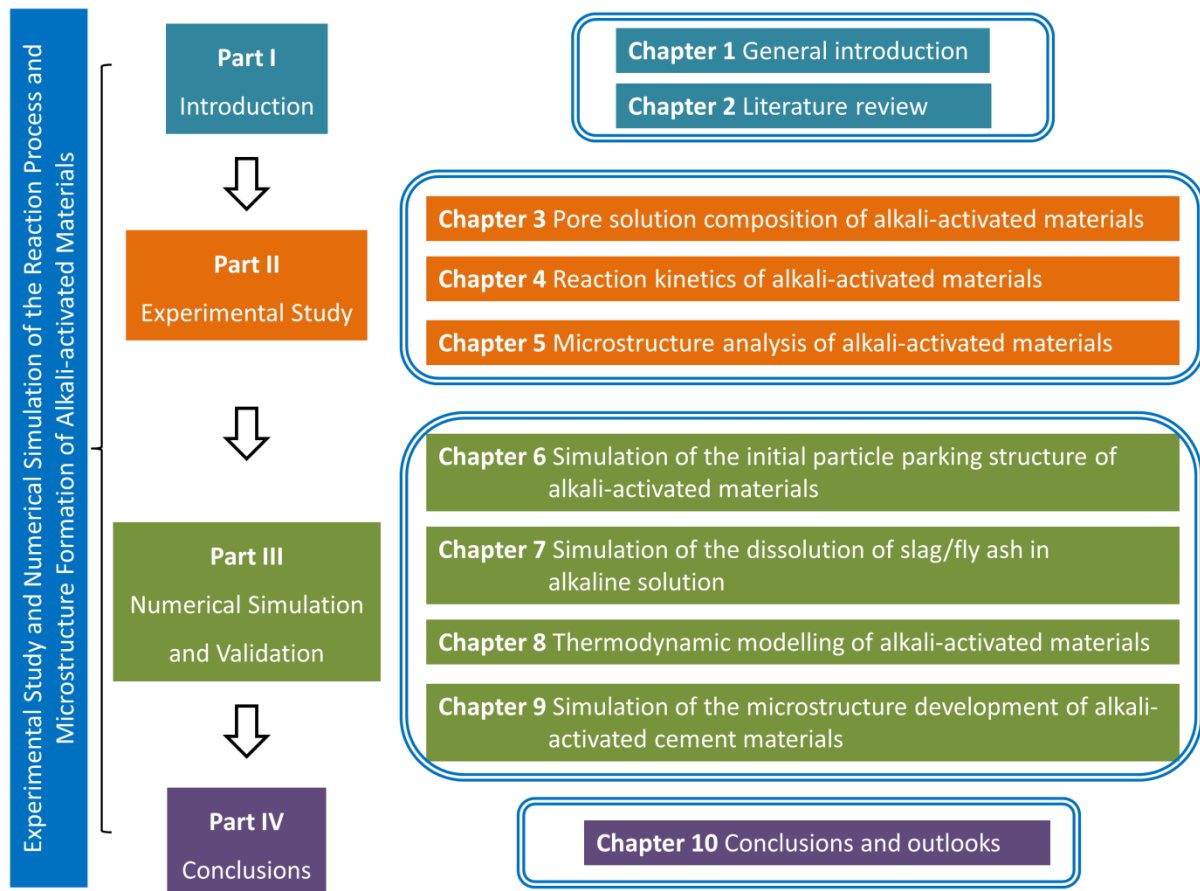
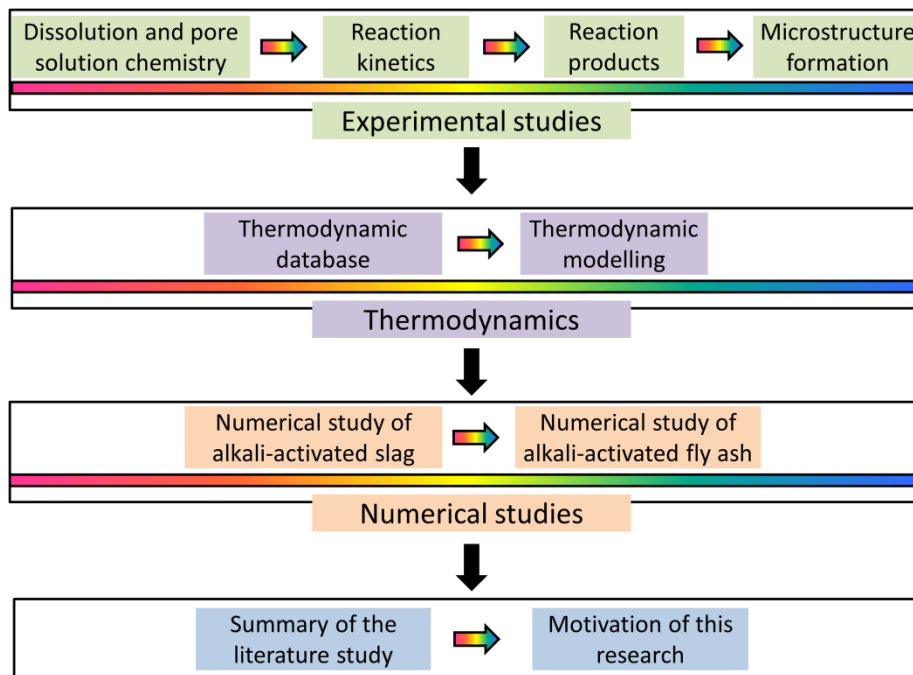


Figure 1.1 Outline of this thesis



# Chapter 2

## Literature review



This chapter presents a literature survey of experimental studies, thermodynamics and numerical studies of alkali-activated materials (AAMs). Experimental studies include dissolution and pore solution chemistry, reaction kinetics, reaction products and microstructure formation. Thermodynamics focus on the thermodynamic database and thermodynamic modelling. Numerical studies are separately surveyed for alkali-activated slag and alkali-activated fly ash. Finally conclusions of the literature study and motivation of this research are given.

## 2.1 Introduction

This chapter presents a literature study of the current state-of-the-art of alkali-activated materials (AAMs). First, the experimental studies of dissolution and pore solution chemistry, reaction kinetics, reaction products and microstructure formation of AAMs, are reviewed. Then, the thermodynamics is discussed in view of thermodynamic database and thermodynamic modelling for AAMs. Afterwards, numerical studies are separately surveyed for alkali-activated slag and alkali-activated fly ash. Finally, the conclusions of the literature study and motivation of this research are given.

## 2.2 Experimental studies of AAMs

### 2.2.1 Dissolution and pore solution chemistry of AAMs

#### *Dissolution of aluminosilicate precursors in alkaline solution*

Aluminosilicate precursors are a class of materials in which Si and Al make up the framework, while alkali and alkali-earth metals like Ca and Mg are the elements that modify the framework [22, 23]. Here the framework refers to the glass network of aluminosilicate materials, as schematically shown in Figure 2.1. The studies of the dissolution of basaltic glass have shown that the dissolution of aluminosilicate precursors can be described in the following four consecutive steps [24-26].

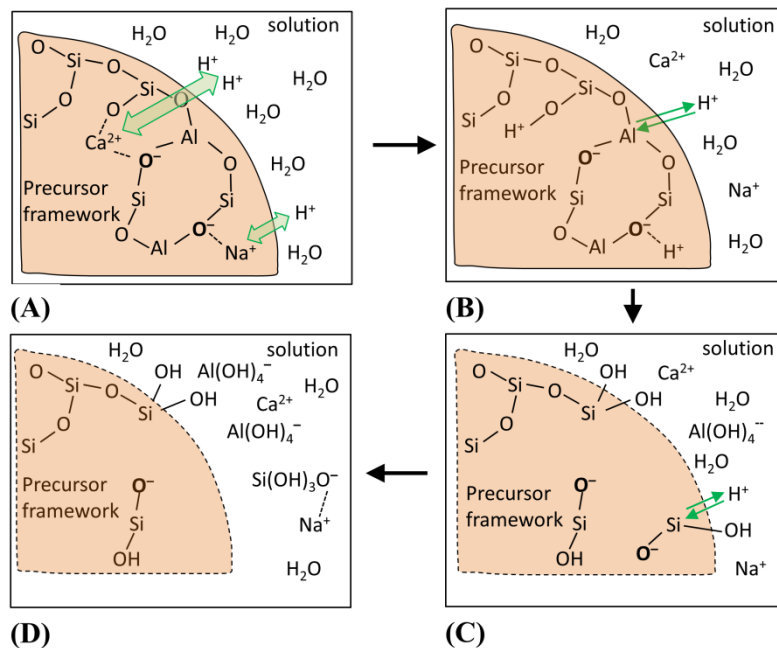


Figure 2.1 Schematic illustration of the dissolution of aluminosilicate glass (modified from [26]). In the graph, all the Si and Al sites within the framework are tetrahedrally coordinated to oxygen, but for clarity additional bonds are not shown.

- (1) First, the alkali and alkali-earth metal elements are initially dissolved from the surface through metal/proton exchange reactions, as shown in Figure 2.1(A).
- (2) Then, the hydrolysis of Al-O bonds starts, as shown in Figure 2.1(B).

- (3) Afterwards, the bonds of Si-O start to break, as shown in Figure 2.1(C).
- (4) Finally, the tetrahedrally coordinated Al and Si in the framework are released into the solution, and the framework is gradually broken down, as shown in Figure 2.1(D).

In this dissolution process, the tetrahedrally coordinated Al dissolves more easily than the tetrahedrally coordinated Si [22]. This is because the Al-O bonds break more easily than the Si-O bonds. Furthermore, the initially dissolved Al leads the fully tetrahedrally coordinated Si to be partially coordinated (Figure 2.1(C)). The partially coordinated Si dissolves faster than the fully coordinated Si. So the framework of aluminosilicate glass dissolves in two steps: initial dissolution of a small fraction of Al (Figure 2.1(B)) and then followed by the dissolution of Si that adjoins the initially dissolved Al (Figure 2.1(C)).

The faster dissolution of Al than Si is supported by experimental findings. Casey et al. investigated the relative dissolution rate of the feldspars as a function of the Al content [27]. The researchers found that a higher content of Al led to a larger dissolution rate of feldspar. In alkali-activated fly ash, it was also reported that Al was preferentially dissolved from fly ash [28]. The leaching characteristics of metakaolin in different alkaline solutions also suggested that the aluminosilicate materials displayed preferential release of Al over Si [29, 30].

The dissolved Al and Si then generate aluminate and silicate species through hydrolysis. In the pore solution of AAMs, the hydrolyzed Si and Al are present in the forms of  $[\text{SiO}(\text{OH})_3]^-$ ,  $[\text{SiO}_2(\text{OH})]^{2-}$  and  $[\text{Al}(\text{OH})_4]^-$  [29-31]. The ratio of  $[\text{SiO}(\text{OH})_3]^-$  to  $[\text{SiO}_2(\text{OH})]^{2-}$  decreased with increase of the pH of the pore solution. So the dissolution and hydrolysis of aluminosilicate precursors in alkaline solution can be described mainly by the following reactions [30]:



### *Pore solution chemistry of AAMs*

The studies of the pore solution chemistry of AAMs are few for alkali-activated slag pastes [11, 32-34], and even rarely reported for alkali-activated fly ash paste and alkali-activated slag/fly ash paste.

Song and Jennings [32] studied the pore solution chemistry of alkali-activated slag. They found that a higher alkalinity of the pore solution led to higher concentrations of Si and Al and lower concentrations of Ca and Mg. In another study it was found that the pore solution influenced the structure and composition of the produced calcium silicate hydrate [33]. In comparison with the pore solution of OPC-based materials, the pore solution of alkali-activated slag paste showed a ten times lower concentration of Ca and ten to hundred times higher concentrations of Si and Na [34]. It was reported that the initiation of pitting at the steel-cement concrete interface started only after the concentration ratio of  $\text{Cl}^-$  relative to  $\text{OH}^-$  exceeded a particular value [35]. This confirms a large dependence of the passivation of reinforcing steel on the alkalinity of the pore solution. Because little soluble Ca is available in

the pore solution of alkali-activated slag to play a buffering role similar to  $\text{Ca}(\text{OH})_2$  in OPC-based materials, the alkalinity of the pore solution of alkali-activated slag is mainly maintained by the content of alkali [11]. Therefore, it is essential to provide a sufficient amount of alkalis to ensure protection of reinforcing steel from corrosion.

It is noted that the elements in solution exist in various forms of aqueous species. In alkaline solution various oligomeric silicate anions and aqueous aluminosilicate species have been detected by  $^{29}\text{Si}$ -NMR (Nuclear Magnetic Resonance) spectroscopy [36]. Figure 2.2 presents the Si distribution in different forms of aqueous species in the sodium silicate solution, obtained by integrating  $^{29}\text{Si}$ -NMR spectra [37]. It showed that the Si was incorporated into monomeric and non-monomeric species in all solutions. The monomeric and non-monomeric silicate species varied with the  $\text{SiO}_2/\text{Na}_2\text{O}$  ratios.

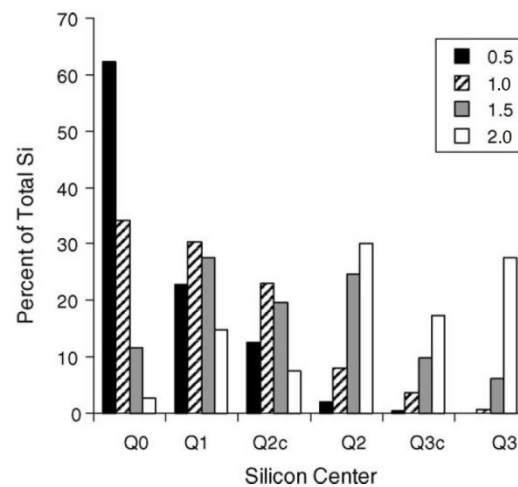


Figure 2.2 The Si distribution in sodium silicate solutions obtained by integrating  $^{29}\text{Si}$ -NMR spectra. The moduli of the sodium silicate solution ( $\text{SiO}_2/\text{Na}_2\text{O}$ ) were 0.5, 1.0, 1.5 and 2.0. In the graph,  $Q_n$  represents a silicate center coordinated to  $n$  other tetrahedral centers and the subscript  $c$  indicates that the sites are present in a three-membered ring. (cited from [37])

### 2.2.2 Reaction kinetics of AAMs

Isothermal calorimetry, as a well-accepted technique for studying the reaction kinetics of OPC based materials, has also been used to study the reaction kinetics of AAMs. Similar to the hydration of OPC, the reaction of AAMs also shows several reaction stages that are controlled by different reaction mechanisms. The types of alkaline activator and aluminosilicate precursors have large impacts on the reaction kinetics of AAMs.

#### *Reaction kinetics of alkali-activated slag*

Through isothermal calorimetry Ravikumar and Neithalath studied the reaction kinetics of alkali-activated slag with *solid* sodium silicate, *liquid* sodium silicate and sodium hydroxide [38]. The calorimetric signal of the *solid* sodium silicate activated slag was similar to that of the sodium hydroxide activated slag paste, showing a very short or even a non-existent induction period. The calorimetric signal of the *liquid* sodium silicate activated slag paste, by contrast, showed a marked induction period, which is similar to that of OPC pastes. The calorimetric signal of the *solid* sodium silicate activated slag paste was different from that of the *liquid* sodium silicate activated slag paste. This difference could be attributed to a higher alkalinity of the *solid* sodium silicate activated system than that of the *liquid* sodium silicate

activated system <sup>5</sup>. Using the in-situ isothermal calorimetry <sup>6</sup>, similar calorimetric characteristics were found in the early-age reaction of sodium hydroxide and sodium silicate activated slag systems [39]. As far as the trends are concerned, the calorimetric responses of the sodium silicate activated slag/fly ash or slag/metakaolin with slag being the dominant component, showed similar calorimetric characteristics to those of the sodium silicate activated slag [40, 41].

Shi and Day [42] used isothermal calorimetry to examine the early reaction of slag activated with different types of alkaline activators at ambient and elevated temperatures. The alkaline activators were sodium hydroxide, sodium carbonate, sodium silicate, and sodium phosphate. Based on the number and location (on the time scale) of the heat release peaks, three models were established to describe the early reaction of alkali-activated slag paste, as shown in Figure 2.3. In the first model (Figure 2.3(A)), only one peak occurs during the first few minutes. The reaction of slag in water is an example of this model. In the second model (Figure 2.3(B)), two peaks appear before and after the induction period, respectively. The reaction of slag in a sodium silicate activated system is an example of this model. In the third model (Figure 2.3(C)), two peaks occur before the induction period and one peak occurs after the induction period. The reaction of slag in a sodium phosphate ( $\text{Na}_3\text{PO}_4$ ) activated system at 50 °C is an example of this model.

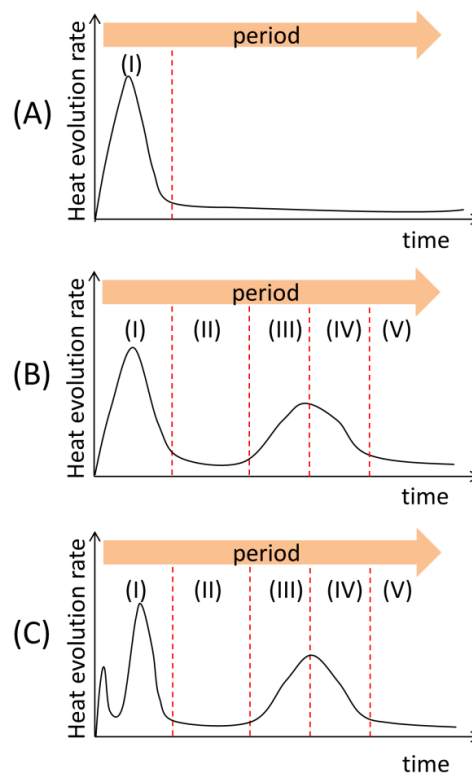


Figure 2.3 Schematic representation of reaction models of alkali-activated slag paste (after [42]).

<sup>5</sup> If not specified, the sodium silicate refers to liquid sodium silicate hereafter.

<sup>6</sup> For in-situ calorimetry test, the binder and solution are stored in a glass ampoule and an attached syringe, respectively, in the calorimeter [39]. Once the thermal equilibrium is reached, the solution is injected into the ampoule and the mixture is mechanically stirred. Then the heat evolution is recorded.

### Reaction kinetics of alkali-activated fly ash

Deir et al. used in-situ isothermal calorimetry to investigate the reaction kinetics of sodium silicate activated fly ash paste at 50 °C [43]. Contrary to the two peaks on the calorimetric curve of sodium silicate activated slag paste, only one peak was observed on the calorimetric curve of sodium silicate activated fly ash paste (see Figure 2.4). This indicated that the exothermic dissolution of fly ash and the formation of reaction products proceeded concurrently in sodium silicate activated fly ash paste. For this reason, the reaction of alkali-activated fly ash paste lacked an induction period. In another study the effect of temperature on the reaction rate of alkali-activated fly ash was investigated by isothermal calorimetry [44]. The alkaline activator was 8 M NaOH solution. At 25 °C, only a small initial dissolution peak was observed, showing that the reaction rate of fly ash was very small at low temperatures. As the temperature increased to 35 and 40 °C, another calorimetric peak appeared and its amplitude was larger for the mixture cured at a higher temperature. This suggests that a higher temperature leads to a higher reaction rate of alkali-activated fly ash.

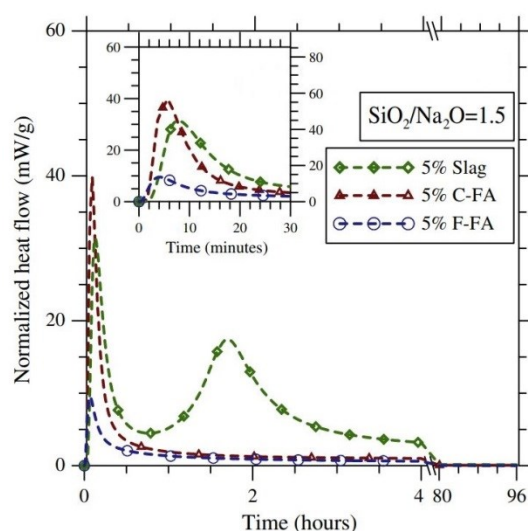


Figure 2.4 Heat evolution of alkali-activated slag and fly ash pastes (cited from [43]). The dosage of  $\text{Na}_2\text{O}$  with respect to precursors and activator moduli ( $\text{SiO}_2/\text{Na}_2\text{O}$ ) were 5 % and 1.5, respectively. The liquid to precursor mass ratio was 0.45.

### Reaction kinetics of alkali-activated slag/fly ash

Gao et al. used the isothermal calorimetry to study the reaction kinetics of alkali-activated slag/fly ash with different activator moduli ( $\text{SiO}_2/\text{Na}_2\text{O}$ ) and different slag/fly ash mass ratios [40]. All samples showed two peaks on the heat flow. The first calorimetric peak, occurring within the first few minutes, mainly reflected the initial wetting/dissolution of aluminosilicate precursors. The second calorimetric peak, occurring after around 6 to 24 hours, reflected the formation of reaction products. After the first calorimetric peak, an induction period appeared and lasted for about 4 to 10 hours before the second calorimetric peak.

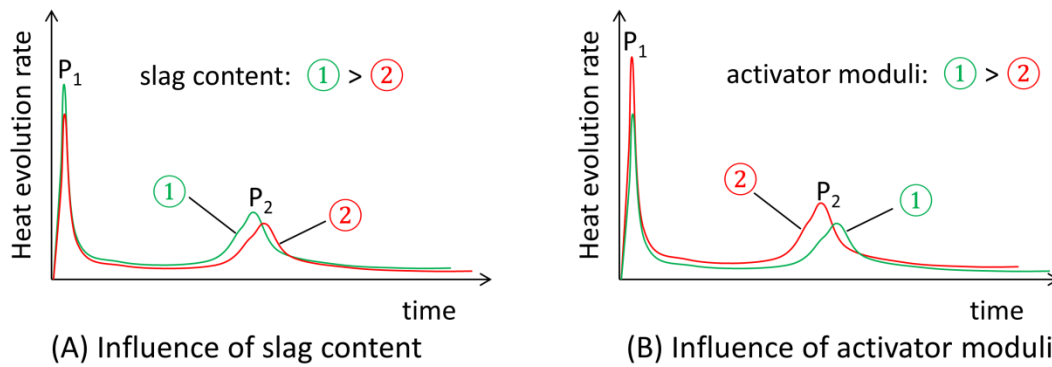


Figure 2.5 Reaction rate curves for describing the influences of slag content (A) and activator moduli (B) on the reaction kinetics of alkali-activated slag/fly ash.

According to the calorimetric signals presented in [40], reaction rate curves are displayed in Figure 2.5 to describe the influences of slag content and activator moduli on the reaction kinetics of alkali-activated slag/fly ash. The mixture with a higher slag content showed a higher dissolution heat flow (Figure 2.5(A)). This indicated that slag dissolves faster than fly ash in alkaline solution at room temperature. In contrast, the decrease of slag content (i.e. the increase of fly ash content) led to a shift of the second calorimetric peak and delayed the formation of reaction products. This is because the decrease of slag content resulted in a smaller overall heat evolution. As shown in Figure 2.5(B), a decrease of the activator moduli led to an increase of the first calorimetric peak. This indicated a more intensive dissolution at the beginning stage. Additionally, the decrease of the activator moduli also resulted in a higher second peak, indicating more intensive reactions.

### 2.2.3 Reaction products of AAMs

The reaction products of AAMs are largely dependent on the type of aluminosilicate precursors. Table 2.1 lists the reaction products of AAMs in comparison with those of OPC-based materials [45]. The reaction products of AAMs are quite different from those of OPC-based materials.

Table 2.1 Reaction products of AAMs and OPC based materials (after [45])

	OPC	AAMs	
		Alkali-activated slag	Alkali-activated fly ash
Primary reaction products	C-S-H	C-(N-)A-S-H	N-A-S-H
Secondary reaction products	CH, AF <sub>m</sub> , AF <sub>t</sub>	hydrotalcite, C <sub>4</sub> AH <sub>13</sub> , C <sub>2</sub> ASH <sub>8</sub> , C <sub>4</sub> AcH <sub>11</sub> , C <sub>8</sub> Ac <sub>2</sub> H <sub>24</sub>	hydroxysodalite, zeolite P, Na-chabazite, zeolite Y, faujasite

Notations: C = CaO, S = SiO<sub>2</sub>, A = Al<sub>2</sub>O<sub>3</sub>, N = Na<sub>2</sub>O, H = H<sub>2</sub>O, c = CO<sub>2</sub>, AF<sub>m</sub> = monosulfate aluminate hydrate, AF<sub>t</sub> = ettringite

#### Reaction products of alkali-activated slag

In alkali-activated slag the primary reaction product is an alkali (mostly sodium) calcium-aluminosilicate hydrate (C-(N-)A-S-H) type gel [46, 47]. As shown in Figure 2.6(A), the C-(N-)A-S-H gel has a layered two-dimensional structure, which is similar to calcium silicate hydrate (C-S-H) in Portland cement-based materials [48]. The structure and composition of C-(N-)A-S-H gels are dependent on the type of alkaline activator. Wang and



Scrivener studied the reaction products of alkali-activated slag paste [49]. It was found that the reaction products (C-(N-)A-S-H gels) formed in sodium hydroxide activated slag paste were more crystalline than those in sodium silicate activated slag paste. Puertas et al. also reported that the type of alkaline activator affected the structure of the C-(N-)A-S-H gels formed in alkali-activated slag paste [50]. In sodium hydroxide activated slag paste, the structure of the C-(N-)A-S-H gel was in between tobermorite 1.4 nm (mean chain length = 5) and tobermorite 1.1 nm (mean chain length = 14). In sodium silicate activated slag, however, the structure of the C-(N-)A-S-H gel showed the co-existence of tobermorite 1.4 nm (chain length = 11) and tobermorite 1.1 nm (chain length = 14). Fernández-Jiménez et al. found that the C-(N-)A-S-H gel had the Ca/Si ratios of 0.6-0.7 in sodium silicate activated slag paste, lower than 0.9-1.0 for Ca/Si ratios in the C-(N-)A-S-H gel in sodium hydroxide activated slag paste [51].

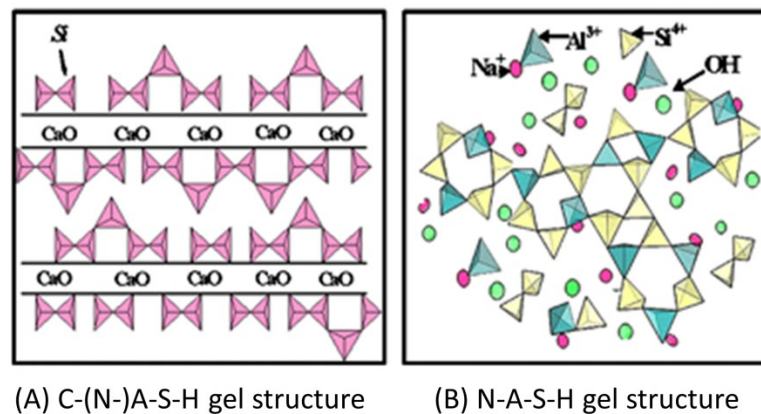


Figure 2.6 Schematic representations of the C-(N-)A-S-H gel structure and N-A-S-H gel structure (cited from [52]).

Besides the primary reaction products, crystalline reaction products (also called secondary reaction products) are usually found in alkali-activated slag paste. Irrespective of the alkaline activator, sodium hydroxide or sodium silicate, a phase known as hydrotalcite is detected [49, 53]. In addition to hydrotalcite, tetracalcium aluminate hydrate [49], katoite [54] and stratlingite [55] are also observed in alkali-activated slag paste.

#### *Reaction products of alkali-activated fly ash*

The primary reaction products of alkali-activated fly ash is a three-dimensional hydrous alkali-aluminosilicate (mostly denoted as N-A-S-H) type gel [46, 56], as schematically represented in Figure 2.6(B). In the three-dimensional structure of N-A-S-H gels, Si and Al are tetrahedrally coordinated and linked by oxygen bonds. The negative charge on the Al tetrahedra is balanced by alkali cations such as  $\text{Na}^+$  and  $\text{K}^+$  [57] (For clarity only  $\text{Na}^+$  is shown in Figure 2.6). The nature of the N-A-S-H gels in alkali-activated fly ash paste depends on the curing time, alkaline activator and curing temperature. Fernández-Jiménez et al. studied the N-A-S-H gels formed in the sodium hydroxide (8 M) activated fly ash paste at 85 °C [58]. After short thermal activation periods (2-5 hours), Si tetrahedra in the formed N-A-S-H gels were surrounded by four Al tetrahedra. As the curing time increased (7 days), a large amount of Si tetrahedra were surrounded by three or two Al tetrahedras. The influence of alkaline activator on the N-A-S-H gels was reviewed in [59]. It was found that the N-A-S-H gels not only depend on the concentration of the soluble silica in the alkaline activator, but also depend on the polymerization degree of silica. Regarding the influence of curing temperature, it is reported that an increase of temperature leads to an increase of



long-range ordering and a higher degree of crosslinking in the N-A-S-H gels [59, 60]. Besides the N-A-S-H gels, secondary reaction products are also found in alkali-activated fly ash paste, such as hydroxysodalite [61], Na-chabazite [58], zeolite Y and zeolite P [62].

#### *Reaction products of alkali-activated slag/fly ash*

In alkali-activated slag/fly ash paste, co-existence of the C-(N-)A-S-H gels and the N-A-S-H gels was identified through selective dissolution and Fourier transform infrared spectroscopy (FTIR) [63]. Ismail et al. studied the phase evolution in alkali-activated slag/fly ash paste and found that the nature of the gel in alkali-activated slag/fly ash depends on the slag/fly ash mass ratio [64]. The C-(N-)A-S-H gel was identified as the main binding product in the systems with the slag content  $\geq 50\%$ . With a lower content of slag in the systems, a hybrid binding phase (N-C-A-S-H type gel) was found.

#### **2.2.4 Microstructure formation of AAMs**

The microstructure formation of AAMs is strongly dependent on the type of alkaline activator. The sodium silicate activated system normally produces a more homogeneous and denser microstructure than the sodium hydroxide activated system. Figure 2.7 shows the microstructure of sodium hydroxide activated slag paste and sodium silicate activated slag paste after 28 days of curing [65]. It can be seen that the sample activated with sodium hydroxide has more capillary pores in the matrix than the sample activated with sodium silicate. The reaction products in the sodium hydroxide activated slag sample were mainly formed around the slag grains, which were less homogeneously distributed than those in the sodium silicate activated slag sample. This activator-dependent microstructure formation of alkali-activated slag paste is also found in other studies [15, 66].

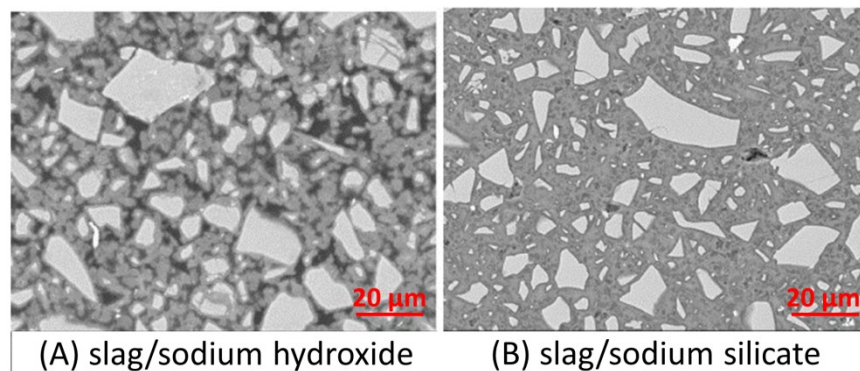


*Figure 2.7 Microstructure of sodium hydroxide and sodium silicate activated slag paste after 28 days of curing (cited from [65]).*

As shown in Figure 2.8 [67], the microstructure formation of alkali-activated fly ash paste is also dependent on the type of alkaline activator. The reaction products in the sodium hydroxide activated fly ash paste were mainly formed on the surface of fly ash grains, leading to a relatively loose microstructure [68]. In contrast, the reaction products in the sodium silicate activated fly ash paste were homogeneously distributed throughout the matrix, not only on the surface of fly ash grains but also in the empty pore space [37]. Therefore, the sodium silicate activated fly ash samples usually exhibit a denser microstructure than the sodium hydroxide activated fly ash samples.

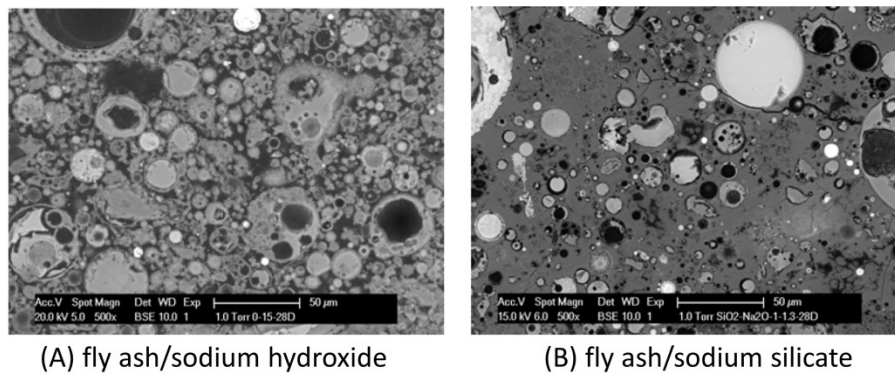


Figure 2.8 Microstructure of sodium hydroxide and sodium silicate activated fly ash paste after 28 days of curing at 40 °C (cited from [67]).

### 2.3 Thermodynamics of AAMs

Thermodynamics is of great significance for understanding chemical reactions [14]. The reactions of AAMs, similar to any other chemical system, also follow the law of thermodynamics. When aluminosilicate precursors are brought into contact with an alkaline activator, their constituents start to dissolve and subsequently various solid reaction products start to be formed if the solution is saturated or oversaturated with respect to the solid reaction products. With thermodynamic modelling it is possible to predict if a reaction will take place and calculate the stable phase assemblage and the aqueous phase composition at the final state when the reaction is completed.

Before performing thermodynamic modelling of AAMs, it is crucial to obtain an appropriate thermodynamic database. A thermodynamic database usually consist of the thermodynamic data for aqueous species and solid phases, such as enthalpy, entropy and Gibbs free energy etc. For alkali-activated slag, the thermodynamic database is available as reported in [54, 69], with which many studies have been carried out on the thermodynamic modelling of alkali-activated slag. For alkali-activated fly ash, however, the thermodynamic data are not complete yet. For this reason, the thermodynamic modelling of alkali-activated fly ash has not been reported in the literature.

#### *CNASH<sub>ss</sub> model and thermodynamic modelling of alkali-activated slag*

Myers et al. were the first who developed a calcium-alkali aluminosilicate hydrate ideal solid solution model (CNASH<sub>ss</sub>) to account for the structurally-incorporated Al and Na into the C-S-H gel [69]. They used this model to thermodynamically simulate the reactions of alkali-activated slag. In this approach, a solid solution was used to describe the C-(N-)A-S-H gel. The solid solution contains two C-A-S-H type gels, two C-N-A-S-H type gels, one C-N-S-H gel and three C-S-H type gels. The thermodynamic properties of these gels were estimated through the optimization of the solubility products for their dissociation reactions. The details of this model will be given in Chapter 8.

In another study, the CNASH<sub>ss</sub> model was used to conduct a thermodynamic modelling study of sodium silicate and sodium carbonate activated slag [54]. Figure 2.9 shows an example of the simulated solid phase evolution of a sodium silicate activated slag paste as a function of the slag reacted (%). The solid phase predictions were in line with the experimentally-determined solid phase assemblage. With the CNASH<sub>ss</sub> model, the phase

diagrams for alkali-activated slag with various alkaline activators could be determined through thermodynamic modelling [70]. By applying the CNASH<sub>ss</sub> model, Ye and Radlinska simulated the phase assemblage and chemical shrinkage of alkali-activated slag [66].

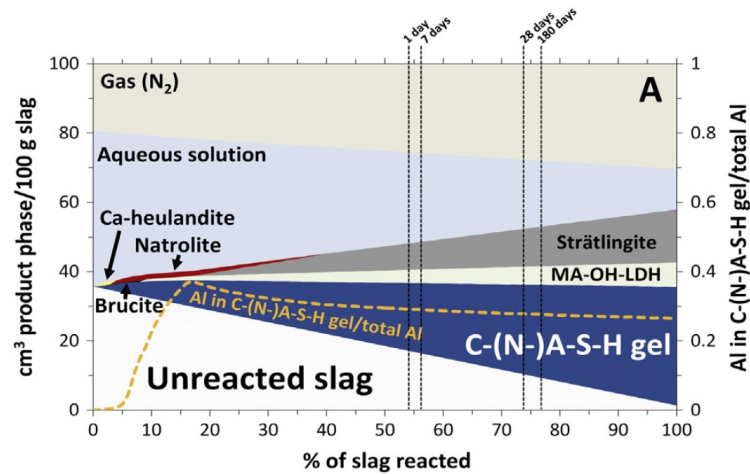


Figure 2.9 Simulated solid phase evolution of a sodium silicate activated slag paste by thermodynamic modelling. In the graph, MA-OH-LDH refers to hydrotalcite. (cited from [54]).

## 2.4 Numerical studies of AAMs

### 2.4.1 Numerical studies of alkali-activated slag

Besides the thermodynamic modelling as discussed in the previous section, the numerical studies of alkali-activated slag has mainly focused on the chemistry and structure of the C-(N-)A-S-H gels. The numerical study of the reaction process and microstructure formation of alkali-activated slag has not been reported yet in the literature.

Puertas et al. established a tobermorite structure based model to describe the C-(N-)A-S-H gels in alkali-activated slag [50]. They found that the type of alkaline activator had a large influence on the structure of the C-(N-)A-S-H gels. This point has been mentioned in Section 2.2.3. Based on the “substituted general model”<sup>7</sup>, Myers et al. developed a generalized model, named the cross-linked substituted tobermorite model (CSTM) [48]. The CSTM model describes the C-(N-)A-S-H gel as a mixture of cross-linked and non-cross-linked tobermorite-based structures, as shown in Figure 2.10. Compared with the models that are based on non-cross-linked tobermorite structure, the CSTM model can describe more appropriately the composition and structure of the C-(N-)A-S-H gels. By combining the CSTM model and the high resolution <sup>29</sup>Si and <sup>27</sup>Al NMR spectroscopy, the role of Al in cross-linking of the C-(N-)A-S-H gels was studied by Myers et al. [72]. The modelling results showed that the Al/Si ratio of the C-(N-)A-S-H gels decreased with curing time.

<sup>7</sup> The “substituted general model” is a structural model that is able to account for the incorporation of elements other than Ca, Si, O and H into the structure of the C-S-H gel [71].

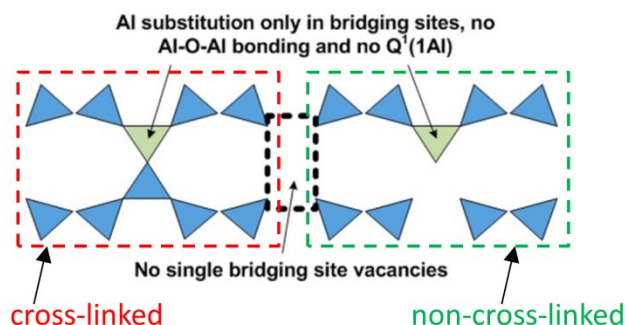


Figure 2.10 An illustration of CSTM model for describing the C-(N-)A-S-H gel. In the graph, the blue and green triangles are Si tetrahedra and Al tetrahedra, respectively. (cited from [48])

According to the stoichiometry, Chen and Brouwers established three stoichiometric models to simulate the reaction products of alkali-activated slag [73]. These three stoichiometric models were established based on the molar balance of each oxide between slag and the solid reaction products. Although the simulation results are in agreement with the experimental results, it should be noted that the influence of alkaline activator and pore solution composition were not taken into account.

## 2.4.2 Numerical studies of alkali-activated fly ash

As far as the literature is reviewed up to now, the numerical simulation of microstructure formation of alkali-activated fly ash has not been reported yet. Instead, the literature mainly focuses on the numerical simulation of aluminosilicate dissolution, speciation and polymerization during the reaction process of alkali-activated fly ash. There are several numerical models or approaches that were used to numerically simulate the gelation of the N-A-S-H gels and the reaction process of alkali-activated fly ash or metakaolin in the current literature.

### (1) Molecular model

Catlow et al. calculated the formation and condensation energies of a range of aluminate, silicate and aluminosilicate clusters by coupled modelling techniques of *ab initio* and molecular mechanics [74]. They found that the formation of Si-O-Si bridges in dimers is energetically favorable, while the formation of Al-O-Al bridges is energetically unfavorable. Lolli et al. presented a molecular model for the N-A-S-H gels by creating vacancies in a sodalite cage [75]. Figure 2.11 shows the simplified scheme of the construction process to obtain a defective structure. Compared with the crystalline and amorphous model structures with analogous chemical compositions, it was found that the defective structure model was the best to capture the position and impact of the Si-O-Si peak at 3.1 Å and the Na-O peak at 2.3 Å.

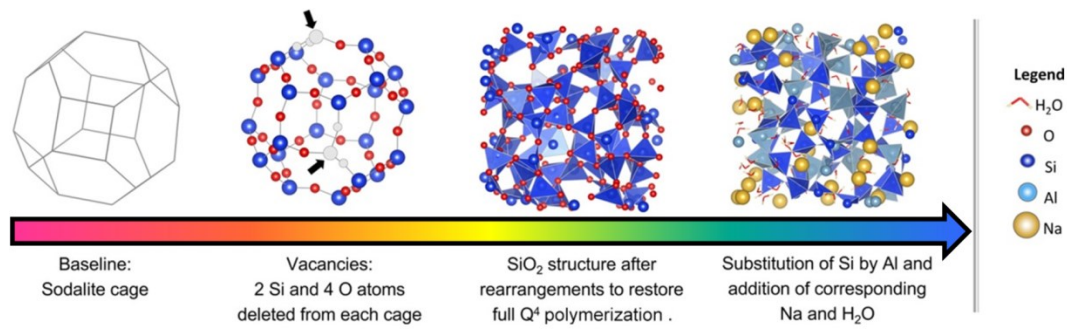


Figure 2.11 Simplified scheme of the construction process to obtain a defective structure (cited from [75]).

## (2) Kinetic model

Based on the aluminosilicate weathering model<sup>8</sup>, Provis et al. developed a reaction kinetic model [77]. This reaction kinetic model was proven to be valuable in highlighting certain factors that determined the setting rate of alkali-activated metakaolin. However, the implementation of this kinetic model is only valid for a single SiO<sub>2</sub>/Al<sub>2</sub>O<sub>3</sub> ratio. Later on, Provis et al. modified this kinetic model to take varying SiO<sub>2</sub>/Al<sub>2</sub>O<sub>3</sub> ratios into account [78]. Figure 2.12 shows the scheme of the modified reaction kinetic model. Based on the reactions in Figure 2.12, the kinetic expressions to describe these reactions can be established and thus the reaction process can be numerically simulated. The results showed that this modified reaction kinetic model was able to provide a plausible description of the reaction process of alkali-activated metakaolin or fly ash. This kinetic model, however, still needs to be developed further based on a broader set of experimental data.

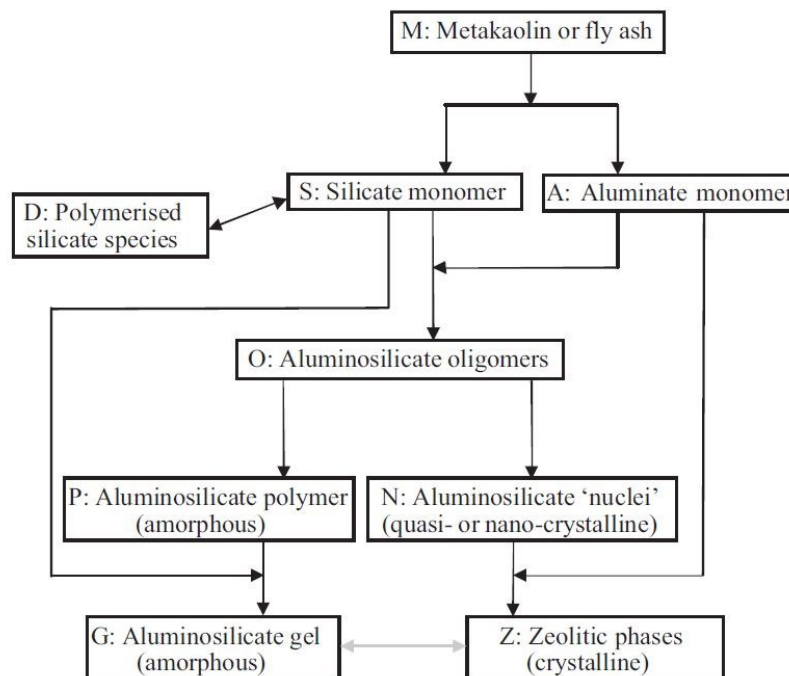
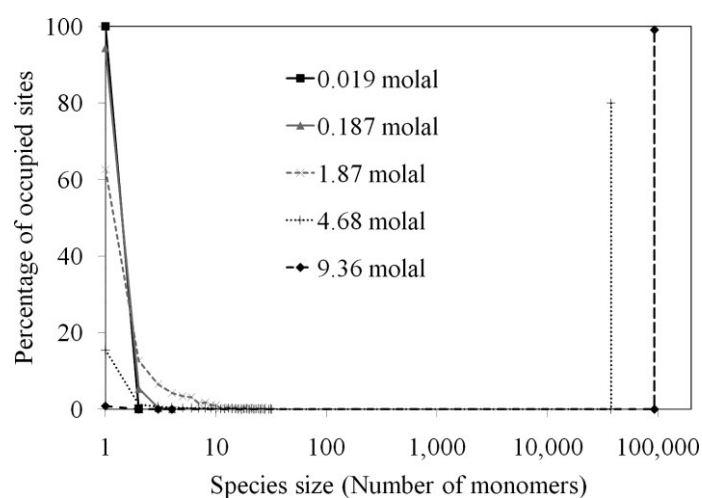


Figure 2.12 Scheme of the modified reaction kinetic model of alkali-activated metakaolin or fly ash (cited from [78]).

<sup>8</sup> The aluminosilicate weathering model is a kinetic model proposed to analyze the dissolution and reprecipitation steps within an overall reaction process [76].

### (3) Multiscale simulation

White et al. developed a multiscale simulation approach to simulate the dissolution and polymerization process of aluminosilicate [79]. This approach was called density functional theory based coarse-grained Monte Carlo (DFT/CGMC) model. The density functional theory was used to calculate Gibbs free energies of the dimerization of silicate species. The coarse-grained Monte Carlo simulation was carried out by considering the interactions of silicate species. With the DFT/CGMC model, the silica solubility and precipitation in sodium silicate solution was studied. The results showed that the silica species tended to form a single large cluster at high silica concentrations, as seen in Figure 2.13. In another study the DFT/CGMC model was used to simulate the reaction process of alkali-activated metakaolin with different alkaline activators [80]. The simulation results revealed that a higher silica content in the alkaline activator led to more precipitation of species in the polymerization process and less monomeric species in the pore solution.



*Figure 2.13 Cluster size distributions at different silica concentration, as obtained by simulation (cited from [79]). The simulation ensemble consists of a 125000 site cubic lattice. An occupied site represent a silica site.*

Through the density functional theory based quantum mechanics, molecular mechanics and molecular dynamics, Kupwade et al. investigated the behavior of the N-A-S-H gels and so called K-A-S-H gels at different temperatures and Si/Al ratios [81]. Here the K-A-S-H gel is also an alkali-aluminosilicate type gel, similar to the N-A-S-H gel. At the atomic scale, the DFT-based quantum mechanics was used to calculate an electronic structure with the considered interactions between atomic nuclei and electrons. At the intermediate molecular scale, the inter-particle energy was obtained through the quantum mechanical calculations at the atomic scale. At the macroscopic scale, the properties obtained from the intermediate scale were used as input and the kinetic Monte Carlo simulation was carried out to obtain the reaction rates of chemical reactions. The multiscale simulation results showed that the N-A-S-H gels exhibited higher thermal stability than the K-A-S-H gels at elevated temperatures, and the N-A-S-H gels with the Si/Al ratio of 2 showed the highest stability compared to all other gels.

## 2.5 Summary of the literature study

Alkali-activated materials (AAMs) show very promising potential for utilization as construction materials [82]. Previous studies have shown that AAMs exhibit many superior properties, such as high early mechanical strength [4] and high resistance to chemical attack [7, 10]. These properties are mainly dependent on the reaction process and microstructure formation of AAMs. However, the reaction process and microstructure formation of AAMs are not fully understood yet.

Aluminosilicate precursors are mixed with alkaline activator to produce AAMs. When the precursors are brought into contact with the alkaline activator, the precursors start to dissolve and subsequently a set of reactions take place to produce the solid reaction products. The pore solution composition of AAMs plays important roles in *dissolution kinetics*, *thermodynamics* and *durability* of AAMs. The chemistry of the pore solution of AAMs, however, has not been intensively studied yet in the literature. There is a lack of experimental data on the pore solution composition of AAMs, particularly for alkali-activated fly ash and alkali-activated slag/fly ash systems.

A lot of researchers have used isothermal calorimetry to study the reaction kinetics of AAMs, such as the effects of temperature [12, 42] and alkaline activator [38-41]. These calorimetric investigations provide a better understanding of the early reaction of AAMs, such as the reaction stages during the reaction process. However, the reaction mechanisms behind the reaction stages are not well studied. Particularly, the origin of the induction period during the reaction process remains unclear.

Thermodynamics is essential for understanding the chemical reactions [14]. With thermodynamic modelling it is possible to predict whether a reaction will take place and calculate the compositions of solid phase and aqueous phase once the reaction is completed. The quality of the thermodynamic modelling results are directly dependent on the quality and completeness of the thermodynamic database. In AAMs, however, the thermodynamic database is far from complete, particularly for the alkali-activated fly ash system. Insufficient thermodynamic data limits the application of thermodynamic modelling in AAMs.

So far the numerical studies of AAMs are mainly limited to the structure of either the C-(N-)A-S-H gels or the N-A-S-H gels. No computer-based simulation models have been developed yet to simulate the microstructure evolution, particularly the pore structure in hardening AAMs. As a result, many microstructure related physical properties could not be studied numerically.

## 2.6 Motivation of this research

The problems defined above motivate to conduct a fundamental research on the reaction process and microstructure formation of AAMs, both experimentally and numerically. The following chapters in this thesis mainly consist of two parts: experimental study and numerical simulation. The experimental study will provide new results for better understanding the reaction process and microstructure formation of AAMs. Better insights from the experimental study then help to develop a robust numerical model. With this numerical model, the reaction process and many microstructure related physical properties can be studied and predicted numerically.







## PART II

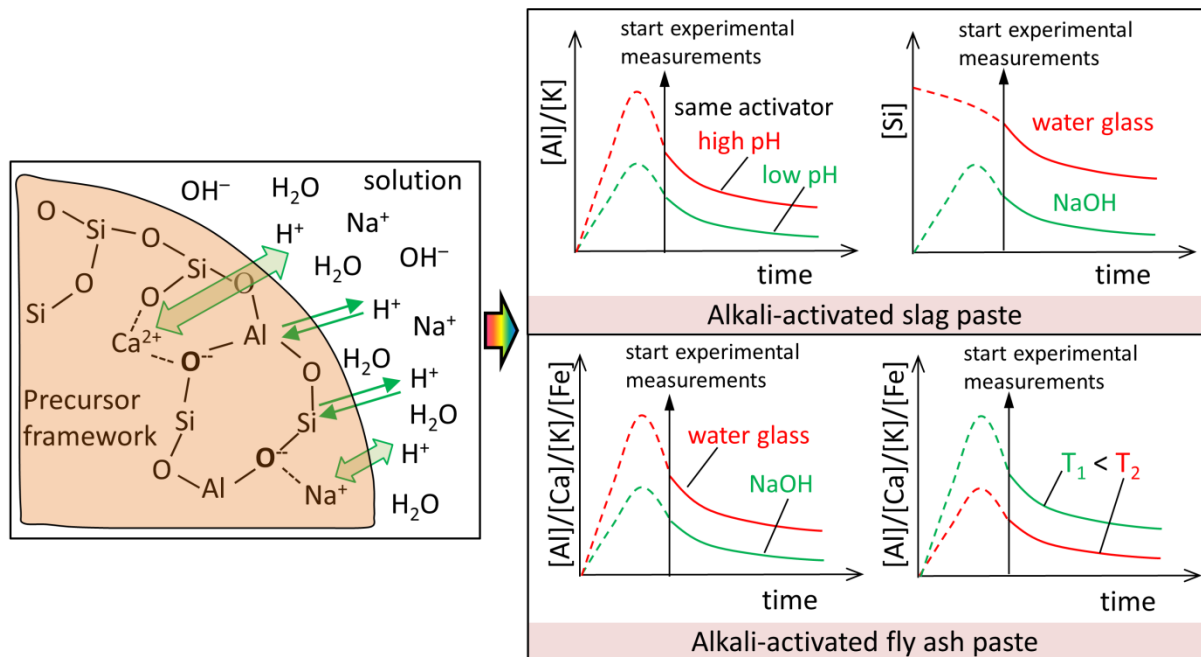
---

# EXPERIMENTAL STUDY



# Chapter 3

## Pore solution composition of alkali-activated materials<sup>9</sup>



Pore solution is an essential component of alkali-activated materials (AAMs). It is in this medium where the powdered aluminosilicate precursors dissolve and subsequently reactions take place to produce solid reaction products. The pore solution composition of AAMs plays important roles in *dissolution kinetics*, *thermodynamics* and *durability* of AAMs. This chapter investigated the pore solution compositions of alkali-activated slag pastes, alkali-activated fly ash pastes and alkali-activated slag/fly ash pastes using the ICP-OES analysis technique. The influences of the type and concentration of alkaline activator and temperature on the pore solution composition were investigated. The obtained results will contribute to new insights regarding the chemistry of pore solution and thermodynamic modelling of AAMs. Particularly, these results will be used to validate the numerical model – GeoMicro3D developed in this research.

<sup>9</sup> This chapter is partially based on:

Yibing Zuo, Marija Nedeljkovic, Guang Ye. Pore solution composition of alkali-activated slag/fly ash pastes, *Cement and Concrete Research*, 115(2019) 230-250.

### 3.1 Introduction

Pore solution is an essential component of alkali-activated materials (AAMs). It is in this medium where the powdered aluminosilicate precursors (mostly slag and fly ash) dissolve and subsequently a set of reactions take place to produce solid reaction products. The role of pore solution can be viewed from the following three aspects.

- (1) *Dissolution kinetics*. In this research, the term “kinetics” is used to describe the rate of chemical reaction processes [83]. In AAMs, the high concentration of  $\text{OH}^-$  ions in the pore solution cause breaking of bonds, such as Si-O and Al-O on the surface of aluminosilicate precursors [31]. A higher alkalinity of the pore solution accelerates the dissolution kinetics of aluminosilicate precursors [15, 84]. The dissolution kinetics of aluminosilicate precursors then determines the degree of reaction and controls the reaction kinetics of AAMs, as well as the amount of solid reaction products produced with time.
- (2) *Thermodynamics*. Thermodynamics is of great significance for understanding the chemical reactions [14]. Similar to any other chemical system, the reactions of AAMs also follow the law of thermodynamics. When aluminosilicate precursors are brought into contact with an alkaline activator, their constituents start to dissolve and subsequently various solid reaction products start to form if the solution is saturated or oversaturated with respect to the respective solid reaction product. At the given temperature and pressure, the pore solution composition controls the ongoing reaction process and determines what reaction products are to be formed [13, 85].
- (3) *Durability*. The dominant phase assemblage in AAMs is an alkali (mostly sodium) calcium-aluminosilicate hydrate (C-(N-)A-S-H) type gel or a hydrous alkali-aluminosilicate (N-A-S-H) type gel, which is dependent on the Ca content in the system [46]. From the durability point of view, the high alkalinity of the pore solution ensures the stability of calcium-aluminosilicate hydrates [86] and alkali-aluminosilicate gels [87] in AAMs. If steel reinforcement is embedded in AAMs, the pore solution plays an important role by forming a passive film on the surface of steel rebars and consequently avoiding the corrosion of the steel rebars [88, 89].

Those three aspects illustrate the significance of the pore solution in AAMs. Furthermore, the chemical and physical properties of aluminosilicate precursors vary significantly from different sources [3, 46, 90], such as chemical composition, reactivity, surface morphology and particle size distribution etc.. For this reason, the alkali activation of aluminosilicate precursors greatly relies on the pore solution composition. However, studies regarding the pore solution composition of AAMs are few for alkali-activated slag paste [11, 32-34, 91], and even rarely reported either for alkali-activated fly ash paste or for alkali-activated slag/fly ash paste.

In this chapter, the pore solutions of alkali-activated slag, alkali-activated fly ash and alkali-activated slag/fly ash pastes were analyzed by means of the inductively coupled plasma-optical emission spectroscopy (ICP-OES) analysis technique. The influences of type and concentration of alkaline activator and temperature on the pore solution composition were investigated. The experimental data of the pore solution composition obtained in this chapter contribute to: validation of thermodynamic modelling in Chapter 8; as well as the formulation and validation of the numerical model (GeoMicro3D) in Chapter 9.

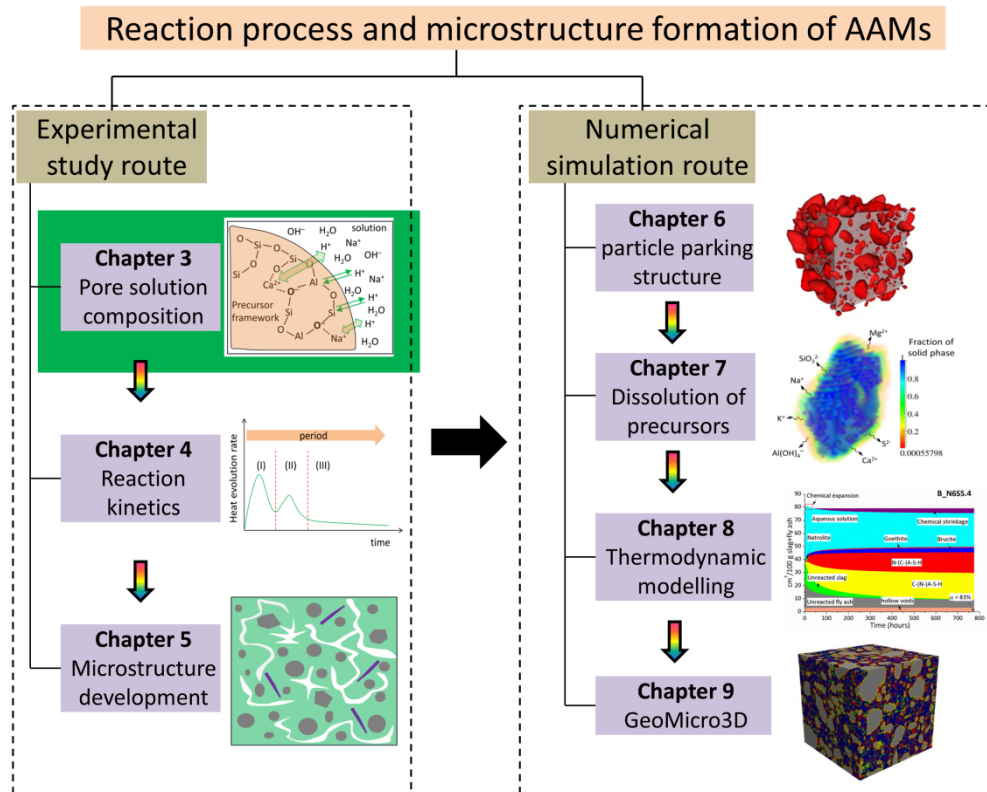


Figure 3.1 Position of chapter 3 in structure of the study of the reaction process and microstructure formation of AAMs in this thesis

Figure 3.1 shows the position of Chapter 3 in structure of the study of the reaction process and microstructure formation of AAMs experimentally and numerically in this thesis.

## 3.2 Materials and methods

### 3.2.1 Materials

In this research ground granulated blast furnace slag and fly ash were used as the aluminosilicate precursors to prepare the alkali-activated slag/fly ash pastes. The chemical compositions of blast furnace slag and fly ash were determined by X-ray fluorescence spectrometry (XRF), and are listed in Table 3.1. The densities of slag and fly ash are  $2.97 \text{ g/cm}^3$  and  $2.33 \text{ g/cm}^3$ , respectively, measured by pycnometer. The particle size distributions (PSDs) of slag and fly ash were measured by laser diffraction, and are plotted in Figure 3.2. The average particle sizes of slag and fly ash are  $19 \text{ }\mu\text{m}$  and  $23 \text{ }\mu\text{m}$ , respectively. Sodium hydroxide (analytical grade, >98 %) and water glass (8.25 wt.%  $\text{Na}_2\text{O}$ , 27.5 wt.%  $\text{SiO}_2$  and 64.25 wt.%  $\text{H}_2\text{O}$ ) were used to prepare two types of alkaline activators: sodium hydroxide activator and sodium silicate activator.

Table 3.1 Chemical compositions of blast furnace slag and fly ash (by weight, %)

Oxide	$\text{SiO}_2$	$\text{CaO}$	$\text{Al}_2\text{O}_3$	$\text{MgO}$	$\text{Fe}_2\text{O}_3$	$\text{SO}_3$	$\text{K}_2\text{O}$	$\text{TiO}_2$	L.I.
Slag	32.91	40.96	11.85	9.23	0.46	1.61	0.33	1.00	1.15
Fly ash	52.90	4.36	26.96	1.50	6.60	0.73	1.31	1.14	3.37

L.I. refers to loss on ignition.

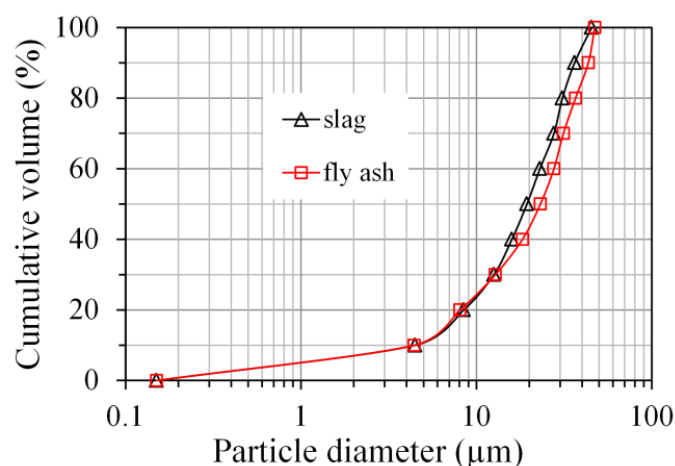


Figure 3.2 Particle size distributions of slag and fly ash

The X-ray diffraction patterns of slag and fly ash are plotted in Figure 3.3. Quartz ( $\text{SiO}_2$ ), mullite ( $(\text{Al}_2\text{O}_3)_{1.136}(\text{SiO}_2)_{0.728}$ ) and hematite ( $\text{Fe}_2\text{O}_3$ ) are the three crystalline phases identified in fly ash. In order to determine the amorphous content of fly ash, corundum ( $\alpha\text{-Al}_2\text{O}_3$ ) was added as an internal standard to replace 20 % of fly ash. Through the Rietveld analysis method [92], the amorphous content of fly ash was determined as 71 %. In this work it is assumed that the amorphous content are reactive and the crystals are non-reactive in fly ash. By subtracting  $\text{SiO}_2$  and  $\text{Al}_2\text{O}_3$  in the crystalline phases from the total  $\text{SiO}_2$  and  $\text{Al}_2\text{O}_3$ , the reactive  $\text{SiO}_2$  and  $\text{Al}_2\text{O}_3$  were determined as 37% and 15%, respectively. These results agree with the measurements (34.9 % and 16.2 %) by Ma using the chemical dissolution treatment (we used a similar fly ash from the same power plant in The Netherlands) [67]. For slag, no crystalline phase was identified from the X-ray diffraction pattern. This is consistent with the fact that usually the ground granulated blast furnace slag contains more than 95 % vitreous phase [73].

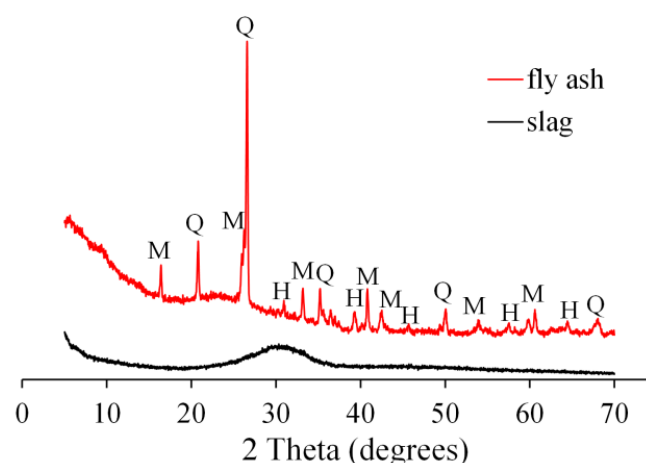


Figure 3.3 X-ray diffraction of slag and fly ash. In the graph, Q, M and H refer to quartz, mullite and hematite respectively.

### 3.2.2 Mixtures

As shown in Table 3.2, a series of alkaline activators with different contents of  $\text{Na}_2\text{O}$  and  $\text{SiO}_2$  were used to prepare alkali-activated slag paste, alkali-activated fly ash paste and alkali-activated slag/fly ash paste. In the notations for the samples, BFS, FA and B indicate alkali-activated slag paste, alkali-activated fly ash paste and alkali-activated slag/fly ash paste, respectively. N and S indicate weight percentages of  $\text{Na}_2\text{O}$  and  $\text{SiO}_2$  with respect to the precursor, and T indicates the temperature in Celsius. The  $\text{Na}_2\text{O}$  in alkaline activator consists of the  $\text{Na}_2\text{O}$  from sodium hydroxide and the  $\text{Na}_2\text{O}$  from water glass. For alkali-activated slag paste and alkali-activated slag/fly ash paste, the water-to-precursor ratio was 0.40. For alkali-activated fly ash paste, the water-to-precursor ratio was 0.35. The water in the water glass was also included in the calculation of the water-to-precursor ratio. For all samples sealed curing was applied. According to the type of alkaline activator the samples can be categorized into two systems: sodium hydroxide activated system (with no  $\text{SiO}_2$  in the alkaline activator) and sodium silicate activated system (with  $\text{SiO}_2$  in the alkaline activator).

Table 3.2 Mixture compositions and curing temperature

Sample	Precursor	$\text{Na}_2\text{O}^a$	$\text{SiO}_2^a$	$M_s^b$	Curing temperature
BFS_N4S0	slag	4	0	0	20 °C
BFS_N6S0	slag	6	0	0	20 °C
BFS_N8S0	slag	8	0	0	20 °C
BFS_N4S2.7	slag	4	2.7	0.6975	20 °C
BFS_N4S5.4	slag	4	5.4	1.395	20 °C
BFS_N6S5.4	slag	6	5.4	0.93	20 °C
BFS_N8S5.4	slag	8	5.4	0.6975	20 °C
FA_N6.2S0T40	fly ash	6.2	0	0	40 °C
FA_N9.3S0T40	fly ash	9.3	0	0	40 °C
FA_N9.3S9T40	fly ash	9.3	9	1	40 °C
FA_N6.2S0T60	fly ash	6.2	0	0	60 °C
FA_N9.3S0T60	fly ash	9.3	0	0	60 °C
FA_N9.3S9T60	fly ash	9.3	9	1	60 °C
B_N6S5.4	blend <sup>c</sup>	6	5.4	0.93	20 °C

a. weight percentage with respect to precursor content (wt. %).

b.  $M_s$  is the molar modulus of alkaline activator, calculated as:  $M_s = \text{SiO}_2(\text{mol})/\text{Na}_2\text{O}(\text{mol})$ .

c. blend = 50 wt.% slag + 50 wt. % fly ash.

The pH and concentrations of Na, Si, and  $\text{OH}^-$  in the alkaline activators are listed in Table 3.3. These results were obtained through the thermodynamic calculations using GEM-Selector V3 (<http://gems.web.psi.ch/>). More details of this software will be introduced in Chapter 8. In sodium hydroxide solution, NaOH is not completely ionized and aqueous sodium hydroxide ( $\text{NaOH}(\text{aq})$ ) normally exists. For this reason, the measured concentration of  $\text{OH}^-$  in the pore solution through titration against hydrochloride acid includes the hydroxide ions from  $\text{NaOH}(\text{aq})$ . In order to be consistent with the experimental data, the hydroxide from  $\text{NaOH}(\text{aq})$  was also included in the obtained concentration of  $\text{OH}^-$  by thermodynamic calculations.

Table 3.3 The pH and concentrations (mmol/L) of Na, Si, and OH<sup>-</sup> in the alkaline activators

Sample	pH	[Na]	[Si]	[OH <sup>-</sup> ]
BFS_N4S0	14.31	3239	0	3239
BFS_N6S0	14.50	4857	0	4857
BFS_N8S0	14.64	6466	0	6466
BFS_N4S2.7	14.14	3204	1117	1757
BFS_N4S5.4	13.87	3193	2227	821
BFS_N6S5.4 and B_N6S5.4	14.30	4773	2219	2218
BFS_N8S5.4	14.52	6339	2211	3636
FA_N6.2S0T40 and FA_N6.2S0T60	14.58	5731	0	5731
FA_N9.3S0T40 and FA_N9.3S0T60	14.79	8564	0	8564
FA_N9.3S9T40 and FA_N9.3S9T60	14.60	8340	4170	3908

### 3.2.3 Pore solution analysis via ICP-OES

#### *Sample preparation*

The aluminosilicate precursor, i.e. slag or fly ash, and alkaline activator were mixed in a commercial Hobart mixer with two minutes low-speed (140±5 r/min) mixing, followed by two minutes high-speed (285±10 r/min) mixing. Subsequently, the alkali-activated slag or fly ash paste was cast into commercial cylinder polyethylene jars (d=35 mm and h=70 mm) and vibrated for 30 seconds on a vibrating table. All the samples were stored in the sealed condition at the defined temperatures in Table 3.2 until the testing age.

The pore solutions of hardened samples were extracted using the steel-die method [93] at different curing ages. Pressures of up to 300 MPa were used to extract the pore fluid from the samples. For each sample two specimens at least were pressed to collect the pore solution. After extraction, the pore solution was immediately filtered using Whatman 41 filter paper.

#### *Measurements of the element concentration*

One part of the filtered solution was diluted using nitric acid (0.2 vol.%). The diluted solutions were analyzed through a PerkinElmer Optima 5300DV ICP-OES spectrometer, by which the concentrations of Si, Al, Ca, Na, K, Fe and Mg were determined. The concentration of OH<sup>-</sup> was measured by titration against hydrochloride acid (0.1 mol/L).

For the measurement of sulfur, another part of the filtered pore solution was diluted with sodium hydroxide solution (0.1 mol/L) instead of nitric acid, and subsequently subjected to ICP-OES analysis. This is because S mostly exists as sulfide (HS<sup>-</sup>) in the pore solution [34, 94]. The dilution with nitric acid acidified HS<sup>-</sup> and led to formation of H<sub>2</sub>S as described by Equation (3.1). On one hand, H<sub>2</sub>S evaporated and resulted in a characteristic foul odor of rotten eggs. On the other hand, H<sub>2</sub>S might be oxidized and led to white precipitation of sulfur as described by Equations 3.1 and 3.2, and shown in Figure 3.4.





Figure 3.4 shows the white precipitation under the scanning electron microscopy (SEM) and its element composition using energy dispersive spectroscopy. This finding confirmed the fact that the nitric acid dilution acidified  $\text{HS}^-$  and the oxidation of  $\text{H}_2\text{S}$  resulted in white precipitation of sulfur.

#### *Accuracy of ICP-OES measurements*

In the preliminary tests, replicates of pore solution samples were prepared and subject to ICP-OES analysis. The variation of the results were within 3.3 %, 2.7 %, 1.7 %, 9 %, 2 % and 2 % for the measurements of the concentrations of Si, Al,  $\text{OH}^-$ , Ca, Na and K, respectively. In addition, the measured element concentrations in the pore solution of alkali-activated slag paste are in line with the values reported in the literature [32-34].

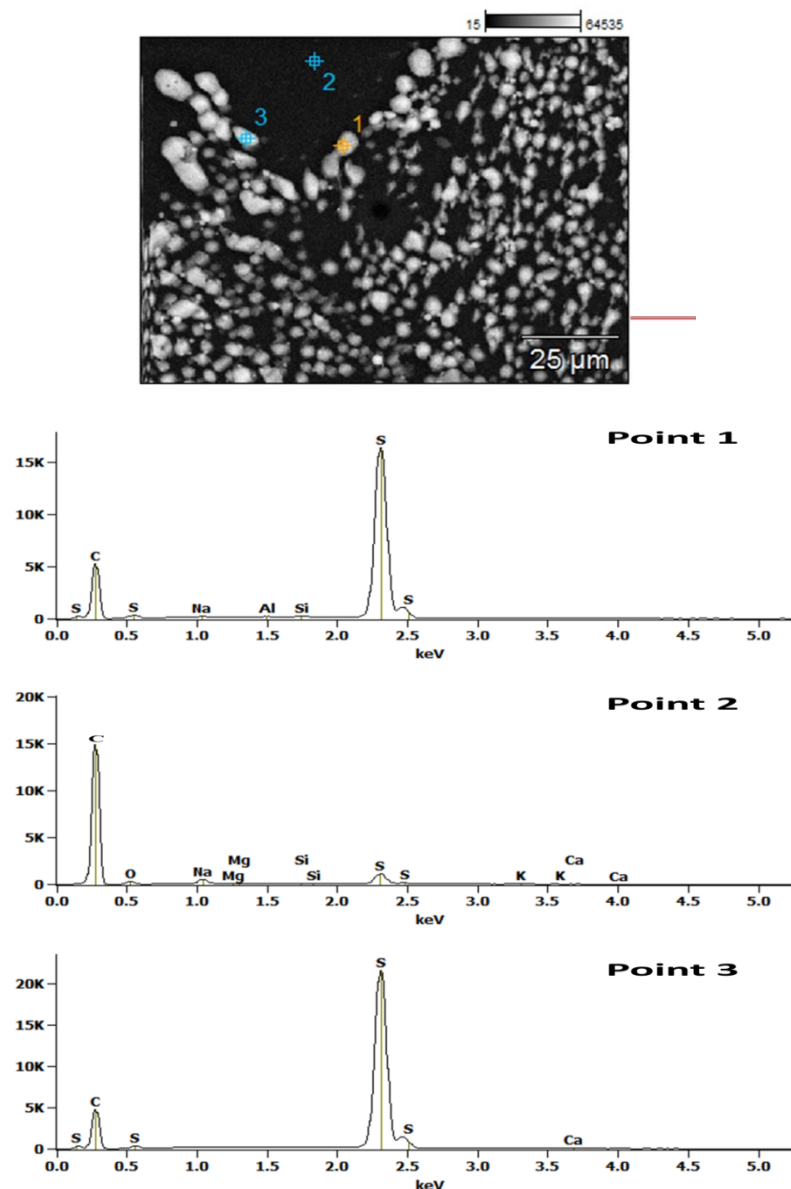


Figure 3.4 White precipitation and its element composition in diluted pore solution using nitric acid.

### 3.3 Results and discussion

#### 3.3.1 Pore solution composition of alkali-activated slag paste

Figure 3.5 presents the concentrations of Si, Al, Ca, OH<sup>-</sup>, K and Na (hereafter denoted as [Si], [Al], [Ca], [OH<sup>-</sup>], [K] and [Na], respectively) in the pore solution of alkali-activated slag paste as a function of time up to 28 days (672 hours). Since the pore solution samples were diluted with nitric acid before ICP-OES analysis, the measurement of S was not correct and thus the concentration of S was not presented for alkali-activated slag. The pore solution composition was dominated by Na and OH<sup>-</sup>, whereas much lower concentrations of Si, Al, K and Ca were observed. The most significant changes in the compositions of pore solutions in alkali-activated slag pastes occurred during the first hours up to 3 days. This can be seen from the changes of element concentrations with time, particularly the decreases of [Si] (Figure 3.5(A)), [OH<sup>-</sup>] (Figure 3.5(C)) and [Na] (Figure 3.5(E)) with time. The concentrations of Si, Al and Ca were in the order: [Si] > [Al] > [Ca].

##### *The development of element concentration with time*

As shown in Figure 3.5, strong decreases of [Si], [OH<sup>-</sup>] and [Na] were observed during the initial period up to 3 days, and then the decreases of these element concentrations continued gradually with time for all samples. The [OH<sup>-</sup>] ranges from 0.589 mol/L to 4.149 mol/L up to 28 days in the pore solution of alkali-activated slag paste. If the alkalinity is expressed in pH, it indicates a pH in the range of 13.77~14.67. This pH is higher than that in the pore solution (pH>12) buffered by Ca(OH)<sub>2</sub> in OPC-based materials, and much higher than the pH of 9.5 below which corrosion commences [91]. The [Al] decreased slightly with time, while the [Ca] remained at a very low level (0.2~2 mmol/L) and did not show much change over time. Contrary to [Na], the [K] increased with time. This is because K was sourced from slag and increased with the dissolution of slag, while Na was sourced from the alkaline activator and decreased as it was taken up into the calcium aluminosilicate hydrates [94].

##### *The effect of sodium content*

Figure 3.5 clearly shows that a higher sodium content (expressed as Na<sub>2</sub>O content) led to higher concentrations of Si, Al, and K. This is because a higher Na<sub>2</sub>O content led to a higher alkalinity of the alkaline activator and accelerated the dissolution of slag [31]. The accelerated dissolution of slag then resulted in higher concentrations of Si, Al and K in the pore solution. However, a higher Na<sub>2</sub>O content led to a lower concentration of Ca in general. This will be discussed later in the plot of [Ca] as a function of [OH<sup>-</sup>].

##### *The effect of silica content*

As shown in Figure 3.5(A), the [Si] was up to ten times higher in the pore solution of sodium silicate activated slag paste than that in the pore solution of sodium hydroxide activated slag paste with the same content of Na<sub>2</sub>O. The higher [Si] in sodium silicate activated slag paste resulted from the soluble Si in the sodium silicate activator. For the sodium hydroxide activated slag system and sodium silicate activated slag system, using the same content of Na<sub>2</sub>O, an addition of SiO<sub>2</sub> (silica content) led to a higher concentration of Al (Figure 3.5(B)). This resulted from different calcium aluminosilicate hydrates formed as a consequence of the different types of alkaline activators used in the alkaline activation of slag. This will be discussed in detail in the following section. For the concentration of K (Figure 3.5(F)), however, the addition of SiO<sub>2</sub> resulted in a lower value. This is because the addition of SiO<sub>2</sub>

led to a lower alkalinity of the alkaline activator when using the same content of  $\text{Na}_2\text{O}$  [95]. A lower alkalinity of the alkaline activator then led to a slower dissolution of slag and, consequently, resulted in a lower concentration of K.

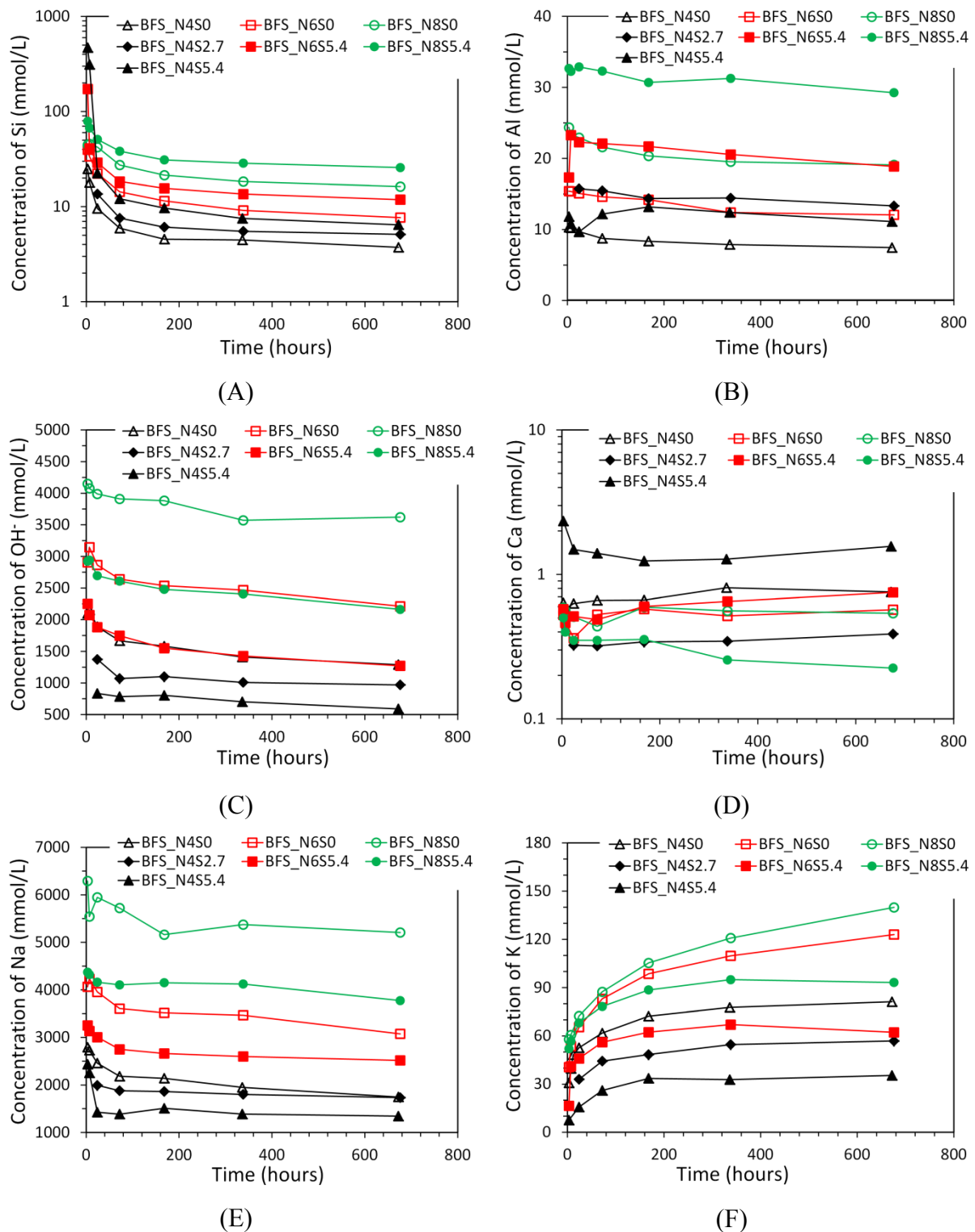
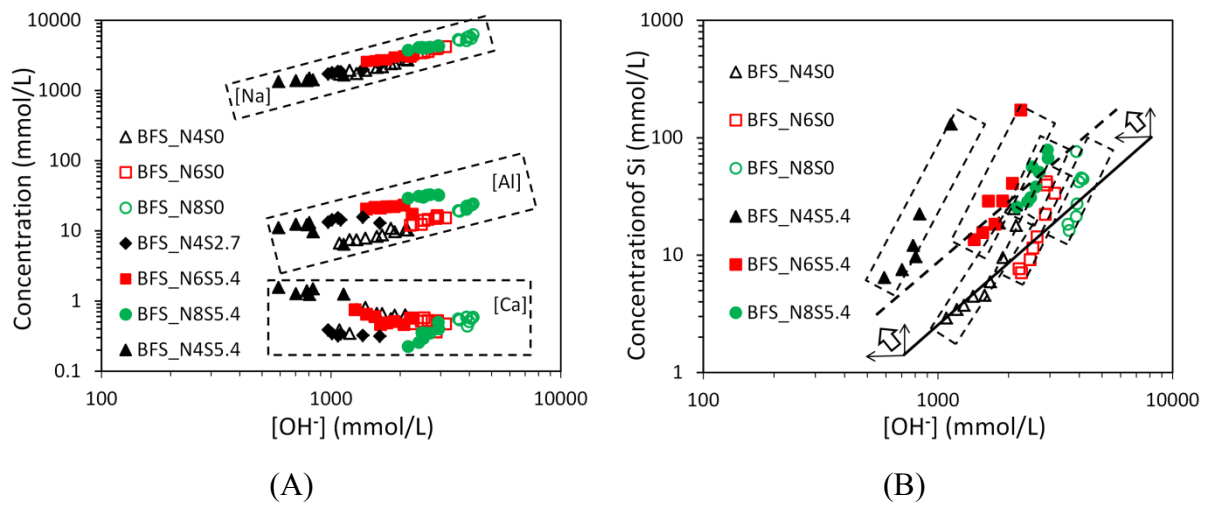


Figure 3.5 Element concentrations in the pore solutions of alkali-activated slag pastes. In the graphs, BFS indicates alkali-activated slag, and N and S indicate weight percentages of  $\text{Na}_2\text{O}$  and  $\text{SiO}_2$  with respect to slag, respectively. The water-to-slag ratio was 0.4 and the curing temperature was 20 °C.

*The plots of  $[Na]$ ,  $[Ca]$ ,  $[Al]$  and  $[Si]$  as a function of  $[OH^-]$*

The plots of the concentrations of Na, Al and Ca as a function of the concentration of  $OH^-$  are shown in Figure 3.6(A). In the pore solution the monovalent positive charge of  $Na^+$  was mostly balanced by the monovalent negative charge of hydroxide ion. Higher  $[Na]$  was thus accompanied with higher  $[OH^-]$ . For this reason the concentration of Na increased linearly with the increase of the concentration of  $OH^-$ , and this relationship was independent of the type of alkaline activator. In the pore solutions the concentration of Ca remained at a very low level and slightly decreased as the concentration of  $OH^-$  increased. This could be attributed to the *common ion effect*<sup>10</sup> [96, 97]. The pore solutions had high concentrations of Si,  $OH^-$  and  $Na^+$ . Those ions will combine with Ca to form solid reaction products and thus lowered the Ca concentration in the pore solution.



*Figure 3.6 Concentrations of major elements as functions of  $[OH^-]$  in the pore solutions of alkali-activated slag pastes. (A):  $[Na]$ ,  $[Al]$  and  $[Ca]$  versus  $[OH^-]$ . (B):  $[Si]$  versus  $[OH^-]$ . In the graphs, BFS refers to alkali-activated slag, N and S indicate the weight percentages of  $Na_2O$  and  $SiO_2$  with respect to slag. The curing temperature was 20 °C. The water to slag ratio was 0.4.*

In the pore solutions, the  $[Al]$  increased with the increasing  $[OH^-]$  for both the sodium hydroxide activated slag system and sodium silicate activated slag system (Figure 3.6(A)), which is in agreement with the literature [32]. However, this relationship only existed for the alkali-activated slag pastes using the same type of alkaline activator. Using the alkaline activators with the same content of  $Na_2O$ , an addition of  $SiO_2$  led to a lower concentration of  $[OH^-]$ , for example BFS\_N4S5.4 in comparison with BFS\_N4S0 as seen in Figure 3.5(C). But the sodium silicate activated slag paste (BFS\_N4S5.4) had a higher concentration of Al than the sodium hydroxide activated slag paste (BFS\_N4S0). This is because of the different calcium aluminosilicate hydrates formed as a consequence of the different types of alkaline activators used in the alkali activation of slag. The calcium aluminosilicate hydrate formed in

<sup>10</sup> *The common ion effect*: In a chemical solution the dissociated aqueous species are associated with each other through an equilibrium process. For example, species A and B are associated with each other in a solution through the following equation:



Increasing the concentration of A or B by adding another chemical, for example AC or DB, will move the equilibrium (Equation 3.3) to the right. This causes an increased amount of AB and decreases the concentration of the other species (B or A) ([https://en.wikipedia.org/wiki/Common-ion\\_effect](https://en.wikipedia.org/wiki/Common-ion_effect)).

the sodium hydroxide activated slag paste had a higher structural order (higher crystallinity) than that formed in the sodium silicate activated slag paste [33]. The higher crystallinity led to a lower solubility of calcium aluminosilicate hydrate in the sodium hydroxide activated slag paste. The lower solubility of calcium aluminosilicate hydrate then resulted in lower solubility of Al and consequently lowered the [Al] in the pore solution.

In alkaline solutions, the solubility of Si increases with the increase of the alkalinity of the solution [84]. This is also observed in the pore solution of sodium hydroxide activated slag paste [32]. In this chapter, the relationship between the alkalinity of the pore solution and the solubility of Si was studied more comprehensively for sodium hydroxide activated slag pastes and sodium silicate activated slag pastes. Figure 3.6(B) shows the plots between the concentration of Si and the concentration of  $\text{OH}^-$  in the pore solutions. The [Si] increased with the increase of  $[\text{OH}^-]$  in the pore solution for each alkali-activated slag paste, as shown by the dotted rectangular boxes. The plots suggest the existence of two separate lines. The line with a higher [Si] is associated with the sodium silicate activated slag pastes, while the line with a lower [Si] corresponds to the sodium hydroxide activated slag pastes. From the sodium hydroxide activated slag system to the sodium silicate activated slag system with the same content of  $\text{Na}_2\text{O}$  in the alkaline activator, the concentration of Si moved up and backward as indicated by the arrows. This is because of the addition of  $\text{SiO}_2$  in the sodium silicate activator. The addition of  $\text{SiO}_2$ , on one hand, resulted in higher [Si] in the pore solution and thus an up translation of the plot. On the other hand it resulted in lower alkalinity of the pore solution and thus a backward translation of the plot.

### 3.3.2 Pore solution composition of alkali-activated fly ash paste

The concentrations of Si, Al,  $\text{OH}^-$ , Ca, Na, K, Fe, Mg and S in the pore solutions of alkali-activated fly ash pastes are presented as a function of time up to 28 days (672 hours) in Figure 3.7. The pore solution composition was dominated by Na,  $\text{OH}^-$  and Si, whereas much lower concentrations of Al, K, Ca, Fe and Mg were observed. The most significant changes in the pore solution compositions took place during the first week. This can be seen from the changes of the element concentrations with time, particularly the decreases of [Si], [Na] and  $[\text{OH}^-]$  with time. The concentrations of Si, Al and Ca were in the order:  $[\text{Si}] > [\text{Al}] > [\text{Ca}]$ . In general, the concentrations of Si, Al and Ca in the pore solution of alkali-activated fly ash paste were several to ten times higher compared to those in the pore solution of alkali-activated slag paste as presented in Figure 3.5.

#### *The development of element concentration with time*

Figure 3.7 clearly shows that all the element concentrations in the pore solution of alkali-activated fly ash paste decreased as a function of time except for the concentration of S. Note that the concentration of K decreased with time (Figure 3.7(F)), which is in contrast with the concentration of K in the pore solution of alkali-activated slag paste (Figure 3.5(F)). In alkali-activated fly ash based materials, sodium based crystalline phases are normally identified as secondary reaction products, such as Na-chabazite and hydroxysodalite [58, 62]. However, potassium based crystalline phases are almost never found. This is due to the better zeolitization capabilities of sodium cations than those of potassium cations, as a result of the smaller sodium cations than potassium cations [98]. Therefore, the decrease of [K] with time was more likely to be attributed to the formation of potassium-aluminosilicate (K-A-S-H) type gels. The formation of K-A-S-H in alkali-activated fly ash has been reported in the literature [99, 100]. The [Ca] decreased with time (Figure 3.7(D)), which is different from the [Ca] in the pore solutions of alkali-activated slag pastes where no substantial change of the

[Ca] was observed (Figure 3.5(D)). The decrease of [Ca] with time is due to the precipitation of Ca into solid reaction products, as observed in [101]. The  $[\text{OH}^-]$  ranges from 0.119 mol/L to 2.525 mol/L up to 28 days of curing, indicating a pH range of 13.08~14.07.

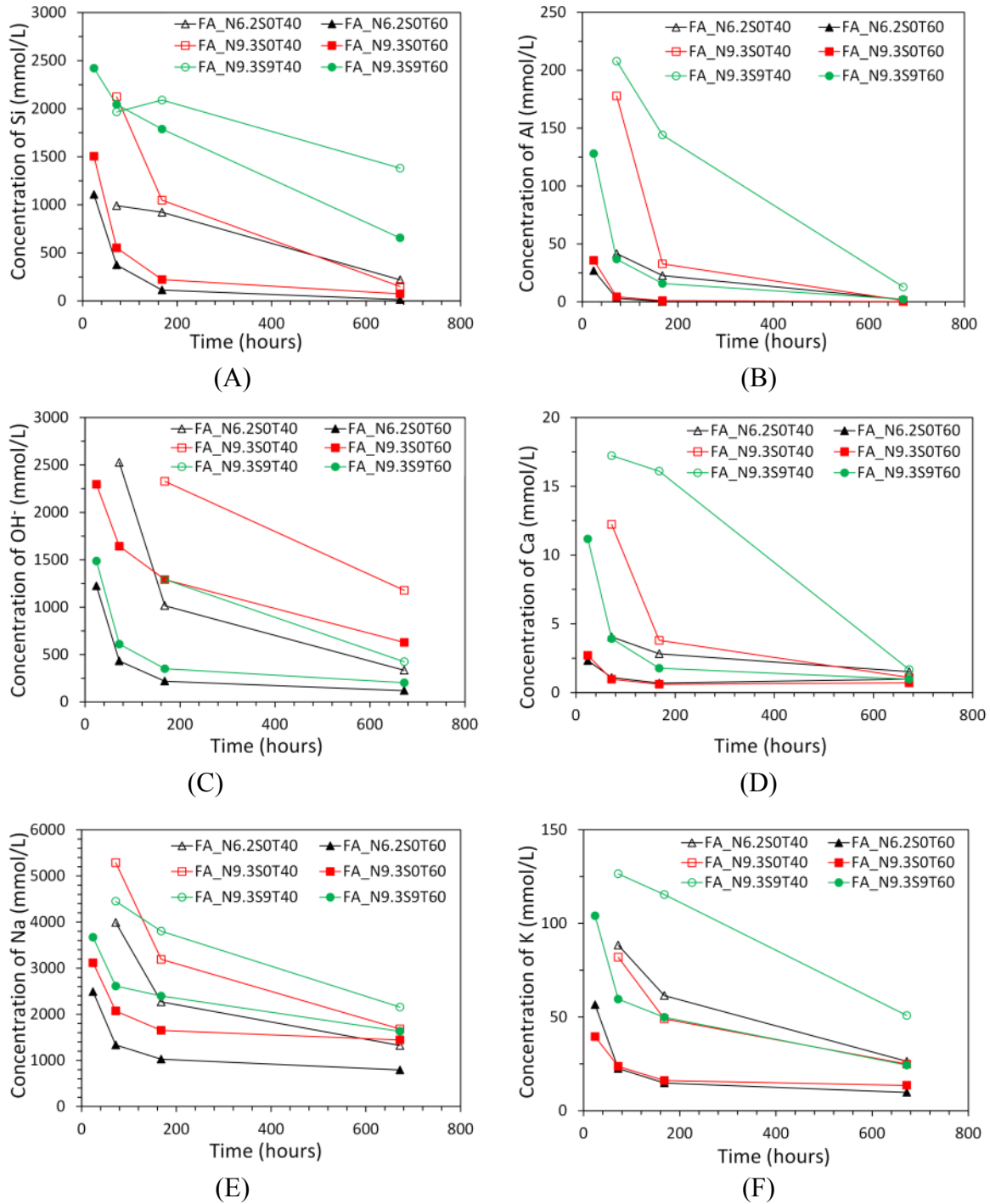


Figure 3.7 Element concentrations in the pore solutions of alkali-activated fly ash pastes. In the graphs, FA refers to alkali-activated fly ash, N and S indicate the weight percentages of  $\text{Na}_2\text{O}$  and  $\text{SiO}_2$  with respect to fly ash, respectively, and T indicates the curing temperature in Celsius. The water-to-fly-ash ratio was 0.35.

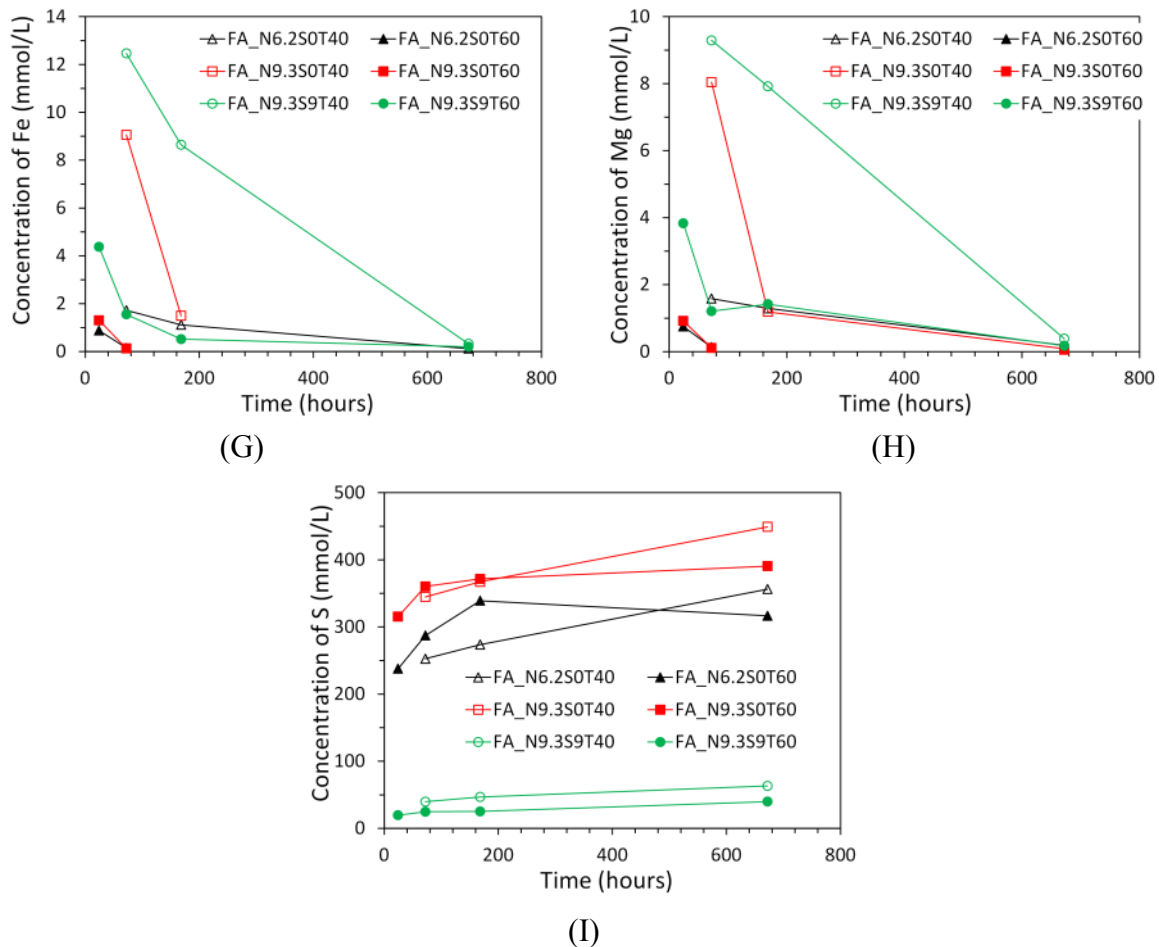


Figure 3.7 (continued) Element concentrations in the pore solutions of alkali-activated fly ash pastes. In the graphs, FA refers to alkali-activated fly ash, N and S indicate the weight percentages of  $\text{Na}_2\text{O}$  and  $\text{SiO}_2$  with respect to fly ash, respectively, and T indicates the curing temperature in Celsius. The water-to-fly-ash ratio was 0.35.

The [S] increased with time for all alkali-activated fly ash samples. Fly ash contains 0.73 % of  $\text{SO}_3$  (see Table 3.1). If the S in the fly ash is completely dissolved in the alkaline activator, the concentration of S is around 250 mmol/L. However, the [S] measured in the pore solution was around 350 mmol/L, much larger than 250 mmol/L. This was because of the decrease of the solution volume that resulted from the dissolution/wetting of fly ash and the polymerization process of alkali-aluminosilicate type gel. It is known that the porosity of alkali-activated fly ash decreases with time [67]. This indicates the decrease of the volume of solution in the alkali-activated fly ash. Therefore, using the volume of alkaline activator to calculate the concentration of S would result in underestimation.

#### The effect of sodium content

In general, the element concentrations in the pore solution of alkali-activated fly ash paste increased as the  $\text{Na}_2\text{O}$  content increased from 6.2 % to 9.3 %, particularly in the first few days. As shown in Figure 3.7(A), for example, the [Si] at 72 hours was about two times higher in the sample FA\_N9.3S0T40 (9.3 % of  $\text{Na}_2\text{O}$ ) than that in the sample FA\_N6.2S0T40 (6.2 % of  $\text{Na}_2\text{O}$ ). The higher content of  $\text{Na}_2\text{O}$  in alkaline activator led to higher alkalinity of the alkaline activator. A higher alkalinity of the alkaline activator helped to accelerate the dissolution of fly ash [102]. For this reason, the element concentration in the pore solution of



alkali-activated fly ash increased with an increase of the sodium content (expressed as  $\text{Na}_2\text{O}$  content). For sodium hydroxide activated fly ash, the [S] also increased with an increase of  $\text{Na}_2\text{O}$  content.

#### *The effect of silica content*

Because of the soluble Si in the sodium silicate activator, the [Si] was much higher in the sodium silicate activated fly ash paste than that in the sodium hydroxide activated fly ash paste with the same content of  $\text{Na}_2\text{O}$  (Figure 3.7(A)). In the pore solution of sodium silicate activated fly ash paste, the concentrations of Al, Ca, K, Fe and Mg increased significantly as compared to those in the sodium hydroxide activated fly ash paste with the same content of  $\text{Na}_2\text{O}$ , e.g. FA\_N9.3S9T40 in comparison with FA\_N9.3S0T40, and FA\_N9.3S9T60 in comparison with FA\_N9.3S0T60 (Figures 3.7(B, D, F, G, H)). This is due to the enhanced dissolution of fly ash by the soluble silicate in the alkaline activator. In the sodium hydroxide activated fly ash paste, the initial dissolved Al from fly ash created a siliceous layer on the fly ash grains and the aqueous Al species absorbed to the surface sites on the siliceous layer, passivating the surface by preventing the approach of hydroxyl ions [28]. So the dissolution of fly ash slowed down. In the sodium silicate activated fly ash paste, the soluble Si in the alkaline activator could quickly react with the initial released Al. This prevented Al from being absorbed at the surface sites and thus reduced the surface passivation and allowed more rapid dissolution of fly ash [101]. It is reported that the soluble silicate can enhance larger breakdown of the framework of fly ash if the concentration of Si in the alkaline activator is larger than 213.6 mmol/L [101]. In this study the concentration of Si in the alkaline activator for the sodium silicate activated fly ash pastes was 4170 mmol/L (Table 3.3), twenty times larger than 213.6 mmol/L. As a result, the dissolution of Si, Al, Ca, K, Fe and Mg from fly ash were enhanced, leading to higher concentrations of these elements in the pore solution. Contrary to the concentrations of Si, Al, Ca, K, Fe and Mg, an addition of  $\text{SiO}_2$  into the alkaline activator led to several times lower concentration of S, as seen in Figure 3.7(I). Further work is needed to examine this phenomenon.

#### *The effect of curing temperature*

From Figure 3.7 it is clear that an increase of curing temperature (from 40 °C and 60 °C) led to decreases of the element concentrations in the pore solutions of alkali-activated fly ash pastes. The influence of curing temperature on the pore solution composition of alkali-activated fly ash paste can be discussed from the viewpoints of kinetics and thermodynamics as follows:

##### *(1) Kinetics*

The dissolution of fly ash releases elements into the pore solution, while the formation of solid reaction products consumes the elements that constitute the solid reaction products. So the element concentrations in the pore solution depend on the competition between the dissolution of fly ash and the formation of solid reaction products. The increase of curing temperature leads to an acceleration of both the dissolution of fly ash and the formation of solid reaction products [59, 103]. It means that the increase of temperature accelerates both the release of elements from fly ash and the consumption of these elements by the formation of solid reaction products.

Figures 3.8(A) and 3.8(B) plot the heat evolution rates of sodium hydroxide activated fly ash pastes at 40 °C and 60 °C respectively. The heat evolution rates were measured with an



isothermal calorimeter (standard ASTM C1679 [104]). More details will be provided in Chapter 4. Two calorimetric peaks can be identified in the heat evolution rate curves. The first calorimetric peak ( $P_1$ ) corresponds to the dissolution/wetting of fly ash. The second calorimetric peak ( $P_2$ ) corresponds to the acceleration of the polymerization process of alkali-aluminosilicate type gel [44]. The calorimetric responses of sodium silicate activated fly ash pastes showed only one calorimetric peak, as seen in Figure 3.8(C). This makes it impossible to separate between the calorimetric response corresponding to the dissolution of fly ash and the calorimetric response corresponding to the formation of alkali-aluminosilicate type gel. Comparing the calorimetric responses at 60 °C to the calorimetric responses at 40 °C, it is clear that the increase of temperature had a larger effect on increasing the intensity of the second calorimetric peak than that of the first peak. This indicates that the increase of curing temperature caused an acceleration effect on the formation of solid reaction products larger than that on the dissolution of fly ash. As a result, the element concentrations in the pore solution of alkali-activated fly ash paste decreased as the curing temperature increased.

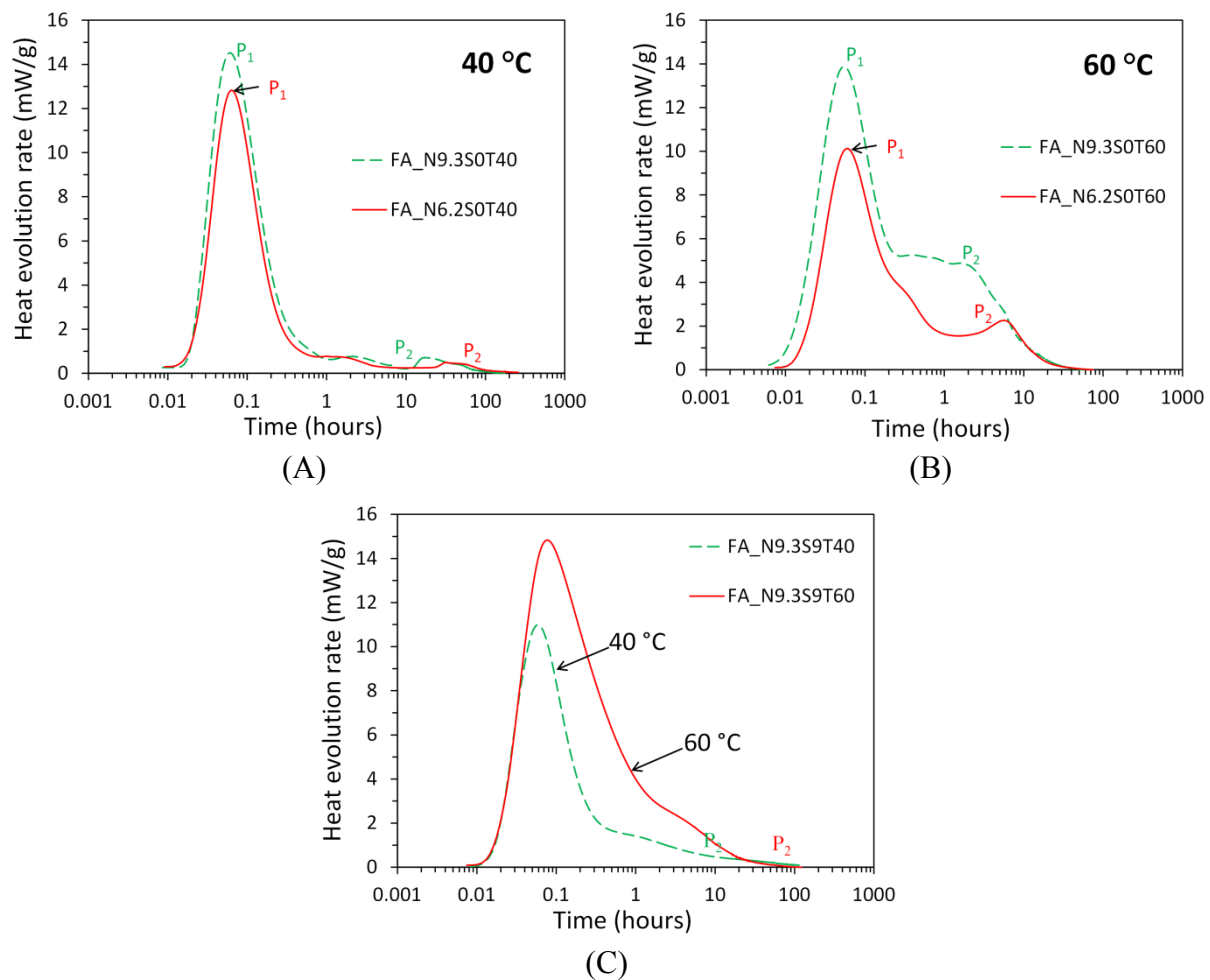


Figure 3.8 Heat evolution rates of sodium hydroxide activated fly ash pastes at 40 °C (A) and 60 °C (B), and sodium silicate activated fly ash (C). In the graphs, FA refers to alkali-activated fly ash, N and S indicate the weight percentages of  $\text{Na}_2\text{O}$  and  $\text{SiO}_2$  with respect to fly ash, respectively, and T indicates the curing temperature in Celsius. The water-to-fly-ash ratio was 0.35.

## (2) Thermodynamics

Thermodynamics assumes a solubility equilibrium between the solid and aqueous species in the liquid that react to form the solid [85]. From this point of view, the solubility of the reaction product also affects the concentrations of the elements that react to form the reaction products. In alkali-activated fly ash paste, the alkali-aluminosilicate type gel is the main reaction product [56]. It is reported that an increase of temperature leads to an increase of long-range ordering and a higher degree of crosslinking in alkali-aluminosilicate type gel [59, 105]. Then the increase of long-range ordering and higher degree of crosslinking lead to a more stable structure of alkali-aluminosilicate type gels, which results in a decrease of the solubility of alkali-aluminosilicate type gel. The decreased solubility of alkali-aluminosilicate type gel results in lower concentrations of the elements that react to form the alkali-aluminosilicate type gel. So the increase of temperature from 40 °C to 60 °C in this study led to decreases of the concentrations of Si, Al, Na and K that reacted to form alkali-aluminosilicate type gel.

### 3.3.3 Pore solution composition of alkali-activated slag/fly ash paste

To study the influence of the replacement of slag by fly ash on the pore solution composition, one mixture of alkali-activated slag/fly ash was used in this study. Figure 3.9(A) presents the element concentrations in the pore solution of alkali-activated slag/fly ash paste (B\_N6S5.4). It can be seen that the [Si], [Na] and [OH<sup>-</sup>] decreased as a function of time, while the [Al] and [Ca] did not show much change over time. The [OH<sup>-</sup>] ranges from 1.128 mol/L to 2.370 mol/L up to 28 days, indicating a pH range of 14.05~14.37. By using the same alkaline activator, 50 wt.% replacement of slag by fly ash did not result in a substantial change on the pore solution composition during the early age within one week when compared to that of the alkali-activated slag (BFS\_N6S5.4, shown in Figure 3.9(B)).

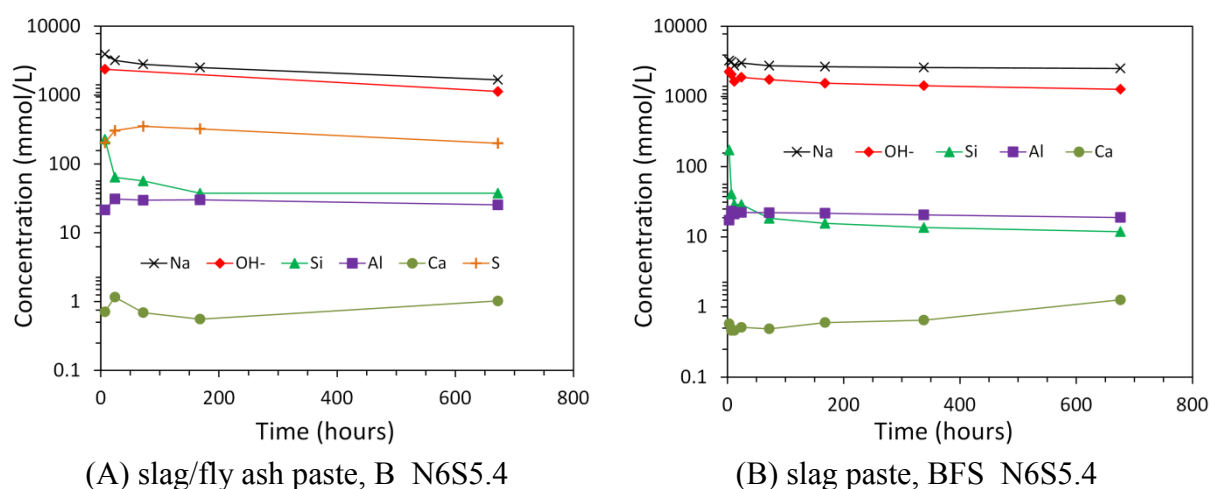


**Figure 3.9** Element concentrations in the pore solutions of alkali-activated slag/fly ash paste (A), and alkali-activated slag paste (B) with the same alkaline activator. In the graphs, B indicates alkali-activated blend of slag and fly ash, and BFS refers to alkali-activated slag, N and S indicate the weight percentages of Na<sub>2</sub>O and SiO<sub>2</sub> with respect to the precursor (slag, or blend of slag and fly ash), respectively. The curing temperature was 20 °C. The water-to-precursor ratio was 0.4.

At 28 days, the pore solution of alkali-activated slag/fly ash paste had higher [Si] and lower [Na] than that of alkali-activated slag paste. In the pore solution of alkali-activated slag/fly ash paste, the concentrations of Si and Na were 37.5 mmol/L and 1670.4 mmol/L respectively, while they were 11.9 mmol/L and 2517.7 mmol/L, respectively, in the pore solution of alkali-activated slag paste. The higher [Si] in the alkali-activated slag/fly ash paste is because fly ash contains more reactive  $\text{SiO}_2$  (37 %) than slag (32.9 %). It has been reported about the co-existence of calcium aluminosilicate hydrate and alkali-aluminosilicate type gel in the alkali-activated slag/fly ash [64]. In the alkali-aluminosilicate type gel, a large amount of Na is taken up to balance the charge of Al in the bonding network [57]. Consequently, the [Na] was smaller in the pore solution of alkali-activated slag/fly ash paste.

### 3.4 Conclusions

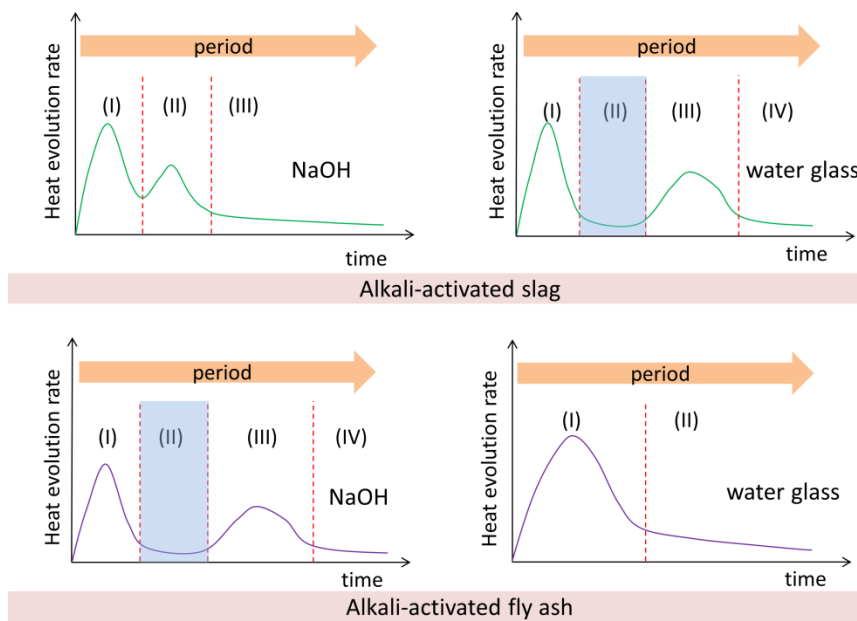
In this chapter, the pore solution composition of alkali-activated slag and/or fly ash paste was studied by means of ICP-OES analysis technique. Particularly, the influences of the type and concentration of alkaline activator and temperature on the pore solution composition were investigated. Based on the experimental results, the following conclusions can be drawn:

- (1) In the pore solution of alkali-activated slag paste, the concentrations of Si, Al, Na and  $\text{OH}^-$  decreased with time and increased with the increasing content of  $\text{Na}_2\text{O}$ , while the concentration of Ca showed no substantial change with time and  $\text{Na}_2\text{O}$  content. The concentrations of Na and Al were positively correlated to the concentration of  $\text{OH}^-$  in a quasi-linear relationship, while the concentration of Si had a large dependence on the initial concentration of  $\text{OH}^-$ .
- (2) In the pore solution of alkali-activated fly ash paste, an increase of temperature led to decreases of the concentrations of Si, Al, Ca, K, Fe and Mg. This was because the increased temperature caused an acceleration effect on the formation of solid reaction products larger than that on the dissolution of fly ash. In the sodium hydroxide activated fly ash pastes the surface sites of fly ash were passivated by the absorbed Al. In contrast the soluble silicate could prevent the released Al from being absorbed and thus reduced the passivation of surface sites in the sodium silicate activated fly ash paste. Therefore, the concentrations of Si, Al, Ca, K, Fe and Mg increased.
- (3) In the pore solution of alkali-activated slag/fly ash, the concentrations of Si, Na and  $\text{OH}^-$  decreased with time, while the concentrations of Al and Ca did not show much change over time. Compared to the alkali-activated slag paste with the same sodium silicate activator, 50 wt.% replacement of slag by fly ash did not have a substantial influence on the pore solution composition of the alkali-activated slag/fly ash paste during the early age within one week. But after 28 days, the replacement led to a lower concentration of Na and a higher concentration of Si.
- (4) The pore solution of alkali-activated slag or fly ash paste maintained high alkalinity up to 28 days:  $[\text{OH}^-]$  ranges from 0.589 mol/L to 4.149 mol/L for alkali-activated slag paste, from 0.119 mol/L to 2.525 mol/L for alkali-activated fly ash paste, and from 1.128 mol/L to 2.370 mol/L for alkali-activated slag/fly ash paste.



# Chapter 4

## Reaction kinetics of alkali-activated materials<sup>11</sup>



Similar to the hydration of Portland cement, the reaction of AAMs also experiences several reaction stages that are controlled by different reaction mechanisms. In this chapter, the reaction kinetics of alkali-activated slag, alkali-activated fly ash and alkali-activated slag/fly ash pastes were studied by using isothermal calorimetry. The reaction process of each alkali-activated system was described. Particularly the origin of the induction period was discussed.

<sup>11</sup> This chapter is partially based on:

Yibing Zuo, Marija Nedeljkovic, and Guang Ye. Coupled thermodynamic modelling and experimental study of sodium hydroxide activated slag. *Construction and Building Materials*, 188(2018) 262-279.



## 4.2 Materials and methods

### 4.2.1 Materials and mixtures

The slag and fly ash used in this chapter were the same as in Chapter 3. The mixtures designed in Chapter 3 (Table 3.2) were also used in this chapter for the study of reaction kinetics.

### 4.2.2 Isothermal calorimetry test

The isothermal calorimetry tests were carried out in accordance with ASTM C1679 [104]. For the measurements of heat evolution at 20 °C, paste samples were prepared outside the calorimeter. All the raw materials were conditioned at the measurement temperature. Alkaline activators with different concentrations of Na<sub>2</sub>O and SiO<sub>2</sub> were prepared and cooled down to the measurement temperature before the sample preparation. After mixing the aluminosilicate precursor with the alkaline activator, the paste samples were immediately placed into the calorimeter at 20 °C. For the measurements of heat evolution at elevated temperatures (50 and 60 °C), in-situ mixing was used to avoid any temperature difference. The aluminosilicate precursor and alkaline activator were conditioned in the calorimeter at the measurement temperature. When the thermal equilibrium was reached, the alkaline activator was injected into the glass ampoule and mixed with the aluminosilicate precursor. Two replicates were measured simultaneously. The heat flow was recorded up to 7 days.

### 4.2.3 Determination of degree of reaction

The degree of reaction of slag or fly ash ( $\alpha(t)$ ) can be calculated as the ratio of the cumulative heat release at time  $t$ ,  $Q(t)$ , to the maximum heat release,  $Q_{\max}$ . It is assumed that the heat release is linearly proportional to the degree of reaction:

$$\alpha(t) = \frac{Q(t)}{Q_{\max}} \quad (4.1)$$

$Q(t)$  is obtained by calorimetry and the determination of  $Q_{\max}$  will be described in Section 4.3.3. In accord with [38, 109],  $Q(t)$  can be described using an exponential function as follows:

$$Q(t) = Q_{\max} \exp\left(-\left(\frac{\lambda}{t}\right)^\beta\right) \quad (4.2)$$

where  $\lambda$  and  $\beta$  are time and shape parameters, respectively. Then the degree of reaction can be described with the following equation:

$$\alpha(t) = \exp\left(-\left(\frac{\lambda}{t}\right)^\beta\right) \quad (4.3)$$

### 4.3 Results and discussion

#### 4.3.1 Isothermal calorimetry study of the reaction kinetics of alkali-activated slag and fly ash

##### 4.3.1.1 Calorimetric response of alkali-activated slag paste

The heat evolution of alkali-activated slag samples with *sodium hydroxide* or *sodium silicate* was measured at 20 °C. In the following the calorimetric response of alkali-activated slag will be discussed separately for *sodium hydroxide* activated slag samples and *sodium silicate* activated slag samples.

##### *Slag samples with sodium hydroxide as the alkaline activator*

The calorimetric responses of *sodium hydroxide* activated slag pastes are presented in Figure 4.2. Figure 4.2(A) shows the heat evolution rate and Figure 4.2(B) shows the cumulative heat release. Two calorimetric peaks were observed from the heat evolution rate curves, which agrees with previous observations [38, 39, 42, 84, 106]. The first peak,  $P_1$ , with very high heat evolution within the first 10 minutes, reflects the dissolution/wetting of slag after mixing with alkaline activators [38, 84]. The second peak,  $P_2$ , occurred between 1 and 3 hours and reflects the formation of a large amount of reaction products [42, 84]. According to these two calorimetric peaks, the entire reaction process of *sodium hydroxide* activated slag was divided into three reaction stages, namely initial dissolution period (I), acceleration/deceleration period (II) and steady period (III). In comparison with the four distinctive reaction stages (dissolution, induction, acceleration/deceleration and steady state) during the hydration process of a normal Portland cement [110], no noticeable induction period was observed in the reaction process of *sodium hydroxide* activated slag pastes.

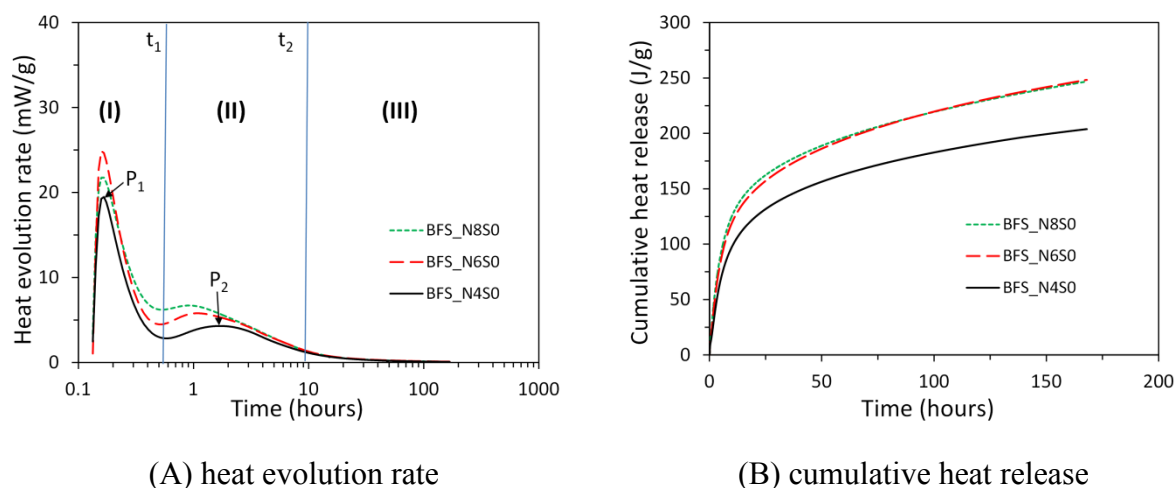


**Figure 4.2** Heat evolution rate and cumulative heat release for sodium hydroxide activated slag pastes with varying contents of  $\text{Na}_2\text{O}$  at 20 °C. In the graphs,  $P_1$  and  $P_2$  are the first and second calorimetric peak respectively;  $t_1$  and  $t_2$  stand for the transition time; the representative vertical separating lines are shown for the sample BFS\_N4S0; I, II and III correspond to the initial dissolution period, acceleration/deceleration period and steady period, respectively.

The magnitude of the acceleration peak (i.e., the second calorimetric peak) was influenced by the content of  $\text{Na}_2\text{O}$ . The acceleration peak was higher for the mixture with a higher content of  $\text{Na}_2\text{O}$ . An increase of the  $\text{Na}_2\text{O}$  content increased the alkalinity of the alkaline activator,



accelerating the dissolution of slag and the formation of reaction products. Consequently, the height of the acceleration peak, reflecting the formation of reaction products, increased and its appearance occurred earlier. The cumulative heat release curve for *sodium hydroxide* activated slag paste (Figure 4.2(B)) shows more heat release for the mixture with a higher  $\text{Na}_2\text{O}$  content. However, a dosage of  $\text{Na}_2\text{O}$  larger than 6 % did not show an obvious influence on the cumulative heat release.

#### *Slag samples with sodium silicate as the alkaline activator*

Figure 4.3 presents the heat evolution rate and cumulative heat release for *sodium silicate* activated slag pastes. Similar to the reaction of *sodium hydroxide* activated slag, the heat evolution rate curve showed two calorimetric peaks. The difference was that a marked induction period was observed between the first and second calorimetric peak. Four reaction stages were identified during the reaction process of *sodium silicate* activated slag pastes, namely initial dissolution period (I), induction period (II), acceleration/deceleration period (III) and steady period (IV). The duration of the induction period shortened and the heights of the first and second calorimetric peaks increased for the mixture with a higher  $\text{Na}_2\text{O}$  content. As shown in Figure 4.3(B), the mixture with a higher  $\text{Na}_2\text{O}$  content exhibited a larger cumulative heat release over time.

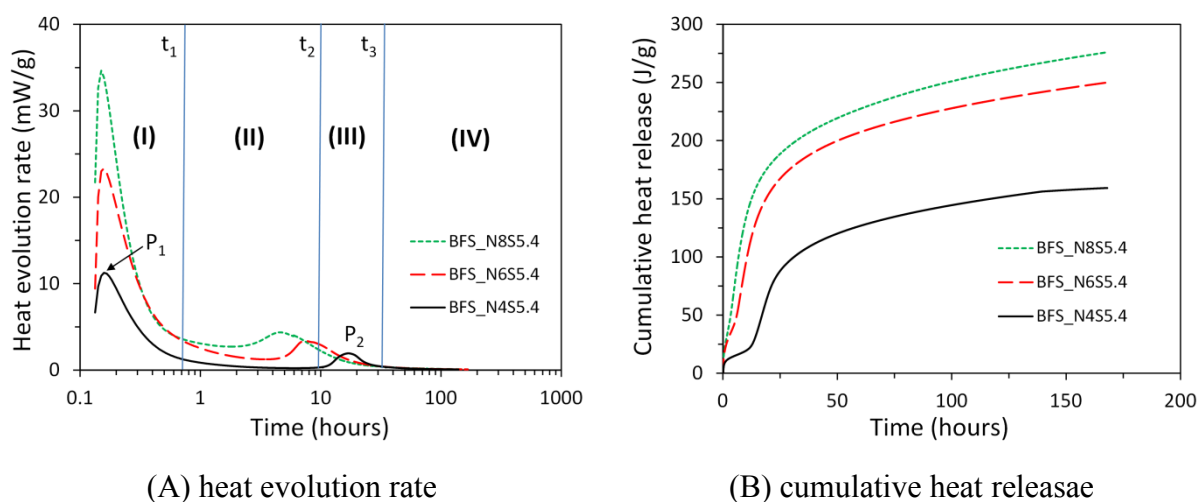


**Figure 4.3** Heat evolution rate and cumulative heat release for sodium silicate activated slag pastes with the same content of  $\text{SiO}_2$  at 20 °C. In the graphs,  $P_1$  and  $P_2$  are the first and second calorimetric peak respectively;  $t_1$ ,  $t_2$  and  $t_3$  stand for the transition time; the representative vertical separating lines are shown for the sample BFS\_N4S5.4; I, II, III and IV correspond to the initial dissolution period, induction period, acceleration/deceleration period and steady period, respectively.

The addition of  $\text{SiO}_2$  in the mixture showed an obvious influence on the reaction kinetics of alkali-activated slag. This can be seen from the comparisons between the calorimetric responses of *sodium hydroxide* activated slag (see Figure 4.2) and those of *sodium silicate* activated slag (see Figure 4.3). In addition to delaying the acceleration peak, resulting in an induction period, the addition of  $\text{SiO}_2$  in the mixture also decreased the height of the acceleration peak (Figure 4.3(A)). For the dissolution peak and cumulative heat release, the influence of  $\text{SiO}_2$  depended on the activator modulus  $M_s$  ( $\text{SiO}_2/\text{Na}_2\text{O}$ ). Comparing

BFS\_N4S5.4 ( $M_s = 1.395$ ) with BFS\_N4S0, the addition of  $\text{SiO}_2$  decreased the height of the dissolution peak and the cumulative heat release. Comparing BFS\_N6S5.4 ( $M_s = 0.93$ ) with BFS\_N6S0, the addition of  $\text{SiO}_2$  decreased the height of the dissolution peak without an obvious influence on the cumulative heat release. Comparing BFS\_N8S5.4 ( $M_s = 0.6975$ ) with BFS\_N8S0, the addition of  $\text{SiO}_2$  increased the height of the dissolution peak and the cumulative heat release. These observations were further confirmed with BFS\_N4S2.7 in Figure 4.4. In comparison with BFS\_N4S0, the height of the dissolution peak and the cumulative heat release increased for BFS\_N4S2.7 ( $M_s = 0.6975$ ). Compared to BFS\_N4S0, however, the height of the dissolution peak and the cumulative heat release decreased for BFS\_N4S5.4 ( $M_s = 1.395$ ).

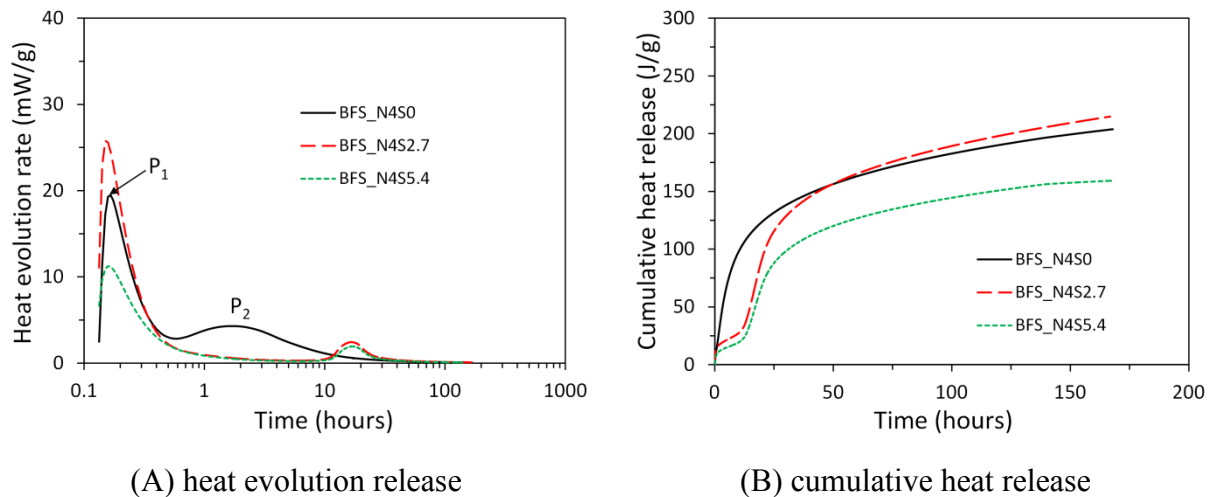


Figure 4.4 Heat evolution rate and cumulative heat release for alkali-activated slag pastes with the same content of  $\text{Na}_2\text{O}$  at 20 °C. In the graphs,  $P_1$  and  $P_2$  are the first and second calorimetric peak, respectively.

#### 4.3.1.2 Calorimetric response of alkali-activated fly ash paste

In this thesis the heat evolution of alkali-activated fly ash samples with *sodium hydroxide* and *sodium silicate* was measured at two elevated temperatures, i.e. 50 °C and 60 °C. In the following the calorimetric response of alkali-activated fly ash will be discussed separately for samples at 50 °C and 60 °C.

##### *Calorimetric response of alkali-activated fly ash samples at 50 °C*

The heat evolution rate and cumulative heat release of alkali-activated fly ash at 50 °C are displayed in Figures 4.5(A) and 4.5(B), respectively. Two calorimetric peaks were identified on the heat evolution rate curve of *sodium hydroxide* activated fly ash, i.e. FA\_N6.2S0 and FA\_N9.3S0. The first calorimetric peak, attributed to the wetting and dissolution of fly ash, occurred within the first few minutes. The second calorimetric peak appeared between 5 and 15 hours, corresponding to the acceleration of polymerization process of alkali-aluminosilicate type gel [44]. According to these two calorimetric peaks, the reaction process of *sodium hydroxide* activated fly ash was divided into four distinct reaction stages as shown in Figure 4.5(A). These reaction stages were the initial dissolution period (I), induction period (II), acceleration/deceleration period (III) and steady period (IV). It is noted that there was also a small peak in the induction period for sodium hydroxide activated fly ash. This

peak reflected a small amount of reactions and those reactions were then suppressed due to the passivation of the leached surface layer by the absorbed Al. This passivation will be discussed in Section 4.3.2.3.

For *sodium silicate* activated fly ash (FA\_N9.3S9), by contrast, only one broad calorimetric peak was observed. The calorimetric peak, corresponding to the accelerated polymerization process, merged into the calorimetric peak that corresponded to the wetting and dissolution of fly ash. As a result, only two reaction stages were identified according to the heat evolution rate curve of *sodium silicate* activated fly ash, i.e. a dissolution and acceleration/deceleration period and a steady period.

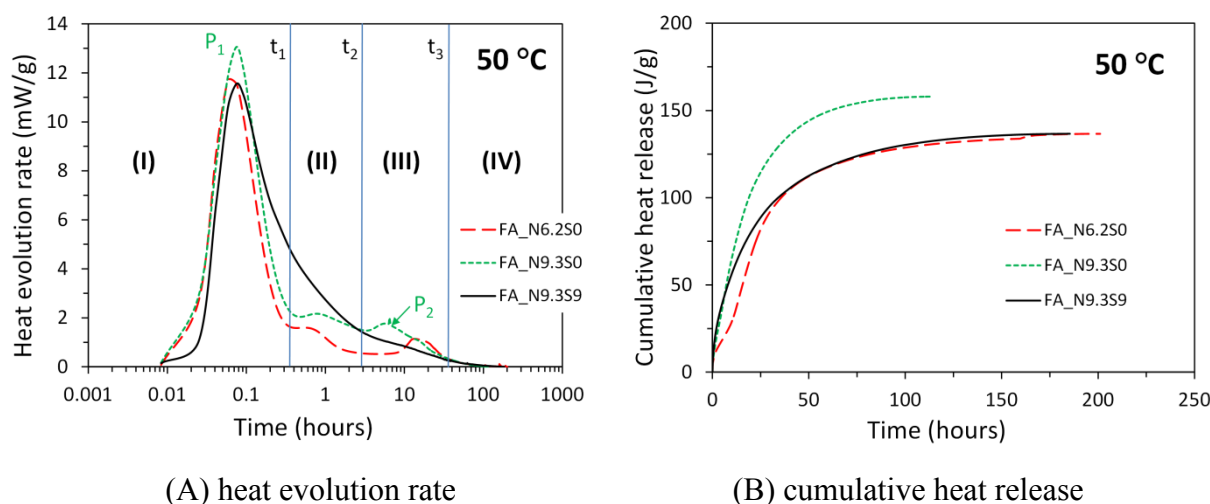


**Figure 4.5** Heat evolution rate and cumulative heat release for alkali-activated fly ash pastes at 50 °C. In the graphs,  $P_1$  and  $P_2$  are the first and second calorimetric peak, respectively;  $t_1$ ,  $t_2$  and  $t_3$  stand for the transition time; the representative vertical separating lines are shown for the sample FA\_N9.3S0; I, II, III and IV correspond to the initial dissolution period, induction period, acceleration/deceleration period and steady period, respectively

For the *sodium hydroxide* activated fly ash with a higher  $\text{Na}_2\text{O}$  content (Figure 4.5(A)), the heights of the calorimetric peaks increased and the acceleration peak occurred earlier. When comparing FA\_N9.3S9 with FA\_N9.3S0, the addition of  $\text{SiO}_2$  in the mixture resulted in a lower height of the dissolution peak and the absence of the acceleration peak. As shown in Figure 4.5(B), the cumulative heat release was larger for the mixture with a higher  $\text{Na}_2\text{O}$  content and smaller for the mixture with an addition of  $\text{SiO}_2$ .

#### Calorimetric response of alkali-activated fly ash samples at 60 °C

In order to investigate the influence of temperature on the reaction kinetics, the heat release of alkali-activated fly ash was also measured at a higher temperature. Figure 4.6 presents the heat evolution rate and cumulative heat release of the alkali-activated fly ash paste at 60 °C. Still the heat evolution rate curve of *sodium hydroxide* activated fly ash showed two calorimetric peaks, but the induction period obviously shortened for FA\_N6.2S0 and even disappeared for FA\_N9.3S0. For the *sodium silicate* activated fly ash, i.e. FA\_N9.3S9, there was only one broad calorimetric peak on the heat evolution rate curve.

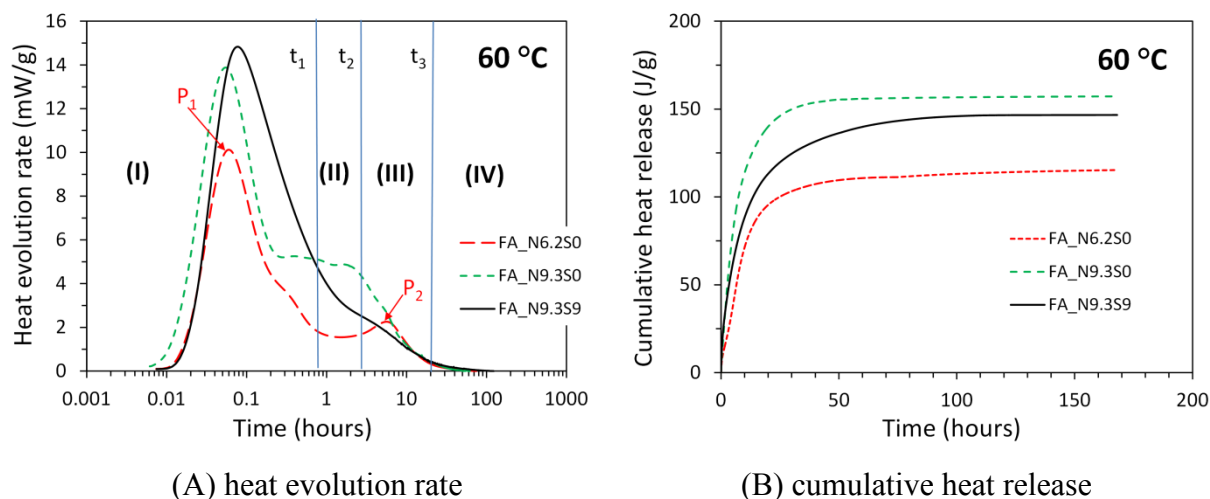


**Figure 4.6** Heat evolution rate and cumulative heat release for alkali-activated fly ash pastes at 60 °C. In the graphs,  $P_1$  and  $P_2$  are the first and second calorimetric peak, respectively;  $t_1$ ,  $t_2$  and  $t_3$  stand for the transition time; the representative vertical separating lines are shown for the sample FA\_N6.2S0; I, II, III and IV correspond to the initial dissolution period, induction period, acceleration/deceleration period and steady period, respectively.

As shown in Figure 4.6(A), the mixture with a higher  $\text{Na}_2\text{O}$  content showed a higher calorimetric peak and earlier appearance of the acceleration peak for the *sodium hydroxide* activated fly ash, i.e. FA\_N6.2S0 and FA\_N9.3S0. As shown in Figure 4.6(B), the cumulative heat release was larger for the mixture with a higher  $\text{Na}_2\text{O}$  content and smaller for the mixture with an addition of  $\text{SiO}_2$ . From Figures 4.5 and 4.6, it can be seen that the heat release was accelerated at the early age. After 1 day the cumulative heat release only slightly increased.

#### 4.3.1.3 Calorimetric response of alkali-activated slag/fly ash

Figure 4.7 displays the heat evolution rate and cumulative heat release of alkali-activated slag/fly ash paste at 20 °C. Three calorimetric peaks can be seen from the heat evolution rate curve. The first calorimetric peak, occurring within the first few minutes, was due to the wetting and dissolution of aluminosilicate precursors. The second and third calorimetric peaks were attributed to the accelerated reactions of slag and fly ash, respectively. Between the first and second calorimetric peaks there was no induction period, while there existed an induction period of the reaction of fly ash between the second and third calorimetric peaks. According to these three calorimetric peaks, five reaction stages could be identified as shown in Figure 4.7(A). They were the initial dissolution period (I), acceleration/deceleration period for slag (II), induction period (III), acceleration/deceleration period for fly ash (IV), and steady period (V).

Compared to the alkali-activated slag paste with the same alkaline activator (BFS\_N6S5.4), 50 % replacement of slag by fly ash slowed down the heat release. The cumulative heat release of B\_N6S5.4 was smaller than that of BFS\_N6S5.4 as seen in Figure 4.7(B). Besides, the replacement also led to one more reaction stage, i.e. the acceleration/deceleration period for fly ash. An induction period was observed between the second and third calorimetric peaks.

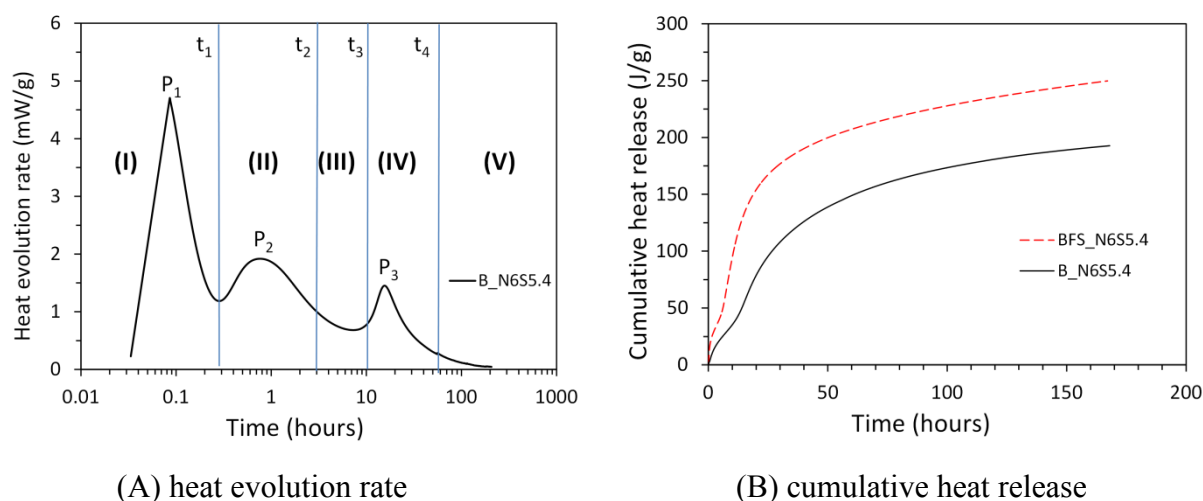


Figure 4.7 Heat evolution rate and cumulative heat release for alkali-activated slag/fly ash paste at 20 °C. In the graphs,  $P_1$ ,  $P_2$  and  $P_3$  are the first, second and third calorimetric peak, respectively;  $t_1$ ,  $t_2$ ,  $t_3$  and  $t_4$  stand for the transition time; the representative vertical separating lines are shown for the sample  $B\_N6.2S5.4$ ; I, II, III, IV and V correspond to the initial dissolution period, acceleration/deceleration period for slag, induction period, acceleration/deceleration period for fly ash and steady period, respectively. For convenient comparison the cumulative heat release of  $BFS\_N6S5.4$  is also plotted in Figure 4.7(B).

### 4.3.2 Assessments of the calorimetric differences caused by aluminosilicate precursors and alkaline activators

#### 4.3.2.1 Concepts of “leached surface layer” and “dissolution theory based mechanism”

An obvious difference of the calorimetric responses of AAMs is the occurrence of an induction period. In the *sodium silicate* activated slag and *sodium hydroxide* activated fly ash systems, the induction period was observed. In contrast it was not identified in the *sodium hydroxide* activated slag and *sodium silicate* activated fly ash systems. The reaction process and origin of the induction period in alkali-activated slag or fly ash paste will be discussed in this section. Before the discussion, the concepts of “leached surface layer” and “dissolution theory based mechanism” are introduced as follows:

##### (1) Leached surface layer

Since the alkali and alkali-earth metals modify the framework of aluminosilicate materials, they are commonly referred to as modifying elements. As illustrated in Figure 4.8(A), the modifying elements are initially released from the surface through metal/proton exchange reactions in the dissolution process of aluminosilicate precursors [22-25]. Compared to the dissolution of the tetrahedrally coordinated Si, the tetrahedrally coordinated Al dissolves more easily (see Figure 4.8(B)). This is because the tetrahedral Al-O bonds are easier to break than the tetrahedral Si-O bonds. Furthermore, the dissolution of Al tetrahedra leads the partially coordinated Si tetrahedra to dissolve easier than the fully coordinated Si tetrahedras. As a result, the exchange reactions lead to a leached surface layer, as shown in Figure 4.8(C). This leached surface layer is rich in Si. The growth of the thickness of this leached surface layer depends on the competition between the diffusion rate of the modifying elements through the leached surface layer and the dissolution rate of the leached layer itself.

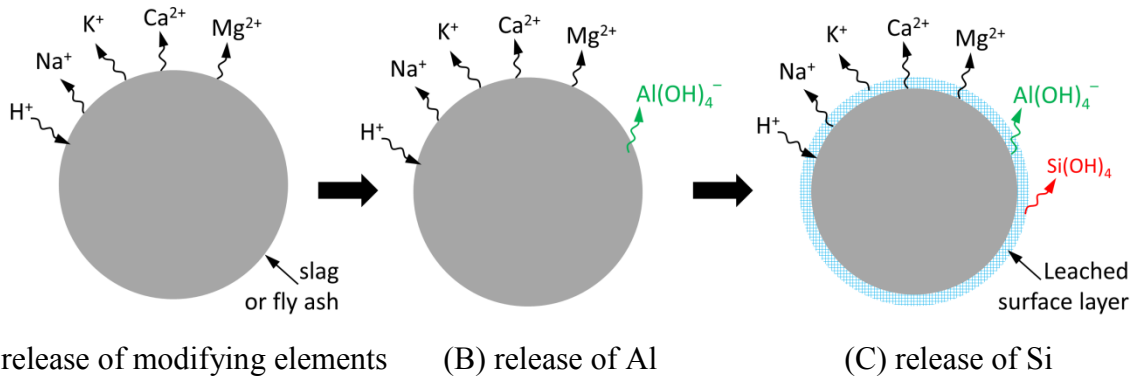


Figure 4.8 Schematic illustration for the dissolution of slag or fly ash.

## (2) A dissolution theory based mechanism

Three main mechanisms of dissolution were proposed for describing the crystal dissolution, i.e. formation of vacancy islands, etch pit formation at dislocations and step retreat at pre-existing roughness [111]. The first two have activation energies, i.e.  $\Delta G_{crit}^n$  and  $\Delta G_{crit}$ , respectively. The energy to overcome these activation energy barriers is provided by the undersaturation of the solution with respect to the constituents of the crystal. Figure 4.9 schematically illustrates the dependence of the two activation energy barriers on the undersaturation degree. The activation energy barrier decreases as the undersaturation degree increases.

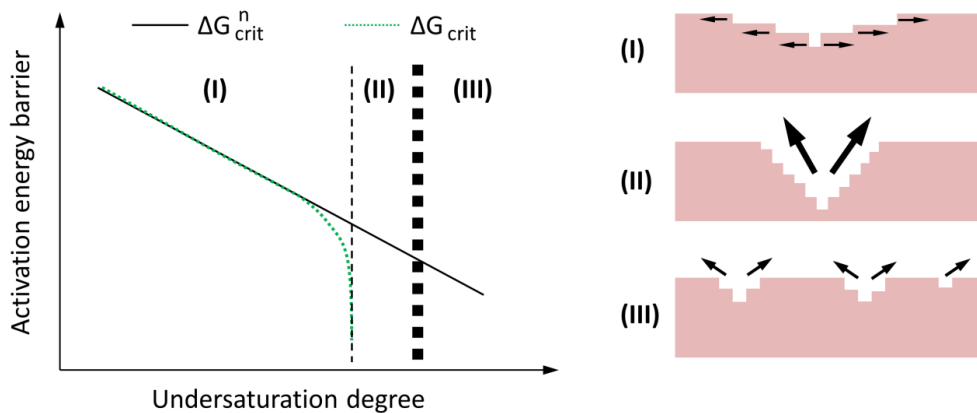


Figure 4.9 Schematic illustration of the dependence of the two activation energy barriers  $\Delta G_{crit}^n$  (2D vacancy islands) and  $\Delta G_{crit}$  (etch pit) as a function of the undersaturation degree. In regimes I, II and III, step retreat, etch pit formation and the formation of 2D vacancy islands, are the rate controlling mechanisms, respectively. The transition between the second and the third is not as clearly defined as for the transition between the first and the second regime. Therefore, a broader separation is used to present this transition. (after [111]).

The two activation energy barriers divides the dissolution into three regimes, i.e. regimes I, II and III, as shown in Figure 4.9. In these three regimes, step retreat, etch pit formation at dislocations and the formation of 2D vacancy islands are the rate controlling mechanisms, respectively. For very large undersaturations, etch pits can form on plain surfaces (regime III). As the undersaturation degree decreases, the activation energy barrier increases and eventually makes it no longer possible to form etch pits on plain surfaces. On the other hand,



etch pits can continue to form at dislocations (regime II). When the undersaturation degree decreases to below that needed to overcome the activation energy for the creation of etch pits, the formation of etch pits at dislocations is no longer spontaneous. Then the dissolution transits to regime I with a slow dissolution rate, since the dissolution process is controlled by step retreat at pre-existing steps. It should be noted that step retreat takes place throughout the dissolution process. At large undersaturation degree, however, its contribution to the overall dissolution rate is small. This is because the dissolution through step retreat is slow at large undersaturation degree.

#### 4.3.2.2 Reaction process and the origin of the induction period in alkali-activated slag

When slag was brought into contact with *sodium hydroxide* activator, the undersaturation degree was initially very large. All the dissolution mechanisms discussed previously were active, thus leading to fast release of ions and a high rate of heat evolution (characterized by the first calorimetric peak). The ions released into solution resulted in a decrease of the undersaturation degree. The initial period of very large undersaturation degree then gave way to regime II, in which etch pits formed only at dislocations. In the meantime, the thickness of the leached surface layer grew with time until the dissolution rate of unreacted slag was dynamically equal to the dissolution rate of the leached surface layer itself. With continuous dissolution, the ions accumulated and started to react to form calcium aluminosilicate hydrate (C-(A-)S-H type gel). The formation of C-(A-)S-H consumed ions from the solution and, therefore, led to an increase of the undersaturation degree. The continuous dissolution of slag and formation of C-(A-)S-H led to a rapid growth of reaction products, which can be characterized by the second calorimetric peak (Figure 4.2(A)). Since the dissolution of slag and formation of C-(A-)S-H progressed very fast, the first calorimetric peak was closely followed by the second calorimetric peak. For this reason, there was no noticeable induction period after the initial dissolution period in the *sodium hydroxide* activated slag. It can be inferred from these findings that the first calorimetric peak and the second calorimetric peak will merge into one broad calorimetric peak if the alkalinity of the *sodium hydroxide* activator increases to a certain higher value, as schematically shown in Figure 4.10. This inference is supported by the observations in the literature [39].

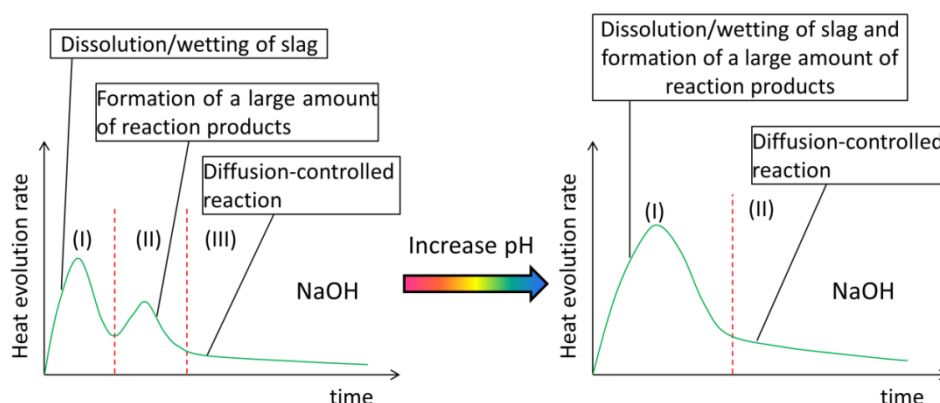


Figure 4.10 Schematic illustration of the effect of increasing the pH of sodium hydroxide activator to a certain higher value on the reaction kinetics of sodium hydroxide activated slag.

Because no nucleation triggers or soluble silicates were present in the *sodium hydroxide* activator, the produced C-(A-)S-H mainly grew on the surface of slag grains. The ongoing growth of C-(A-)S-H led to formation of shells of reaction products around slag grains, as

shown in Figure 4.11(A). This can be visually confirmed by the SEM observations that will be presented in Chapter 5. The shells of reaction products acted as diffusion barriers for the diffusion of hydroxide ions from the solution to the unreacted slag. As a result, the heat evolution rate slowed down after the second calorimetric peak and the reaction of slag came into a steady period controlled by a diffusion process.

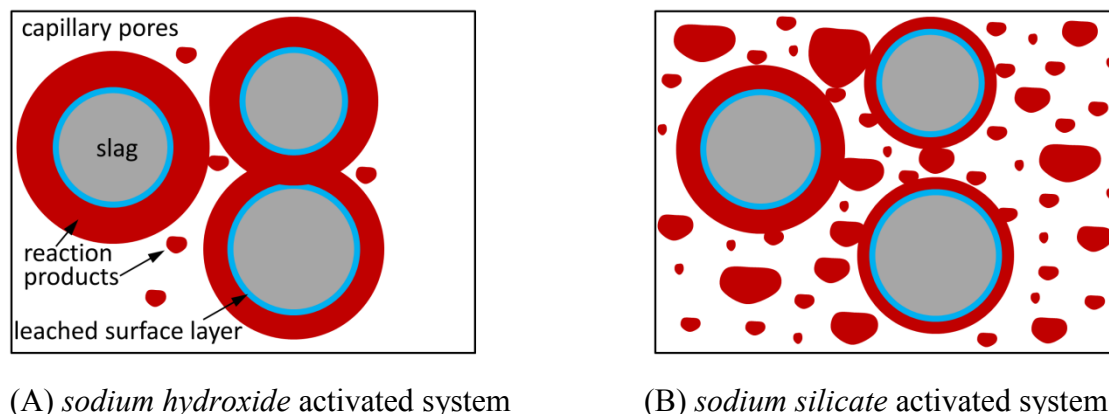


Figure 4.11 Schematic illustration of the reaction products formation in alkali-activated slag.

In *sodium silicate* activated slag, the undersaturation degree of the modifying elements (Ca, Mg, and K) and Al was initially very large when slag was brought into contact with the *sodium silicate* activator. This led to fast release of the modifying elements and Al and thus a high rate of heat evolution (characterized by the first calorimetric peak). However, the undersaturation degree with respect to Si was very low, since a large amount of soluble silicates were already present in the *sodium silicate* activator. The energy provided by the undersaturation was below that needed to overcome the activation energy barrier for the creation of etch pits on the leached surface layer. Therefore, the dissolution of the leached surface layer was slow as it was limited to the step retreat (regime III in Figure 4.9). Therefore, the dissolution rate of the leached surface layer was smaller than the dissolution rate of unreacted slag. This resulted in a rapid growth of the leached surface layer around slag grains. As the thickness of the leached surface layer increased, the diffusion rate of modifying elements through the leached surface layer decreased. Consequently, the dissolution of slag slowed down and the reaction of slag came into an induction period.

In the meantime, the released ions of calcium and aluminum reacted with soluble silicates to form the C-(A-)S-H gel, which gradually consumed ions, especially the soluble silicate species. When the undersaturation degree of Si increased beyond that needed to overcome the energy barrier, the dissolution rate of the leached surface layer increased and thus its thickness decreased. Therefore, the diffusion rate of modifying elements through the leached surface layer increased, leading to a faster dissolution of unreacted slag. The dissolution of the leached surface layer and unreacted slag then led to rapid release of ions into solution. This accelerated the reactions of ions to form reaction products. Therefore reaction products grew rapidly around slag grains as well as in solution space, as schematically shown in Figure 4.11(B). The fast growth of reaction products reflected intensive reactions, as characterized by the second calorimetric peak (Figure 4.3(A)).

Since the soluble silicates in solution provided large numbers of reactive sites [17, 28], the reaction products grew not only on the surface of slag grains but also in the solution space [15]. As the microstructure got denser, more and more diffusion paths of hydroxide ions from solution to unreacted slag were blocked. This slowed down the dissolution of slag and



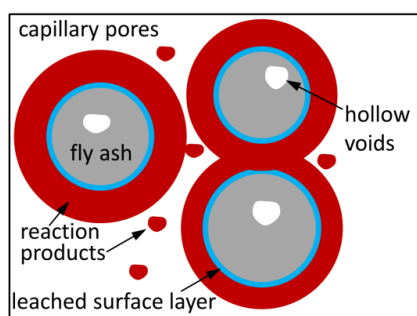
reactions of ions. Therefore, the heat evolution rate slowed down after the second calorimetric peak and the reaction process came into a steady period controlled by a diffusion process.

#### 4.3.2.3 Reaction process and the origin of the induction period in alkali-activated fly ash

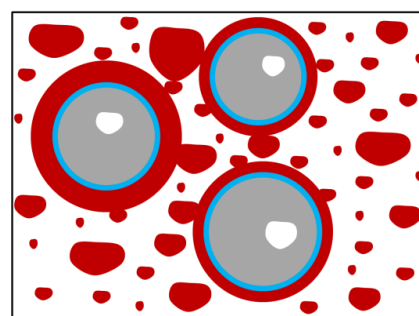
When fly ash was brought into contact with *sodium hydroxide* activator, the undersaturation degree was initially very large. The energy provided by the undersaturation could overcome the activation energy barriers for creation of etch pits. Then the dissolution of fly ash started rapidly and led to fast release of ions into solution, resulting in a high heat evolution rate. After the initial dissolution period, an induction period followed. The origin of the induction period could be explained by the following two aspects:

- On one hand, the fast release of ions led to a rapid increase of the concentration of ions in solution and thus a decrease of the undersaturation degree. As a result the activation energy barrier increased. So the dissolution slowed down.
- On the other hand, the initially released aqueous Al species adsorbed at the leached surface layer. This passivated the surface by preventing the approach of hydroxide ions on the unreacted fly ash [28]. As a result, the dissolution slowed down.

In the induction period, the leached surface layer dissolved slowly, releasing Si to react with the absorbed aqueous Al to form an alkali-aluminosilicate type gel. This reduced the surface passivation and gradually reduced the suppression of dissolution. When the suppression ceased, the induction period ended. After the induction period, the formation of alkali-aluminosilicate type gel consumed ions and lowered the concentration of ions in solution, thus increasing the undersaturation degree. Then the dissolution of fly ash started rapidly and led to fast growth of reaction products. The fast growth of reaction products corresponded to another high rate of heat evolution as characterized by the second calorimetric peak (Figure 4.5(A)). Because no nucleation triggers and soluble silica were present in the *sodium hydroxide* activator, the reactions mainly occurred around fly ash grains and reaction products were formed predominately on the surface of fly ash grains, as schematically shown in Figure 4.12(A). The shells of reaction products around fly ash grains acted as diffusion barriers and reduced the rate of diffusion of hydroxide ions from the solution to unreacted fly ash. This slowed down the dissolution of fly ash, further slowing down the reactions of ions. Therefore, the heat evolution rate slowed down after the second calorimetric peak and the reaction of fly ash came into a steady period controlled by a diffusion process.



(A) *sodium hydroxide* activated system



(B) *sodium silicate* activated system

Figure 4.12 Schematic illustration of the reaction products formation in alkali-activated fly ash.

For *sodium silicate* activated fly ash, the soluble silicate species in solution quickly reacted with the initially released Al [101]. This had two effects. One was a reduction of the passivation of the leached surface layer by the adsorbed Al and allowed rapid dissolution of fly ash. The other was the formation of gel nuclei in solution. The formed gel nuclei grew gradually with reactions of the released Si and Al from fly ash grains. The rapid dissolution of fly ash resulted in fast release of ions, thus accelerating the growth of gel nuclei. The growth of gel nuclei consumed the released ions and led to an increase of the undersaturation degree. With an increase of the undersaturation the dissolution of fly ash was accelerated. Due to these two effects, the calorimetric peak that corresponded to the dissolution of fly ash and the calorimetric peak that corresponded to the rapid growth of reaction products merged into one broad calorimetric peak. No induction period was observed. The initial dissolution period and the acceleration/deceleration period merged into one long reaction period. Since the soluble Si in solution provided nucleation sites, the reaction products were produced homogeneously in the *sodium silicate* activated fly ash – not only on the surface of fly ash grains but also in the solution [37, 67], as schematically shown in Figure 4.12(B). The reaction products grew with time throughout the sample, which gradually blocked the diffusion paths of hydroxide ions from the solution to unreacted fly ash. This slowed down the dissolution of fly ash and the reactions of ions. Therefore, the heat evolution rate slowed down and the reaction process came into a steady period controlled by a diffusion process.

#### **4.3.2.4 Reaction process and the origin of the induction period in alkali-activated slag blended with fly ash**

When a blend of slag and fly ash was brought into contact with *sodium silicate* solution, the undersaturation degree with respect to the modifying elements and Al was initially very large. All the dissolution mechanisms in Section 4.3.2.1 were active and the dissolution started rapidly, leading to fast release of ions into solution. Along with the fast dissolution a high heat evolution rate was expected. This was characterized by the first calorimetric peak (Figure 4.7(A)). Contrary to the alkali-activated slag with the same alkaline activator (BFS\_N6S5.4), there was no induction period after the initial dissolution period in the alkali-activated slag/fly ash (B\_N6S5.4). This may be due to the fact that fly ash grains acted as nucleation sites. The nucleation sites accelerated the reactions of the released ions and thus promoted rapid growth of reaction products. Then the second calorimetric peak that reflected the accelerated reaction of slag was advanced. Consequently, no induction period occurred after the initial dissolution period.

After the first acceleration/deceleration period, the reaction of slag came into the induction period (see Figure 4.7(A)). This was because the formation of reaction products prevented the approach of hydroxide ions on the unreacted slag. On the other hand, the reaction of fly ash was very slow due to its low reactivity and the ambient curing temperature. The induction period lasts until the onset of the rapid reaction of fly ash. The rapid reaction of fly ash led to another fast growth of reaction products and another high heat evolution rate. This high heat evolution rate was characterized by the third calorimetric peak and reflected the accelerated reaction of fly ash (Figure 4.7(A)). In the meantime, the formation of reaction products around fly ash grains started to prevent hydroxide ions from approaching the unreacted fly ash (Figure 4.13). As a result, the reaction of fly ash slowed down after the third calorimetric peak. Afterwards, the reaction process of the alkali-activated slag/fly ash came into a steady period that was controlled by a diffusion process.

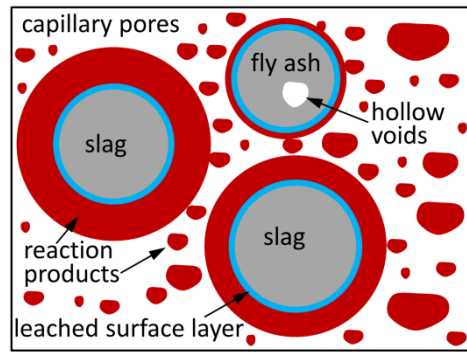


Figure 4.13 Schematic illustration of the reaction products formation in sodium silicate activated slag/fly ash.

### 4.3.3 Degree of reaction

In this section, the degree of reaction was determined by using Equation 4.1. In order to obtain the maximum heat release, the degree of reaction at 7 days was determined from SEM-image analysis. The details will be provided in Chapter 5. Given the degree of reaction and cumulative heat release at 7 days, the maximum heat release can be obtained based on Equation 4.1. It is noteworthy that the degree of reaction determined for the alkali-activated slag/fly ash paste was an overall degree of reaction of slag and fly ash. The results for some selected mixtures were presented, e.g. BFS\_N4S0, BFS\_N6S0 and BFS\_N6S5.4 for alkali-activated slag, FA\_N6.2S0, FA\_N9.3S0 and FA\_N9.3S9 for alkali-activated fly ash cured at 60 °C, and B\_N6S5.4 for alkali-activated slag/fly ash. By following the same procedure, the results for other mixtures can also be obtained.

Table 4.1 Degree of reaction and cumulative heat release at 7 days, the calculated maximum heat release and the determined parameters ( $\tau$  and  $\beta$ ).

Sample	$\alpha$ (7 days)	Q (7 days)	$Q_{\max}$ (J/g)	$\lambda$	$\beta$
BFS_N4S0	$0.537 \pm 0.030$	203	$379 \pm 20$	32.22	0.28
BFS_N6S0	$0.626 \pm 0.044$	248	$396 \pm 29$	20.02	0.33
BFS_N6S5.4	$0.564 \pm 0.041$	249	$442 \pm 34$	28.41	0.33
FA_N6.2S0T60	$0.582 \pm 0.064$	115	$198 \pm 24$	- <sup>a</sup>	-
FA_N9.3S0T60	$0.661 \pm 0.053$	157	$237 \pm 20$	-	-
FA_N9.3S9T60	$0.751 \pm 0.085$	146	$194 \pm 25$	-	-
B_N6S5.4	$0.643 \pm 0.070$	192	$299 \pm 36$	32.59	0.54

a. The degree of reaction of fly ash was not simulated using Equation 4.3, since reactive phases in fly ash was almost completely reacted within 7 days (see Figure 4.6(B)).

The degree of reaction, derived from SEM-image analysis, and the cumulative heat release at 7 days, and the calculated maximum heat release are listed in Table 4.1 for alkali-activated slag, alkali-activated fly ash, and alkali-activated slag/fly ash. The maximum heat release varied with the type and concentration of alkaline activator. This was because the alkaline activator affected the chemical reactions taking place during the reaction process and thus led to different reaction products. As different chemical reactions have different reaction enthalpies, this then resulted in different reaction enthalpy changes and thus led to different maximum heat release. Given the maximum heat release, the degree of reaction was

calculated as a function of time using Equation 4.1. By fitting the experimental data of the degree of reaction, parameters ( $\tau$  and  $\beta$ ) in Equation 4.3 were determined. The results are listed in Table 4.1. With these parameters, the degree of reaction can be predicted as a function of time.

#### 4.3.3.1 Degree of reaction of slag in alkali-activated slag paste

Figure 4.14 presents the calculated degree of reaction of slag for BFS\_N4S0, BFS\_N6S0 and BFS\_N6S5.4 based on the calorimetry measurements using Equation 4.3. For *sodium hydroxide* activated slag, BFS\_N4S0 and BFS\_N6S0, the degree of reaction was influenced by the content of  $\text{Na}_2\text{O}$ . The mixture with a higher  $\text{Na}_2\text{O}$  content had a higher degree of reaction of slag. Comparing the *sodium silicate* activated slag with the *sodium hydroxide* activated slag with the same content of  $\text{Na}_2\text{O}$ , addition of  $\text{SiO}_2$  into the mixture led to a lower degree of reaction.

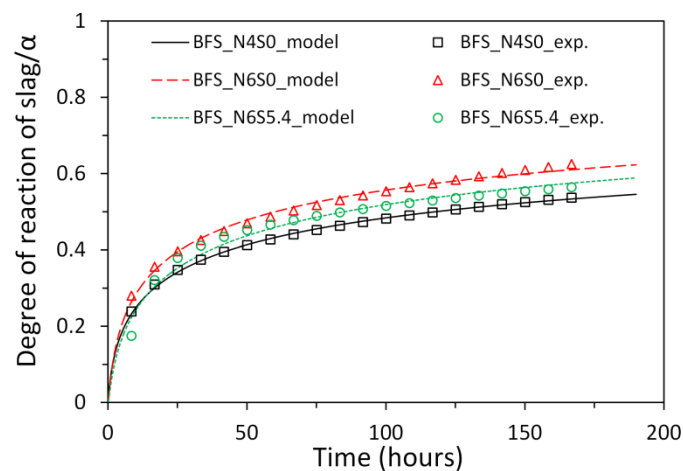


Figure 4.14 Calculated degree of reaction of the alkali-activated slag samples based on the calorimetry measurements using Equation 4.3.

#### 4.3.3.2 Degree of reaction of fly ash in alkali-activated fly ash paste

The degree of reaction of fly ash is presented in Figure 4.15 for the alkali-activated fly ash cured at 60 °C. For *sodium hydroxide* activated fly ash, i.e. FA\_N6.2S0 and FA\_N9.3S0, the mixture with an increase of  $\text{Na}_2\text{O}$  content had a higher degree of reaction of fly ash. Comparing the *sodium silicate* activated fly ash with the *sodium hydroxide* activated fly ash with the same content of  $\text{Na}_2\text{O}$ , the addition of  $\text{SiO}_2$  showed no influence on the degree of reaction of fly ash in the early age (during the first day), but led to clearly higher degree of reaction in a later age (after the first day). After about 2 days of curing, the degree of reaction of fly ash exhibited little increase with time.

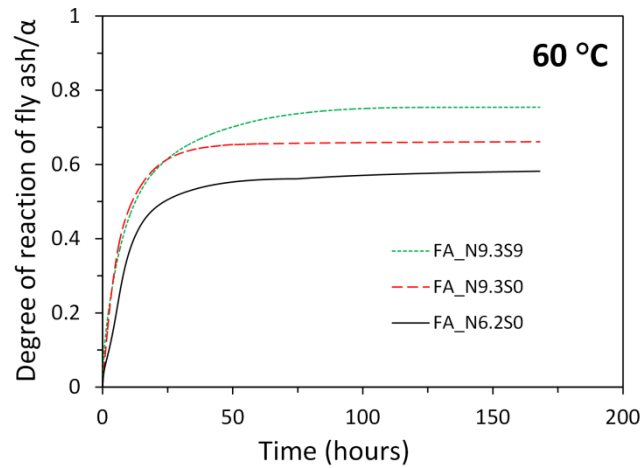


Figure 4.15 Calculated degree of reaction of the alkali-activated fly ash samples based on the calorimetry measurements using Equation 4.1.

#### 4.3.3.3 Overall degree of reaction of slag and fly ash in alkali-activated blended slag/fly ash paste

The calculated overall degree of reaction of slag and fly ash is shown in Figure 4.16 for the alkali-activated slag/fly ash paste.

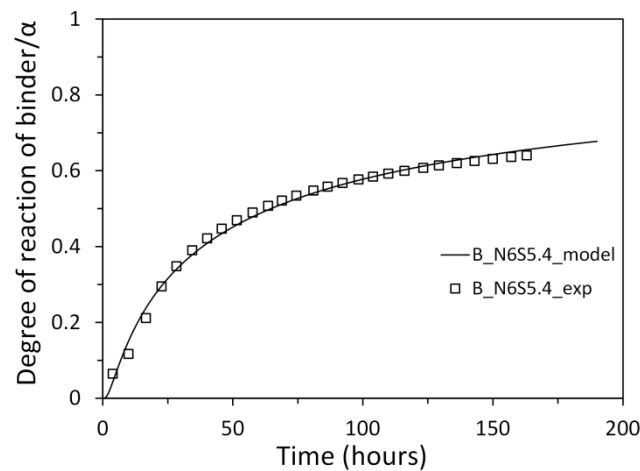


Figure 4.16 Calculated overall degree of reaction of the alkali-activated slag/fly ash sample based on the calorimetry measurements using Equation 4.3.

## 4.4 Conclusions

In this chapter the reaction kinetics of alkali-activated slag, alkali-activated fly ash and alkali-activated slag/fly ash, were studied by using isothermal calorimetry. Particularly the origin of the induction period during the reaction process was discussed. From the experimental results and discussions, the following remarks can be made:

### *Calorimetric response*

- (1) The heat evolution rate curve of alkali-activated slag paste showed two calorimetric peaks. According to these two calorimetric peaks, three reaction stages were identified for *sodium hydroxide* activated slag, i.e. the initial dissolution period, acceleration/deceleration period and steady period. For *sodium silicate* activated slag, one more reaction stage was identified, i.e. the induction period between the two calorimetric peaks.
- (2) The heat evolution rate curve of *sodium hydroxide* activated fly ash showed two calorimetric peaks. The number of reaction stages depended on the curing temperature. For *sodium silicate* activated fly ash, the calorimetric peak that corresponded to the dissolution of fly ash and the calorimetric peak that corresponded to the rapid growth of reaction products merged into one broad calorimetric peak. Therefore, the heat evolution rate curve showed only one calorimetric peak and only two reaction stages were identified.
- (3) The heat evolution rate curve of alkali-activated slag/fly ash paste showed three calorimetric peaks. According to those three calorimetric peaks, the entire reaction process were divided into five reaction stages, i.e. the initial dissolution period, acceleration/deceleration period for slag, induction period, acceleration/deceleration period for fly ash and steady period.

### *Origin of the induction period*

- (1) The origin of the induction period in alkali-activated slag was discussed by using a dissolution theory based mechanism. In *sodium hydroxide* activated slag, a large undersaturation degree led to fast dissolution of slag, resulting in no noticeable induction period. In *sodium silicate* activated slag, the undersaturation with respect to Si was below that needed to overcome the activation energy barrier for the creation of etch pits on the leached surface layer. This slowed down the dissolution of the leached surface layer and the dissolution of unreacted slag. Consequently, an induction period occurred.
- (2) The induction period occurred in *sodium hydroxide* activated fly ash. This was mainly attributed to the passivation of the leached surface layer by the absorbed Al. In *sodium hydroxide* activated fly ash, the initially dissolved Al absorbed to the leached surface layer, passivating the surface by preventing the approach of hydroxide ions on the unreacted fly ash. Then the dissolution of fly ash slowed down and the reaction came to an induction period. It is noted that a higher curing temperature reduced the surface passivation and prevented the induction period. For *sodium silicate* activated fly ash, the soluble silicates in the activator quickly reacted with the initially dissolved Al and reduced the surface passivation. Consequently, the induction period did not occur.
- (3) In *sodium silicate* activated slag/fly ash, the absence of the induction period between the first calorimetric peak and the second calorimetric peak might be due to the fact that fly ash grains provided nucleation sites, which accelerated the reaction of slag. The induction period occurred between the second calorimetric peak and the third calorimetric peak. This was due to the low reactivity of fly ash and the ambient curing temperature.

*Effects of Na<sub>2</sub>O content, SiO<sub>2</sub> content and curing temperature*

- (1) An increase of Na<sub>2</sub>O content led to higher calorimetric peaks and accelerated the reaction of alkali-activated slag or fly ash.
- (2) The influence of SiO<sub>2</sub> content on the reaction kinetics varied with the type of aluminosilicate precursor. The addition of SiO<sub>2</sub> in the mixture resulted in an induction period during the reaction of alkali-activated slag, while it prevented the induction period during the reaction of alkali-activated fly ash.
- (3) A higher curing temperature for alkali-activated fly ash accelerated the reaction and reduced the passivation of the leached surface layer. So, the induction period might not occur in *sodium hydroxide* activated fly ash at a certain higher temperature, for example the mixture FA\_N9.3S0T60.

*Outlook*

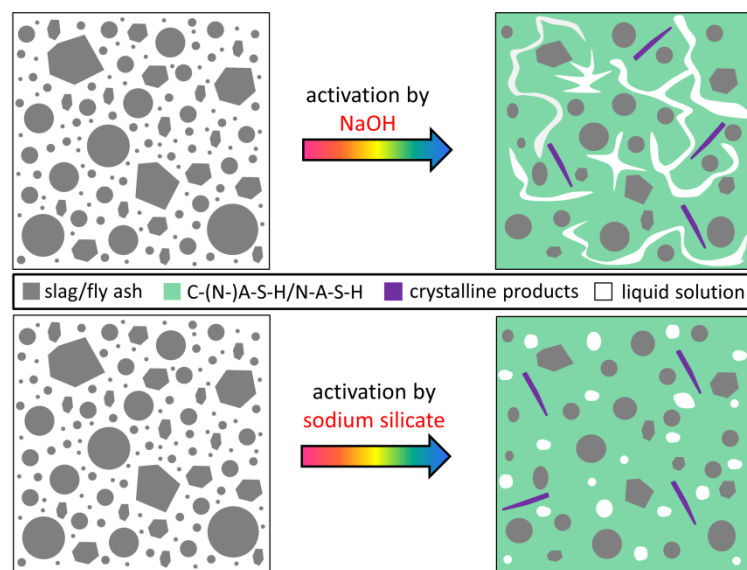
With the quantified reaction kinetics in this chapter it is possible to perform thermodynamic modelling of the reactions in AAMs in a time domain. The results of thermodynamic modelling will be presented in Chapter 8. More importantly, the obtained results on reaction kinetics in this chapter provide insights to develop the numerical model – GeoMicro3D. This numerical model, to be presented in Chapter 9, should account for the effects of the types of alkaline activator and aluminosilicate precursor on the reaction kinetics.





# Chapter 5

## Microstructure analysis of alkali-activated materials<sup>12</sup>



Alkali-activated material, similar to any Portland cement-based material, has a porous microstructure that contains solid phases and pores. In this chapter, the microstructures of alkali-activated slag paste, alkali-activated fly ash paste, and alkali-activated slag/fly ash paste were studied using scanning electron microscopy (SEM) and mercury intrusion porosimetry (MIP). The effects of alkaline activator (i.e. contents of  $\text{Na}_2\text{O}$  and  $\text{SiO}_2$ ) and curing temperature on the microstructure formation were investigated.

<sup>12</sup> This chapter is partially based on:

Yibing Zuo and Guang Ye. Pore structure characterization of sodium hydroxide activated slag using mercury intrusion porosimetry, nitrogen adsorption, and image analysis. *Materials*, 11(2018) 1035.

## 5.1 Introduction

When aluminosilicate precursor (mostly slag and fly ash) is brought into contact with an alkaline activator, the precursor starts to dissolve and subsequently a set of reactions commence, leading to the formation of various solid reaction products [45, 46]. With progress of the reactions, capillary pores, i.e. the empty or initially-liquid-filled space, are gradually filled with reaction products. In addition to the capillary pores, the reaction products also contain gel pores. The size of capillary pores ranges from several nanometers (nm) to several micrometers ( $\mu\text{m}$ ), while a gel pore has a size of approximately several nanometers. Thus, the alkali-activated material, similar to any Portland cement-based material, has a porous microstructure that contains solid phases and pores. Many properties of alkali-activated materials are directly or indirectly related to the microstructure, such as strength [112], shrinkage and creep [113], and permeability [112]. Therefore, a good understanding of the microstructure formation, such as distribution of reaction products and pore structure etc., is of great importance to interpret these properties and to develop numerical models for alkali-activated materials.

In this chapter the microstructures of alkali-activated slag paste, alkali-activated fly ash paste, and alkali-activated slag/fly ash paste were studied using scanning electron microscopy (SEM) and mercury intrusion porosimetry (MIP). The effects of alkaline activator (i.e. contents of  $\text{Na}_2\text{O}$  and  $\text{SiO}_2$ ), and curing temperature on the microstructure formation were investigated. The studied parameters included the distribution of reaction products, total porosity, pore size distribution, and differential pore size distribution. The obtained results in this chapter will provide new insights into the microstructure formation of alkali-activated materials, which then helps to formulate and validate the numerical model (GeoMicro3D) in Chapter 9. Figure 5.1 shows the position of Chapter 5 in structure of the study of the reaction process and microstructure formation of AAMs in this thesis.

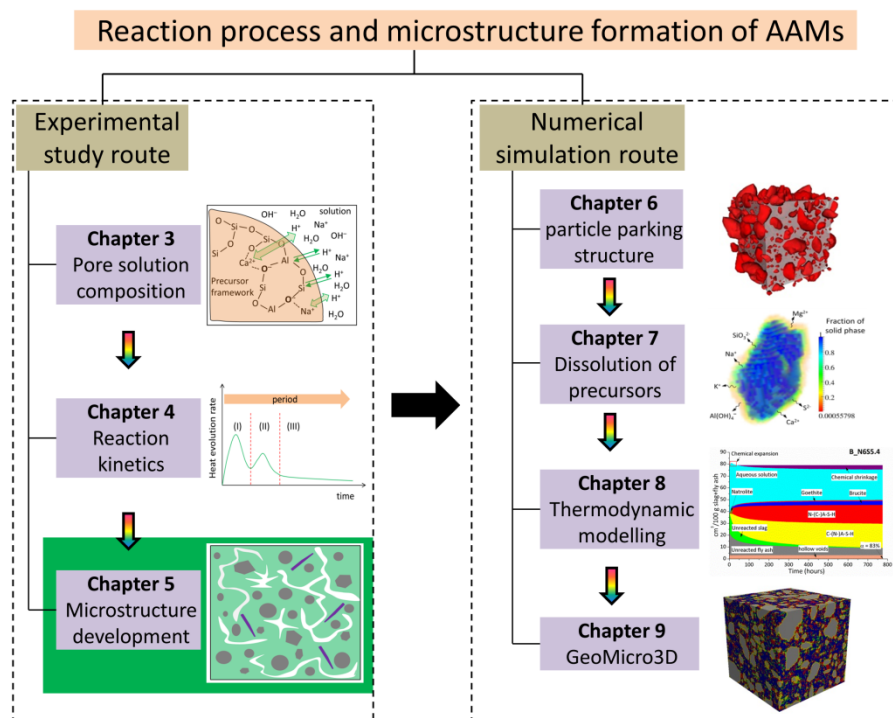


Figure 5.1 Position of Chapter 5 in structure of the study of the reaction process and microstructure formation of AAMs in this thesis

## 5.2 Materials and methods

### 5.2.1 Materials and mixtures

The slag and fly ash used in this chapter are the same as in Chapter 3. The mixtures designed in Chapter 3 (Table 3.2) were also used in this chapter. It is noted that only the selected mixtures were used to study the microstructure of alkali-activated materials, i.e. BFS\_N4S0, BFS\_N6S0 and BFS\_N6S5.4 for alkali-activated slag paste, FA\_N9.3S0T40, FA\_N9.3S9T40, FA\_N6.2S0T60, FA\_N9.3S0T60 and FA9.3S9T60 for alkali-activated fly ash paste, and B\_N6S5.4 for alkali-activated slag/fly ash paste.

The samples were prepared by following the procedures given in Chapter 3. At the designed testing age, the samples were crushed into small pieces with dimensions of 1-2 cm<sup>3</sup>, and then the small pieces of samples were immersed in isopropanol for at least two weeks to stop the reaction. After that, the samples were dried in a vacuum at 20 °C for one week. Then the vacuum dried samples were stored in a desiccator until testing.

### 5.2.2 Scanning electron microscopy (SEM)

For preparing samples for SEM test, the vacuum dried samples were impregnated using a low viscosity epoxy resin and then polished down to 0.25 μm (more details of the sample preparation procedures can be found in [114]). Then, the polished samples were examined by Philips XL30 with backscattering electron (BSE) mode at an acceleration voltage of 20 kV under low vacuum mode. The water vapor pressure was kept at 1.0 Torr. The size of each image was 254 μm in length and 190 μm in width. The magnification of each image was 500×, and the image size was 1424 × 968 pixel. The resolution of the image was 0.1786 μm/pixel. Those obtained SEM images with the magnification of 500× were submitted to image analysis for the determination of the degree of reaction and pore size distribution (see Section 5.2.4). On the other hand, SEM images with the magnification of 1000× were also obtained for clearer observations of the microstructure morphology.

### 5.2.3 Mercury intrusion porosimetry (MIP)

MIP measurements were carried out with a Micrometrics PoreSizer<sup>®</sup> with a maximum intrusion pressure of 210 MPa. In each measurement, the test was conducted in two stages. The first stage was the low-pressure stage with the pressure running from 0 to 0.14 MPa. The second stage was the high-pressure stage. The intrusion procedure started with the pressure running from 0.14 to 210 MPa. After the applied pressure reached the highest pressure (210 MPa), i.e. the end of intrusion procedure, the extrusion procedure started with the applied pressure decreasing to 0.17 MPa. In the high-pressure stage, two cycles of intrusion and extrusion procedures were conducted in this study. By assuming the pores were cylindrical, the diameter of pores intruded by mercury at each pressure step was calculated using the Washburn equation [115] as follows:

$$d = \frac{-4\gamma_m \cdot \cos \omega}{p} \quad (5.1)$$

where  $d$  is the pore diameter,  $\gamma_m$  is the surface tension of mercury (0.485 N/m used here [116]),  $\omega$  is the contact angle between mercury and sample surface, and  $p$  is the applied pressure (from 0 to 210 MPa). The contact angle was taken as 138° for the mercury intrusion process [117]. Figure 5.2 shows the typical cumulative pore size distribution curves obtained from the sample BFS\_N4S0 at 1 day by MIP test. The total porosity is calculated as the total

volume of pores divided by the bulk volume of the sample, and the total volume of pores is defined as the total volume of mercury intruded at the maximum applied pressure in the first intrusion.

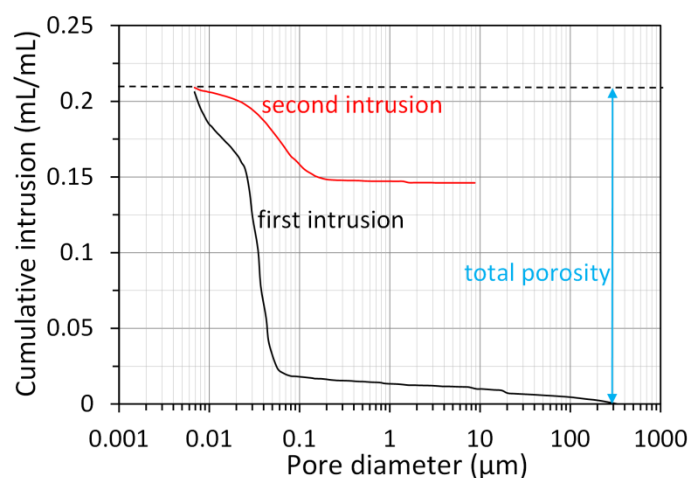


Figure 5.2 Typical cumulative pore size distribution curves obtained from the sample BFS\_N4S0 at 1 day by MIP measurement.

#### 5.2.4 SEM-image analysis

The SEM image includes 256 grey level values, ranging from 0 (black) to 255 (white). The higher the average atomic number and atomic number density of a phase, the brighter the phase appears in the SEM image [118]. In the SEM images of alkali-activated materials, the brightest phases mainly correspond to the unreacted precursors, while the darkest phase corresponds to porosity. According to the brightness contrast, the SEM image can be segmented into different phases, i.e. unreacted precursors, reaction products and porosity. Then the degree of reaction as well as the pore size distribution of alkali-activated materials can be determined.

##### *Phase segmentation of alkali-activated slag paste*

A typical BSE image of alkali-activated slag paste is shown in Figure 5.3(A) and its grey level histogram is shown in Figure 5.3(B). Three distinguished phases can be clearly identified, i.e. pores, reaction products and unreacted slag. According to the grey level histogram, a threshold was applied on the original BSE image and the pores (distinguished as black) were obtained as shown in Figure 5.3(C). Based on the obtained images the pore size distribution will be determined. Similarly, the unreacted slag (distinguished as white) was obtained as shown in Figure 5.3(D). So the area fraction of unreacted slag can be obtained.

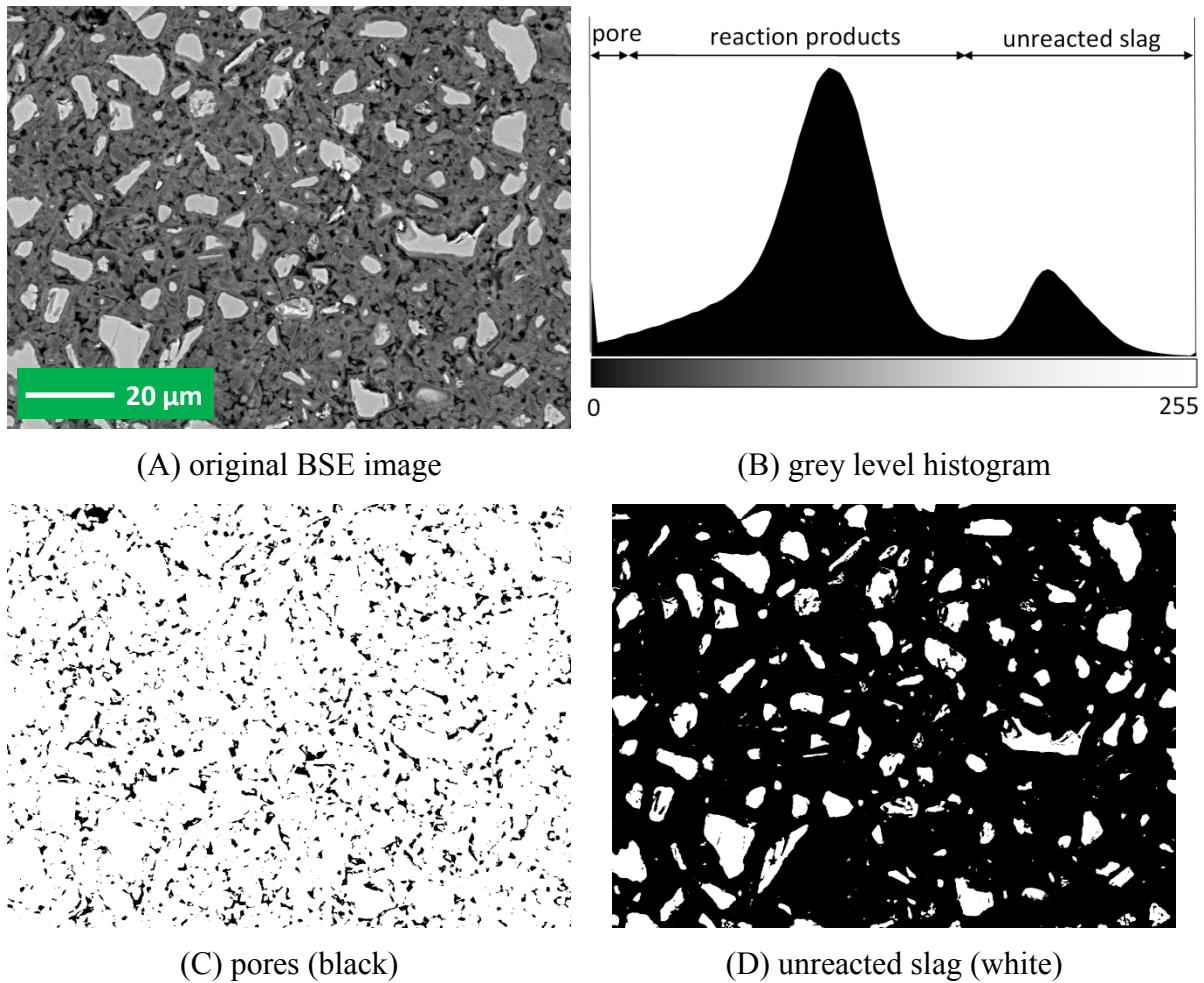


Figure 5.3 Phase segmentation of alkali-activated slag paste by applying thresholds on the original BSE image.

#### Phase segmentation of alkali-activated fly ash paste or alkali-activated slag/fly ash paste

Figure 5.4(A) shows a typical BSE image of alkali-activated fly ash paste. Because the grey level of some fly ash particles is similar to the grey level of the reaction products and some pores exist in fly ash particles as empty voids, the segmentation between pores, reaction products and unreacted fly ash cannot be achieved by simply applying the threshold segmentation according to the grey level histogram (Figure 5.4(B)).

In order to solve those problems, a technique, similar to an *area selection tool*, developed by Ma [67], was used to segment the phases from each other. First, the original BSE image was submitted to the *Trainable Weka Segmentation* in ImageJ [119]. The reference pixels corresponding to pores, reaction products and unreacted fly ash were selected, and then all the pixels in the BSE image with similar grey levels to those of the reference pixels were automatically segmented by running the function *Train Classifier*. Figure 5.4(C) shows the output image after the *Trainable Weka Segmentation*. In the image, black, grey and white represent pores, reaction products and unreacted fly ash, respectively. In the second step, the pixels that actually corresponded to unreacted fly ash were manually turned into white based on careful observations on the zoomed in images. Figure 5.4(D) shows the final segmented image. In this way, the pores, reaction products, and unreacted fly ash could be clearly



segmented. For alkali-activated slag blended with fly ash paste, similar procedures were applied. As such, the pores, reaction products, unreacted slag and unreacted fly ash in alkali-activated slag/fly ash could be segmented. Compared to the method used in [120], the approach proposed in this work is simpler and more efficient.

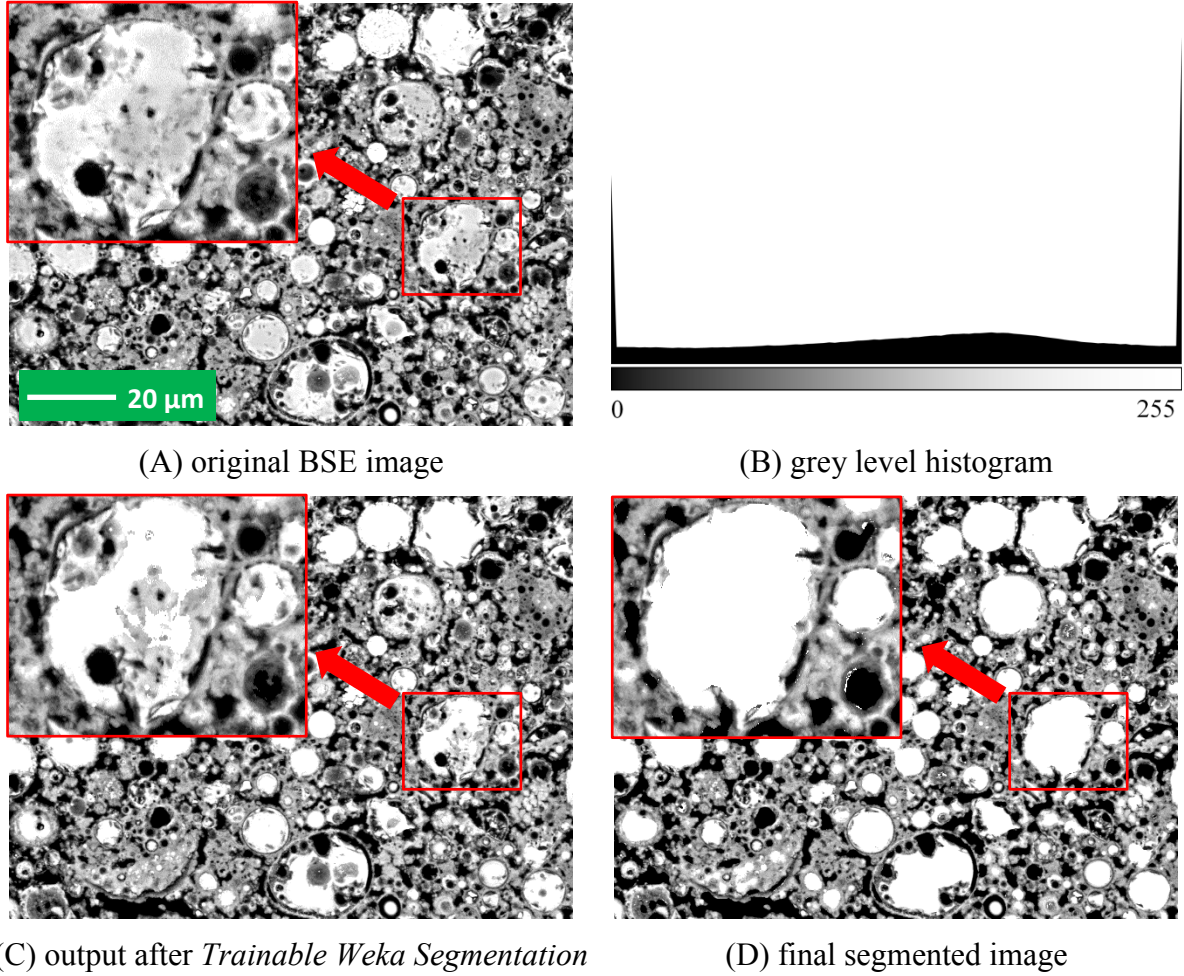


Figure 5.4 Phase segmentation of alkali-activated fly ash paste through coupling *Trainable Weka* segmentation and manual segmentation.

#### *Degree of reaction*

Chayes mathematically solved the problem of transferring the pore area fraction to the pore volume fraction [121]. The result is that the pore area fractions, calculated from a two-dimensional image, can be assumed to be equal to the volume fractions in three dimensions. This result has been used by many researchers in image analysis [67, 114, 122]. Then the degree of reaction can be calculated as follows:

$$\alpha(t) = \left(1 - \frac{F_t}{F_0}\right) \times 100\% \quad (5.2)$$

where  $\alpha(t)$  is the degree of reaction at age  $t$ ,  $F_t$  is the volume fraction of slag or fly ash at age  $t$  (obtained from phase segmentation based on SEM-image analysis),  $F_0$  is the initial volume

fraction of slag or fly ash. The obtained degree of reaction helped to quantify the reaction kinetics of alkali-activated materials, as discussed in Chapter 4.

### *Pore size distribution*

Yang et al. developed an image-based algorithm to obtain the pore size distribution of porous media [123]. This algorithm was employed in this study to calculate the pore size distribution based on the pores obtained from the BSE image. The details of this method will be provided in Chapter 6. It has been reported that the image analysis based on 12 or more BSE images could guarantee a 95% degree of confidence [114]. In this study, a total number of 15 images on randomly selected locations for each sample were subjected to image analysis. The average pore size distribution was used as the final pore size distribution for the sample, for instance BFS\_N4S0 at 1 day, as shown in Figure 5.5.

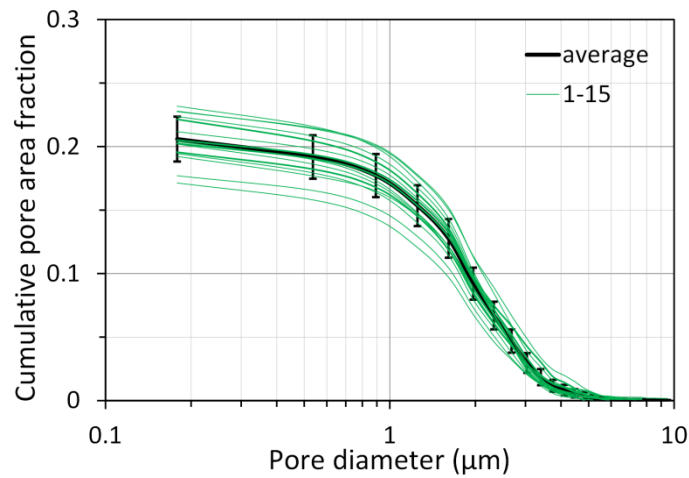


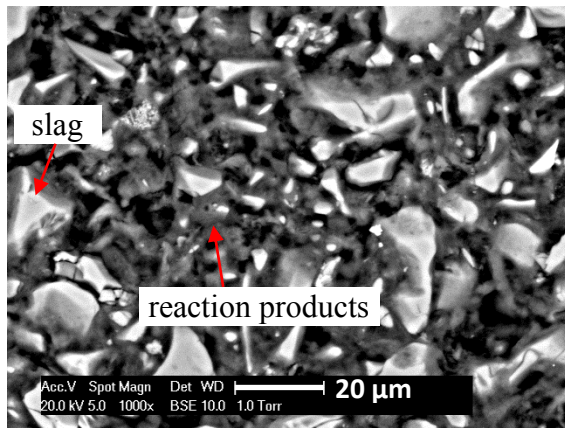
*Figure 5.5 Calculated pore size distribution of sample BFS\_N4S0 at 1 day through SEM-image analysis.*

## **5.3 Results**

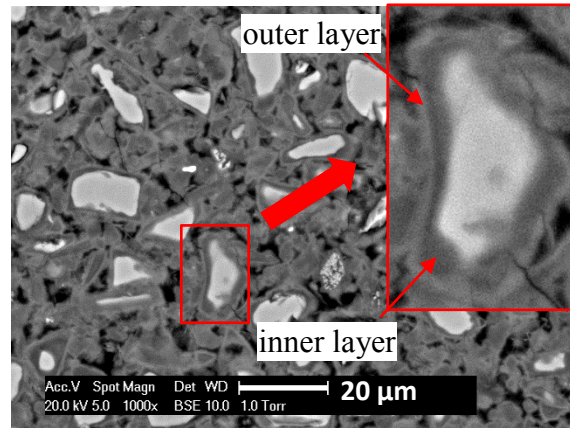
### **5.3.1 Morphology and degree of reaction of hardened alkali-activated slag paste**

Figure 5.6 shows the SEM-micrographs of the alkali-activated slag samples at 1 day and 28 days. It is clear that for all samples grey reaction products surrounded the bright unreacted slag grains. The sample with higher  $\text{Na}_2\text{O}$  content exhibited a larger volume of reaction products and hence a denser microstructure. In sodium hydroxide activated samples, i.e. BFS\_N4S0 and BFS\_N6S0, two layers of reaction products were found surrounding the unreacted slag grains at 28 days. This observation has also been reported in the literature [15].

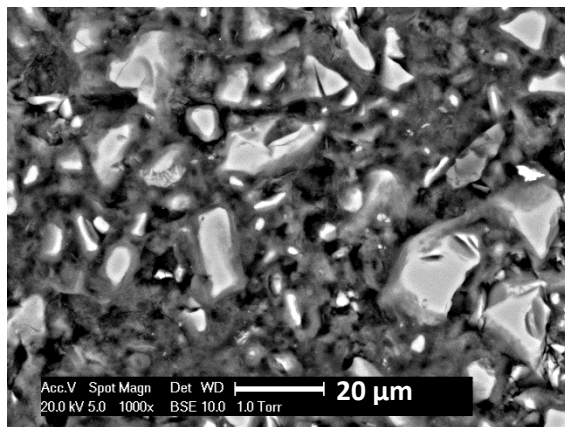
The layer formed later, i.e. inner layer of reaction products, was darker than the layer formed earlier, i.e. outer layer of reaction products. The difference in grey level is due to the different nanoporosities and, therefore, to different densities [15]. It is reported that the inner layer of reaction products, containing more Na, was less dense than the outer layer of reaction products [15]. In contrast, the reaction products in sodium silicate activated samples, i.e. BFS\_N6S5.4, were homogeneously distributed and the two layers of reaction products were not observed.



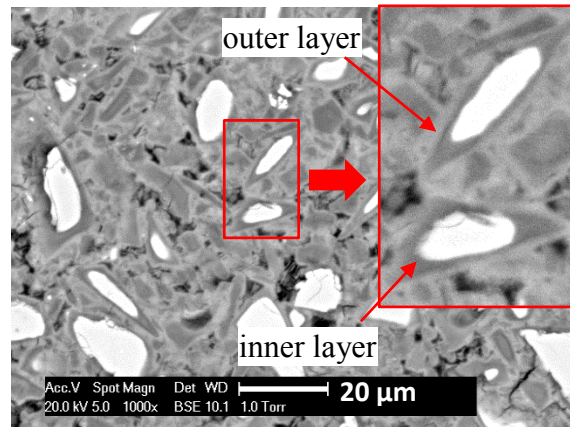
(A) BFS\_N4S0, 1 day



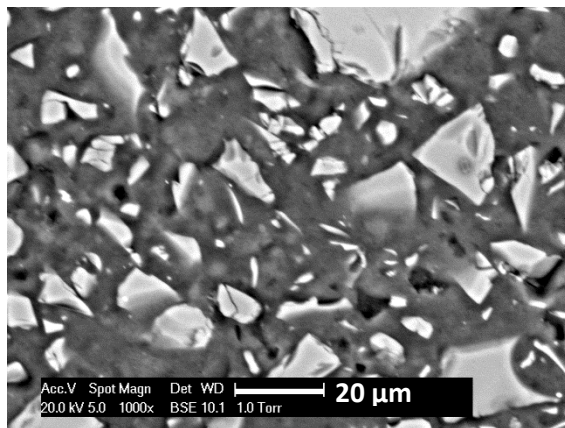
(B) BFS\_N4S0, 28 days



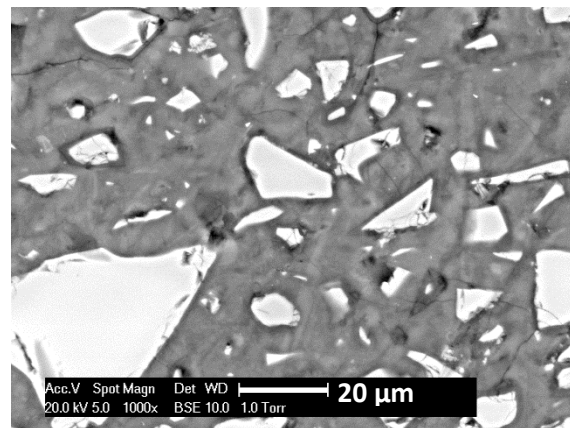
(C) BFS\_N6S0, 1 day



(D) BFS\_N6S0, 28 days



(E) BFS\_N6S5.4, 1 day



(F) BFS\_N6S5.4, 28 days

*Figure 5.6 Microstructure of samples BFS\_N4S0 (A, B), BFS\_N6S0 (C, D), and BFS\_N6S5.4 (E, F) at 1 day and 28 days. In the graphs, BFS indicates alkali-activated slag, and N and S indicate weight percentage of  $\text{Na}_2\text{O}$  and  $\text{SiO}_2$  with respect to slag, respectively. The water-to-slag ratio was 0.4 and the curing temperature was 20 °C. See more details of the mixtures in Table 3.2.*

Figure 5.7 shows the degree of reaction of slag in alkali-activated slag samples, derived from SEM-image analysis (Equation 5.2). The presented results are consistent with the values in the literature [15, 124]. The degree of reaction increased rapidly during the first day, reaching 48.5 %, 57.0 % and 50.4 % after 1 day for BFS\_N4S0, BFS\_N6S0 and BFS\_N6S5.4,



respectively. After 1 day, the degree of reaction increased slowly with time. The influences of  $\text{Na}_2\text{O}$  and  $\text{SiO}_2$  contents on the degree of reaction were different. The mixture with a higher  $\text{Na}_2\text{O}$  content had a higher degree of reaction, while the mixture with an addition of  $\text{SiO}_2$  had a lower degree of reaction. This is because the increase of  $\text{Na}_2\text{O}$  content led to a higher alkalinity of the alkaline activator, while the addition of  $\text{SiO}_2$  resulted in a lower alkalinity of the alkaline activator. A higher alkalinity of the alkaline activator accelerates the reaction of slag and, therefore, results in a higher degree of reaction. Furthermore, as discussed in Section 4.3.1, the addition of  $\text{SiO}_2$  resulted in an induction period during the reaction process, hampering the reaction of slag and thus leading to a lower degree of reaction.

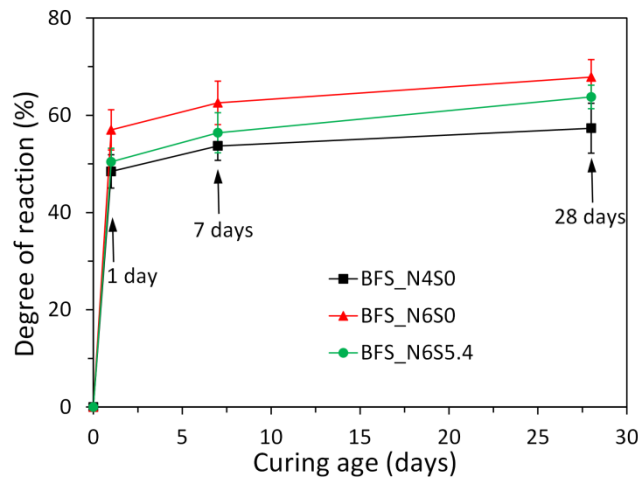
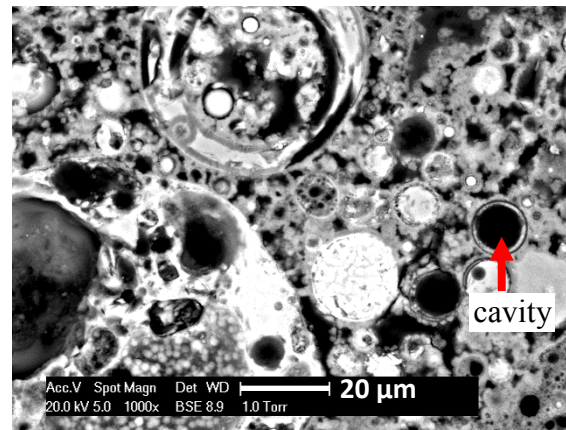


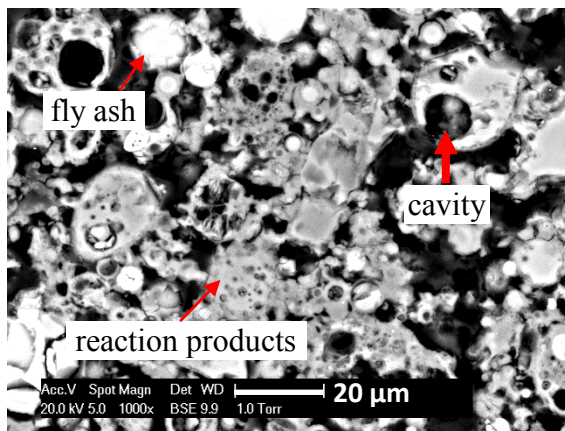
Figure 5.7 Degree of reaction of slag, derived from SEM-image analysis, for BFS\_N4S0, BFS\_N6S0 and BFS\_N6S5.4. In the graph, BFS indicates alkali-activated slag, and N and S indicate weight percentage of  $\text{Na}_2\text{O}$  and  $\text{SiO}_2$  with respect to slag, respectively. The water-to-slag ratio was 0.4 and the curing temperature was 20 °C. See more details of the mixtures in Table 3.2.

### 5.3.2 Morphology and degree of reaction of hardened alkali-activated fly ash paste

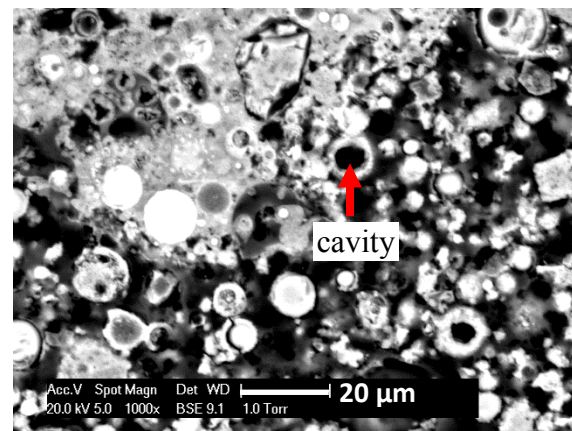
Figures 5.8 and 5.9 show the SEM-micrographs of the alkali-activated fly ash samples at 7 days and 28 days, respectively. In sodium hydroxide activated fly ash samples, for example FA\_N6.2S0T40 and FA\_N9.3S0T40, the amount of reaction products was limited and mainly grew around the unreacted fly ash particles. A loose and porous microstructure was observed in sodium hydroxide activated fly ash samples at both 7 days and 28 days. In the sodium silicate activated fly ash samples, by contrast, the reaction products occupied most of the empty pore space and were homogeneously distributed in the matrix, leading to a very dense microstructure. These results are in line with the literature, saying that an increase of the silicate content in alkaline activator leads to a denser and more homogeneous microstructure [16, 17, 125].



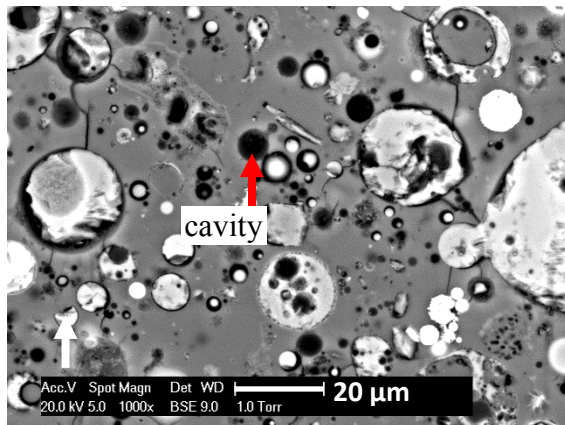
(A) FA\_N6.2S0T60



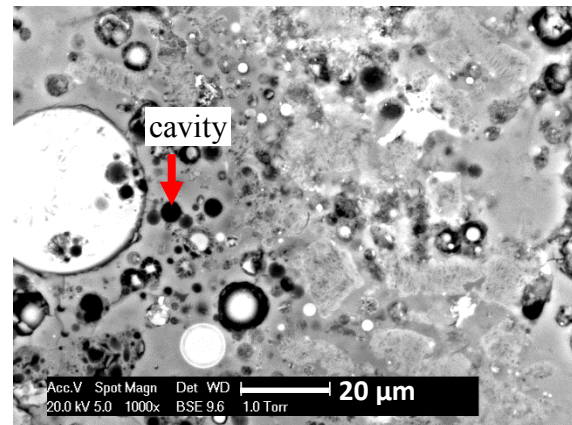
(B) FA\_N9.3S0T40



(C) FA\_N9.3S0T60



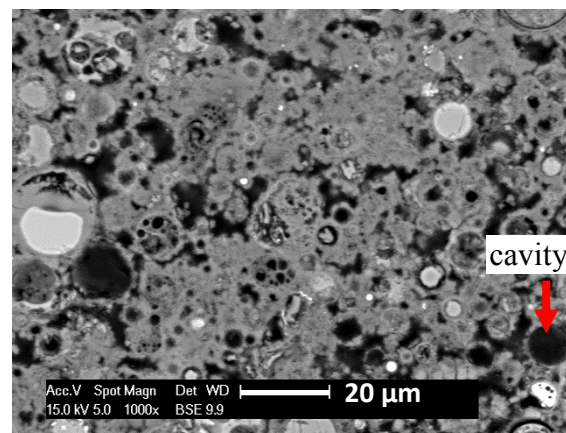
(D) FA\_N9.3S9T40



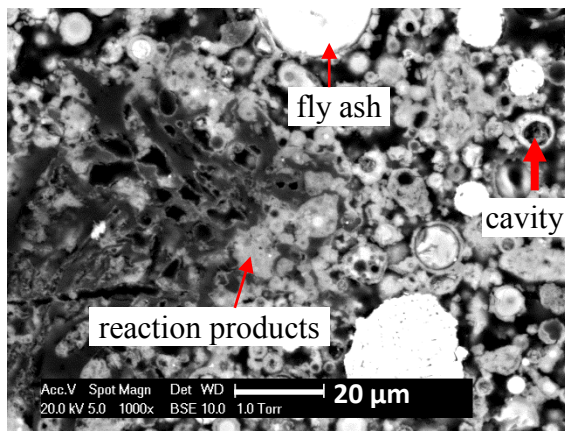
(E) FA\_N9.3S9T60

Figure 5.8 Microstructure of alkali-activated fly ash samples at 7 days. In the notations, FA indicates alkali-activated fly ash, N and S indicate weight percentage of  $\text{Na}_2\text{O}$  and  $\text{SiO}_2$  with respect to fly ash, respectively, and T refers to temperature in Celsius. The water-to-fly-ash ratio was 0.35 and the curing temperature was 40 °C or 60 °C. See more details of the mixtures in Table 3.2.

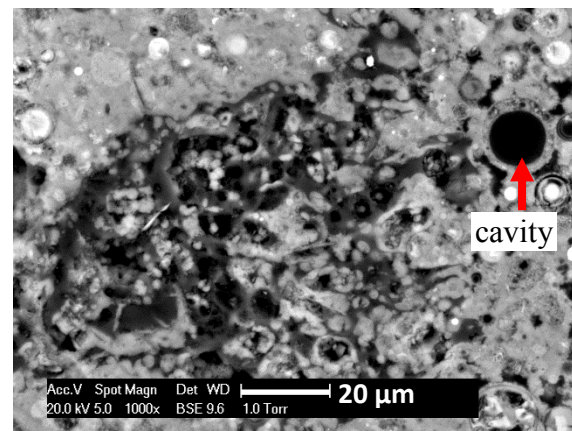




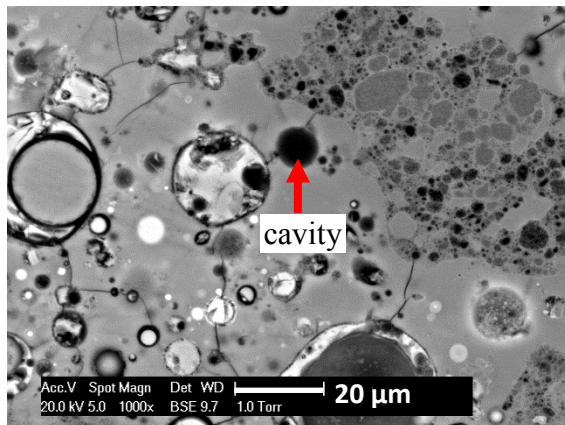
(A) FA\_N6.2S0T60



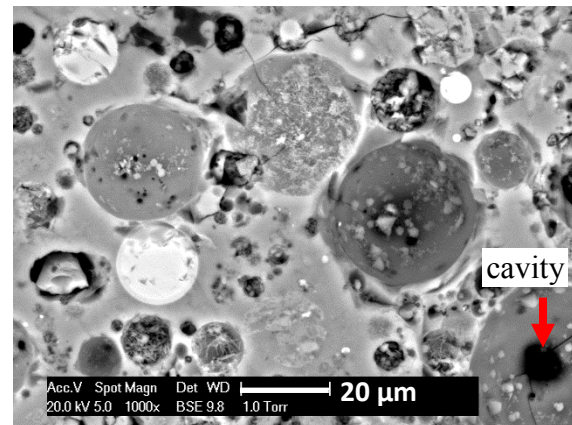
(B) FA\_N9.3S0T40



(C) FA\_N9.3S0T60



(D) FA\_N9.3S9T40



(E) FA\_N9.3S9T60

*Figure 5.9 Microstructure of alkali-activated fly ash samples at 28 days. In the notations, FA indicates alkali-activated fly ash, N and S indicate weight percentage of  $\text{Na}_2\text{O}$  and  $\text{SiO}_2$  with respect to fly ash, respectively, and T refers to temperature in Celsius. The water-to-fly-ash ratio was 0.35 and the curing temperature was 40 °C or 60 °C. See more details of the mixtures in Table 3.2.*

All the mixtures showed a number of large cavities as indicated by arrows in the images. Some were formed due to the dissolved fly ash particles, some were actually the hollow voids in the unreacted fly ash particles, and some were likely to result from the unreacted fly ash

grains that had been fallen out of the sample during polishing. These cavities, with several microns in diameters, were separated by the reaction products. These cavities in alkali-activated fly ash were also observed using Wood's metal intrusion together with SEM images, as reported by Lloyd et al. [126]. It was found that these large cavities in the matrix of alkali-activated fly ash were accessible by Wood's metal even at later curing age [126].

The degree of reaction of fly ash, derived from SEM-image analysis (Equation 5.2), is presented in Figure 5.10. The presented results are comparable with the values in the literature [67]. It is clear that the degree of reaction of fly ash was influenced by the contents of  $\text{Na}_2\text{O}$  and  $\text{SiO}_2$ , and curing temperature.

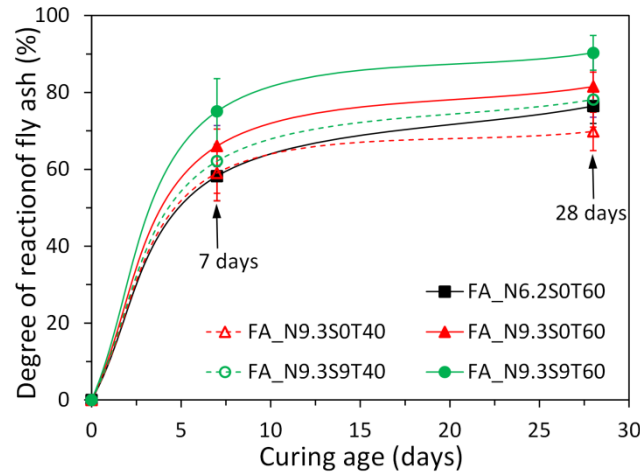


Figure 5.10 Degree of reaction of fly ash, derived from SEM-image analysis, for FA\_N6.2S0T60, FA\_N9.3S0T60, FA\_N9.3S9T60, FA\_N9.3S0T40 and FA\_N9.3S9T40. In the graphs, FA indicates alkali-activated fly ash, N and S indicate weight percentage of  $\text{Na}_2\text{O}$  and  $\text{SiO}_2$  with respect to fly ash, respectively, and T refers to temperature in Celsius. The water-to-slag ratio was 0.35 and the curing temperature was 40 °C or 60 °C. For more details of the mixtures, see Table 3.2.

#### Influence of $\text{Na}_2\text{O}$ content

When the  $\text{Na}_2\text{O}$  content increased from 6.2 % to 9.3 % (see samples FA\_N6.2S0T60 and FA\_N9.3S0T60 in Figure 5.10), the degree of reaction of fly ash at 7 and 28 days increased from 58.2 % to 66.1 % and from 76.4 % to 81.5 %, respectively. The increase of  $\text{Na}_2\text{O}$  content in alkaline activator has two effects that could lead to a higher degree of reaction [67]. On one hand, the increase of  $\text{Na}_2\text{O}$  content leads to a higher alkalinity of the alkaline activator. A high amount of hydroxide ions promotes the breaking of Si-O-Si and Si-O-Al bonds of the reactive fly ash, releasing silicon and aluminum monomers into solution [26]. On the other hand, sodium cations are incorporated in N-A-S-H gels to balance the electric charge in the three-dimensional tetrahedral Al structure [57], which therefore promotes the reaction.

#### Influence of $\text{SiO}_2$ content

At the same content of  $\text{Na}_2\text{O}$ , the degree of reaction of the mixture with an addition of  $\text{SiO}_2$  was obviously larger than that of the mixture with no addition of  $\text{SiO}_2$ . This could be seen from the comparisons between the sodium silicate activated samples (FA\_N9.3S9T40 and FA\_N9.3S9T60) and the sodium hydroxide activated samples (FA\_N9.3S0T40 and FA\_N9.3S0T60) with the same content of  $\text{Na}_2\text{O}$  in Figure 5.10. When the  $\text{SiO}_2$  content

increased from 0 to 9.0 % for the alkali-activated fly ash samples with the  $\text{Na}_2\text{O}$  content of 9.3 % and cured at 40 °C, the degree of reaction of fly ash increased from 59.0 % to 62.1 % at 7 days and from 69.9 % to 78.1 % at 28 days. As discussed in Chapter 3 (Section 3.3.2), the dissolution rate of fly ash is reduced due to the passivation of surface sites of fly ash particles in sodium hydroxide activated fly ash. In sodium silicate activated fly ash the soluble silicate could quickly react with the initially released Al and prevent Al from being absorbed to the surface sites. So the surface passivation was reduced. This resulted in more rapid dissolution of fly ash and led to a higher degree of reaction.

#### *Influence of curing temperature*

It is clear that an increase of curing temperature led to a higher degree of reaction. Comparing FA\_N9.3S0T40 with FA\_N9.3S0T60, for instance, the degree of reaction at 7 days and 28 days increased from 59.0 % to 66.1 % and from 69.9 % to 81.5 %, respectively, when the curing temperature increased from 40 °C to 60 °C. The higher curing temperature accelerated both the dissolution of fly ash and the reaction of silicon and aluminum species to form N-A-S-H gels [61]. As a result, a higher degree of reaction was achieved. According to the Arrhenius equation, an increase of temperature accelerates the reactions of alkali-activated fly ash. But it is not straightforward to quantify the effect of temperature by using this equation. An increase of temperature not only increases the rate of reaction but also changes the nature of reaction products [59, 60].

### **5.3.3 Morphology and degree of reaction of hardened alkali-activated slag/fly ash paste**

Figure 5.11 shows the SEM-micrographs of alkali-activated slag/fly ash samples at the ages of 1 day and 28 days. The cracks in Figure 5.11(A) were caused during the preparation of samples for SEM test. The images show a homogeneous morphology with well-distributed reaction products and embedded unreacted slag and fly ash particles. Similar to the alkali-activated fly ash samples (Figures 5.7 and 5.8), cavities were also observed in the alkali-activated slag/fly ash samples. As curing age increased from 1 day to 28 days, a number of small slag and fly ash particles seemed to be completely dissolved.

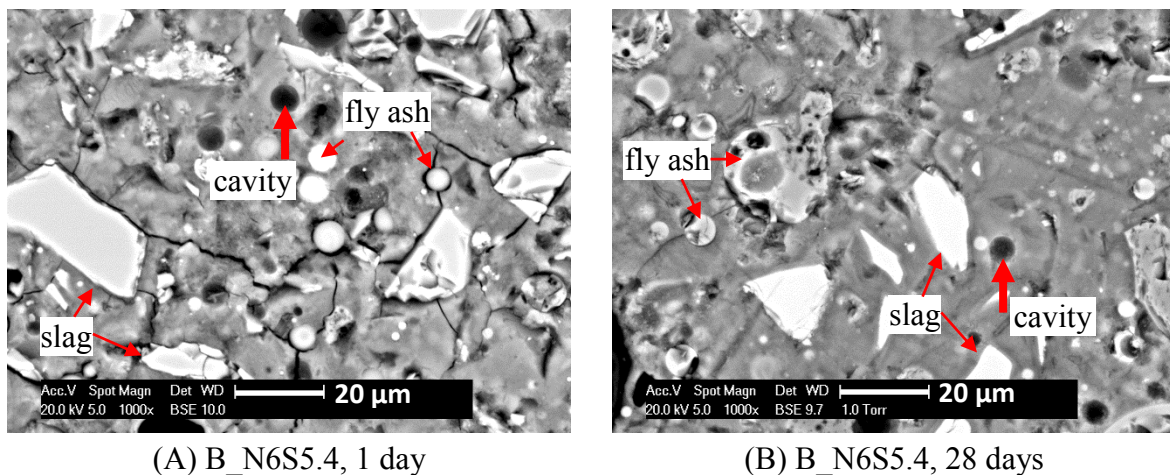


**Figure 5.11** Microstructure of B\_N6S5.4 at 1 day (A) and 28 days (B). Here, B indicates alkali-activated slag/fly ash, N and S indicate weight percentage of  $\text{Na}_2\text{O}$  and  $\text{SiO}_2$  with respect to precursor, respectively. The water-to-precursor ratio was 0.4 and the curing temperature was 20 °C. For more details of the mixtures, see Table 3.2.



According to the SEM-image analysis, the overall degree of reaction of slag and fly ash, the degree of reaction of slag and the degree of reaction of fly ash were determined (Equation 5.2). The results are presented in Figure 5.12. The degree of reaction of slag was 64.6 % at 1 day, 72.9 % at 7 days and 79.8 % at 28 days in the alkali-activated slag/fly ash samples. These values were much higher than those of alkali-activated slag with the same alkaline activator (BFS\_N6S5.4, 50.4 % at 1 day, 56.4 % at 7 days and 63.8 % at 28 days). It suggests that the reactions were enhanced in the alkali-activated slag/fly ash. This could be attributed to the fact that replacement of slag by fly ash provided the nucleation sites and increased the effective activator/slag ratio, which accelerated the reaction of slag.

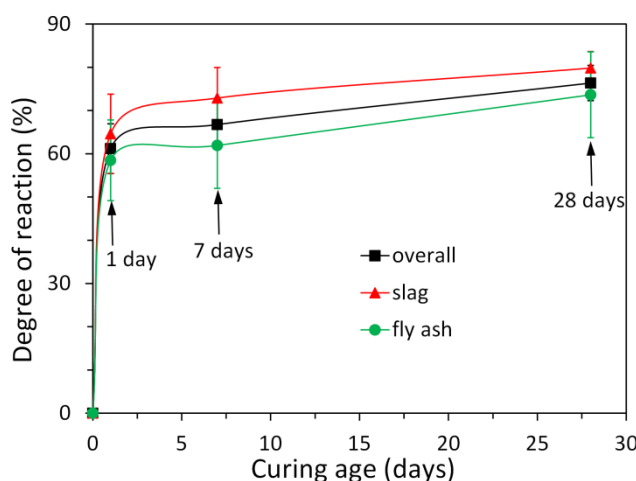


Figure 5.12 Overall degree of reaction of slag and fly ash, degree of reaction of slag and degree of reaction of fly ash, derived from SEM-image analysis, for alkali-activated slag/fly ash (N6S5.4B). Here, B indicates alkali-activated slag/fly ash, and N and S indicate weight percentage of  $\text{Na}_2\text{O}$  and  $\text{SiO}_2$  with respect to precursor, respectively. The water-to-precursor ratio was 0.4 and the curing temperature was 20 °C. For more details of the mixtures, see Table 3.2.

### 5.3.4 Pore structure of alkali-activated slag paste

#### Total porosity derived from MIP for alkali-activated slag

The total porosity of alkali-activated slag samples, derived from MIP, is presented in Figure 5.13. For the mixtures discussed in Chapter 3, the total porosity of samples at the initial moment, when slag was brought into contact with the alkaline activator, was calculated as 54.2 %. As the reaction of slag proceeded, more and more reaction products were formed. This resulted in a continuous decrease of the total porosity of samples with time. Particularly, the total porosity dropped considerably (about 70 %) within the first day, which is in line with the literature [15]. At 1 day, the total porosity was 20.6 %, 16.7 % and 8.9 % for BFS\_N4S0, BFS\_N6S0 and BFS\_N6S5.4, respectively. After 1 day, the total porosity decreased only slightly with time until 28 days. At 28 days, the total porosity was 19.4 %, 14.0 % and 5.9 %, respectively. As the  $\text{Na}_2\text{O}$  content increased from 4 % (BFS\_N4S0) to 6 % (BFS\_N6S0), the total porosity decreased about 28 %. By comparing BFS\_N6S5.4 with BFS\_N6S0, it was found that the addition of  $\text{SiO}_2$  led to a decrease of the total porosity by about 57 %. The decreases of the total porosity by the increase or addition of  $\text{Na}_2\text{O}$  or  $\text{SiO}_2$  content can also be evidenced from the observations in SEM-micrographs in Figure 5.6. The mixture with  $\text{Na}_2\text{O}$  content of 6 % (BFS\_N6S0) had less pores than the mixture with  $\text{Na}_2\text{O}$  content of 4 %

(BFS\_N4S0) at 1 day and 28 days. The mixture with SiO<sub>2</sub> content of 5.4 % (BFS\_N6S5.4) had less pores than the mixture without addition of SiO<sub>2</sub> (BFS\_N6S0) at 1 day and 28 days.

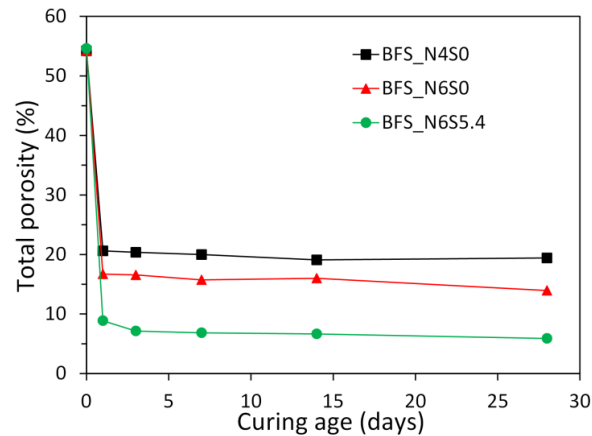


Figure 5.13 Total porosity, derived from MIP, for BFS\_N4S0, BFS\_N6S0 and BFS\_N6S5.4. In the graphs, BFS indicates alkali-activated slag, and N and S indicate weight percentage of Na<sub>2</sub>O and SiO<sub>2</sub> with respect to slag, respectively. The water-to-slag ratio was 0.4 and the curing temperature was 20 °C. For more details of the mixtures, see Table 3.2.

Figure 5.14 displays the total porosity (obtained by MIP) as a function of the degree of reaction of slag. The total porosity decreased only slightly for a degree of reaction beyond 50 %. This suggests that the reaction products were mainly formed in the place where slag dissolved when slag reacted beyond 50 %. Further reaction of slag contributed little to the solid phase growth. This is different from OPC-based materials, in which the total porosity decreases linearly with the increase of the degree of hydration [114].

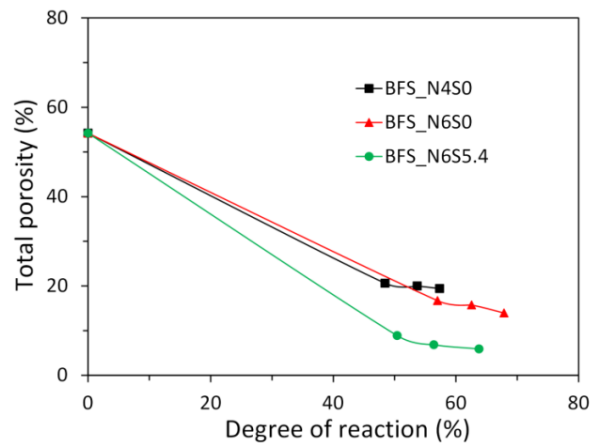
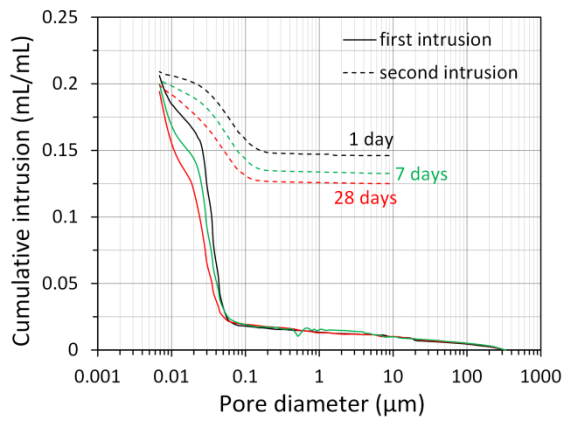


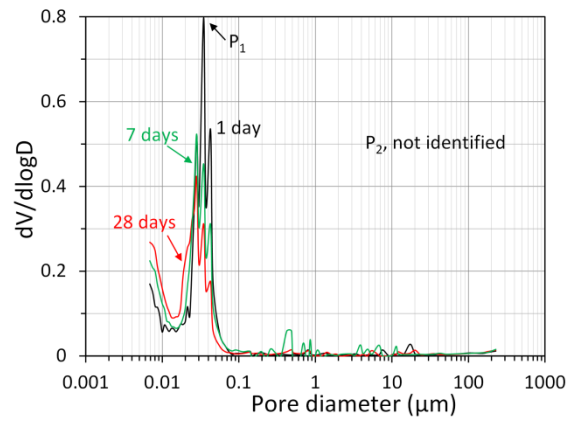
Figure 5.14 Total porosity versus degree of reaction of slag. The total porosity was determined by MIP. BFS indicates alkali-activated slag, and N and S indicate weight percentage of Na<sub>2</sub>O and SiO<sub>2</sub>. The water-to-slag ratio was 0.4 and the curing temperature was 20 °C. For more details of the mixtures, see Table 3.2.

#### Pore size distribution determined by MIP for alkali-activated slag

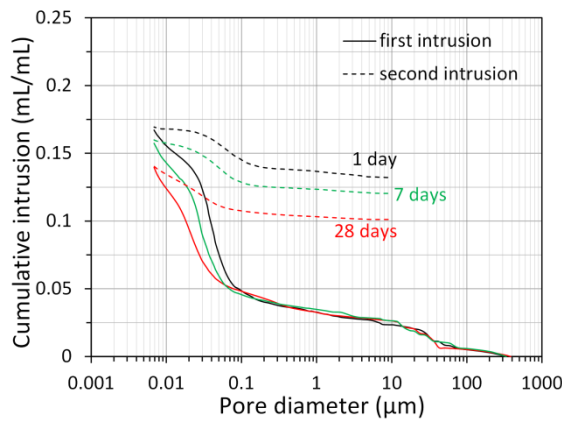
Figure 5.15 shows the pore size distribution and differential pore size distribution of the first MIP intrusion, derived from MIP, for BFS\_N4S0, BFS\_N6S0 and BFS\_N6S5.4 at 1 day, 7 days and 28 days.



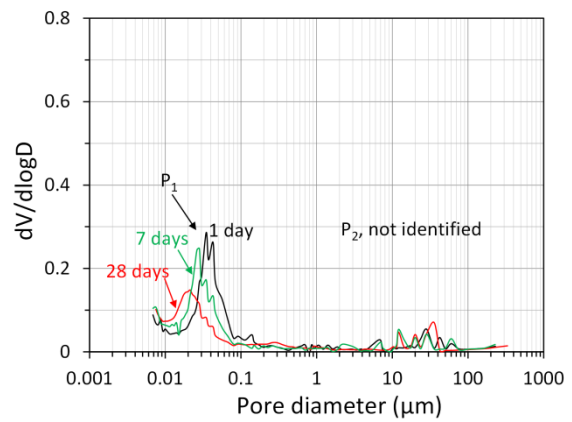
(A) pore size distribution, BFS\_N4S0



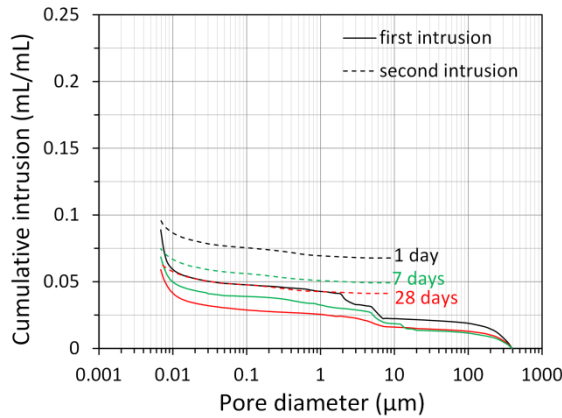
(B) differential pore size distribution, BFS\_N4S0



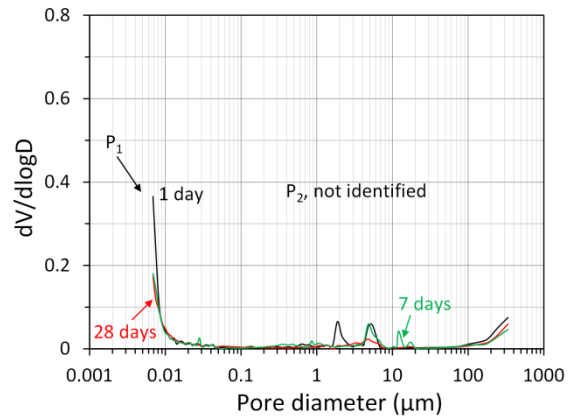
(C) pore size distribution, BFS\_N6S0



(D) differential pore size distribution, BFS\_N6S0



(E) pore size distribution, BFS\_N6S5.4



(F) differential pore size distribution, BFS\_N6S5.4

Figure 5.15 Pore size distribution and differential pore size distribution of the first MIP intrusion. BFS indicates alkali-activated slag, and N and S indicate weight percentage of  $\text{Na}_2\text{O}$  and  $\text{SiO}_2$ . See more details of the mixtures in Table 3.2.

It is clear that the total porosity decreased and the pore size distribution shifted to smaller pore sizes as the curing age increased, indicating a denser microstructure of the sample. The reduced total porosity and refined microstructure is attributed to a higher reaction degree of



samples at the later curing age (see Figure 5.7). A higher reaction degree led to more reaction products filling the pore space and consequently resulting in a denser microstructure. The reduced total porosity and shift of the pore size distribution to smaller pore sizes were also observed when the  $\text{Na}_2\text{O}$  content increased and  $\text{SiO}_2$  was added. The effect of  $\text{Na}_2\text{O}$  resulted from a higher reaction degree (see Figure 5.7). The effect of  $\text{SiO}_2$  resulted from a different microstructure formation mechanism due to the presence of soluble silicate added by  $\text{SiO}_2$ . The soluble silicate in the alkaline activator enabled a homogeneous distribution of reaction products throughout the matrix (see Figure 5.6). The detailed discussion of this observation will be presented in Section 5.4.2.

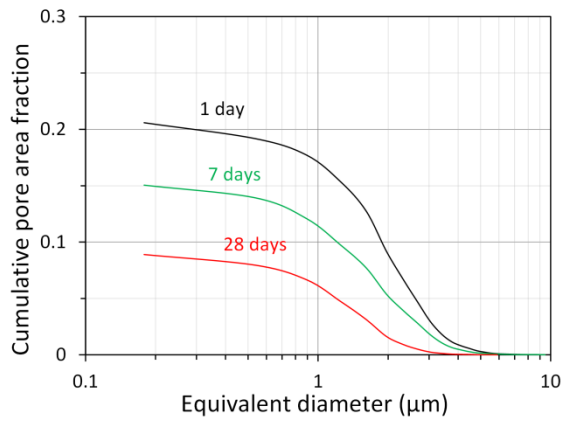
In Portland cement paste, the differential curve of MIP pore size distribution has two peaks, corresponding to two different pore systems [127, 128]. The first peak has a pore diameter smaller than  $0.1\ \mu\text{m}$ , corresponding to the threshold pore diameter of the gel pore system. The second peak, with a pore size larger than  $0.1\ \mu\text{m}$ , corresponds to the threshold pore diameter of the capillary pore system [67, 114, 129]. The physical meaning of a threshold pore diameter is that pores with diameter larger than this diameter can form no connected path through the sample [130].

In alkali-activated slag pastes, however, only the first peak ( $P_1$ ) was identified on the differential pore size distribution curve of MIP, as shown in Figure 5.15(B, D and F). The first peak, i.e. corresponding to gel pores, was found from  $0.01$  to  $0.04\ \mu\text{m}$  for BFS\_N4S0 and BFS\_N6S0, and below  $0.01\ \mu\text{m}$  for BFS\_N6S5.4. This indicates a much denser microstructure of the BFS\_N6S5.4 sample than those of the BFS\_N4S0 and BFS\_N6S0 samples. As the curing time and  $\text{Na}_2\text{O}$  content increased, the first peak shifted to a smaller pore diameter and its height decreased, showing a denser microstructure.

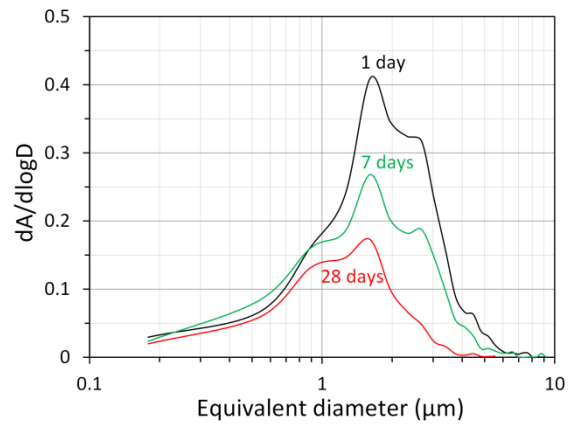
The second peak ( $P_2 > 0.1\ \mu\text{m}$ ), corresponding to the threshold pore diameter of capillary pores, was not identified on the differential pore size distribution curve. The second peak was also not identified for the cement paste (water/cement ratio=0.4) and the blended cement pastes (30 % fly ash, water/binder=0.4) after 180 days of sealed curing [131]. The total porosities of these two samples at 180 days were 12.5 % and 20.3 %, respectively, very close to the total porosity of alkali-activated slag samples after 1 day of sealed curing ( $< 20\%$ , see Figure 5.13). This suggests that alkali-activated slag samples at 1 day had a dense microstructure already, comparable to those of cement paste and blended cement pastes at 180 days. The absence of the second peak was mainly due to the fact that reaction products continuously grew into the pore space, resulting in a decrease of the capillary porosity. When the total porosity decreased below around 20 %, a large amount of capillary pores were disconnected. As a result, the second peak became weak and even disappeared.

#### *Pore size distribution determined by SEM-image analysis for alkali-activated slag*

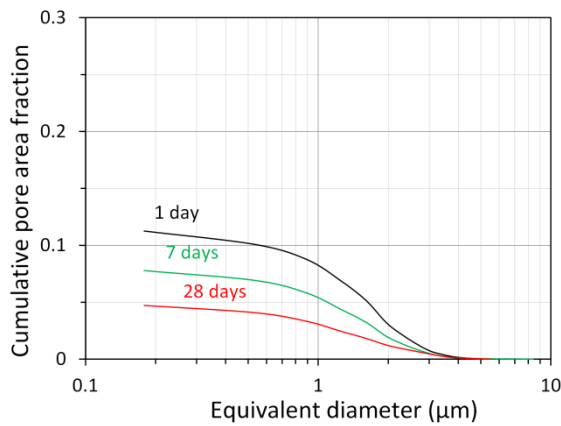
It should be borne in mind that the pore structure derived from SEM-image analysis only reveals the geometry of pores, but not the interconnectivity of the pore paths in the sample. Figure 5.16 shows the pore size distribution and differential pore size distribution, derived from SEM-image analysis, for BFS\_N4S0, BFS\_N6S0 and BFS\_N6S5.4 at 1 day, 7 days and 28 days. The sample with a longer curing time and higher contents of  $\text{Na}_2\text{O}$  and  $\text{SiO}_2$ , had a lower total pore area. The influences of the contents of  $\text{Na}_2\text{O}$  and  $\text{SiO}_2$  on the pore structure are consistent with the observations based on the MIP results as discussed in the previous section.



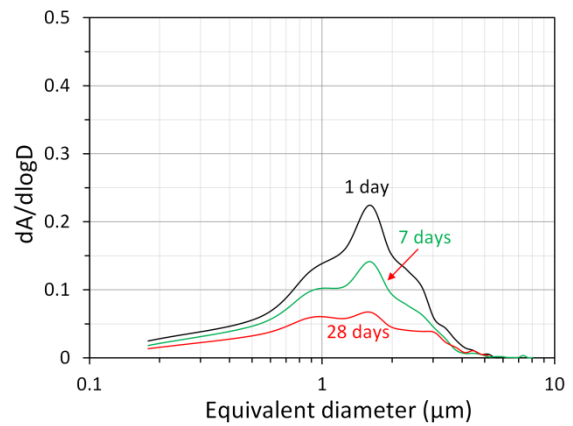
(A) pore size distribution, BFS\_N4S0



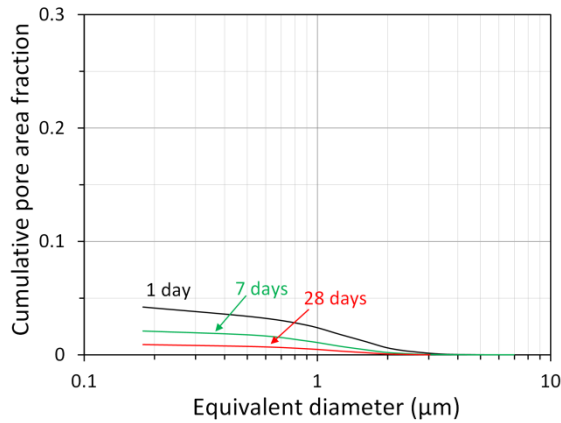
(B) differential pore size distribution, BFS\_N4S0



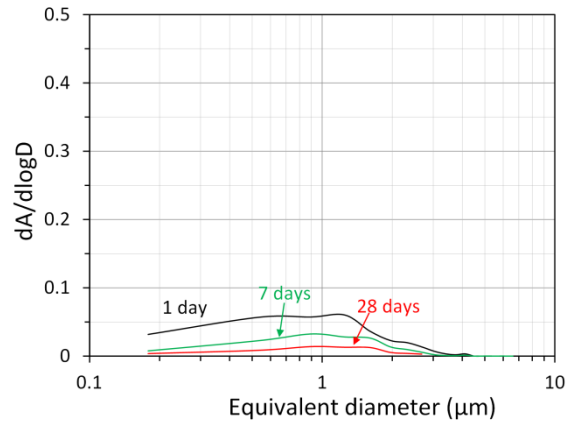
(C) pore size distribution, BFS\_N6S0



(D) differential pore size distribution, BFS\_N6S0



(E) pore size distribution, BFS\_N6S5.4



(F) differential pore size distribution, BFS\_N6S5.4

Figure 5.16 Pore size distribution and differential pore size distributions, derived from SEM-image analysis. BFS indicates alkali-activated slag, N and S indicate weight percentage of  $\text{Na}_2\text{O}$  and  $\text{SiO}_2$ . The water-to-slag ratio was 0.4 and the curing temperature was 20 °C. See more details of the mixtures in Table 3.2.

As seen in Figure 5.16 (right column), only the peak that corresponds to capillary pores was identified on the differential pore size distribution curve. This is different from the differential pore size distributions derived from MIP. From the SEM image analysis the peak that corresponds to gel pores could not be identified. This is because the gel pores with average diameter around  $\sim 0.04 \mu\text{m}$  are about one order of magnitude smaller than the resolution of SEM images ( $0.1786 \mu\text{m}/\text{pixel}$ ). Therefore, the SEM-image analysis could not detect the gel pores.

### 5.3.5 Pore structure of alkali-activated fly ash paste

#### *Total porosity derived from MIP for alkali-activated fly ash*

Figure 5.17 presents the total porosity of alkali-activated fly ash samples, derived from MIP. For the mixtures discussed in Chapter 3, the initial total porosity was calculated as 44.9 %, 45.6 %, 44.8 %, 44.9 % and 45.6 % for FA\_N9.3S0T40, FA\_N9.3S9T40, FA\_N6.2S0T60, FA\_N9.3S0T60 and FA\_N9.3S9T60, respectively. From 1 day to 7 days, the total porosity dropped 12.5 %, 22.5 %, 14.3 %, 16.1 % and 30.1 %, respectively. These reductions are much smaller than the reduction of the total porosity of alkali-activated slag samples (about 70 % after 1 day, see Figure 5.13). This phenomena shows slower growth of solid phase in alkali-activated fly ash than that in alkali-activated slag. For the alkali-activated fly ash cured at  $60^\circ\text{C}$ , an increase of  $\text{Na}_2\text{O}$  content from 6.2 % to 9.3 % did not show much influence on the total porosity (see the comparison between FA\_N6.2S0T60 and FA\_N9.3S0T60). For the alkali-activated fly ash cured at  $40^\circ\text{C}$  or  $60^\circ\text{C}$ , an addition of  $\text{SiO}_2$  by 9.0 % led to a lower total porosity (see the comparisons between FA\_N9.3S9T40 and FA\_N9.3S0T40, and between FA\_N9.3S9T60 and FA\_N9.3S0T60). An increase of curing temperature, i.e. from  $40^\circ\text{C}$  to  $60^\circ\text{C}$ , led to decreases of the total porosity, as inferred from the comparison between FA\_N9.3S0T60 with FA\_N9.3S0T40. This was mainly due to a higher degree of reaction of fly ash at a higher temperature, as shown in Figure 5.10.

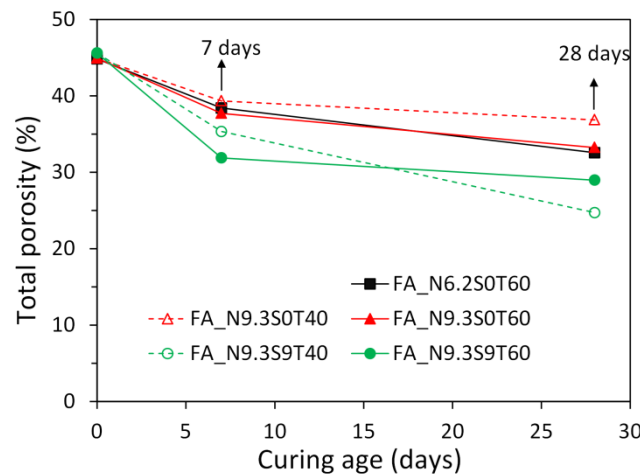


Figure 5.17 Total porosity, derived from MIP, for alkali-activated fly ash samples. In the graph, FA indicates alkali-activated fly ash, N and S indicate weight percentage of  $\text{Na}_2\text{O}$  and  $\text{SiO}_2$  with respect to fly ash, respectively, and T refers to temperature in Celsius. The water-to-fly-ash ratio was 0.35 and the curing temperature was  $40^\circ\text{C}$  or  $60^\circ\text{C}$ . See more details of the mixtures in Table 3.2.

Figure 5.18 displays the total porosity of alkali-activated fly ash samples as a function of the degree of reaction of fly ash. Contrary to the alkali-activated slag samples (see Figure 5.14),

the total porosity of alkali-activated fly ash samples decreased continuously with the increase of the degree of reaction until 90 %. This suggests that the reaction products were continuously formed in the empty pore space. This is similar to the observations in OPC-based materials, in which the total porosity decreases linearly with the increase of the degree of hydration [114].

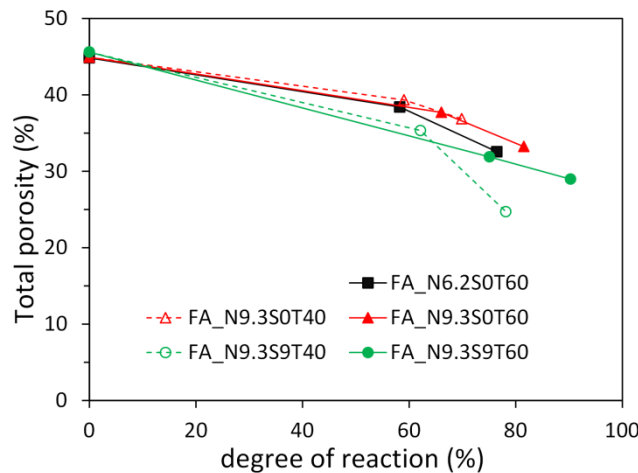


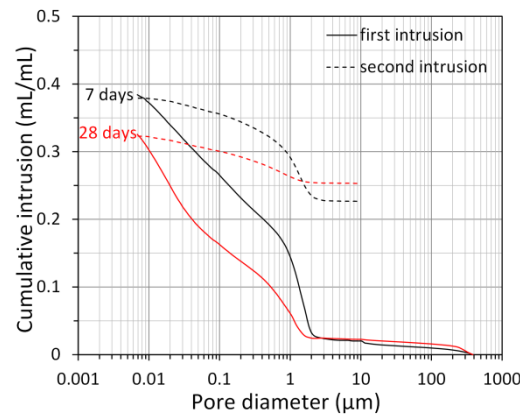
Figure 5.18 Total porosity versus degree of reaction of fly ash. In the graphs, FA indicates alkali-activated fly ash, N and S indicate weight percentage of  $\text{Na}_2\text{O}$  and  $\text{SiO}_2$  with respect to fly ash, respectively, and T refers to temperature in Celsius. The water-to-fly-ash ratio was 0.35 and the curing temperature was 40 °C or 60 °C. The total porosity was determined by MIP.

#### Pore size distribution determined by MIP for alkali-activated fly ash

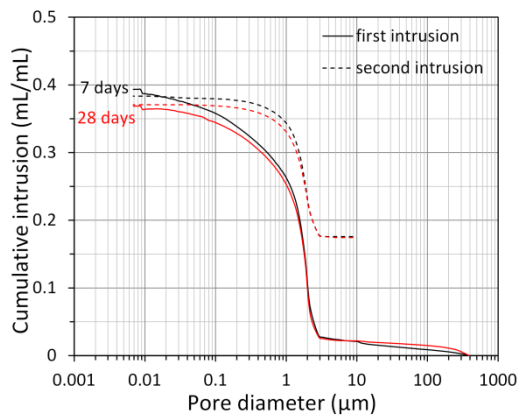
Figure 5.19 presents the pore size distribution of alkali-activated fly ash, derived from MIP, for alkali-activated fly ash samples. From 7 days to 28 days, the total porosity of mixtures decreased and the pore size distribution of mixtures shifted to smaller pore sizes. This indicates a denser microstructure. Although the increase of  $\text{Na}_2\text{O}$  content did not affect the total porosity, it led to a shift of the pore size distribution curve to larger pore sizes, as seen from the comparisons between FA\_N6.2S0T60 (Figure 5.19(A)) with FA\_N9.3S0T60 (Figure 5.19(C)). For the alkali-activated fly ash samples with the same content of  $\text{Na}_2\text{O}$ , an addition of  $\text{SiO}_2$  by 9.0 % reduced the total porosity and led to a shift of the pore size distribution to small pore sizes. This result can be seen from the comparison, for example, between FA\_N9.3S9T40 (Figure 5.19(B)) and FA\_N9.3S0T40 (Figure 5.19(D)).

The differential pore size distribution of the first MIP intrusion is plotted in Figure 5.20 for alkali-activated fly ash samples. In general, two peaks were observed from the differential pore size distribution, representing two pore systems. The first peak ( $P_1$ ) was found for a pore size from several nm to 0.02  $\mu\text{m}$ , corresponding to the threshold pore size of gel pores. The second peak had a pore size larger than 0.1  $\mu\text{m}$ , which corresponds to the threshold pore size of the capillary pores. These observations are in line with the literature [67]. Longer curing time, from 7 days to 28 days, led to a shift of these two peaks to smaller pore sizes, reflecting a denser microstructure. Mixtures with a higher  $\text{Na}_2\text{O}$  content had a larger pore size and a higher height of the second peak. In contrast the increase of  $\text{Na}_2\text{O}$  content resulted in a smaller pore size and a lower height of the first peak. This further confirms that mixtures with a higher  $\text{Na}_2\text{O}$  content had a microstructure with more large pores and less small pores. In the systems with added  $\text{SiO}_2$ , the pore sizes of both peaks were smaller, suggesting a denser

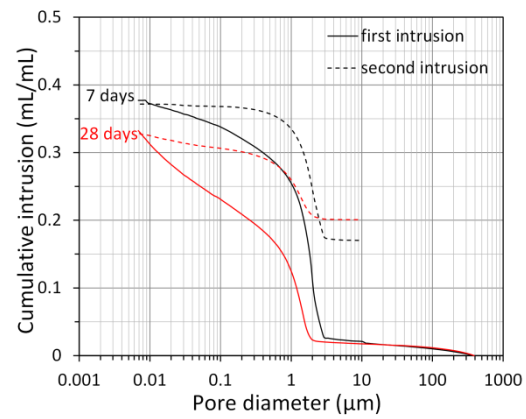
microstructure compared to the sodium hydroxide activated fly ash samples with the same content of  $\text{Na}_2\text{O}$ .



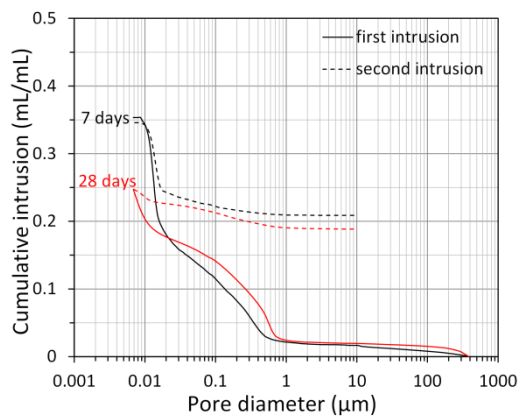
(A) FA\_N6.2S0T60



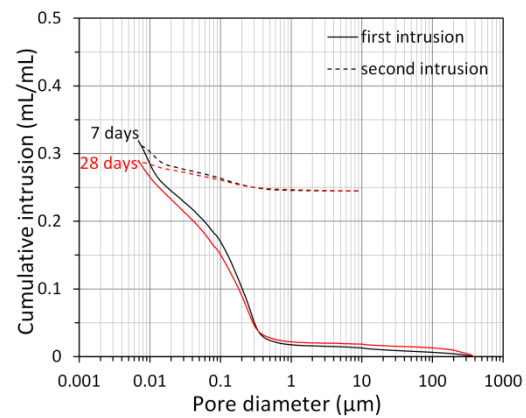
(B) FA\_N9.3S0T40



(C) FA\_N9.3S0T60



(D) FA\_N9.3S9T40



(E) FA\_N9.3S9T60

Figure 5.19 Pore size distribution, derived from MIP, for alkali-activated fly ash samples. In the notations, FA indicates alkali-activated fly ash, N and S indicate weight percentage of  $\text{Na}_2\text{O}$  and  $\text{SiO}_2$  with respect to fly ash, respectively, and T refers to temperature in Celsius. The water-to-fly-ash ratio was 0.35 and the curing temperature was 40 °C or 60 °C. See more details of the mixtures in Table 3.2.

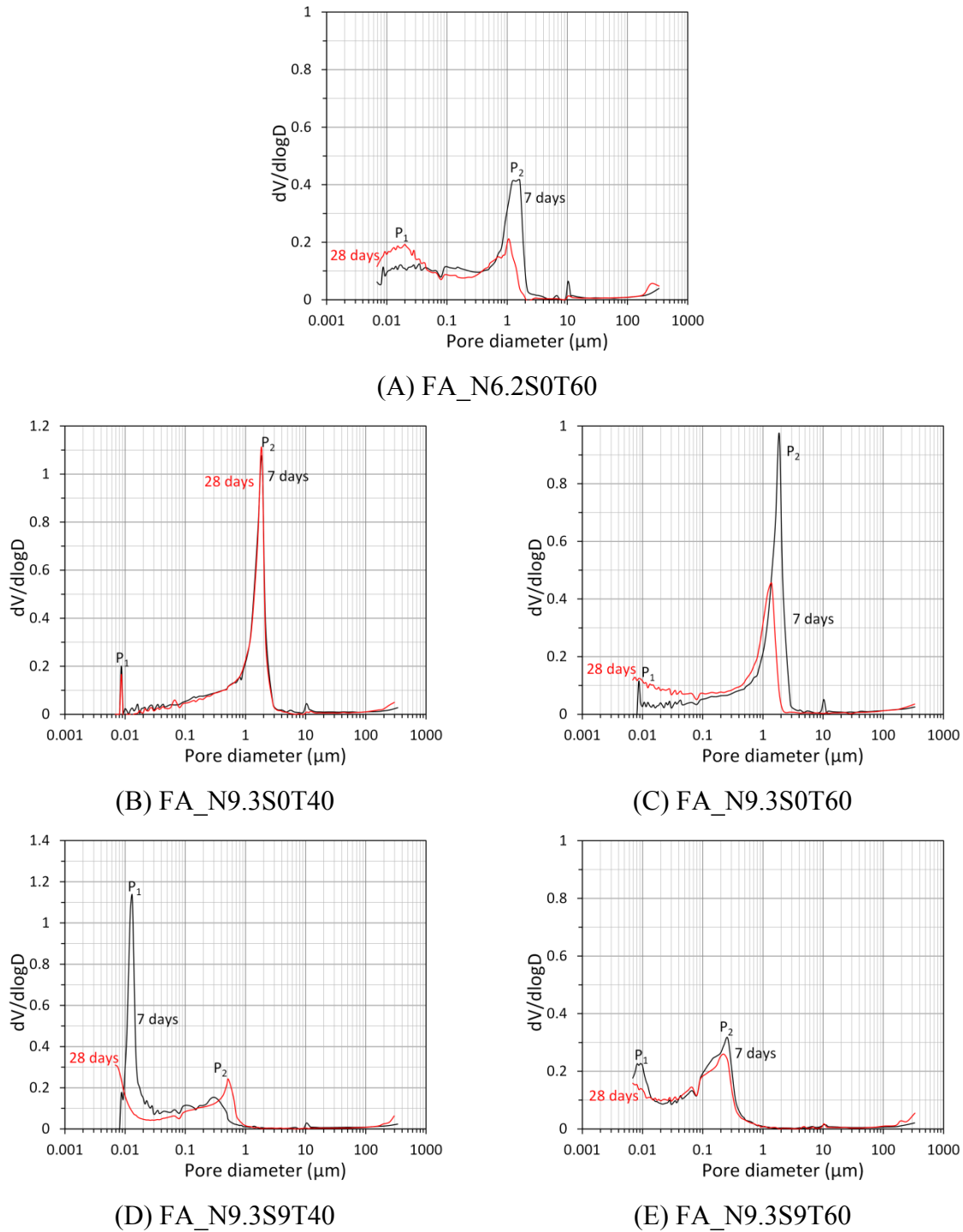


Figure 5.20 Differential pore size distribution of the first MIP intrusion, derived from MIP, for alkali-activated fly ash samples. In the notations, FA indicates alkali-activated fly ash, N and S indicate weight percentage of  $\text{Na}_2\text{O}$  and  $\text{SiO}_2$  with respect to fly ash, respectively, and T refers to temperature in Celsius. The water-to-fly-ash ratio was 0.35 and the curing temperature was 40 °C or 60 °C. See more details of the mixtures in Table 3.2.

*Pore size distribution determined by SEM-image analysis for alkali-activated fly ash*

Figure 5.21 depicts the pore size distribution of alkali-activated fly ash samples, derived from SEM-image analysis, for alkali-activated fly ash samples. It is clear that most of the pores had

sizes of 1-10  $\mu\text{m}$ . For instance, the area fraction of the pores with sizes of 1-10  $\mu\text{m}$  occupied 78.2 % and 87.0 % in the total pore area fraction of FA\_N9.3S0T40 at 7 days and 28 days, respectively. On one hand, the longer curing time (from 7 to 28 days) and addition of  $\text{SiO}_2$  led to a significant decrease of the total pore area fraction and a shift of pore size distribution curve to smaller pore sizes (equivalent diameter). On the other hand, the increase of  $\text{Na}_2\text{O}$  content did not have much effect on the pore structure. These results are consistent with the observations based on MIP.

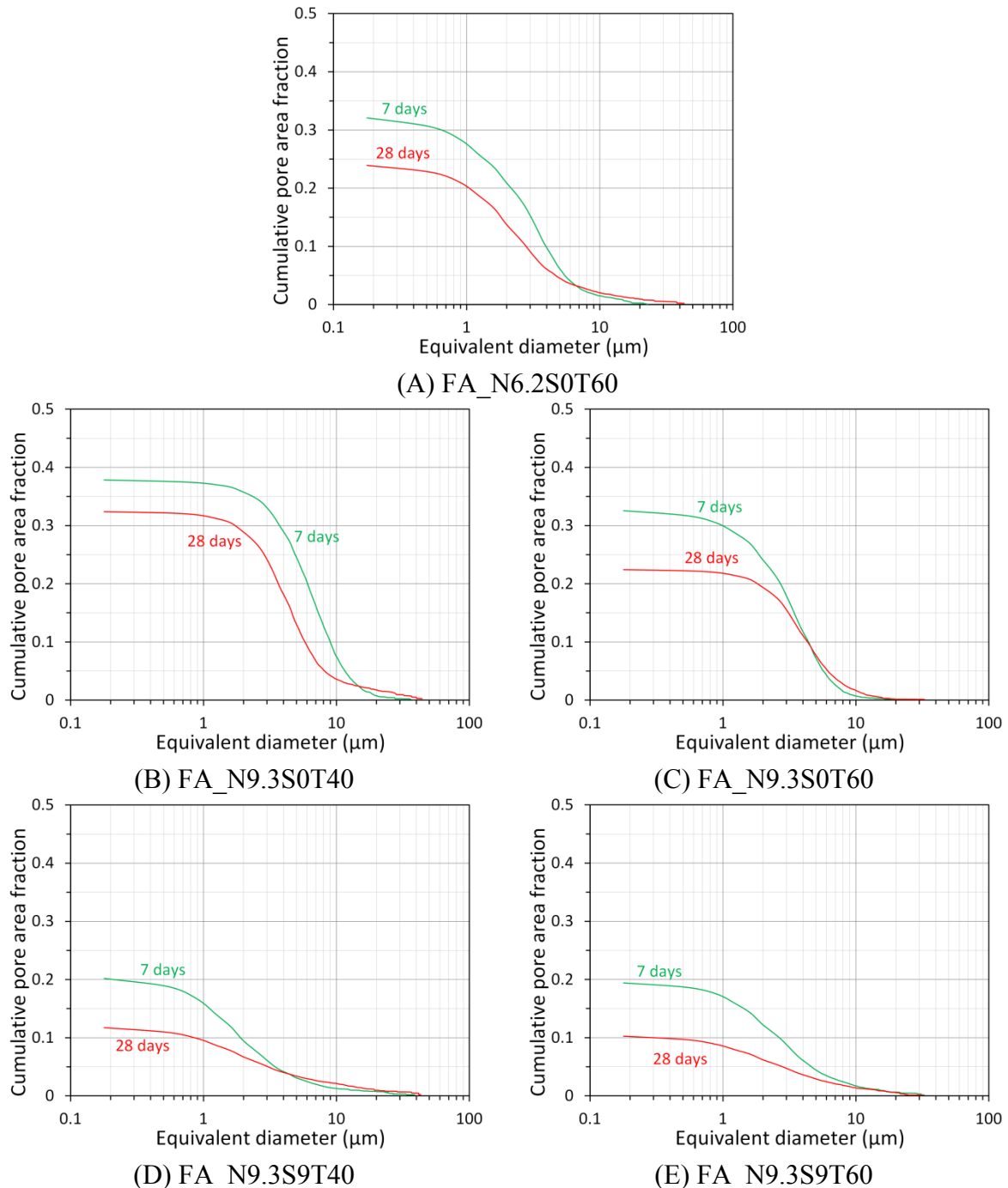
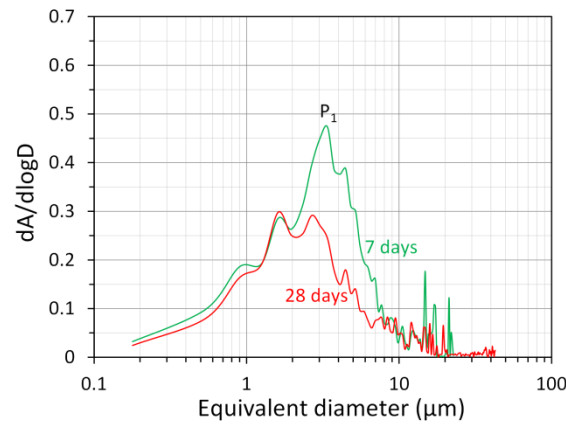
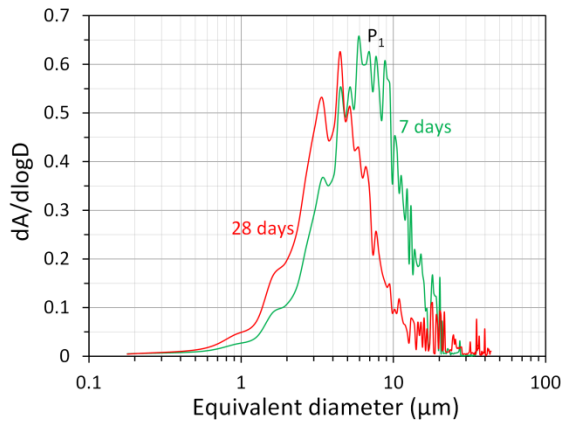


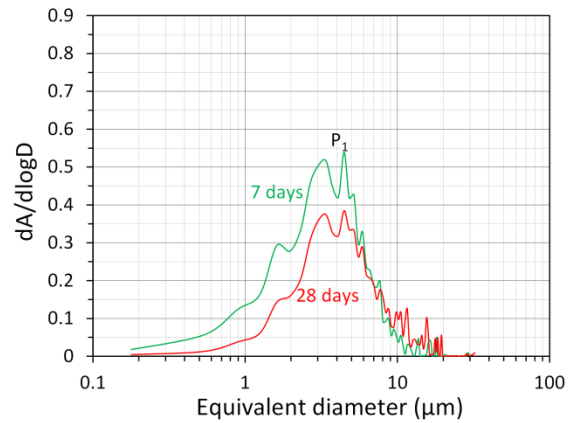
Figure 5.21 Pore size distribution, derived from SEM-image analysis, for alkali-activated fly ash samples. FA indicates alkali-activated fly ash, N and S indicate weight percentage of  $\text{Na}_2\text{O}$  and  $\text{SiO}_2$ , and T refers to temperature in Celsius. The water-to-fly-ash ratio was 0.35. See more details of the mixtures in Table 3.2.



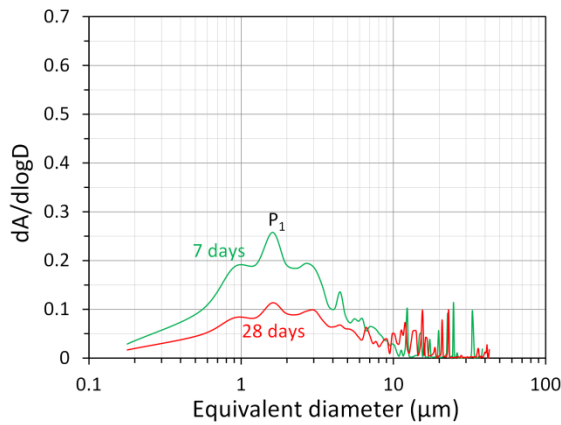
(A) FA\_N6.2S0T60



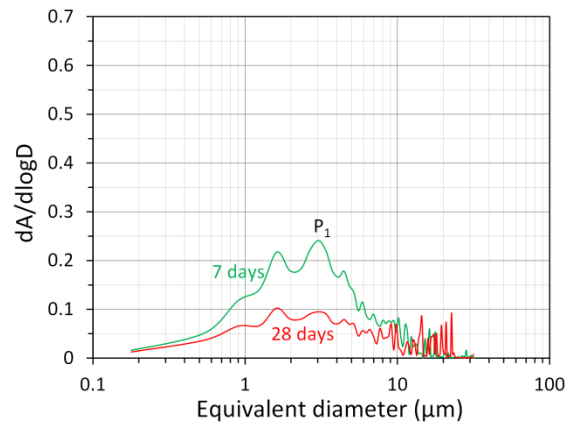
(B) FA\_N9.3S0T40



(C) FA\_N9.3S0T60



(D) FA\_N9.3S9T40



(E) FA\_N9.3S9T60

Figure 5.22 Differential pore size distribution, derived from SEM-image analysis, for alkali-activated fly ash samples. In the notations, FA indicates alkali-activated fly ash, N and S indicate weight percentage of  $\text{Na}_2\text{O}$  and  $\text{SiO}_2$  with respect to fly ash, respectively, and T refers to curing temperature in Celsius. The water-to-fly-ash ratio was 0.35. See more details of the mixtures in Table 3.2.

Figure 5.22 plots the differential pore size distribution, derived from SEM-image analysis, for alkali-activated fly ash samples. All the differential pore size distributions showed only one peak with pore sizes of several microns, representing capillary pores. The peak that corresponds to the gel pores was not identified. This is because the gel pores are smaller than



0.1  $\mu\text{m}$ , which is below the detection limit of SEM-image analysis (0.1786  $\mu\text{m}/\text{pixel}$ ). When the curing time increased from 7 days to 28 days, the identified peak shift to small pore sizes for FA\_N9.3S0T40 and FA\_N6.2S0T60, but did not for FA\_N9.3S9T40, FA\_N9.3S0T60 and FA\_N9.3S9T60. This shows that the differential pore size distribution obtained by SEM-image analysis did not sufficiently reflect the influence of curing age on the refinement of pore structure of alkali-activated fly ash paste.

### 5.3.6 Pore structure of alkali-activated slag/fly ash paste

#### *Total porosity derived from MIP for alkali-activated slag/fly ash*

Figure 5.23 shows the total porosity, derived from MIP, for alkali-activated slag/fly ash paste (B\_N6S5.4), in comparison with the alkali-activated slag paste with the same alkaline activator (BFS\_N6S5.4). According to the mixture design (see Chapter 3), the calculated total porosity of B\_N6S5.4 was 51.4 % at the initial state prior to the commence of reaction. Similar to BFS\_N6S5.4, the total porosity of B\_N6S5.4 dropped considerably during the first day, from 51.4 % to 12.2 %, and then decreased slightly with time until 28 days. Because fly ash had a lower density than slag, 50 wt.% replacement of slag by fly ash led to a smaller initial total porosity in B\_N6S5.4 than that in BFS\_N6S5.4. However, the total porosity of B\_N6S5.4 was larger than that of BFS\_N6S5.4 after 1 day, although B\_N6S5.4 had higher degrees of reaction (61.2 % at 1 day, 66.7 % at 7 days and 76.3 % at 28 days) than BFS\_N6S5.4 (50.4 % at 1 day, 56.4 % at 7 days and 63.8 % at 28 days). This is because the C-(N-)A-S-H gels have higher space-filling capacity than the N-A-S-H gels [132]. In BFS\_N6S5.4 the primary reaction products were C-(N-)A-S-H gels. However, the primary reaction products consisted of C-(N-)A-S-H gels and N-A-S-H gels in the alkali-activated blend of slag and fly ash system [133], for instance in B\_N6S5.4.

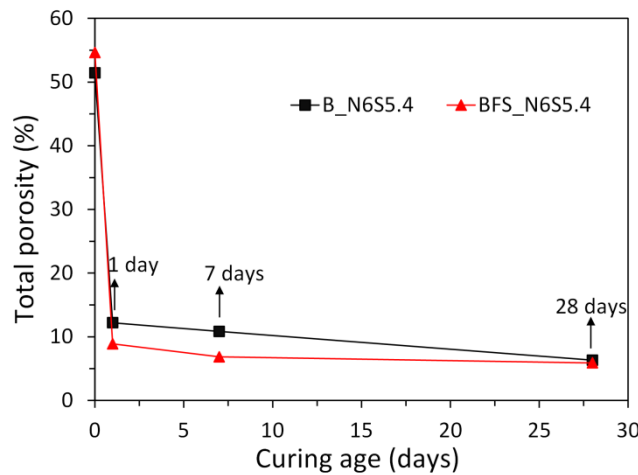


*Figure 5.23 Total porosity, derived from MIP, for alkali-activated slag/fly ash (B\_N6S5.4), in comparison with alkali-activated slag with the same alkaline activator (BFS\_N6S5.4). In the graphs, B and BFS indicate alkali-activated slag blended with fly ash and alkali-activated slag, and N and S indicate weight percentage of  $\text{Na}_2\text{O}$  and  $\text{SiO}_2$  with respect to precursor, respectively. The water-to-precursor ratio was 0.4 and the curing temperature was 20 °C. See more details of the mixtures in Table 3.2.*

*Pore size distribution determined by MIP for alkali-activated slag/fly ash*

Figure 5.24 shows the pore size distribution and differential pore size distribution of the first MIP intrusion, derived from MIP, for alkali-activated slag/fly ash (B\_N6S5.4). Longer curing time led to a decrease of the total porosity, particularly from 7 days to 28 days. The peak, corresponding to capillary pores, was observed on the differential pore size distribution curve. This peak, however, was not observed on the differential pore size distribution of BFS\_N6S5.4 (Figure 5.15(F)). For this discrepancy two reasons are discussed. On one hand, the N-A-S-H gels had a lower space-filling capacity than the C-(N-)A-S-H gels, leading to a larger total porosity in B\_N6S5.4 (Figure 5.23). On the other hand, the cavities in B\_N6S5.4 also contributed to the increase of large capillary pores. As the curing age increased from 7 days to 28 days, this peak shifted to smaller pore sizes, reflecting a denser microstructure. From 1 day to 7 days this peak showed a small shift to larger pore sizes. This might be due to the dissolution of fly ash particles with empty voids, which exposed the empty voids to the “outside”. The exposed hollow voids were clearly seen from the SEM-micrographs (Figure 5.11). As a result of the opening of hollow voids, the pore structure was coarsened. This point was further supported by the SEM-image analysis results that will be presented later.

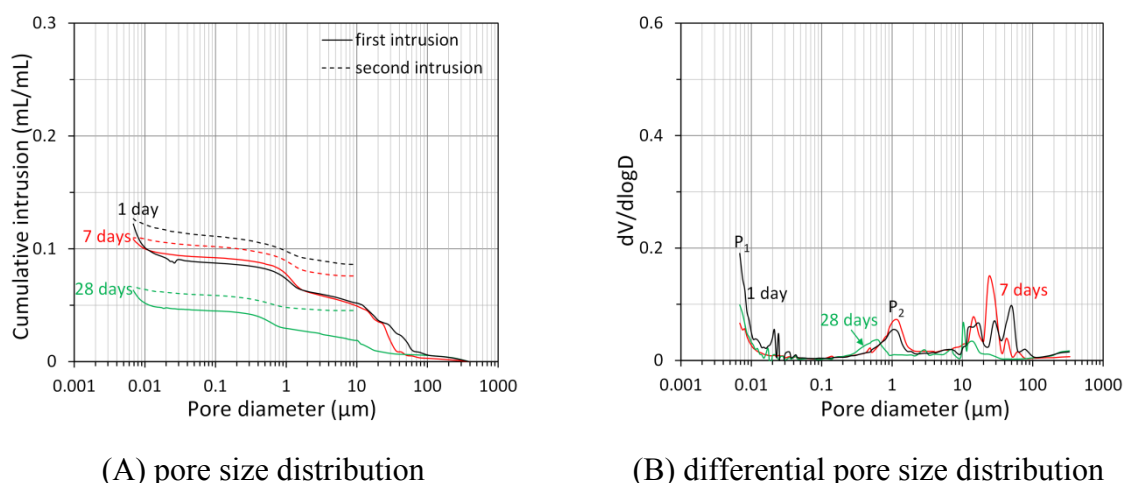


**Figure 5.24** Pore size distribution and differential pore size distribution of the first MIP intrusion, derived from MIP, for alkali-activated slag/fly ash (B\_N6S5.4). B indicates alkali-activated slag blended with fly ash, and N and S indicate weight percentage of Na<sub>2</sub>O and SiO<sub>2</sub> with respect to precursor, respectively. The water-to-precursor ratio was 0.4 and the curing temperature was 20 °C. See more details of the mixtures in Table 3.2.

*Pore size distribution determined by SEM-image analysis for alkali-activated slag/fly ash*

The pore size distribution and differential pore size distribution of alkali-activated slag/fly ash samples, obtained from SEM-image analysis, are presented in Figure 5.25. In line with the MIP results, it was found that longer curing time resulted in smaller total pore area fraction. The peak that corresponds to capillary pores was identified on the differential pore size distribution curve. It is clear that this peak shifted to larger pore sizes when the curing time increased. This might support the previous inference that the opening of hollow voids in fly ash particles coarsened the pore structure.

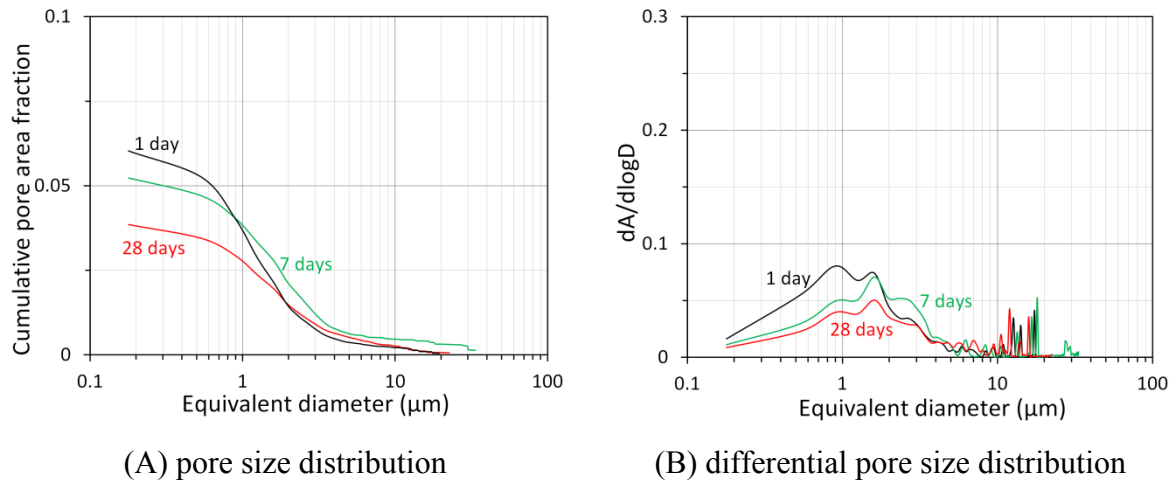
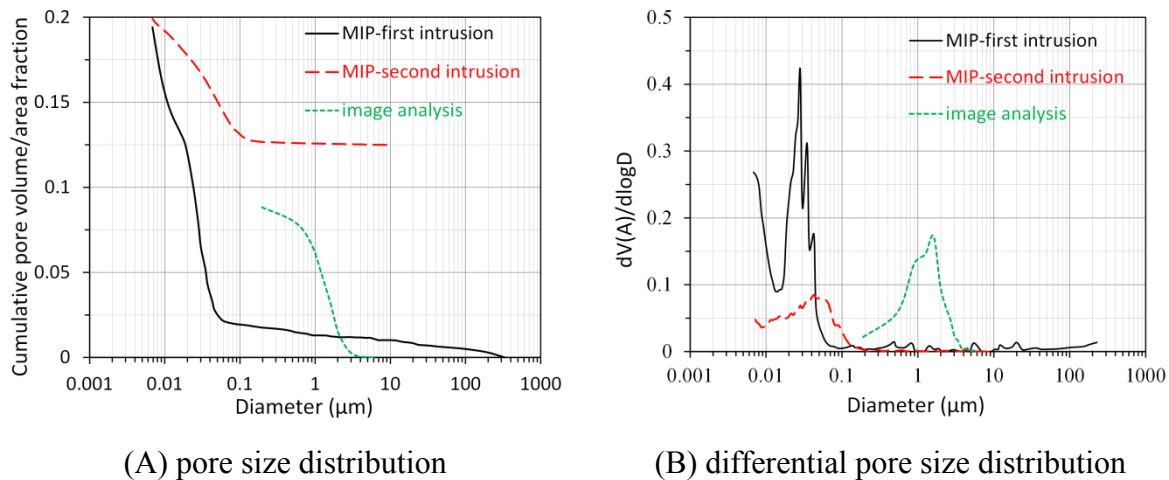


Figure 5.25 Pore size distribution and differential pore size distribution, derived from SEM-image analysis, for alkali-activated slag blended with fly ash (B\_N6S5.4). In the notations, B indicates alkali-activated slag/fly ash, and N and S indicate weight percentage of  $\text{Na}_2\text{O}$  and  $\text{SiO}_2$  with respect to precursor, respectively. The water-to-precursor ratio was 0.4 and the curing temperature was 20 °C. See more details of the mixtures in Table 3.2.

## 5.4 Discussion

### 5.4.1 Comparison of the results from MIP and SEM-image analysis

As an illustration of the comparison of the results from MIP and SEM-image analysis, the pore size distribution and differential pore size distribution for BFS\_N4S0 at 28 days, derived from MIP and SEM-image analysis, are shown in Figure 5.26. The figure shows that the pore sizes obtained from image analysis were two orders of magnitude larger than those obtained from MIP. Compared with the total pore area fraction obtained from SEM-image analysis, MIP measured a total porosity about two times larger. All those observations are in agreement with the findings reported for Portland cement paste [114, 134]. Because of the “ink-bottle” effect during the MIP measurement, the volume of larger pores is counted as the volume of smaller pores, which leads to an underestimation of large pores and an overestimation of small pores [117]. For this reason, the pore size distribution obtained by MIP shifted to smaller pore sizes. In contrast, the pore size distribution obtained from SEM-image analysis represented the sizes of the pores actually visible with SEM. Because of the resolution limit of BSE images, the SEM-image analysis cannot detect the pores with diameter smaller than 0.1786  $\mu\text{m}$ . So the total pore area fraction obtained from SEM-image analysis did not take all pores into account and, as a result, it was smaller than the total porosity obtained by MIP.



**Figure 5.26** Pore size distribution and differential pore size distribution, derived from MIP and SEM-image analysis, for alkali-activated slag sample BFS N4S0 at 28 days. In the notations, BFS indicates alkali-activated slag, and N and S indicate weight percentage of  $\text{Na}_2\text{O}$  and  $\text{SiO}_2$  with respect to slag, respectively. The water-to-slag ratio was 0.4 and the curing temperature was 20 °C.

As seen from Figure 5.26(B), the threshold pore diameter of gel pores obtained from the first MIP intrusion (0.028 μm) was smaller than that obtained from the second MIP intrusion (0.043 μm). Compared with the first MIP intrusion, the second MIP intrusion has little ink-bottle effect and provides a more reliable size distribution of pores [135]. In other words, the pore sizes obtained from the second MIP intrusion were little underestimated. So the threshold pore diameter of gel pores obtained from the second MIP intrusion was larger. The pore diameter that corresponds to the peak derived from SEM-image analysis (1.6 μm) was about two orders of magnitude larger than the threshold pore diameters of gel pores obtained from the first MIP intrusion (0.028 μm) and the second MIP intrusion (0.043 μm). This result is expected, since the capillary pores have larger pore sizes than the gel pores.

#### 5.4.2 Microstructure formation of alkali-activated materials

##### *Microstructure formation of alkali-activated slag*

The microstructure formation of sodium hydroxide activated slag samples is schematically illustrated in Figure 5.27. When slag is brought into contact with sodium hydroxide activator, slag starts to dissolve and subsequently various chemical reactions occur to produce solid reaction products. According to the observations from SEM images (Figures 5.6(B) and 5.6(D)), there are mainly two periods during the microstructure formation of sodium hydroxide activated slag. In the early period (Figure 5.27(B)), the high initial rate of reaction does not leave time for diffusion of the dissolved ions and the slag grains provide nucleation sites. As a result the reaction products are built up in the zone immediately surrounding the slag grains. The reaction products, e.g. outer C-(N-)A-S-H, formed in this stage grow with continuous reaction of slag. In the subsequent period (Figure 5.27(C)), the reaction products are mainly formed in the place of the original slag particles, forming the inner layer of reaction products surrounding the slag grains, e.g. inner C-(N-)A-S-H. Along with those two periods, crystalline reaction products, such as hydrotalcite phase, are formed in the empty pore space in the matrix, as reported in [15]. Since the reaction products are mainly formed around the slag grains, a relatively coarse microstructure is produced with connected capillary pores.

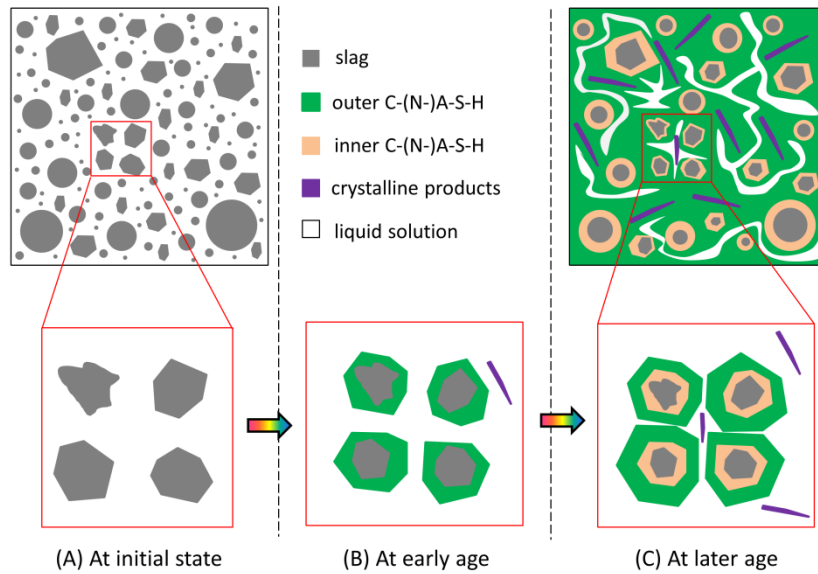


Figure 5.27 Schematic illustration of the microstructure formation of sodium hydroxide activated slag samples. For clear representation, gel pores were not represented in the graphs.

In the sodium silicate activated slag samples, the sodium silicate activator provides soluble silicate, and then the dissolved calcium and aluminum could immediately react with the soluble silicate to form nuclei in the solution (Figure 5.28(B)). With the formation and growth of nuclei in the solution, the reaction products can grow homogeneously in the empty pore space as well as around the slag grains (Figure 5.28(C)). The homogeneous distribution of reaction products throughout the whole matrix can also be observed in the SEM-micrographs (Figures 5.6(E) and 5.6(F)). So a relatively homogeneous microstructure is produced with only a number of disconnected small capillary pores (Figure 5.28(C)).

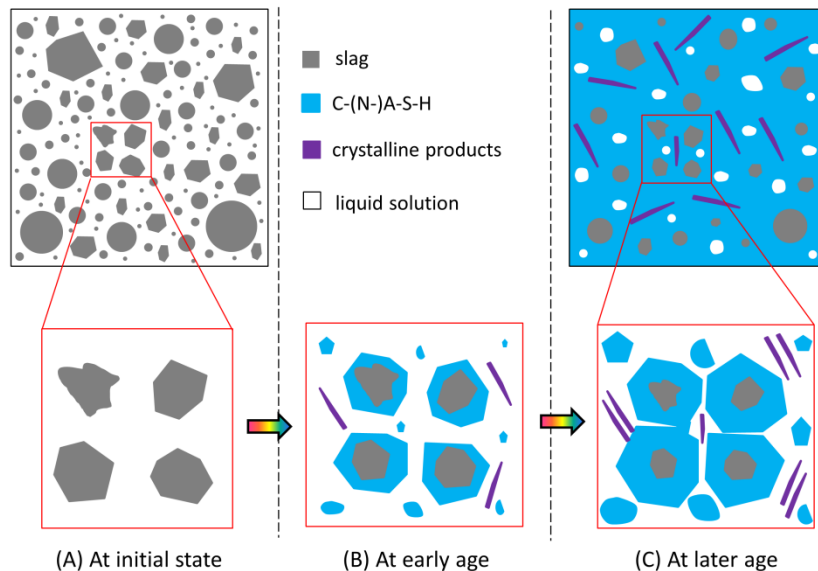
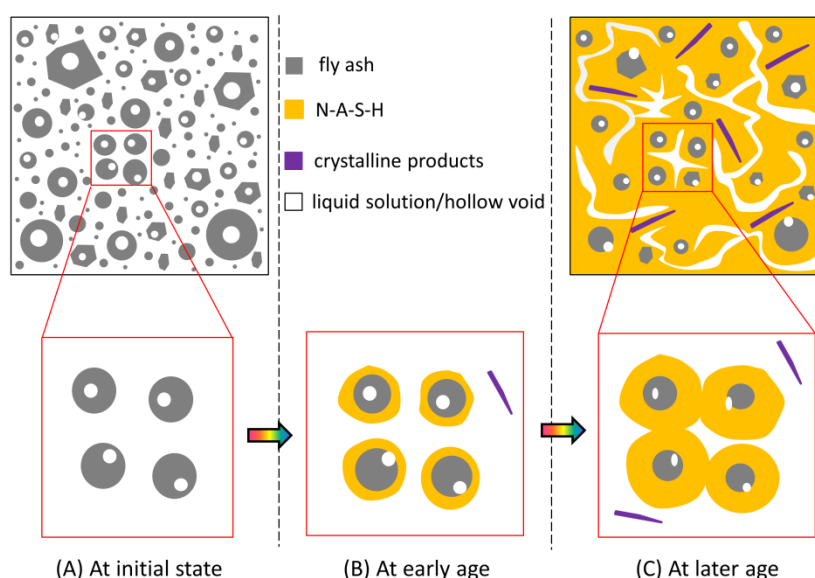


Figure 5.28 Schematic illustration of the microstructure formation of sodium silicate activated slag samples. For clear representation, gel pores were not represented in the graphs.

### *Microstructure formation of alkali-activated fly ash*

Figure 5.29 presents a schematic illustration of the microstructure formation of sodium hydroxide activated fly ash samples. Besides the dissolving fly ash grains, there are no nucleation triggers and soluble silicate in the sodium hydroxide activated fly ash samples. So the reactions mainly occur around the fly ash grains and the reaction products are predominately formed on the surface of fly ash grains [17], as schematically represented in Figure 5.29(B). Shells of reaction products can also be observed from the SEM-micrographs (Figures 5.8 and 5.9). On the other hand, the small labile species, such as silicate and aluminate monomers in solution, lead to a large degree of structural reorganization and densification of N-A-S-H gels [37]. This decreases the space-filling capacity of N-A-S-H gels. These two aspects lead to a coarse microstructure with connected big capillary pores (Figure 5.29(C)).



*Figure 5.29 Schematic illustration of the microstructure formation of sodium hydroxide activated fly ash samples. For clear representation, gel pores were not represented in the graphs.*

In sodium silicate activated fly ash samples, the soluble silicate species react with the dissolved aqueous aluminum to form gel nuclei in the solution [101], as schematically represented in Figure 5.30(B). With the formation and growth of gel nuclei in the solution, the reaction products grow homogeneously throughout the matrix – not only around the fly ash particles but also in the empty pore space (Figures 5.8 and 5.9). On the other hand, the degree of structural reorganization and densification of N-A-S-H gels are reduced due to the presence of cyclic or cage-like oligomeric species in solution [37]. This leads to a higher space-filling capacity of the N-A-S-H gels in sodium silicate activated fly ash than that of the N-A-S-H gels in sodium hydroxide activated fly ash. Therefore, there are no obvious connected big capillary pores in the matrix (Figure 5.30(C)).



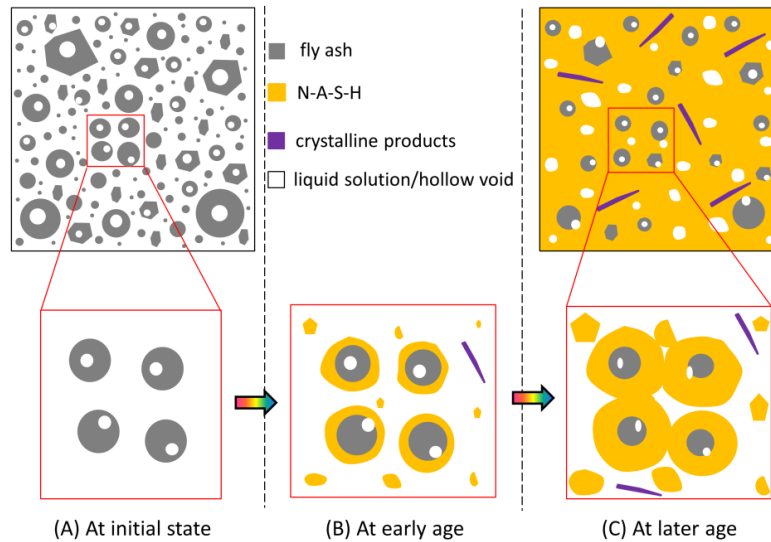


Figure 5.30 Schematic illustration of the microstructure formation of sodium hydroxide activated fly ash samples. For clear representation, gel pores were not represented in the graphs.

#### Microstructure formation of alkali-activated materials

From the discussions above it can be concluded that the type of alkaline activators has a large influence on the microstructure formation of alkali-activated materials. Figure 5.31 presents a simplified schematic illustration of the microstructure formation of alkali-activated materials with different alkaline activators. In the sodium hydroxide activated systems, the reaction products are predominately formed on the surface of slag or fly ash grains. This is similar to the growth of reaction products in OPC based materials [114]. As a result, the produced microstructure exhibits a relatively coarse pore structure with connected capillary pores. In the sodium silicate activated systems, by contrast, the soluble silicate in the solution provide nucleation sites or form gel nuclei in the solution. With the formation and growth of nuclei in the solution, the reaction products can grow homogeneously in the empty pore space as well as on the surface of slag or fly ash grains. Therefore a relatively dense microstructure can be formed with no obvious connected big capillary pores in the matrix.

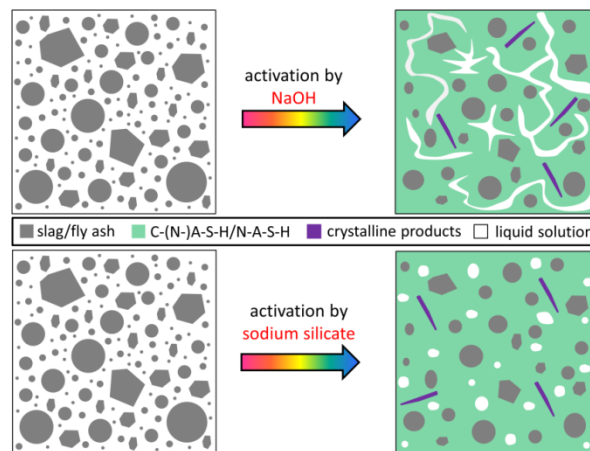


Figure 5.31 Schematic illustration of the microstructure formation of alkali-activated materials. For clear representation, gel pores and cavities of fly ash were not represented in the graphs.

## 5.5 Conclusions

In this chapter the microstructure, particularly the pore structure, of alkali-activated slag, fly ash and slag/fly ash pastes were studied using SEM and MIP. Based on the experimental results and discussion, the following remarks can be made:

- (1) *Development with time*: The pore structure of alkali-activated materials changes significantly at the early age. For instance, the total porosity of alkali-activated slag paste, from initially 54.2 %, dropped about 62 % - 83 % within the first day and then decreased slowly with time.
- (2) *Influence of Na<sub>2</sub>O content*: A higher Na<sub>2</sub>O content led to a higher alkalinity of the alkaline activator, which accelerated the reactions of alkali-activated slag and fly ash and led to a higher degree of reaction. The increase of Na<sub>2</sub>O content led to a lower total porosity and a refined microstructure for alkali-activated slag paste. However, the increase of Na<sub>2</sub>O content did not significantly affect the total porosity of alkali-activated fly ash paste. In contrast, it altered the microstructure by increasing the amount of large pores and decreasing the amount of small pores of alkali-activated fly ash samples.
- (3) *Influence of SiO<sub>2</sub> content*: The addition of SiO<sub>2</sub>, providing soluble silicate in the alkali-activated materials, have different effects on the reactions of alkali-activated slag and alkali-activated fly ash. On one hand, the increase of SiO<sub>2</sub> content led to a decrease of the alkalinity of the alkaline activator, leading to a smaller degree of reaction of slag in alkali-activated slag paste. On the other hand, the soluble silicate accelerated the dissolution of fly ash and thus led to a higher degree of reaction of fly ash in alkali-activated fly ash paste. Furthermore, the soluble silicate resulted in a different microstructure formation compared to the sodium hydroxide activated system, which will be concluded in “(6) Microstructure formation” later.
- (4) *Influence of curing temperature*: On one hand, a higher curing temperature led to a higher degree of reaction of fly ash, producing more reaction products in alkali-activated fly ash paste. So the total porosity was reduced and the pore size distribution shifted to smaller pore sizes as seen from the comparison between FA\_N9.3S0T40 and FA\_N9.3S0T60. On the other hand, an increase of temperature could also coarsen the pore structure as seen from the comparison between FA\_N9.3S9T40 and FA\_N9.3S9T60 at 28 days.
- (5) *MIP vs. SEM-image analysis*: MIP was capable of detecting the total porosity of alkali-activated materials, but it underestimated the large pores and overestimated the small pores due to the “ink-bottle” effect. On the other hand, SEM-image analysis was able to eliminate the “ink-bottle” effect and revealed the “real” pore structure, especially the capillary pores. However, the minimum pore size that SEM-image analysis could detect was limited to the resolution of the obtained SEM images.
- (6) *Microstructure formation*: Because only the dissolving slag/fly ash grains acted as nucleation sites in the sodium hydroxide activated systems, the reactions mainly occurred around the slag/fly ash grains and thus shells of reaction products were formed on the surface of slag/fly ash grains. With growth of the reaction products, a relatively coarse microstructure was produced with the connected big capillary pores. In the sodium silicate activated systems, by contrast, the soluble silicate reacted with the dissolved calcium and/or aluminum to form nuclei, in addition to the nuclei sites provided by the dissolving slag/fly ash grains. With the formation and growth of nuclei, the reaction products grew



homogeneously throughout the matrix. This led to a relatively dense microstructure with disconnected small capillary pores.



## **PART III**

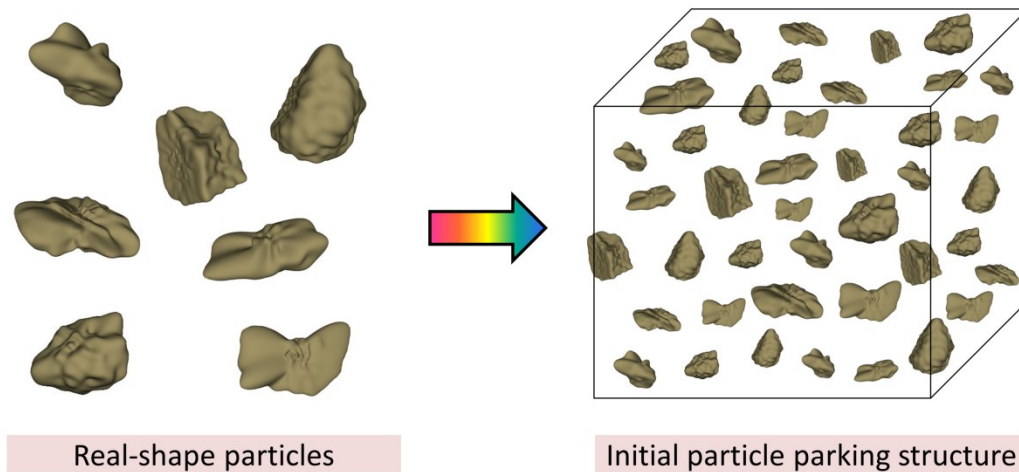
---

# **NUMERICAL SIMULATION AND VALIDATION**



# Chapter 6

## Simulation of the initial particle parking structure of alkali-activated materials<sup>13</sup>



In many particle-based numerical models spherical particles are used to represent the particles of cement, slag, and fly ash. However, the real particle shapes of cement, slag, and fly ash are irregular and non-spherical. In this chapter, the real-shape particles of slag and fly ash were used to simulate the initial particle parking structure of slag and fly ash in alkali-activated systems. For comparisons these initial particle parking structures were also simulated using spherical particles. The cumulative surface area, specific surface area and pore size distribution of the simulated initial particle parking structures were evaluated.

<sup>13</sup> This chapter is partially based on:

Yibing Zuo, Zhiwei Qian, Edward J. Garboczi and Guang Ye. Numerical simulation of the initial particle parking structure of cement/geopolymer paste and the dissolution of amorphous silica using real-shape particles. *Construction and Building Materials*, 185(2018) 206-219.

## 6.1 Introduction

The initial particle parking structure is the starting point for performing numerical simulations of the reactions and microstructure formation of alkali-activated materials. In this study, the initial particle parking structure is defined as the state of precursors in alkaline activator prior to the start of the reaction. In literature several particle-based numerical models have been used to simulate the hydration and microstructure formation of cementitious materials [136-139]. In these models, regular shape particles, usually spherical particles, are used to represent the particles of cement, slag, or fly ash. However, the real particle shapes of cement, slag and fly ash are irregular and non-spherical due to the manufacturing processes and particle grinding methods used. The particle shape influences the dissolution of slag and fly ash in alkaline solution, since the dissolution follows a set of surface-controlled reactions [22-24]. Besides, fly ash particles may have hollow voids inside, which also influence the dissolution.

In this chapter, the Anm material model, as mentioned in Chapter 1, was extended to simulate the initial particle parking structures of alkali-activated materials using real-shape particles. For comparisons, the initial particle parking structures were also simulated with HYMOSTRUC3D [114, 139, 140] using spherical particles. The cumulative surface area, specific surface area, and pore size distribution of the simulated initial particle parking structures were then evaluated.

The Anm material model, extended in this chapter, will be used to generate the initial particle parking structures as input to simulate the binder reaction process in the following chapters, such as the dissolution of slag and fly ash in Chapter 7 and microstructure formation of alkali-activated materials in Chapter 9. Figure 6.1 shows the position of Chapter 6 in structure of the study of the reaction process and microstructure formation of AAMs in this thesis.

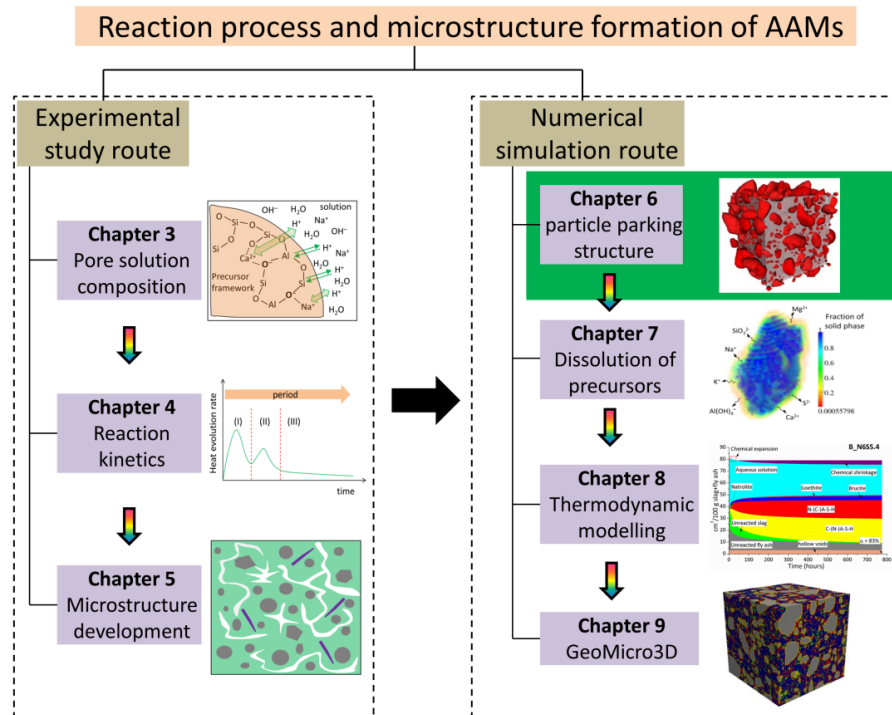


Figure 6.1 Position of Chapter 6 in structure of the study of the reaction process and microstructure formation of AAMs in this thesis.

## 6.2 Methodology

### 6.2.1 Extended Anm material model

#### *Original Anm material model*

In the Anm material model, particle shapes are described with spherical harmonic expansion coefficients  $a_{nm}$  [141, 142]. In a 3D spherical polar coordinate system, the surface of a particle can be represented by a function  $r(\theta, \varphi)$ . Once the spherical harmonic coefficients are known, the particle shape can be determined with Equations (6.1) and (6.2).  $Y_{nm}(\theta, \varphi)$  is the spherical harmonic function with indices  $n$  and  $m$  ( $-n \leq m \leq n$ ),  $P_{nm}(\cos \theta)$  is the associated Legendre polynomial, and  $i$  is the square root of -1 [143]. Figure 6.2 shows an irregular shape particle described by spherical harmonics.

$$r(\theta, \varphi) = \sum_{n=0}^{\infty} \sum_{m=-n}^n a_{nm} Y_{nm}(\theta, \varphi) \quad (6.1)$$

$$Y_{nm}(\theta, \varphi) = \sqrt{\frac{(2n+1)(n-m)!}{4\pi(n+m)!}} P_{nm}(\cos \theta) e^{im\varphi} \quad (6.2)$$

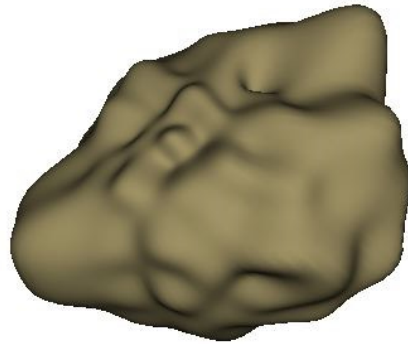


*Figure 6.2 An irregular shape particle described by spherical harmonics. The particle width is 15.56  $\mu\text{m}$ . (In this study the particle width was used as the measure of particle size, see details in the text)*

The spherical harmonic expansion coefficients can be obtained from digital images of particles by micro X-ray computed tomography scans [144]. Once the spherical harmonic coefficients are known, many geometric properties can be calculated, such as the particle volume, surface area, length, width, and thickness [145]. Length is the longest surface-surface distance in the particle; width is the longest surface-surface distance in the particle such that width is perpendicular to length; and thickness is the longest surface-surface distance in the particle such that thickness is perpendicular to both length and width [145]. Since the particle width is thought to match best with the usual standard experimental sieve classification of particles [146, 147], it is preferentially used for computational sieve analysis [144]. In this study, the particle width was used as the measure of particle size.

In the Anm material model, the particles are parked one after another into the container, from larger ones to smaller ones. So, in a simulation of the initial particle parking structure, all the particles are separated into several size ranges according to the particle sizes indicated by the particle widths. The largest size range is processed first. A width within this size range is picked randomly and assigned to a particle which is chosen from the particle shape database.

Then a number of random attempts are allowed per particle to find a position/orientation in which the particle can be parked without overlapping the other particles. More details on parking procedures and algorithms are found in [141, 142]. Figure 6.3 shows a simulated initial particle parking structure using the Anm material model.

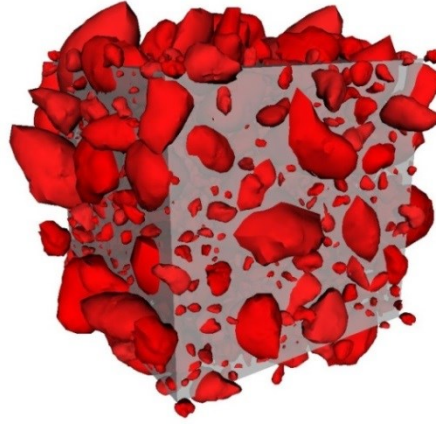


*Figure 6.3 A simulated initial particle parking structure using Anm material model. The size of the cubic unit cell was  $125\ \mu\text{m} \times 125\ \mu\text{m} \times 125\ \mu\text{m}$ . The liquid to binder ratio was 0.47.*

#### *Extensions of the Anm material model*

The spherical harmonics requires the particles to be star-shaped. It means that one must not intersect the surface twice when extending any line segment from the center of mass to the surface. The real-shape particles of slag typically satisfy this requirement, while the particles of fly ash do not due to the hollow voids in fly ash particles. Furthermore, the original Anm material model was designed to simulate the initial particle parking structure of *only* one type of particles in a system, for example, one type of aggregates [18, 148] in concrete or mortar. It cannot deal with the system with two types of particles, for example, slag and fly ash particles with two different particle shape databases. In this study, two extensions were added to the original Anm model. One is to deal with the hollow voids in fly ash particles. The other is to park two types of particles in a system. In this study these two types of particles are slag and fly ash, respectively.

##### *(1) Extension of the Anm model in order to deal with the hollow voids in fly ash particles*

In order to deal with the hollow voids in fly ash particles, first, one can assume no voids, and analyze and park the fly ash particles using the spherical harmonic series (Figure 6.4(A)), and then remove material to create voids in the fly ash particles (Figure 6.4(B)).

In this study, the hollow voids are assumed to be distributed in all the parked fly ash particles. For a parked fly ash particle, its volume is an apparent volume ( $V_a$ ), including the volume of voids ( $V_v$ ) inside the particle. If the apparent density and the real density of fly ash particles are  $\rho_a$  and  $\rho_r$ , respectively, then there exists the relationship:

$$V_a \rho_a = (V_a - V_v) \rho_r \quad (6.3)$$

Thus the volume of voids in this parked fly ash particle can be computed. It is assumed that the void exists as a sphere and the spherical coordinates are randomly located inside the fly ash particle [149]. Then the amount of the material within the sphere could be removed to



create the internal voids in the fly ash particles. In this way, the hollow voids in fly ash particles could be described.

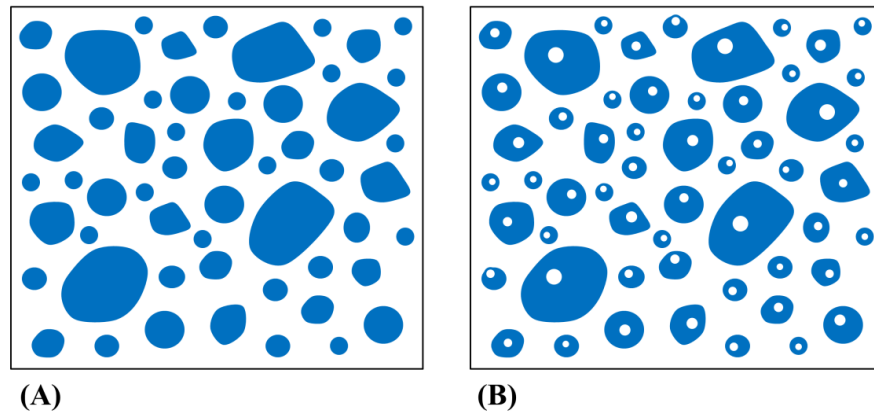


Figure 6.4 Schematic representation of the strategy to deal with the hollow voids in fly ash particles: (A) park fly ash particles assuming no voids; (B) remove material to create hollow voids in fly ash particles.

## (2) Extension of the Anm model in order to park particles from two different databases

In the extended Anm material model, all the particles (either single binder system or binary-blended system) are separated into several size ranges according to their sizes indicated by the particle widths, and in each size range a flag is added to indicate which type of binder a particle belongs to. The size range flag indicates the particle shape database from which the particle shape should be chosen to park the particle into the cubic unit cell. A flag is also added to the parked particle according to which size range it is chosen from. In this way all parked particles are identified with flags and the initial particle parking structures of binary-blended systems could be simulated. The following is an example to show schematically the strategy according to which the slag and fly ash particles are parked.

Table 6.1 Sieve ranges with flags showing which component the particle belongs to

	Sieve range <sup>a</sup>	Fraction <sup>b</sup>	Flag (1-slag; 2-fly ash)
First size range	$(a_2, a_1]$	$f_1$	2
Second size range	$(b_2, b_1]$	$f_2$	1
Third size range	$(a_3, a_2]$	$f_3$	2
Forth size range	$(b_3, b_2]$	$f_4$	1
Fifth size range	$(a_4, a_3]$	$f_5$	2
...	...	...	...
n <sup>th</sup> sieve range	$[a_{n+1}, a_n]$	$f_n$	2

a.  $a_1, a_2, b_1, b_2, a_3, b_3, a_4, \dots, a_n$  and  $a_{n+1}$  are the size range bounds, where  $a_1 > a_2 > \dots > a_{n+1}$  and  $b_1 > b_2 > b_3$ .

b.  $f_1, f_2, f_3, f_4, f_5, \dots$ , and  $f_n$  are the size range fraction, where  $f_1 + f_2 + \dots + f_n = 1$ .

According to the particle size distribution, slag and fly ash are separated into several size ranges. For each size range, a flag is added to indicate which component the particle belongs to. Then the size ranges are sorted from larger ones to smaller ones according to the maximum

size that a particle can be selected. The size range is processed from the largest to the smallest. For parking a particle the particle size is randomly selected within its corresponding size range and the particle shape is randomly selected from its corresponding particle shape database. Table 6.1 lists the size ranges and size range flags. 1-valued flag indicates slag and 2-valued flag indicates fly ash.

Figure 6.5 schematically displays the procedures to park the slag and fly ash particles. First, the particles within the first size ranges are parked. According to the sieve range flag, the particle shape is chosen from the fly ash particle shape database. A 2-valued flag is added to the parked particles from the first size range. The parked particles are schematically represented in Figure 6.5(A). Afterwards, these operations are repeated for the second size range (Figure 6.5(B)), and finally for the last size range (Figure 6.5(C)). In this way, fly ash and slag particles are parked into the cubic unit cell to represent the initial particle parking structure of slag/fly ash in the system.

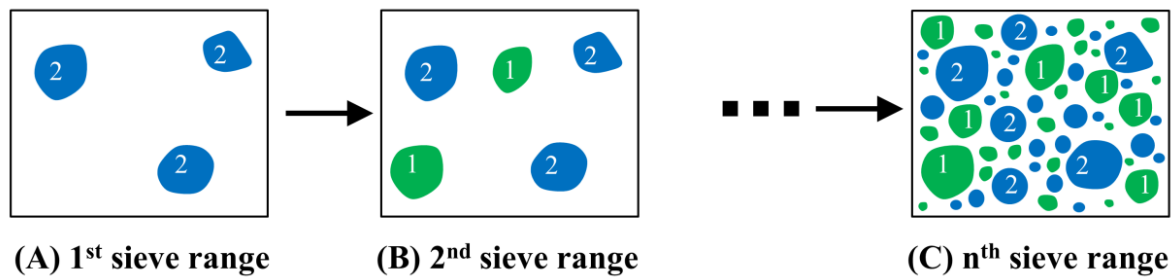


Figure 6.5 Schematic representation of the procedures to park slag and fly ash particles: (A) park particles within the first sieve range; (B) park particles within the second sieve range; and (C) park particles within the last sieve range.

However, this (Figure 6.5(C)) is not the final particle parking structure, since the hollow voids are not dealt with. By using the methods described previously, hollow voids are created and the final particle parking structure is obtained, as seen in Figure 6.6.

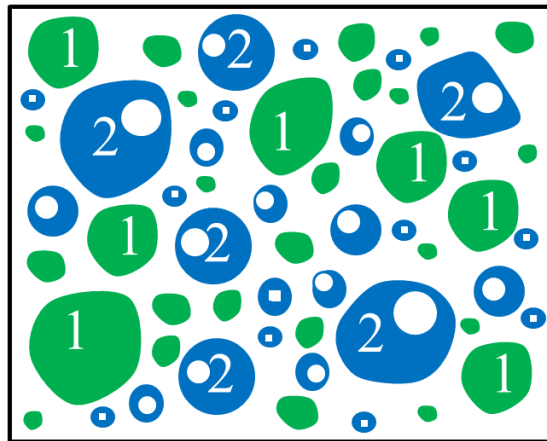


Figure 6.6 Schematic representation of the final particle parking structure of binary blended slag with fly ash.

## 6.2.2 Characterization of the initial particle parking structure

Previous simulation results suggest that the additional specific surface area (surface/volume) of real-shape particles relative to spherical particles accelerates hydration of cement [150], and also influences the microstructure formation of cement paste [114, 150]. The pore structure of a hydrated cement paste has a great impact on its diffusive properties [151, 152], which further affects its resistance to environmental aggressive ingredients such as chloride and sulfate ions. With this in mind, the simulated initial particle parking structures, using real-shape particles and spherical particles, were evaluated with regard to cumulative surface area, specific surface area, and pore size distribution.

### *Cumulative surface area of particles and specific surface area of a particle*

The cumulative surface area of particles in the initial particle parking structure is calculated as the total surface areas of the parked particles from the largest to the smallest.

The specific surface area of a particle is determined as the ratio between its surface area and its volume, i.e. particle surface area/particle volume ( $\mu\text{m}^{-1}$ ).

### *Pore size distribution*

Yang et al. developed an image-based algorithm to obtain the pore size distribution of porous media in 2D [123]. The current study extended this algorithm from 2D to 3D to calculate the pore size distribution of the digitized initial particle parking structure. Figure 6.7 shows a schematic representation of the initial parking structure in 2D before and after digitization. The vacant space left after parking particles was considered as pores. The particle occupied pixels are set with the value of unity, and the rest pixels are set with the value of zero. The procedures to determine the pore size distribution are outlined in the following four steps.

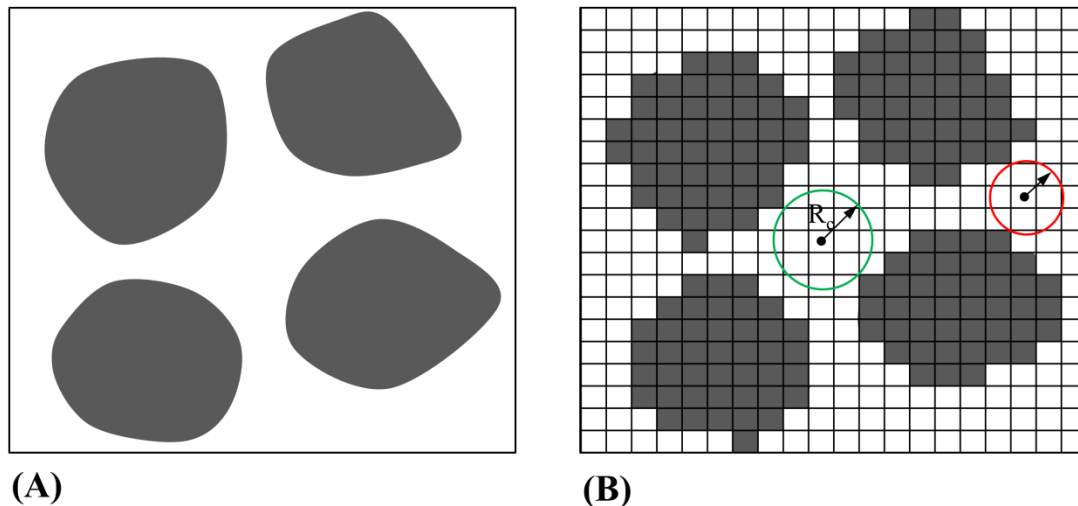


Figure 6.7 Schematic representation of the initial particle parking structure in 2D: (A) before digitization; (B) after digitization. In the graph,  $R_c$  is the critical radius of a pixel.

- (1) Determine the critical radius  $R_c$  for each zero-valued pixel (2D) or voxel (3D), as shown in Figure 6.7(B). The critical radius is defined as the maximum radius of a circle (for a 2D structure) or a sphere (for a 3D structure) that has its center at the considered pixel or voxel and covers only the zero-valued pixels or voxels.

- (2) For each pixel or voxel that has the largest  $R_{c,0}$ , its surrounding pixels or voxels within the distance of  $R_{c,0}$  are identified and denoted as the area or volume of the largest pores.
- (3) For each pixel or voxel that has the second largest  $R_{c,1}$ , its surrounding pixels or voxels within the distance of  $R_{c,1}$  are identified. If these pixels or voxels have not been included in the region covered by the largest radius, they are denoted as the area or volume of the second largest pores.
- (4) Repeat step 3 for pixels or voxels having the third largest, and then for the fourth largest, ... until the critical radius reaches half of the pixel or voxel side length.

### 6.3 Simulation parameters

The database of spherical harmonic coefficients for slag and fly ash were provided by the National Institute of Standards and Technology (NIST), USA. The slag and fly ash used in this chapter are the same as in Chapter 3. The maximum particle sizes of slag and fly ash are 45  $\mu\text{m}$ , and 47  $\mu\text{m}$ , respectively. According to Qian et al. [141], the size of specimen should be at least 2.5 times larger than the largest particle. So this study used a predefined cubic container with the dimensions of 125  $\mu\text{m} \times 125 \mu\text{m} \times 125 \mu\text{m}$ . The minimum particle size was set at 1  $\mu\text{m}$ .

A 4 mol/L sodium hydroxide simulated solution with the density of 1.15  $\text{g/cm}^3$  was used to formulate the alkali-activated materials. The mix proportions, given in terms of the mass needed for the predefined cube (125  $\mu\text{m} \times 125 \mu\text{m} \times 125 \mu\text{m}$ ), are tabulated in Table 6.2. The binder can be slag or/and fly ash. For all simulations, periodic boundary condition was employed. Periodic boundary condition allows a particle to pass through the surface of the simulation box and the part outside the simulation box is put on the opposite surface by placing a duplicate particle with the same orientation [18].

*Table 6.2 Mix proportions of alkali-activated materials, given in terms of the mass needed for the predefined cube (125  $\mu\text{m} \times 125 \mu\text{m} \times 125 \mu\text{m}$ )*

Pastes	Binder ( $\times 10^{-6}\text{g}$ )	Liquid/binder	Slag/binder	Fly ash/binder
BFS	2.2985	0.59	1	-
FA	2.1944	0.53	-	1
BFS + FA	2.4672	0.47	0.5	0.5

### 6.4 Results and discussion

#### 6.4.1 Simulated initial particle parking structures of alkali-activated materials

This section presents the simulated initial particle parking structures of alkali-activated materials using spherical particles and real-shape particles. The cumulative particle size distribution (PSD) and the *total* mass of the parked particles are presented and compared to the target values. The target values were calculated according to the mixture design (Table 6.2) and experimental PSD (Figure 3.2).

*Initial particle parking structures simulated with spherical particles*

The simulation of the initial particle parking structures with spherical particles was performed using HYMOSTRUC3D-E<sup>14</sup>. Figure 6.8 displays the simulated initial particle parking structure of alkali-activated materials using spherical particles. In the images, the colors of green, blue, gray and black represent slag, fly ash, liquid and voids in fly ash particles, respectively. The numbers of particles parked in the simulated initial particle parking structures were 13515, 16413 and 15744 for alkali-activated slag paste, alkali-activated fly ash paste, and alkali-activated slag blended with fly ash paste, respectively.

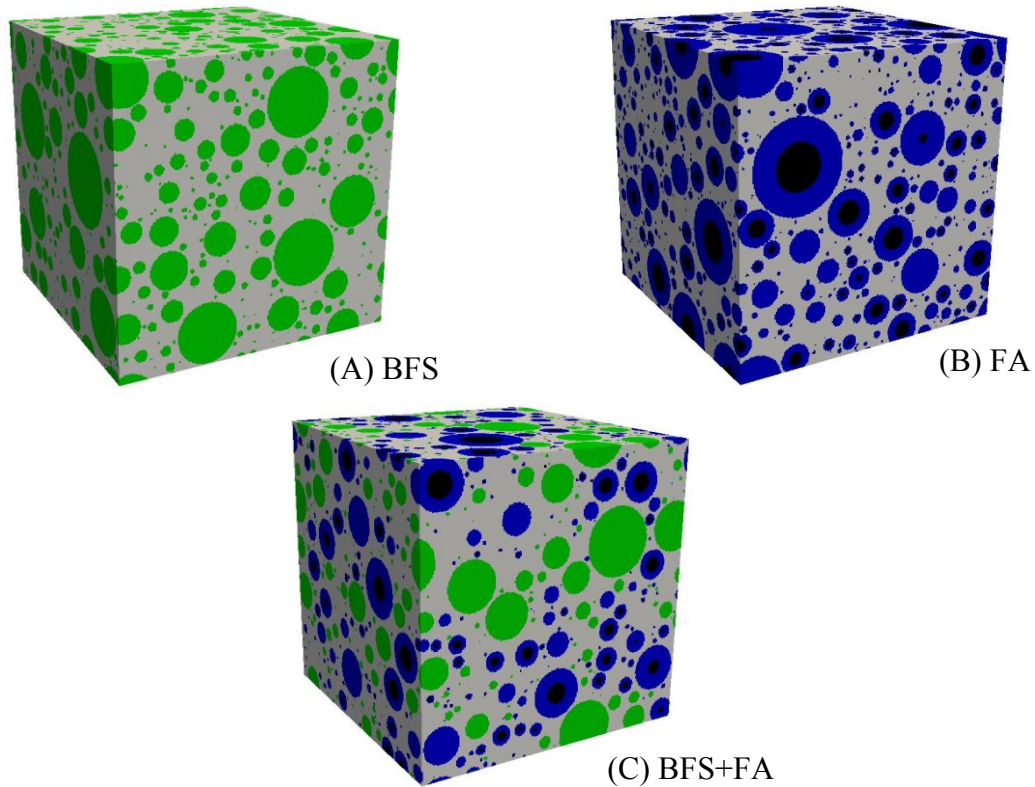


**Figure 6.8** Digital images of the simulated initial particle parking structures using spherical particles for alkali-activated slag paste (A), alkali-activated fly ash paste (B) and alkali-activated slag blended with fly ash paste (C). The size of the cubic unit cell is  $125\ \mu\text{m} \times 125\ \mu\text{m} \times 125\ \mu\text{m}$ . See more details of mixtures in Table 6.2.

The experimental PSD has ten size ranges. The parked particles in the cube were grouped into these ten size ranges according to particle size. Then the simulated cumulative PSD of the particles parked in the cube could be obtained. Figure 6.9 plots the simulated cumulative PSD of the particles parked in the cube and the target cumulative PSD. The simulated cumulative PSD was smaller than the target cumulative PSD for particles with diameters smaller than  $10\ \mu\text{m}$ , and larger for larger particles. The *total* mass of the particles parked in the cube were  $2.2983 \times 10^{-6}\ \text{g}$ ,  $2.1944 \times 10^{-6}\ \text{g}$ , and  $2.4693 \times 10^{-6}\ \text{g}$  for alkali-activated slag paste, alkali-activated fly ash paste and alkali-activated slag blended with fly ash paste, respectively. The errors of the simulated *total* masses relative to the target total masses (Table 6.2) were 0.008 %, 0.000 %, and 0.085 %, respectively.

<sup>14</sup> The HYMOSTRUC3D-E was developed based on HYMOSTRUC3D [114, 139, 149]. It is able to simulate hydration and microstructure development of blended cements.

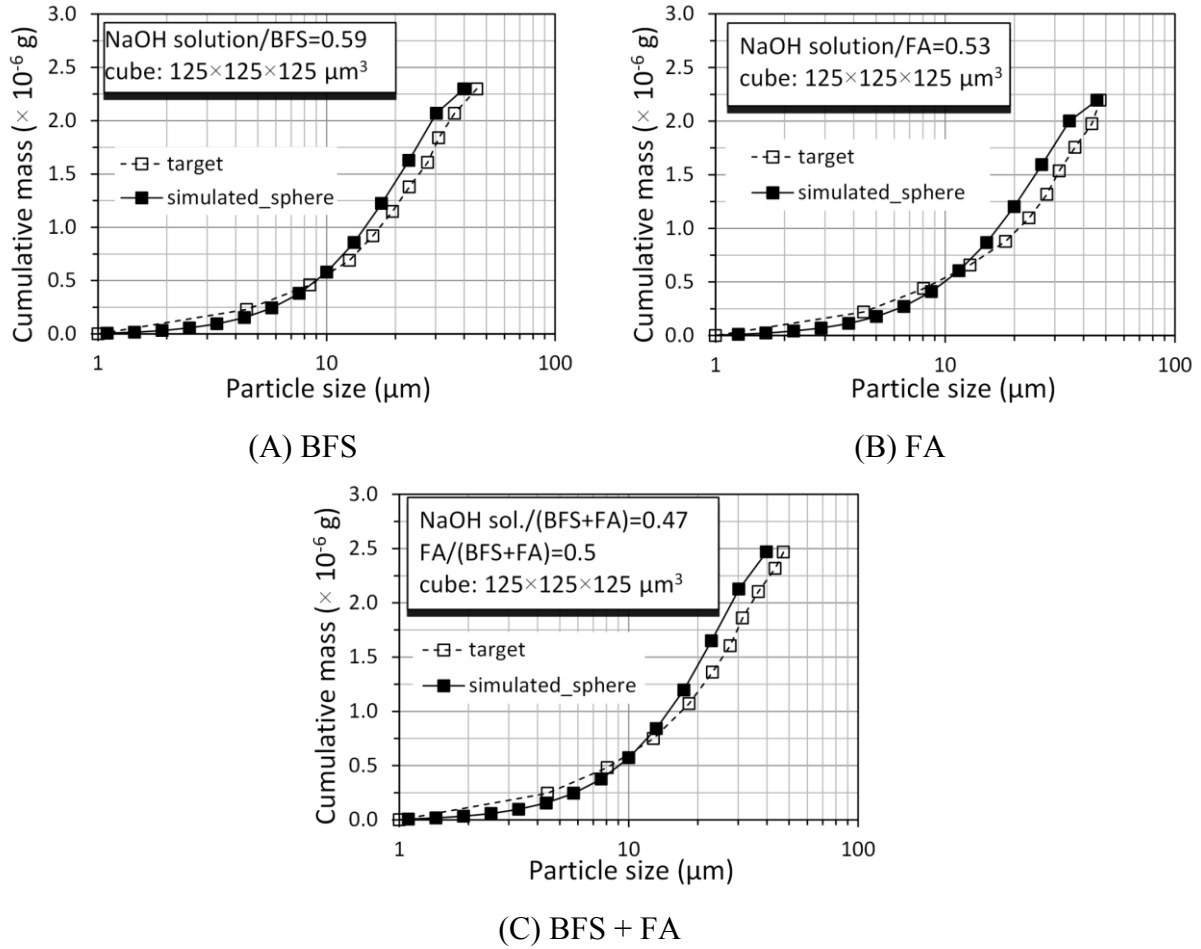


Figure 6.9 Simulated cumulative PSDs of the particles parked in the cube using spherical particles and the target cumulative PSDs for alkali-activated slag paste (A), alkali-activated fly ash paste (B) and alkali-activated slag/fly ash paste (C). See more details of mixtures in Table 6.2.

#### Initial particle parking structures simulated with real-shape particles

In addition to the visualization by digital imaging, the simulated initial particle parking structure by Anm material model can also be visualized directly using Virtual Reality Modeling Language (VRML). The VRML image displays virtual reality environments of objects, including surface color, image mapped textures, light and reflection mapping, and transparency [153]. Figure 6.10 displays the simulated initial particle parking structure using real-shape particles as VRML and digital images for alkali-activated slag paste, alkali-activated fly ash paste and alkali-activated slag blended with fly ash paste. Because the periodic boundary conditions allow a particle to pass through the surface of the simulation box there were particles sticking out beyond the simulation box in the VRML images. In the digitization process from the VRML image to the digital image, all the parts outside the simulation box were removed, so there were no particles sticking out beyond the simulation box in the digital images. The numbers of particles parked in the simulated initial particle parking structures were 8558, 9154 and 9342 for alkali-activated slag paste, alkali-activated fly ash paste, and alkali-activated slag blended with fly ash paste, respectively.



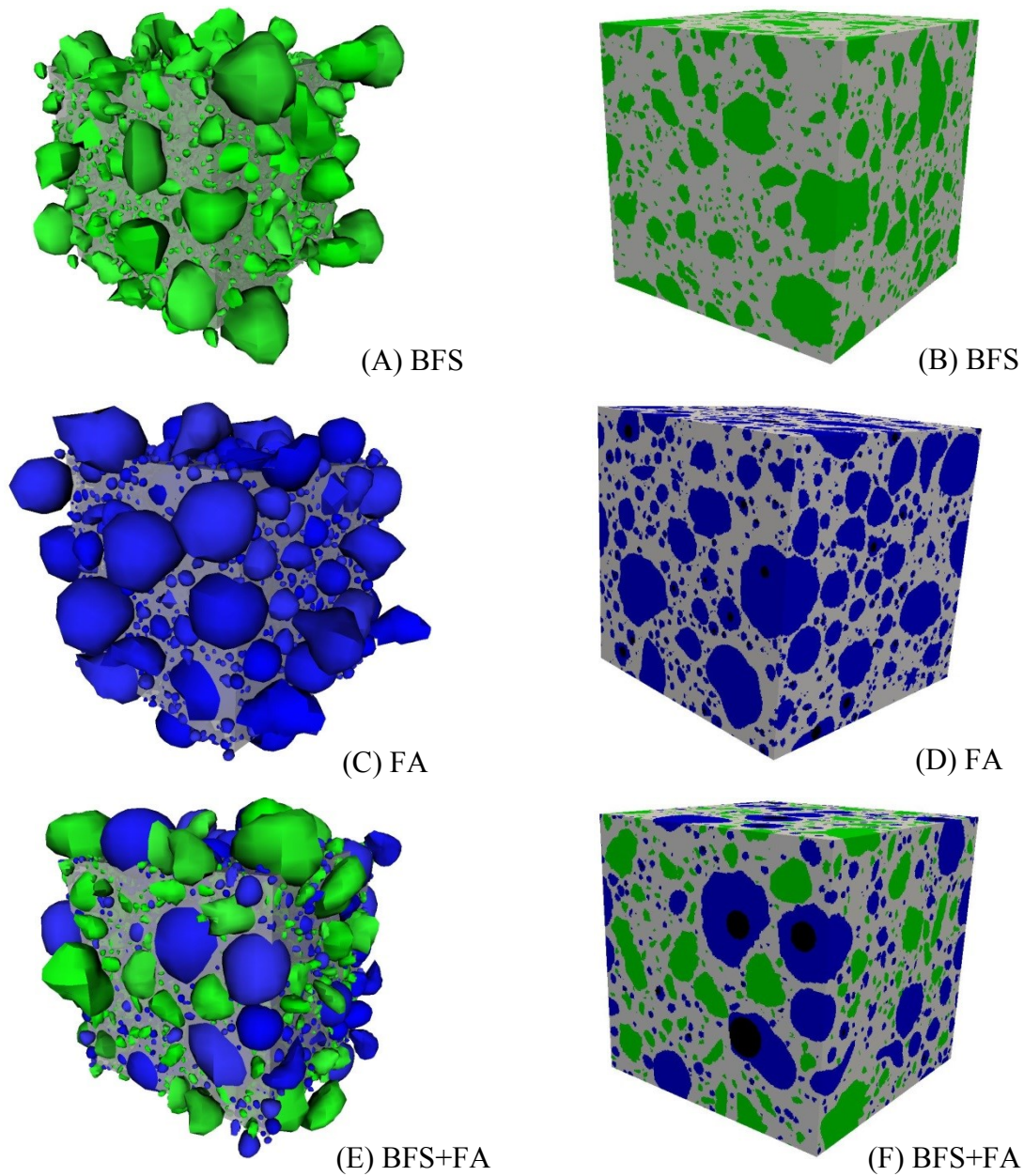


Figure 6.10 VRML images (A, C, E) and digital images (B, D, F) of the simulated initial particle parking structures using real-shape particles for alkali-activated slag paste (A, B), alkali-activated fly ash paste (C, D) and alkali-activated slag blended with fly ash paste (E, F). The size of the cubic unit cell is  $125\ \mu\text{m} \times 125\ \mu\text{m} \times 125\ \mu\text{m}$ . See more details of mixtures in Table 6.2.

The simulated cumulative PSD of the particles parked in the cube and the target cumulative PSD are plotted in Figure 6.11. The simulated cumulative PSDs of alkali-activated material pastes agreed very well with their target ones. The *total* masses of particles parked in the initial particle parking structures were  $2.2906 \times 10^{-6}\ \text{g}$ ,  $2.1965 \times 10^{-6}\ \text{g}$  and  $2.4609 \times 10^{-6}\ \text{g}$  for alkali-activated slag paste, alkali-activated fly ash paste, and alkali-activated slag blended with fly ash paste, respectively. The errors of the simulated *total* masses relative to the target total amounts (Table 6.2) were 0.344 %, 0.096 % and 0.255 %, respectively.

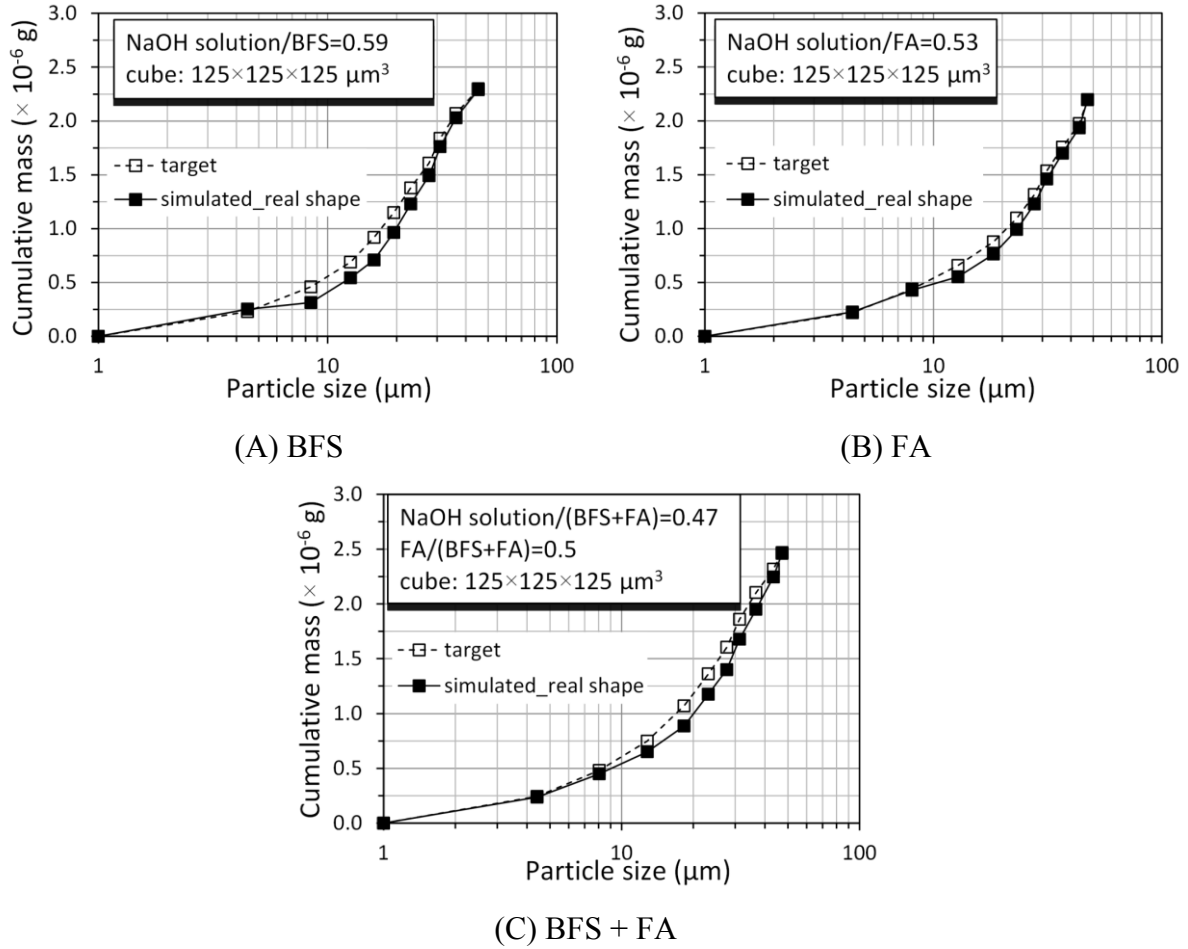


Figure 6.11 Simulated cumulative PSDs of the particles parked in the cube using real-shape particles and the target cumulative PSDs for alkali-activated slag paste (A), alkali-activated fly ash paste (B) and alkali-activated slag blended with fly ash paste (C). See more details of mixtures in Table 6.2.

#### 6.4.2 Evaluation of the simulated initial particle parking structure

In this section, the initial particle parking structures, simulated with spherical particles and real-shape particles, are evaluated with regard to cumulative surface area, specific surface area and pore size distribution.

##### Cumulative surface area

Figure 6.12 shows the cumulative surface area of the parked particles in the simulated initial particle structures as a function of particle size for alkali-activated slag paste, alkali-activated fly ash paste, and alkali-activated slag/fly ash paste. The cumulative surface areas of the parked particles using real-shape particles and spherical particles were close to each other at large particle sizes. However, the cumulative surface area of the parked particles using real-shape particles was much larger at small particle sizes. This is because the real-shape particles at small particle sizes had much larger specific surface areas, which will be discussed in the following subsection. The total surface areas of the particles parked in the cube ( $125^3 \mu\text{m}^3$ ) using real-shape particles were  $5.053 \times 10^5 \mu\text{m}^2$ ,  $5.284 \times 10^5 \mu\text{m}^2$  and  $5.669 \times 10^5 \mu\text{m}^2$  for alkali-activated slag paste, alkali-activated fly ash paste, and alkali-activated slag blended with fly ash paste, respectively. By using spherical particles, the total surface areas of the particles parked in the cube were  $4.083 \times 10^5 \mu\text{m}^2$ ,  $4.705 \times 10^5 \mu\text{m}^2$  and  $4.746 \times 10^5 \mu\text{m}^2$ ,



respectively. The total surface areas of the parked particles using real-shape particles were 23.76 %, 12.31 % and 19.45 % larger, respectively, than those using spherical particles.

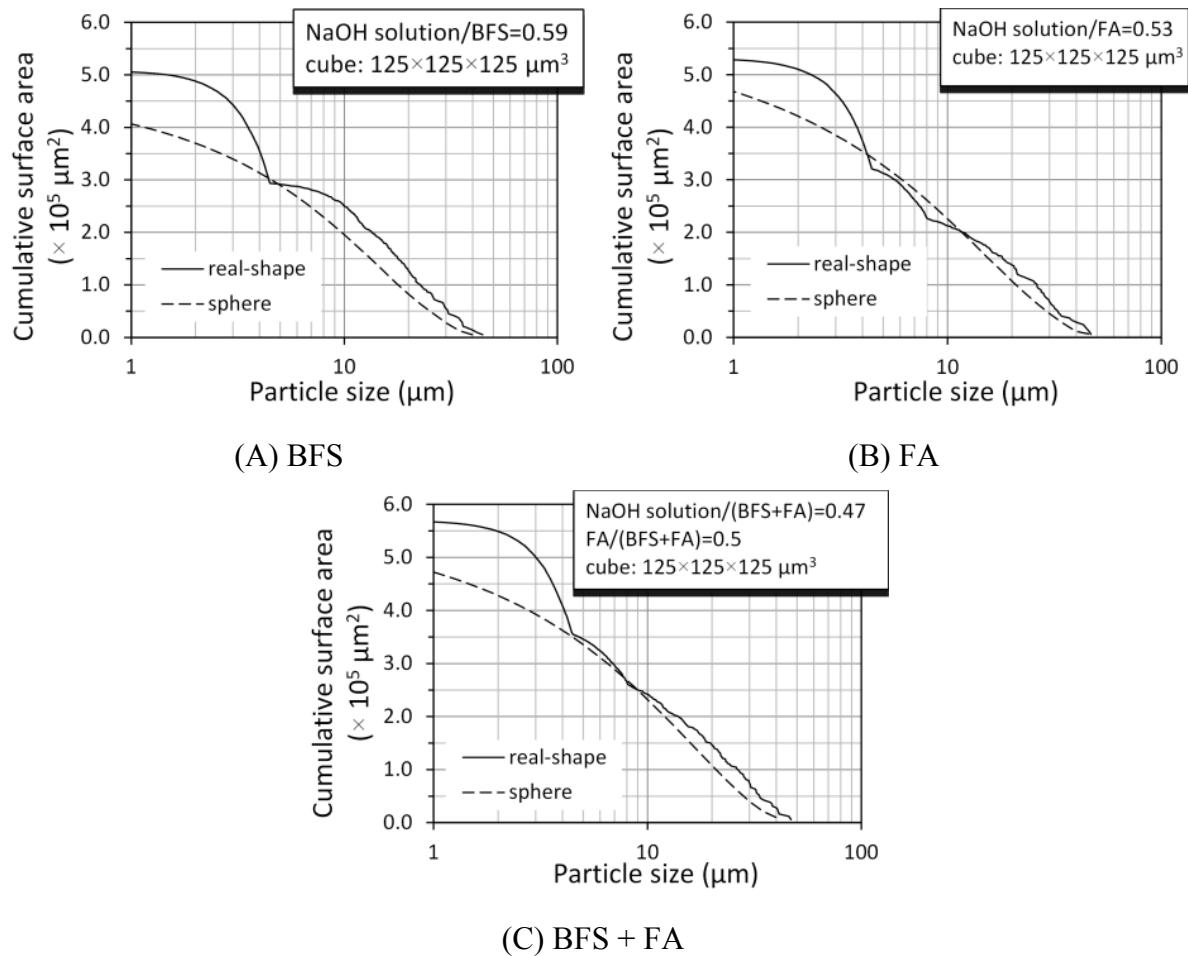


Figure 6.12 Cumulative surface areas of the particles parked in the cube for alkali-activated slag paste (A), alkali-activated fly ash paste (B) and alkali-activated slag blended with fly ash paste (C). See more details of mixtures in Table 6.2.

### Specific surface area

In the following paragraphs the effect of particle shape on the specific surface area of particles in the simulated initial particle parking structures is discussed in two aspects, i.e. effect on specific surface area of individual parked particles and effect on the bulk specific surface area of all the parked particles.

#### (1) Effect of particle shape on the specific surface area of individual parked particles

The specific surface area (*SSA*) of the individual parked particles in the initial particle parking structure is presented as a function of particle size (*D*) in Figure 6.13. It is clear that the specific surface area of individual parked particles was larger, particularly for small particles, in the simulated initial particle parking structure using real-shape particles than in that using spherical particles. A decreasing trend of the specific surface area was observed as a function of particle size. The fitted relationship of specific surface area as a function of particle size for the parked real-shape particles also suggests a large dependency of the specific surface area on the particle size. Besides the particle size, the particle shape also affected the specific surface area of the parked real-shape particles. The particle with a more irregular shape has a

larger specific surface area. For this reason, a particle with a larger size may still have a larger specific surface area than a particle with a smaller size. This is opposite to the decreasing trend of the specific surface area as a function of particle size.

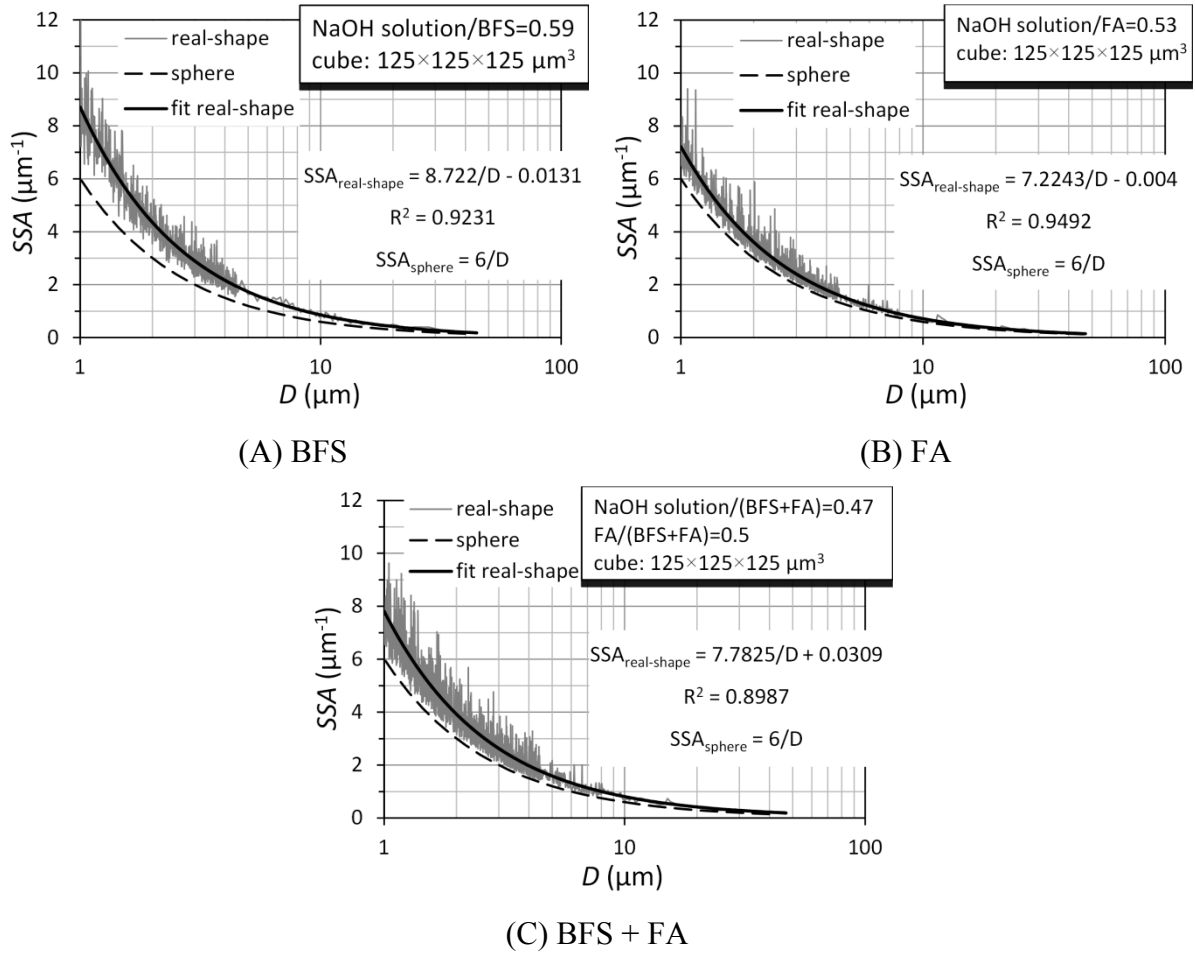


Figure 6.13 Specific surface area of the individual parked particles in the cube for alkali-activated slag paste (A), alkali-activated fly ash paste (B) and alkali-activated slag blended with fly ash paste (C). See more details of mixtures in Table 6.2.

For a spherical particle with diameter  $D$ , its specific surface area is  $6/D$ . It can be seen that the specific surface area of a spherical particle only depends on the particle diameter. Therefore, the specific surface area of the parked spherical particles had the same distribution as a function of particle size/diameter for all the simulated initial particle parking structures using spherical particles. For all the simulated initial particle parking structures, a relationship existed between the specific surface area and particle size:  $SSA = F_{ac}/D$ , where  $F_{ac}$  is a pre-factor. Compared to the relationship for the parked spherical particles, the relationship for the parked real-shape particles had a pre-factor with 45.37 %, 20.41 % and 29.71 % larger for alkali-activated slag paste, alkali-activated fly ash paste, and alkali-activated slag blended with fly ash paste, respectively. A larger pre-factor resulted in a larger specific surface area.

## (2) Effect of particle shape on bulk specific surface area of all the parked particles

Cement fineness (Blaine,  $m^2/kg$ ) significantly influence the hydration process and early-age properties of cement-based materials [114, 154, 155]. Since the specific surface areas of individual particles cannot explicitly reflect the binder fineness, the bulk specific surface area

was introduced. It was defined as the ratio of the total surface area of the parked particles divided by the total volume of the parked particles. A larger bulk specific surface area led to a larger binder fineness. The bulk specific surface areas of the parked particles in the initial particle parking structures using real-shape particles were  $0.6552 \mu\text{m}^{-1}$ ,  $0.5606 \mu\text{m}^{-1}$  and  $0.6011 \mu\text{m}^{-1}$  for alkali-activated slag paste, alkali-activated fly ash paste, and alkali-activated slag/fly ash paste, respectively. By using spherical particles, the bulk specific surface areas were  $0.5277 \mu\text{m}^{-1}$ ,  $0.4996 \mu\text{m}^{-1}$  and  $0.5043 \mu\text{m}^{-1}$ , respectively. Compared to those of the parked particles using spherical particles, the bulk specific surface areas of the parked particles using real-shape particles were 24.16 %, 12.21 % and 19.19 % larger, respectively.

### Pore size distribution

In the simulated initial particle parking structure the space filled with liquid phase was defined as pore. Figure 6.14 presents the pore size distributions of the simulated initial particle parking structure at digitization resolutions of 1, 0.5 and  $0.25 \mu\text{m}$  per cubic voxel edge for alkali-activated slag paste. Regardless of using real-shape or spherical particles, the simulated initial particle parking structure exhibited a finer pore size distribution when it was digitized with a higher resolution. At all digitization resolutions, the simulated initial particle parking structure using real-shape particles had a slightly finer pore size distribution than that using spherical particles.

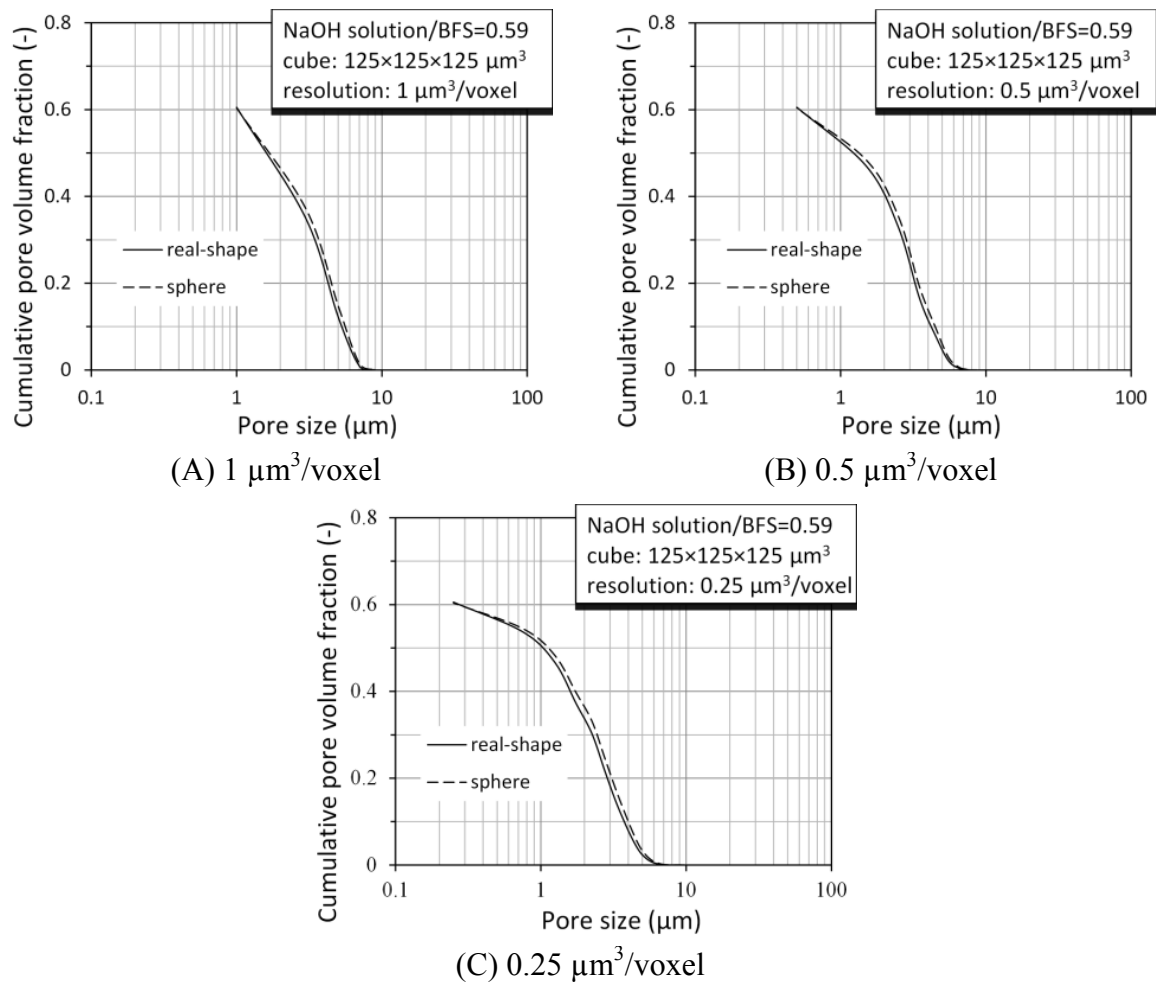


Figure 6.14 Pore size distribution of the simulated initial particle parking structure digitized at different resolutions. See more details of mixtures in Table 6.2.

Figure 6.15 presents the pore size distributions of the simulated initial particle parking structures for alkali-activated slag paste, alkali-activated fly ash paste and alkali-activated slag blended with fly ash paste. All the simulated initial particle parking structures were digitized with a resolution of  $0.5\ \mu\text{m}$  per cubic voxel edge. It can be seen that the pore size distributions were very close to each other for the simulated initial particle parking structures using real-shape particles and spherical particles. In general, the pore size distributions of the simulated initial particle parking structures using real-shape particles shifted slightly to small pores when compared to those using spherical particles.

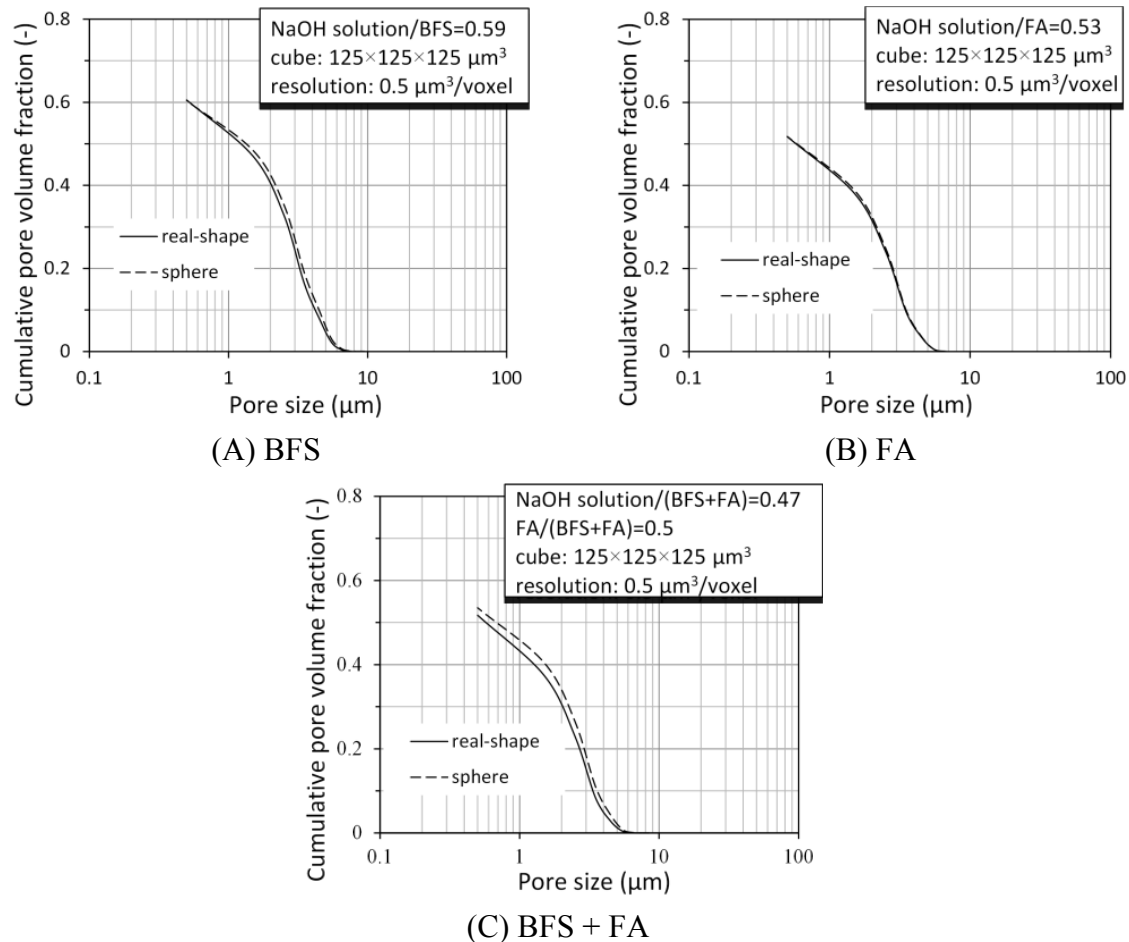


Figure 6.15 Pore size distributions of the simulated initial particle parking structures for alkali-activated slag paste (A), alkali-activated fly ash paste (B) and alkali-activated slag blended with fly ash paste (C). See more details of mixtures in Table 6.2.

Figure 6.16 plots the pore size distribution of the simulated initial particle parking structures for alkali-activated slag paste with a liquid/binder ratio of 0.45. In contrast, an obvious shift of the pore size distribution to small pores was observed between the simulated initial particle parking structure using real-shape particles and that using spherical particles. This is because the lower liquid/binder ratio reduced the distances between particles, which made the effect of particle shape on the pore structure more pronounced. From these comparisons, it can be concluded that particle shape did not significantly influence the pore size distribution of the simulated initial particle parking structure at high liquid/binder ratios. At low liquid/binder ratios, however, using the real-shape particles led to a shift of the pore size distribution to small pores.

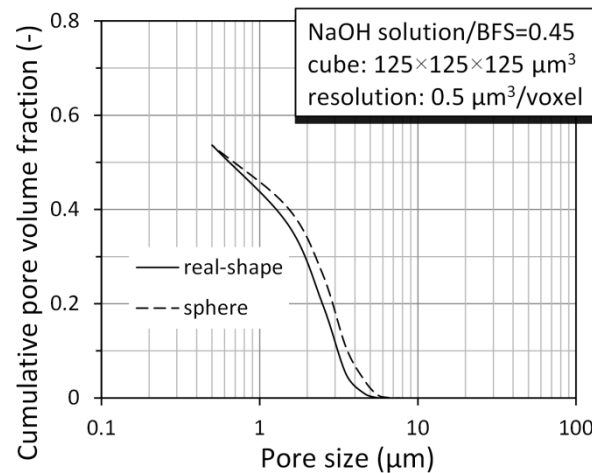


Figure 6.16 Pore size distributions of the simulated initial particle parking structures for alkali-activated slag paste with a liquid/slag ratio of 0.45.

### 6.4.3 Computation efficiency of the simulations

The simulations using spherical particles were carried out using a desktop computer (basic frequency = 2.99 GHz). It took *only* few minutes for the simulation of the initial particle parking structures using spherical particles. The simulations using real-shape particles were carried out using a computer server (basic frequency = 3.6 GHz). It took 135, 270 and 297 hours for the simulation of the initial particle parking structure of alkali-activated slag paste (liquid/binder ratio = 0.59), alkali-activated fly ash (liquid/binder ratio = 0.53) and alkali-activated slag/fly ash paste (liquid/binder ratio = 0.47), respectively. When the liquid/binder ratio decreased to 0.45 for an alkali-activate slag paste, it took 443 hours for simulating the initial particle parking structure. The simulation efficiency was low due to its high calculation load. This can be explained by the following two reasons. To park a particle successfully without overlapping the previously parked particles required a number of attempts to find an appropriate place, particle size and particle orientation. This process took a lot of time. Furthermore, the number of attempts increased rapidly with the number of particles that were already parked.

## 6.5 Conclusions

By implementing the spherical harmonics to characterize particle shape, the initial particle parking structure of alkali-activated material paste was simulated using real-shape particles. The simulated initial particle parking structures using real-shape particles were evaluated with regard to cumulative surface area, specific surface area and pore size distribution, by comparing them to those simulated using spherical particles. Based on the numerical results in this chapter, the following conclusions can be drawn:

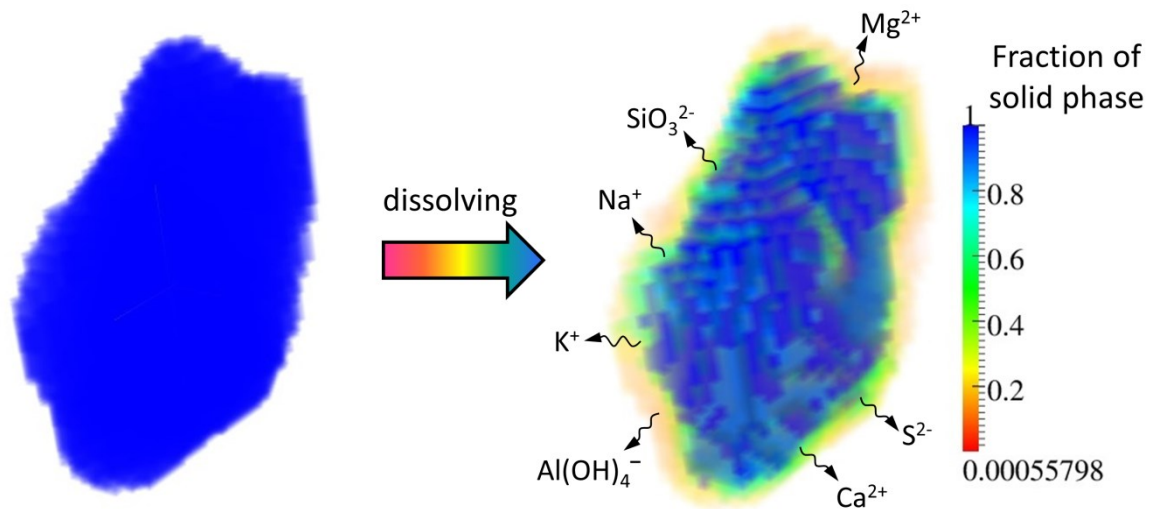
- (1) The simulated cumulative PSD and *total* mass of the particles parked in the initial particle parking structure using real-shape particles were in good agreement with the target values.
- (2) The simulated initial particle parking structures using real-shape particles had *total* surface areas with 23.76 %, 12.31 % and 19.45 % larger than those using spherical particles for

alkali-activated slag, alkali-activated fly ash and alkali-activated slag blended with fly ash, respectively.

- (3) For alkali-activated slag, alkali-activated fly ash and alkali-activated slag blended with fly ash, the bulk specific surface area was 24.16 %, 12.21 % and 19.19 % larger, respectively, for the simulated initial particle parking structures using real-shape particles than those using spherical particles.
- (4) For the investigated alkali-activated precursor paste with high liquid/binder ratios ( $> 0.47$ ), the pore size distributions of the simulated initial particle parking structures were not significantly influenced by the particle shape. At low liquid/binder ratios, however, using real-shape particles led to a significant shift of the pore size distribution to small pores as compared to using the spherical particles.
- (5) The computation efficiency of the simulations using real-shape particles is quite low. This is because a number of attempts are needed for finding an appropriate place, particle size and particle orientation to park the particle successfully with no overlap with previously parked particles.

# Chapter 7

## Simulation of the dissolution of slag and fly ash in alkaline solution<sup>15</sup>



This chapter presents a numerical model to simulate the dissolution of slag and fly ash in alkaline solution. This numerical model consists of three modules, i.e. simulation of the initial particle parking structure, dissolution rate of slag/fly ash and transport of aqueous ions. The influences of temperature, reactivity of precursors, alkalinity of solution and inhibiting effect of aqueous Al etc. on the dissolution are taken into account in the model. After build-up of these three modules, the presented numerical model was then used to simulate the dissolution of slag and fly ash in alkaline solution.

<sup>15</sup> This chapter is partially based on:

Yibing Zuo and Guang Ye. Experimental study and numerical simulation of the dissolution of blast furnace slag in alkaline solution. Conference on Alkali Activated Materials and Geopolymers: Versatile Materials offering high performance and low emissions. May 27 – June 1 2018, Tomar, Portugal.

## 7.1 Introduction

The reaction process of alkali-activated materials (AAMs) consists of dissolution of aluminosilicate precursors (mostly slag and fly ash), diffusion of aqueous ions, chemical reactions among these aqueous ions and nucleation and growth of solid reaction products. As the first step the dissolution of aluminosilicate precursors is of great significance to promote the reaction process. For an alkali-activated slag system, the pH of the alkaline activator should be higher than 11.5 to effectively activate the dissolution of slag [156, 157]. For an alkali-activated fly ash system, a high pH of the alkaline activator and an elevated curing temperature are usually needed to activate the dissolution of fly ash due to its low reactivity. Some experimental studies have been carried out on the dissolution of slag and fly ash in alkaline solution [158-160]. However, the numerical simulation of the dissolution of slag or fly ash in alkaline solution has not been reported yet in the literature.

This chapter presents a numerical model to simulate the dissolution of slag and fly ash in alkaline solution. As displayed in Figure 7.1, this numerical model consists of three modules. In the first module the extended Anm model discussed in Chapter 6 was used to simulate the initial particle parking structure of slag/fly ash in alkaline solution. In the second module, thermodynamics was used to consider the chemical reactions between slag/fly ash and alkaline solution, and the rate of dissolution was described based on the transition state theory. In the last module, the lattice Boltzmann method was used to simulate the physical transport of aqueous ions in solution. The influences of temperature, reactivity of aluminosilicate precursors, alkalinity of solution and inhibiting effect of aqueous Al etc. on the dissolution are taken into account in the model.

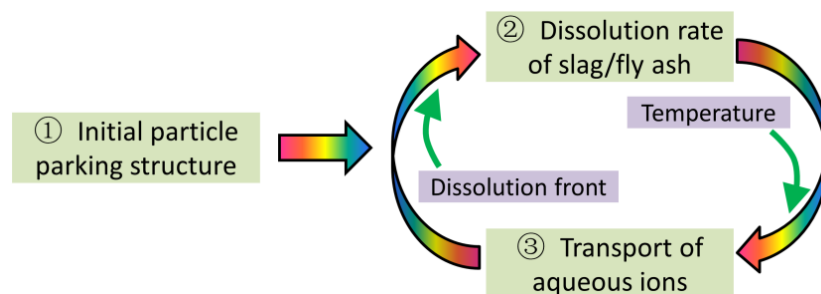


*Figure 7.1 Modules of the numerical model to simulate the dissolution of slag/fly ash in alkaline solution.*

Finally, the numerical model was implemented to simulate the dissolution of slag and fly ash in alkaline solution. Particularly, the inhibiting effect of aqueous Al on the dissolution of fly ash, as discussed in Chapter 4, was explicitly simulated. The numerical model presented in this chapter will make up the dissolution module of the GeoMicro3D model in Chapter 9. Figure 7.2 shows the position of Chapter 7 in structure of the study of the reaction process and microstructure formation of AAMs in this thesis.





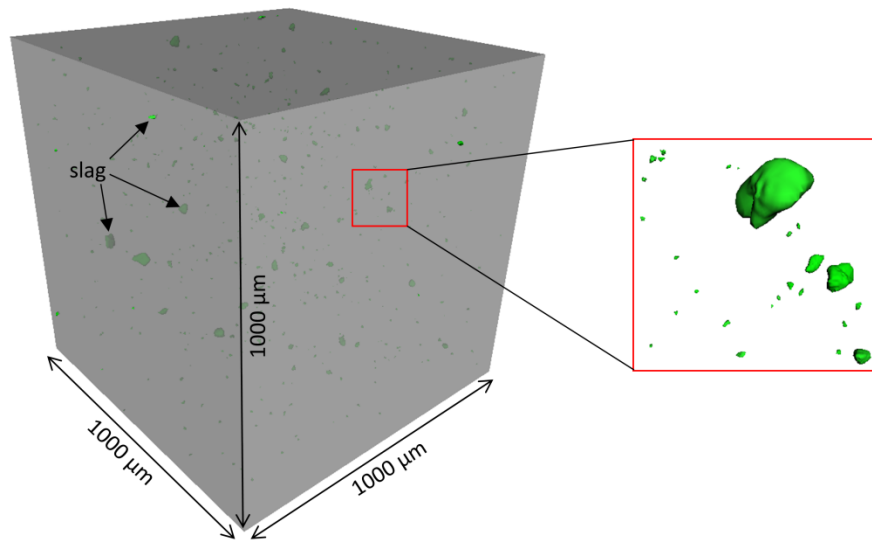


*Figure 7.3 One example of the simulated initial particle parking structure of slag in alkaline solution.*

## 7.2.2 Dissolution rate

### 7.2.2.1 Stoichiometric dissolution of Si and Al

The framework of aluminosilicate material consists of the framework forming elements like the tetrahedral Si and Al, and the framework modifying elements like the alkali and earth-metals. Since the framework modifying elements dissolve more easily than the framework forming elements, the dissolution of aluminosilicate material in alkaline solution actually depends on the dissolution of Si and Al tetrahedras from the frameworks. The dissolution of Si and Al from the framework into alkaline solution is reported to be stoichiometric for aluminosilicate materials, such as synthetic aluminosilicate glass [159] and natural aluminosilicate glass [161].

Snellings synthesized 6 types of glasses and studied the dissolution of these synthetic glasses in alkaline solution [159]. Figure 7.4 displays the plot of Al to Si concentrations normalized to their respective molar fraction in the glass ( $v_{Al}$  and  $v_{Si}$ ). G1 and G2 were used to represent the glasses encountered in slags, G3 and G4 were used to represent the glasses encountered in fly ashes and, G5 and G6 were used to represent the glasses encountered in natural pozzolans and silica fume, respectively. The linear relationship between the normalized concentrations of Al and Si indicates that the dissolution of Al and Si from the framework is stoichiometric.

The stoichiometric dissolution of Al and Si is not only found for the synthetic glasses, but also for the natural glasses. Figure 7.5 presents the plot between the normalized concentration of Al and the normalized concentration of Si for the natural aluminosilicate glasses. The plot shows a linear relationship between the normalized concentrations of Al and Si. This also indicates a stoichiometric dissolution of Al and Si for the natural aluminosilicate glasses.

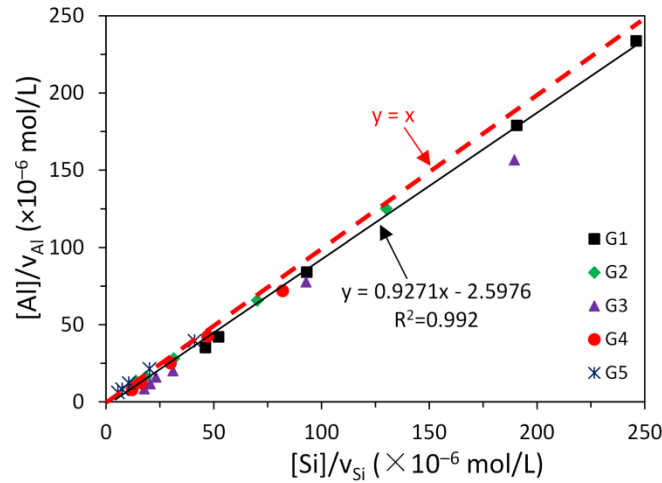


Figure 7.4 Al concentrations in solution normalized by the molar fraction of Al in the glass plotted in function of the normalized Si concentration by the molar fraction of Si in the glass. In the graph,  $[Al]$  and  $[Si]$  were concentrations of Al and Si in solution,  $v_{Al}$  and  $v_{Si}$  were molar fraction of Al and Si in the glass, respectively, and G1, G2, G3, G4, G5 and G6 were synthetic glasses. (the data are from [159])

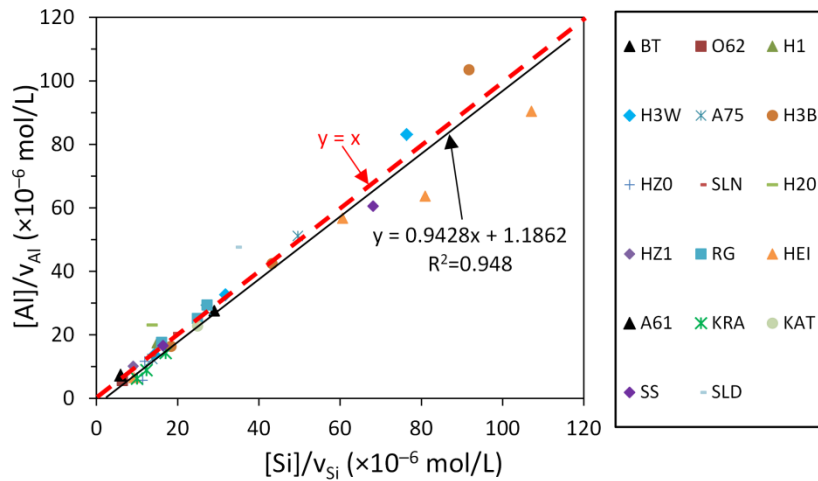


Figure 7.5 Al concentrations in solution normalized by the molar fraction of Al in the glass plotted in function of the normalized Si concentration by the molar fraction of Si in the glass. In the graph,  $[Al]$  and  $[Si]$  were concentrations of Al and Si in solution,  $v_{Al}$  and  $v_{Si}$  were molar fraction of Al and Si in the glass and, BT, O62, H1 and H3W etc. in the legend were codes that represent different natural aluminosilicate glasses. (the data are from [161])

### 7.2.2.2 Dissolution rates of Si and Al

In accord with the transition state theory, the dissolution rate of glass can be described by Equation 7.1 [23, 25]. This equation is able to accurately describe various glass dissolution behaviors from far-from-equilibrium conditions [24, 159] to near-to-equilibrium conditions [162, 163].

$$r = r_+ \left( 1 - \exp \left( -\frac{A^*}{\sigma RT} \right) \right) \quad (7.1)$$

where  $r$  and  $r_+$  are overall and forward dissolution rate, respectively.  $\sigma$  is the ratio of the rate of dissolution of the *activated complex*<sup>16</sup> relative to the overall reaction rate.  $R$  and  $T$  are the gas constant and the absolute temperature, respectively.  $A^*$  is the chemical affinity<sup>17</sup> that can be calculated as:

$$A^* = -RT \ln \left( \frac{IAP}{K_{sp}} \right) \quad (7.2)$$

where  $IAP$  is the ion activity product and  $K_{sp}$  is the solubility product. Substituting Equation 7.2 into Equation 7.1 yields the following equation:

$$r = r_+ \left( 1 - \left( \frac{IAP}{K_{sp}} \right)^{1/\sigma} \right) \quad (7.3)$$

It is reported that the dissolution of aluminosilicate glass can be described from the dissolution of individual constituent oxide [162, 164]. The dissolution of silica and aluminum oxides in alkaline solution can be described by the following chemical reactions:



where  $SiO_2$  and  $Al_2O_3$  are amorphous silica and aluminum oxide, respectively. Then the dissolution rate of amorphous silica and aluminum oxide, i.e.  $r_{Si}$  and  $r_{Al}$ , can be obtained by the following equations.

$$r_{Si} = r_{+,Si} \left( 1 - \left( \frac{IAP_{Si}}{K_{sp,Si}} \right)^{1/\sigma} \right) \quad (7.6)$$

$$r_{Al} = r_{+,Al} \left( 1 - \left( \frac{IAP_{Al}}{K_{sp,Al}} \right)^{1/\sigma} \right) \quad (7.7)$$

where  $r_{+,Si}$  and  $r_{+,Al}$  are the forward dissolution rates of silica and aluminum oxides, respectively.  $K_{sp,Si}$  and  $K_{sp,Al}$  are the solubility products of silica and aluminum oxides, respectively.  $IAP_{Si}$  and  $IAP_{Al}$  are the ion activity products that can be calculated as follows:

$$IAP_{Si} = \frac{a_{SiO_3^{2-}} * a_{H_2O}}{a_{OH^-} * a_{OH^-}} \quad (7.8)$$

$$IAP_{Al} = \frac{a_{AlO_2^-} * a_{AlO_2^-} * a_{H_2O}}{a_{OH^-} * a_{OH^-}} \quad (7.9)$$

where  $a_i$  represents the ion activity.  $i$  can be  $SiO_3^{2-}$ ,  $AlO_2^-$ ,  $H_2O$  or  $OH^-$ .

The alkali and earth-metals distort the framework structure of aluminosilicate materials. The more intensive the structure is distorted, the higher the reactivity of the aluminosilicate

<sup>16</sup> The term *activated complex* is used in the transition-state theory, referring to an intermediate configuration with the maximum potential energy between the reactant and the products.  
(after <https://www.britannica.com/science/transition-state-theory>)

<sup>17</sup> Chemical affinity refers to the tendency of an atom or compound to combine by chemical reaction.  
(after [https://en.wikipedia.org/wiki/Chemical\\_affinity](https://en.wikipedia.org/wiki/Chemical_affinity))

materials will be [26]. The ratio of the non-bridging oxygen atoms to oxygen atoms in tetragonal coordination, i.e. NBO/T, can be used to describe how severe the structure is distorted [165]. The NBO/T of aluminosilicate materials can be calculated using the oxide molar fractions according to the following equation [160]:

$$NBO/T = \frac{2(CaO + MgO + K_2O + Na_2O + 3f_{Fe}Fe_2O_3 + 3f_{Al}Al_2O_3 - (1-f_{Fe})Fe_2O_3 - (1-f_{Al})Al_2O_3)}{SiO_2 + TiO_2 + 2(1-f_{Fe})Fe_2O_3 + 2(1-f_{Al})Al_2O_3} \quad (7.10)$$

where the oxides represent molar fractions in the aluminosilicate material and,  $f_{Fe}$  and  $f_{Al}$  are parameters that specify the molar fractions of  $Fe_2O_3$  and  $Al_2O_3$  acting as framework modifier.

The log forward dissolution rate of Si depends on the reactivity of aluminosilicate materials (NBO/T) and alkalinity of solution (pH). This can be described using the following equation. The detailed derivation of this equation can be found in Appendix A.5.

$$\text{Log } r_{+,Si} = 0.0155pH \cdot NBO/T + 0.0727pH + 0.6199 NBO/T - 9.0309 \quad (7.11)$$

According to the stoichiometric dissolution of Al and Si in aluminosilicate materials, the log forward dissolution rate of Al can be obtained as:

$$\text{Log } r_{+,Al} = \text{Log} \left( \frac{v_{Al}}{v_{Si}} r_{+,Si} \right) = \text{Log} \left( \frac{v_{Al}}{v_{Si}} \right) + \text{Log } r_{+,Si} \quad (7.12)$$

### 7.2.2.3 Dissolution rate of alkali and earth-metals

The dissolution of calcium oxide in solution can be described by the following chemical reaction:



Similar to the dissolution rates of Si (Equation 7.6) and Al (Equation 7.7), the dissolution rate of Ca can be written as:

$$r_{Ca} = r_{+,Ca} \left( 1 - \left( \frac{IAP_{Ca}}{K_{sp,Ca}} \right)^{1/\sigma} \right) \quad (7.14)$$

where  $r_{Ca}$  and  $r_{+,Ca}$  are the overall and forward dissolution rates of Ca, respectively.  $K_{sp,Ca}$  is the solubility product of calcium oxide.  $IAP_{Ca}$  is the ion activity products that can be calculated using the following equation:

$$IAP_{Ca} = \frac{a_{Ca^{2+}} \cdot a_{OH^-} \cdot a_{OH^-}}{a_{H_2O}} \quad (7.15)$$

The log forward dissolution rate of Ca can be determined using Equation 7.16. The details of the experimental data and calculation results are provided in Appendix A.4.

$$\text{Log } r_{+,Ca} = 0.1868pH - 8.7729 \quad (7.16)$$

Compared with Si, Al and Ca, the modifying elements like Mg, Na, K and S are minor constituents in aluminosilicate materials, particularly for slag and fly ash. Similar to Ca, these

elements dissolve relatively fast. The dissolution rate of Mg, Na, K and S can be obtained by taking the dissolution rate of Ca as the reference.

$$r_{Mg} = f_{Mg} \frac{v_{Mg}}{v_{Ca}} r_{Ca} \quad (7.17)$$

$$r_{Na} = f_{Na} \frac{v_{Na}}{v_{Ca}} r_{Ca} \quad (7.18)$$

$$r_K = f_K \frac{v_K}{v_{Ca}} r_{Ca} \quad (7.19)$$

$$r_S = f_S \frac{v_S}{v_{Ca}} r_{Ca} \quad (7.20)$$

where  $r_{Mg}$ ,  $r_{Na}$ ,  $r_K$  and  $r_S$  are the dissolution rates of Mg, Na, K and S, respectively.  $f_{Mg}$ ,  $f_{Na}$ ,  $f_K$  and  $f_S$  are ratios of the dissolution rates of Mg, Na, K and S relative to the dissolution rate of Ca, respectively.  $v_{Ca}$ ,  $v_{Mg}$ ,  $v_{Na}$ ,  $v_K$  and  $v_S$  are molar fractions of Ca, Mg, Na, K and S in the precursor, respectively.

#### 7.2.2.4 Dissolved amount of elements at each lattice Boltzmann simulation step

The initial particle parking structure is digitized into digital voxels, so the precursor particles consist of voxels (or lattice cells). Since slag is totally amorphous, the elements (Si, Al, Ca, Mg, S and K) are assumed to be homogeneously distributed in slag particles. In other words, each slag lattice cell has the same element composition as the chemical composition of slag. Since fly ash may be not totally amorphous, one part of the fly ash lattice cells are set as crystalline cells to represent the crystalline phases in fly ash. The remaining lattice cells of fly ash are set as reactive cells to represent the amorphous phases in fly ash. Only the reactive fly ash cells can be dissolved. For reactive fly ash cells, each of them is assumed to have the same element composition as the chemical composition of amorphous phases in fly ash.

The simulation of the dissolution of precursors is carried out by simulating the dissolution of the precursor lattice cells. Each precursor lattice cell has six neighbor lattice cells, so it has six interfaces where dissolution may occur. For each interface of a precursor lattice cell, the dissolved amount of elements at one lattice Boltzmann time step can be calculated using Equation 7.21. The factor  $f_{dissolving-area}$  is introduced to consider the fraction of the interface area that is dissolving in the current lattice Boltzmann time step. To calculate the dissolution rate of the element, ion activity products and pH are taken from the neighbor lattice nodes that are in contact with the dissolving interfaces. By summing up the dissolved amount at each interface, the total dissolved amount can be obtained according to Equation 7.22.

$$\Delta n_{X,i} = f_{dissolving-area} \cdot r_{X,i} \cdot t_0 \cdot l_0^2 \quad (7.21)$$

$$\Delta N_X = \sum_{i=1}^6 \Delta n_{X,i} \quad (7.22)$$

where  $\Delta n_{X,i}$  and  $\Delta N_X$  are the dissolved amount of element  $X$  at interface  $i$  and six interfaces at one lattice Boltzmann time step  $t_0$ , respectively. Element  $X$  can be Si, Al, Ca, Mg, S or K.  $r_{X,i}$  is the dissolution rate of element  $X$  at the interface  $i$  and,  $l_0$  is the side length of lattice cell.

### 7.2.3 Transport of aqueous ions

In this research, the lattice Boltzmann (LB) method was used to simulate the transport of aqueous ions. The aqueous ions considered in the model are  $\text{SiO}_3^{2-}$ ,  $\text{AlO}_2^-$ ,  $\text{Ca}^{2+}$ ,  $\text{Mg}^{2+}$ ,  $\text{K}^+$ ,  $\text{Na}^+$ ,  $\text{S}^{2-}$  and  $\text{OH}^-$ . Usually, a cubic lattice model D3Q19 is used for 3D mass transport simulation<sup>18</sup>. However, the velocity directions may be reduced from 19 (D3Q19) to 7 (D3Q7) without degrading the accuracy when modelling purely diffusive transport without the convective term [167]. Usually, the transport of aqueous ions during the hydration process of cementitious materials is purely diffusive without a convective term. In order to reduce the computational load and improve the simulation efficiency, a cubic lattice model D3Q7 was employed to simulate the ion transport during the dissolution of precursors in an alkaline solution. The evolution of particle distribution function satisfies the following LB equation [168]:

$$f_j(x + e_j \delta t, t + \delta t) = f_j(x, t) - \frac{\delta t}{\tau} [f_j(x, t) - f_j^{eq}(x, t)] + \omega_j \delta t S \quad (7.23)$$

where  $f_j$  and  $f_j^{eq}$  are the non-equilibrium and equilibrium particle distribution function at location  $x$  at time  $t$  and in the direction of the velocity  $j$  (in this study  $j = 0, 1, 2, 3, 4, 5, 6$ ), respectively.  $\tau$  is the relaxation time,  $\delta t$  is the time step,  $e_j$  is the microscopic velocity at location  $x$  at time  $t$  and in velocity direction  $j$ , and  $\omega_j$  is the weighting factor in the velocity direction  $j$ .  $S$  is the source term to consider the influence of dissolution. Without considering the convection term,  $f_j^{eq}$  can be calculated using the following equation, in which  $F$  is the ion concentration in the lattice cell:

$$f_j^{eq}(x, t) = \omega_j F(x, t) \quad (7.24)$$

$$F(x, t) = \sum_{j=0}^6 f_j(x, t) \quad (7.25)$$

Figure 7.6 displays a flowchart of the LB simulation of the dissolution of precursors in alkaline solution. After initialization, the simulation starts from the calculations of  $f_j^{eq}$  for all lattice cells according to Equation 7.24. Then the amount of dissolved precursors in the current LB time step is calculated to obtain the source terms of aqueous ions for each lattice node. After the calculations of  $f_j^{eq}$  and  $S$ , the collision process is followed to calculate the new equilibrium particle distribution function, i.e.  $f_j(x + e_j \delta t, t + \delta t)$ , according to Equation 7.23. Then  $f_j(x + e_j \delta t, t + \delta t)$  streams in each direction of velocity. If the next node in direction of velocity is not permeable<sup>19</sup> then  $f_j(x + e_j \delta t, t + \delta t)$  bounces back. After the streaming process, periodic boundary conditions are applied to calculate the  $f_j(x + e_j \delta t, t + \delta t)$  for the lattice nodes on the boundaries of the simulation box. Finally, ion concentrations are updated according to Equation 7.25. If the current time ( $T$ ) is larger than the target dissolution period ( $T_{target}$ ) or the precursors are completely dissolved, the data is quantified as output and the program ends; otherwise, the calculation moves to the next iteration.

<sup>18</sup> DdQq refers to a lattice structure with  $q$  lattice directions in  $d$  dimensions [166]. The lattice structure defines the path for streaming of distribution function from current cell to the neighboring cell.

<sup>19</sup> Here “permeable” means that ions are able to diffuse through the lattice cell.

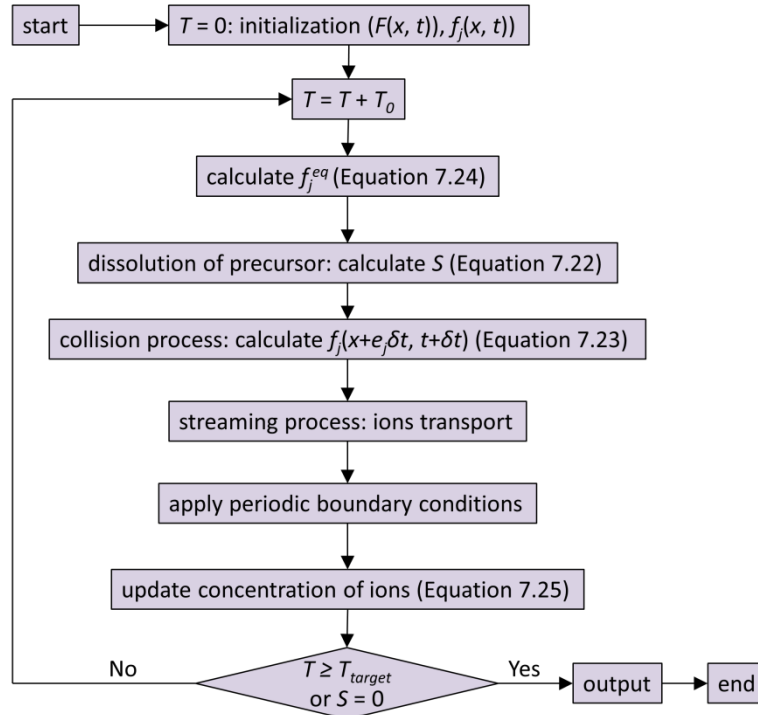


Figure 7.6 A flowchart of LB simulation of the dissolution of precursors in alkaline solution.

Three basic physical units are involved in the ionic transport in porous materials, i.e. length ( $x_p$ ), time ( $t_p$ ) and mass ( $\rho_p$ ), which are different from their corresponding lattice units. For the practical application of LB simulation, conversion is established by dimensional mapping between the lattice units and the real physical units:  $x_l L_0 \rightarrow x_p$  (length),  $t_l T_0 \rightarrow t_p$  (time), and  $\rho_l M_0 \rightarrow \rho_p$  (mass), where  $x_l$ ,  $t_l$ , and  $\rho_l$  are dimensionless lattice units, and  $L_0$ ,  $T_0$ , and  $M_0$  are conversion factors. With these conversion factors ( $L_0$ ,  $T_0$ ,  $M_0$ ), the simulation results can be related to any quantity in the physical system. For example, the time mapping  $T_0$  can be obtained from the ion diffusivity in physical unit, i.e.  $D_p$  ( $\text{m}^2/\text{s}$ ), and the diffusivity in LB unit, i.e.  $D_{LB}$ . From the dimensions of diffusivity in LB simulation, it can be deduced that  $D_p = D_{LB} L_0^2 / T_0$ . In the lattice models, the lattice diffusivity ( $D_{LB}$ ) is related to the relaxation time ( $\tau$ ) and the lattice speed of sound ( $e_s$ ):  $D_{LB} = e_s^2 (\tau - \delta t / 2)$  [169]. The lattice speed of sound is a constant depending on the type of lattice structure. So the time factor ( $T_0$ ) can be calculated as follows:

$$T_0 = \frac{L_0^2 e_s^2 (\tau - \frac{\delta t}{2})}{D_p} \quad (7.26)$$

#### 7.2.4 Dissolution front

The dissolution of precursors starts immediately at the particle surface when it is brought into contact with alkaline solution. In the digitized initial particle parking structure of precursor particles in alkaline solution, the precursor particles are composed of layers of voxels. The dissolution of precursor particles starts from the surface layer of voxels. The solid volume fraction of the dissolving voxel decreases with continuous dissolution. When the solid volume fraction decreases to a critical value, the dissolving voxel is permeable or percolated. Then the aqueous ions have access to the inside layer of voxels that are closest to the surface layer,



initiating the dissolution of the inside layer of voxels. In this way, the dissolution of precursor particles starts from the surface to inside, layer by layer, of voxels until the precursor particle is completely dissolved. The initiation of the dissolution of inside layers of voxels depends on the permeability of the dissolving layer of voxels. It is obvious that the permeability or percolation of a voxel is mainly dependent on the solid volume fraction.

In order to determine the percolation probability of a voxel as a function of its solid volume fraction, numerical simulations on 2D and 3D systems were carried out. Figure 7.7 shows a schematic representation of percolation using a  $10 \times 10$  grid of sites. In the numerical simulation, a number of sites was randomly set as blocked sites and the rest were open sites. Then the percolation of the grid was calculated. For each number of blocked sites, 50 computation experiments were carried out. If the grid was percolated, the counts of percolation was added by one. Then the percolation probability at this number of blocked sites was calculated as the counts of percolation out of 50. For a grid of sites, different numbers of blocked sites were tested. By doing so, the percolation probability was obtained as a function of the fraction of blocked sites. Since the blocked sites represent the solid phase, the percolation probability of a voxel as function of solid volume fraction can be obtained.

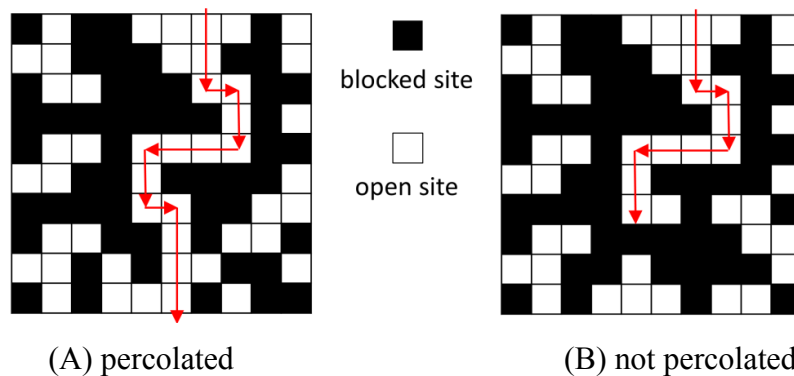
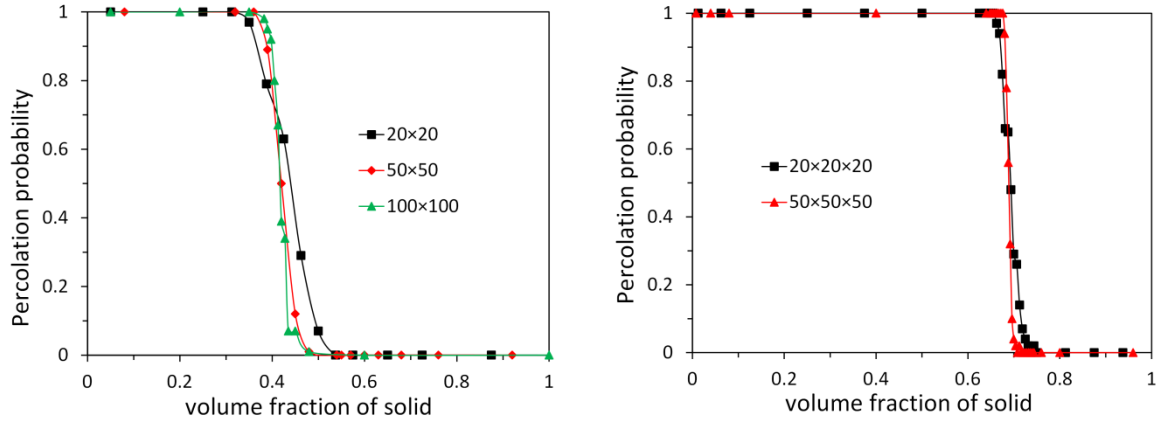


Figure 7.7 Schematic representation of percolation of a pixel.

Figure 7.8 presents the percolation probability of a pixel and a voxel as a function of its solid volume fraction in 2D and 3D, respectively. For a pixel in 2D, a threshold solid volume fraction of 0.42 was found. When the solid volume fraction of a pixel is larger than 0.42, the pixel almost never percolates. When the solid volume fraction is smaller than 0.42, the pixel almost always percolates. This simulation result is consistent with the numerical simulation result in [170]. For a voxel in 3D, a threshold solid volume fraction of 0.688 was found. The threshold solid volume fraction is much larger for a voxel than that for a pixel. This is because a porous material percolates much easier in 3D than in 2D. Compared with the percolation probability of a pixel, the percolation probability of a voxel is much more easily divided into the almost-never-being-percolated-region and the almost-always-being-percolated-region by the threshold solid volume fraction.



(A) percolation probability of a pixel

(B) percolation probability of a voxel

Figure 7.8 Percolation probability of a pixel and a voxel plotted in function of volume fraction of solid.

Figure 7.9 displays the progressing dissolution front as a function of lattice Boltzmann simulation (LBS) step. When the solid volume fraction of a dissolving voxel decreases to a value smaller than the critical solid volume fraction, the dissolving voxel is permeable and the inside voxel that is next to it starts to dissolve.

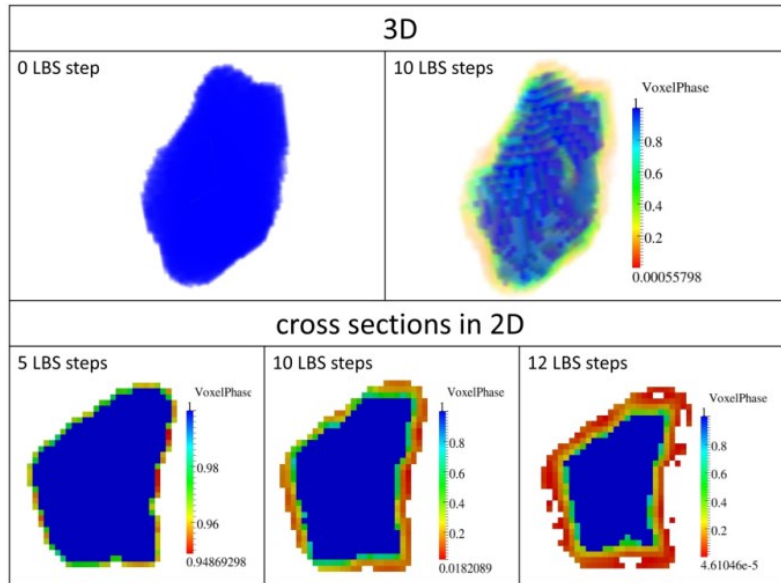


Figure 7.9 Progressing dissolution front as a function of lattice Boltzmann simulation (LBS) step.

### 7.2.5 Influence of temperature

Temperature has a great influence on the diffusion coefficient of aqueous ions and the rate of dissolution. Based on the Arrhenius equation, Equations 7.27 and 7.28 are employed to take into account the influences of temperature on the diffusion coefficient and the rate of dissolution, respectively.

$$D_{new} = D_{ref} \exp \left[ \frac{E_{diff}}{R} \left( \frac{1}{T_{ref}} - \frac{1}{T_{new}} \right) \right] \quad (7.27)$$

$$r_{new} = r_{ref} \exp \left[ \frac{E_a}{R} \left( \frac{1}{T_{ref}} - \frac{1}{T_{new}} \right) \right] \quad (7.28)$$

where  $D_{new}$  and  $D_{ref}$  are the diffusion coefficients at the Kelvin temperatures  $T_{new}$  and  $T_{ref}$ , respectively.  $r_{new}$  and  $r_{ref}$  are the rates of dissolution at the Kelvin temperatures  $T_{new}$  and  $T_{ref}$ , respectively.  $R$  is the gas constant and,  $E_{diff}$  and  $E_a$  are the activation energy of diffusion and activation energy of the dissolving element, respectively.

### 7.3 Three affecting factors

#### 7.3.1 Depression of dissolution rate by aqueous aluminum species

The discussion in Chapter 4 (Section 4.3.2) showed that the initially released aqueous Al species were absorbed to the leached surface layer and slowed down the dissolution of fly ash in the sodium hydroxide activated fly ash system. The depression of the dissolution rate by aqueous Al species has also been reported to occur in the dissolution of aluminosilicate minerals and glasses [22, 25]. According to Bickmore et al. [171], the depression of the dissolution rate of quartz is related to the adsorption of  $\text{Al}(\text{OH})_4^-$  at silanol sites on the surface of quartz. The depression of the dissolution rate of quartz was considered using the following equation:

$$r_{Si,with} = r_{Si,without} (1 - \theta_{Al}) \quad (7.29)$$

where  $r_{Si,with}$  and  $r_{Si,without}$  are the dissolution rates of quartz with and without depression by the adsorption of  $\text{Al}(\text{OH})_4^-$ , respectively.  $\theta_{Al}$  is the fraction of the quartz surface that is passivated.

As described in Section 4.3.2, a leached surface layer is formed on the surface of aluminosilicate particles during the dissolution (see Figure 4.8). This leached surface layer mostly consists of Si. So the aqueous Al species are mainly absorbed at the silanol sites and reduce the dissolution rate of Si in the dissolution of aluminosilicate materials. By introducing Equation 7.29 into Equation 7.6, the inhibiting effect of aqueous Al species on the dissolution rate of Si can be considered as:

$$r_{Si} = r_{+,Si} \left( 1 - \left( \frac{IAP_{Si}}{K_{sp,Si}} \right)^{1/\sigma} \right) (1 - \theta_{Al}) \quad (7.30)$$

where  $\theta_{Al}$  can be obtained using the method proposed by Bickmore et al. [171], but modified to account for the effect of NBO/T, via the following equation:

$$\theta_{Al} = \frac{bC_{Al}}{(1+bC)(1+k \cdot \text{NBO}/T)} \theta_{Al,max} \quad (7.31)$$

where  $C_{Al}$  is the concentration of aqueous Al,  $k$  is a parameter (1.473),  $\theta_{Al,max}$  is the maximum fraction of the surface that can be passivated and  $b$  is a parameter.  $b$  and  $\theta_{Al,max}$  can be calculated as a function of the pH with the following equations. The derivation of these equations and determination of  $k$  are provided in Appendix A.6.

$$b = -2.12 \times 10^3 pH + 3.18 \times 10^4 \quad (7.32)$$

$$\theta_{Al,max} = -0.177 pH + 3.23 \quad (7.33)$$

### 7.3.2 Factor of the solution-volume to precursor-surface-area ratio

Since the dissolution always start from the surface that is accessible for hydroxide ions, the surface area of aluminosilicate material has a large influence on its dissolution rate in alkaline solution. The surface area of particles in the generated particle structure depends on the digitization resolution. The following two equations are used to calculate the element concentration change in experiment and numerical simulation, respectively.

$$\Delta C_{exp} = \frac{r_{+,exp} \cdot S_{exp} \cdot \Delta t}{V_{exp}} \quad (7.34)$$

$$\Delta C_{model} = \frac{r_{+,model} \cdot S_{model} \cdot \Delta t}{V_{model}} \quad (7.35)$$

where  $\Delta C$ ,  $r_{+}$ ,  $S$  and  $V$  represent element concentration change over time  $\Delta t$ , forward dissolution rate, surface area and solution volume, respectively, in experiment and numerical simulation. In order to replicate the experimental results through the numerical simulation, Equation 7.35 must be equal to Equation 7.34. So the following equation can be obtained.

$$r_{+,model} = \frac{V_{model}/S_{model}}{V_{exp}/S_{exp}} r_{+,exp} \quad (7.36)$$

Let  $F_{V-S} = \frac{V_{model}/S_{model}}{V_{exp}/S_{exp}}$ , then the dissolution rate of element X can be obtained as:

$$r'_{+,X} = F_{V-S} \cdot r_{+,X} \quad (7.37)$$

where  $r_{+,X}$  and  $r'_{+,X}$  are the forward dissolution rates of X before and after considering the effect of solution-volume/surface-area ratio.  $X$  represents Si or Ca.

### 7.3.3 Factor of non-steady dissolution

The dissolution of aluminosilicate materials usually first exhibits a non-steady-state dissolution period prior to the steady-state dissolution period [159]. In the non-steady-state period the dissolution shows nonlinear increases of element concentrations. In the steady-state period, by contrast, the dissolution shows a linear increase of element concentrations and the dissolution rate is independent of time. Since the forward dissolution rate of elements are mainly obtained based on the dissolution in the steady-state period, another factor (denoted as  $F_{non-steady}$ ) should be used to account for the non-steady-state dissolution.

The influence of  $F_{non-steady}$  on the dissolution was investigated by a parameter study. In the parameter study, the generated particle structure was digitized at different resolutions. Then the digitized structures were used as the input to simulate the dissolution of slag in sodium hydroxide solution with different alkali concentrations. The dissolution of slag in sodium hydroxide solution in experiments was presented in Appendix A. With the parameter study, the following equations were found for taking into account the factors  $F_{V-S}$  and  $F_{non-steady}$ .

$$\text{Non-steady-state period: } r_{+,X,new} = F_{non-steady} \cdot F_{V-S} \cdot r_{+,X} \quad (7.38)$$

$$\text{Steady-state period: } r_{+,X,new} = F_{V-S} \cdot r_{+,X} \quad (7.39)$$

where  $r_{+,X}$  and  $r_{+,X,new}$  are the dissolution rate of X before and after accounting for the effects of solution-volume/surface-area ratio and non-steady dissolution. X represents Si or Ca. From the amended forward dissolution rate of Si, the forward dissolution rate of Al can be amended using Equation 7.12.

The parameter study reveals that the factor  $F_{non-steady}$  is weakly correlated to the factor  $F_{V-S}$ . Figure 7.10 displays the plot of  $F_{non-steady}$  as a function of  $F_{V-S}$  for the dissolution rates of Si and Ca. In this research  $F_{non-steady}$  was approximated as a function of  $F_{V-S}$  with the following equations:

$$\text{For Si: } F_{non-steady} = 2.88F_{V-S} + 2.89 \quad (7.40)$$

$$\text{For Ca: } F_{non-steady} = 8.81F_{V-S} + 7.26 \quad (7.41)$$

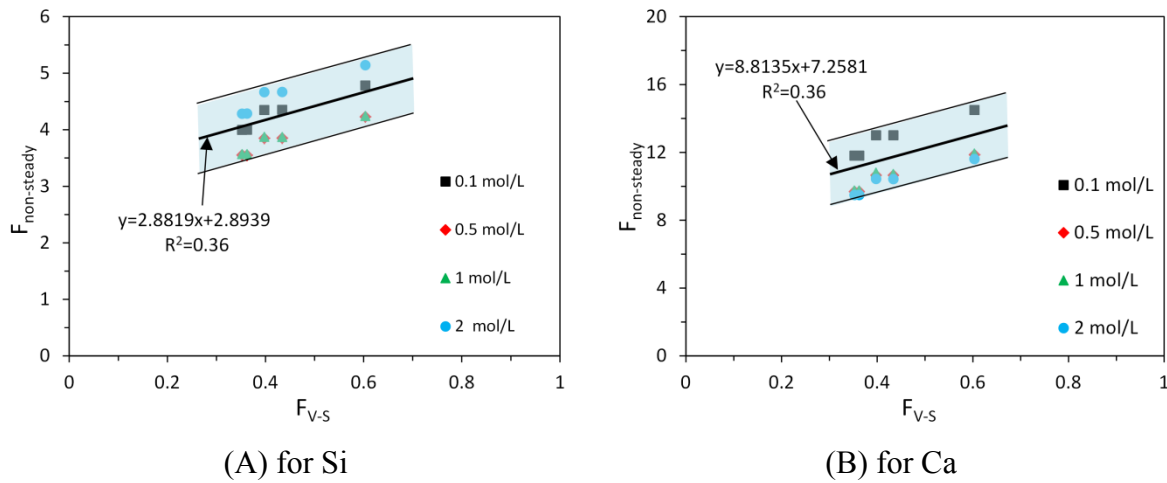


Figure 7.10 Non-steady factor ( $F_{non-steady}$ ) plotted as a function of solution-volume to precursor-surface-area ratio factor ( $F_{V-S}$ ) for the dissolution of slag in sodium hydroxide solution with different alkali concentrations.

## 7.4 Implementation of the numerical model

### 7.4.1 Simulation parameters

The activation energies of Si and Al for dissolution were reported in the ranges of  $7.7 \times 10^4$  to  $8.8 \times 10^4$  J/mol [172] and  $7.6 \times 10^4$  to  $8.3 \times 10^4$  J/mol [173], respectively. In the simulations, the activation energies of Si and Al for dissolution were taken as  $8.3 \times 10^4$  J/mol and  $8.0 \times 10^4$  J/mol, respectively. The activation energy of Ca for dissolution was taken as  $1.36 \times 10^4$  J/mol [174]. According to the reactivity of elements Mg, S, K and Na relative to Ca,  $f_{Mg}$ ,  $f_S$ ,  $f_K$  and  $f_{Na}$  were taken as 1.1, 1.1, 1.2 and 1.2, respectively, in all the simulations. In line with [163], the value of  $\sigma$  was taken as 1 in the model. The solubility products of  $\text{SiO}_2$ ,  $\text{Al}_2\text{O}_3$  and CaO for dissolution are taken as  $1.230 \times 10^2$ , 3.548 and  $3.801 \times 10^4$ , respectively, from the literature [175, 176]. In determination of NBO/T,  $f_{Fe}$  and  $f_{Al}$  were taken as 0.15. The factor  $f_{dissolving-area}$  is taken as 1.1 times of the liquid volume fraction of the voxel. The diffusion coefficients and the activation energy of diffusion of ions are presented in Table 7.1.

Table 7.1 Diffusivities of aqueous ions at 25 °C [177, 178]

Ions	SiO <sub>3</sub> <sup>2-</sup>	AlO <sub>2</sub> <sup>-</sup>	Ca <sup>2+</sup>	Mg <sup>2+</sup>	S <sup>2-</sup>	K <sup>+</sup>	Na <sup>+</sup>	OH <sup>-</sup>
$D_{\text{ref}} (\times 10^{-9} \text{ m}^2/\text{s})$	0.7 <sup>a</sup>	0.6 <sup>b</sup>	0.72	0.71	1.01 <sup>c</sup>	1.96	1.33	5.28
$E_{\text{diff}} (\times 10^4 \text{ J/mol})^{\text{d}}$	2.46	2.04	2.32	1.26	1.43	1.60	1.67	1.80

a. This value was taken from the diffusivity of H<sub>2</sub>SiO<sub>4</sub><sup>2-</sup>;

b. This value was taken from the diffusivity of Al<sup>3+</sup>;

c. This value was taken from the diffusivity of SO<sub>4</sub><sup>2-</sup>;

d. The activation energy of diffusion of aqueous ions were calculated based on [179-181].

## 7.4.2 Simulation of the dissolution of slag in alkaline solution

The dissolution of slag in sodium hydroxide solution with alkali concentrations of 0.1, 0.5 and 1.0 mol/L was simulated using the numerical model presented in this chapter. The ratio of the volume of solution divided by the surface area of slag in the experiment was  $1.996 \times 10^{-2} \text{ m}$ . The chemical composition of slag can be found in Table 3.1. In the simulation,  $4.99 \times 10^{-7} \text{ g}$  of slag was parked in a cube of  $1000 \mu\text{m} \times 1000 \mu\text{m} \times 1000 \mu\text{m}$ . This amount of slag in the cube is equivalent to 0.1 g slag in 200 mL NaOH solution. The generated particle structure of slag in solution was digitized with a resolution of  $2 \mu\text{m} \times 2 \mu\text{m} \times 2 \mu\text{m}$ . The ratio of the volume of solution divided by the surface area of slag in the generated particle structure was  $7.034 \times 10^{-3} \text{ m}$ . In order to take into account the effect of continuous stirring on the dissolution of slag, the ions (Table 7.1) in the liquid nodes were evenly distributed in the solution in each LB step.

Figure 7.11 shows an example of the simulated concentration of Ca in comparison with the experimental results (see Appendix A.2) for the dissolution of slag in sodium hydroxide solutions with alkali concentrations of 0.1, 0.5 and 1.0 mol/L. More simulation results for the concentrations of Si and Al are provided in Appendix A.7 (see Figure A.7). The simulated concentration of Ca was calculated as the average of concentrations of Ca in liquid lattice cells. It can be seen that the simulated concentration of Ca was in good agreement with the experimental results. This indicates that the numerical model presented in this chapter is able to simulate the dissolution of slag in alkaline solution with reasonable accuracy.

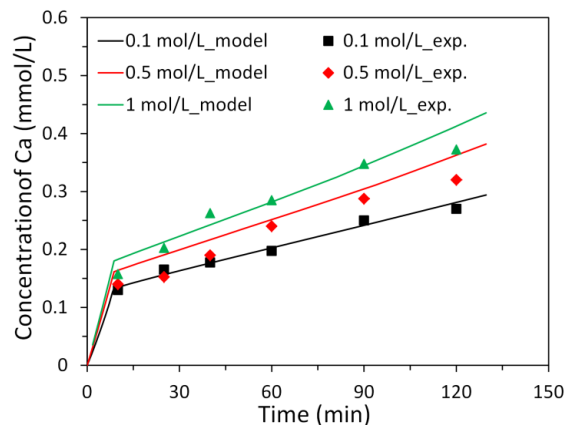


Figure 7.11 Simulated concentration of Ca compared to the experimental results. The experimental results can be found in Appendix A.2.

### 7.4.3 Simulation of the dissolution of fly ash in alkaline solution

As mentioned in the beginning of Section 7.2.2, Snellings studied the dissolution of six types of synthetic glasses in alkaline solution with a pH of 13 [159]. G4 is one of these six types of synthetic glasses, representing the glasses encountered in fly ashes. The dissolution of glass G4 in alkaline solution was simulated using the numerical model presented in this chapter. In the simulation,  $9.98 \times 10^{-7}$  g of G4 was parked in a cube of  $1000 \mu\text{m} \times 1000 \mu\text{m} \times 1000 \mu\text{m}$ . This amount of G4 in the cube is equivalent to a water-to-glass mass ratio of 1000 as used in the experiment. The generated particle structure of glass G4 in solution was then digitized with a resolution of  $2 \mu\text{m} \times 2 \mu\text{m} \times 2 \mu\text{m}$ . The specific surface area of particles in the digitized particle structure was  $0.0397 \text{ m}^2/\text{g}$ , which is slightly lower than the measured value of  $0.044 \text{ m}^2/\text{g}$  by BET [159]. This is mainly because the roughness of G4 particles was not considered in the numerical simulation.

Figure 7.12 shows the simulated concentration of Si in comparison with the experimental results for the dissolution of G4 in solutions with different concentrations of aqueous Al. The simulated concentrations of Ca and Al are presented in Appendix A.7 (see Figure A.8). The trends of the simulated results were consistent with the experimental results. The solution with a *higher* concentration of aqueous Al led to a *lower* concentration of Si for both experimental and simulation results. This shows that the inhibiting effect of aqueous Al on the dissolution of G4 can explicitly be simulated with the numerical model. However, the concentration of Si was not well simulated for the dissolutions at  $[\text{Al}] = 1$  and  $5 \text{ mmol/L}$ , particularly in the non-steady period. It shows that the non-steady factor was overestimated, leading to overestimation of the predicted concentration of Si. This is because the derivation of Equations 7.40 and 7.41 was based on the experimental data of the dissolution of slag in sodium hydroxide solution. The effect of aqueous Al on the non-steady factor was not taken into account. So a further study is needed to investigate the influence of non-steady state factor on the dissolution rate of precursors in alkaline solution with aqueous Al.

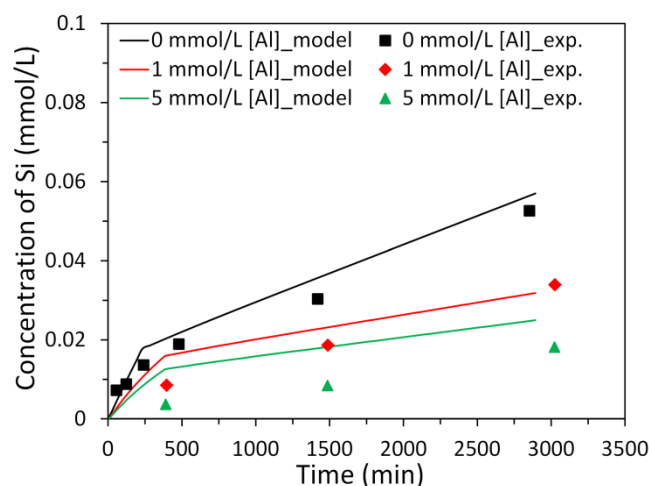


Figure 7.12 Simulated concentration of Si compared to the experimental results for the dissolution of G4 in solutions with different concentrations of aqueous Al. The experimental results can be found in [159].

## 7.5 Conclusions

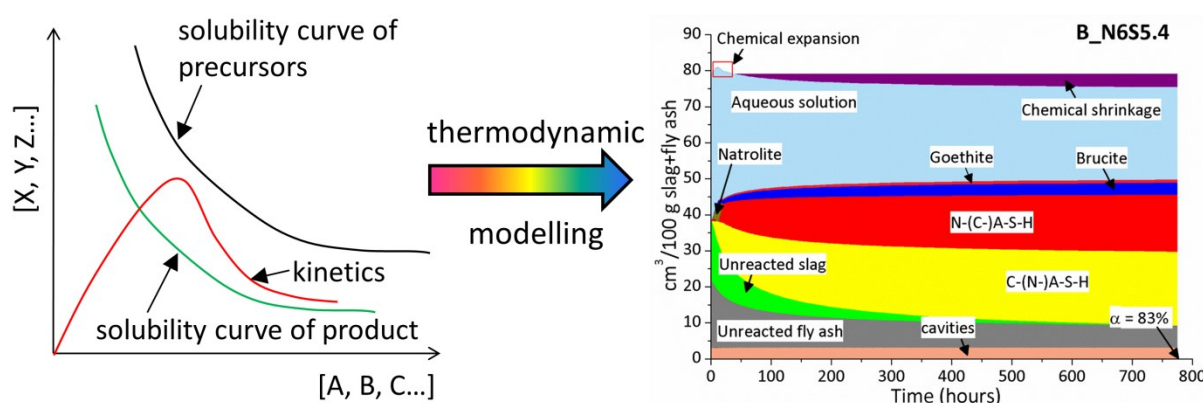
This chapter presented a numerical model to simulate the dissolution of slag and fly ash in alkaline solution. From this chapter, the following conclusions can be drawn:

- (1) For a voxel in 3D, a threshold solid volume fraction of 0.688 was found. Compared with the percolation probability of a pixel in 2D, the percolation probability of a voxel in 3D is much more easily divided into the almost-never-being-percolated-region and the almost-always-being-percolated-region by the threshold solid volume fraction.
- (2) The simulation results were in line with the experimental results. This suggests that the numerical model presented in this chapter is able to simulate the dissolution of slag and fly ash in alkaline solution with reasonable accuracy.



# Chapter 8

## Thermodynamic modelling of the reactions in alkali-activated materials<sup>20</sup>



This chapter presents a thermodynamic modelling investigation of the reactions in alkali-activated materials (AAMs). The thermodynamic database was introduced from the literature for the alkali-activated slag systems. Particularly the thermodynamic database for the alkali-activated fly ash systems is established for the first time in this work. With these thermodynamic databases the thermodynamic modelling of the reactions in alkali-activated slag, alkali-activated fly ash and alkali-activated slag/fly ash was performed.

<sup>20</sup> This chapter is partially based on:

Yibing Zuo, Marija Nedeljkovic, and Guang Ye. Coupled thermodynamic modelling and experimental study of sodium hydroxide activated slag. *Construction and Building Materials*, 188(2018) 262-279.



## 8.2 Methods

### 8.2.1 Thermodynamics, thermodynamic database and thermodynamic modelling

Thermodynamics is of great significance for understanding chemical reactions [14]. The chemical reactions in AAMs, similar to any other chemical system, follow the law of thermodynamics. Figure 8.2 shows a schematic illustration of thermodynamics in AAMs. When aluminosilicate precursors are brought into contact with an alkaline activator, their constituents start to dissolve, leading to an increase of the concentrations of aqueous ions in solution as shown by the red curve (kinetics). When the concentrations of the aqueous ions increase to a certain level, such that the solution is saturated or supersaturated with respect to solid reaction products, these aqueous ions are thermodynamically favored to precipitate and form solid reaction products. Consequently, the concentrations of these aqueous ions start to decrease. Afterwards, two kinds of thermodynamic interactions are present in the system. One thermodynamic interaction is between the precursors and the solution, continuously releasing elements into solution. The other one is between the solution and the solid reaction products, leading to growth of the solid reaction products. These thermodynamic interactions finally reach a thermodynamic equilibrium between the liquid phase and the solid phase. In this process, the precursors are gradually transferred into the solid reaction products.

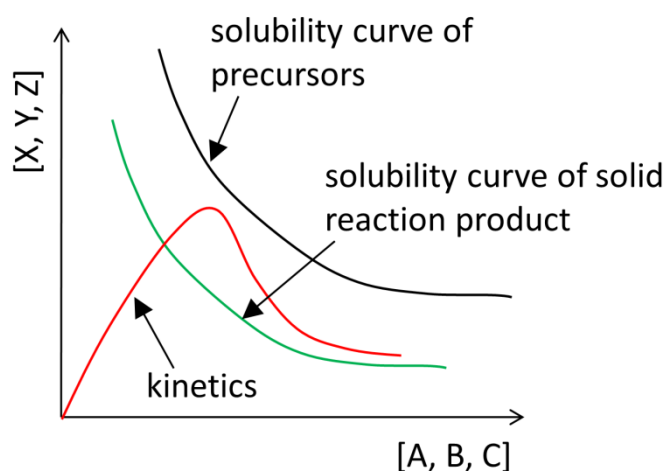


*Figure 8.2 An illustration of thermodynamics in AAMs. In the graph,  $[X, Y, Z]$  and  $[A, B, C]$  represent the concentrations of aqueous ions  $X, Y, Z$  and  $A, B, C$ , respectively.*

The alkali activation conditions and sources of aluminosilicate precursors can be very different. This leads to different types of solid reaction products in AAMs. Given a specific condition, the type of solid reaction products that will precipitate is largely dependent on the thermodynamic data. The thermodynamic data (e.g. enthalpy, entropy and solubility products etc.) of all the solids, aqueous and gaseous species make up the thermodynamic database. With the thermodynamic database, the thermodynamic modelling of chemical reactions can be carried out by using software tools. The quality of the thermodynamic modelling results is directly dependent on the quality and completeness of the thermodynamic database.

### 8.2.2 Thermodynamic models for the C-(N-)A-S-H gel and hydrotalcite-like phase in alkali- activated slag

Myers et al. are the first who proposed a calcium-alkali aluminosilicate hydrate ideal solid solution model (CNASH<sub>ss</sub>) to describe the C-(N-)A-S-H gel in alkali-activated slag systems [69]. The CNASH<sub>ss</sub> model was derived based on the “substituted general model” [71], that is able to account for the incorporation of elements other than Ca, Si, O and H into the structure of C-S-H gel. Figure 8.3 shows the schematic representations of non-crosslinked and crosslinked C-(N-)A-S-H gel structures, while expression 8.1 was derived as the fundamental formulae to represent the chemistry of the C-(N-)A-S-H gel [69]. By substituting six species into the *BCI* sites given in formulae 8.1, a set of eight end-members (see Table 8.1) were selected to define the C-(N-)A-S-H gel. Among these eight end-members, 5CA and INFCA are two C-A-S-H end-members, 5CNA and INFCNA are two C-N-A-S-H end-members, INFCN is a C-N-S-H end-member and, T2C\*, T5C\* and TobH\* are three C-S-H end-members. The thermodynamic properties of these end-members, such as enthalpy and entropy, were estimated through the optimization of the solubility products for their dissociation reactions. Full details of the derivation of the CNASH<sub>ss</sub> thermodynamic model can be found in [69]. The dissociation reactions and solubility products of these end-members are listed in Table 8.1. The thermodynamic properties of these end-members are presented in Appendix B (Table B.1).

$$\frac{[TU^-]_1 \cdot [IW^*]_1 \cdot [BCI^{0.125+}]_2 \cdot [BCI^{0.125+}]_2 \cdot [BCI^{0.125+}]_2 \cdot [BCI^{0.125+}]_2 \cdot [BCI^{0.125+}]_2}{[IW]_1} \quad (8.1)$$

where  $BCI = BT + CB + IC$  as shown in Figure 8.3, and  $IW^*$  represents a fixed interlayer water site. The full details are presented in [69].

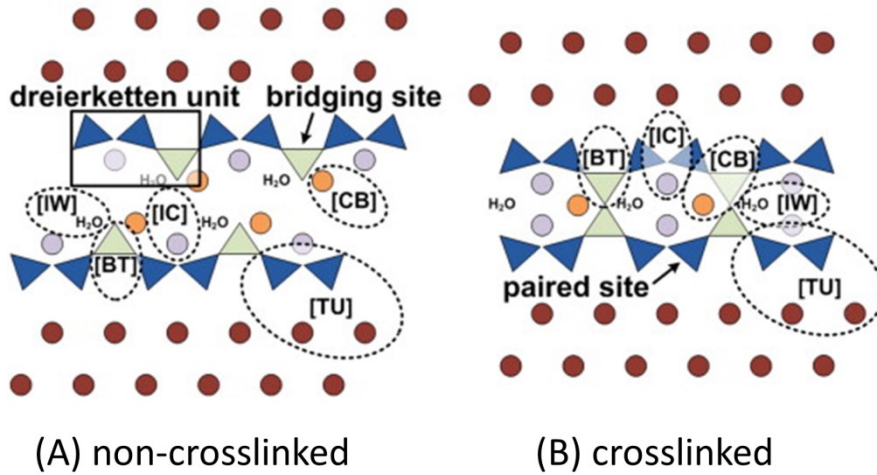


Figure 8.3 Schematic representations of non-crosslinked and crosslinked C-(N-)A-S-H gel structures. In the graph, TU, BT, CB, IC and IW are sublattice sites. Light green and dark blue triangles are bridging and paired tetrahedral sites, respectively. Dark red circles represent Ca sites in the Ca-O sheets. The orange and purple circles represent positively charged species, such as  $Ca^{2+}$ ,  $H^+$ ,  $Na^+$  and  $K^+$ . (cited from [69])

Table 8.1 Chemical reactions and solubility products ( $\log K_{sp}$ ) at 25 °C and 1 bar for C-(N-)A-S-H and hydrotalcite-like phases

Solids	Dissociation reactions	$\log K_{sp}$
<i>CNASH<sub>ss</sub> model</i> [69]		
5CA	$(\text{CaO})_{1.25} \cdot (\text{Al}_2\text{O}_3)_{0.125} \cdot (\text{SiO}_2) \cdot (\text{H}_2\text{O})_{1.625}$ $\leftrightarrow 1.25\text{Ca}^{2+} + \text{SiO}_3^{2-} + 0.25\text{AlO}_2^- + 0.25\text{OH}^- + 1.5\text{H}_2\text{O}$	-10.75
INFCA	$(\text{CaO}) \cdot (\text{Al}_2\text{O}_3)_{0.15625} \cdot (\text{SiO}_2)_{1.1875} \cdot (\text{H}_2\text{O})_{1.65625} + 0.6875\text{OH}^-$ $\leftrightarrow \text{Ca}^{2+} + 1.1875\text{SiO}_3^{2-} + 0.3125\text{AlO}_2^- + 2\text{H}_2\text{O}$	-8.90
5CNA	$(\text{CaO})_{1.25} \cdot (\text{Na}_2\text{O})_{0.25} \cdot (\text{Al}_2\text{O}_3)_{0.125} \cdot (\text{SiO}_2) \cdot (\text{H}_2\text{O})_{1.25}$ $\leftrightarrow 1.25\text{Ca}^{2+} + \text{SiO}_3^{2-} + 0.25\text{AlO}_2^- + 0.5\text{Na}^+ + 0.75\text{OH}^- + \text{H}_2\text{O}$	-10.40
INFCNA	$(\text{CaO}) \cdot (\text{Na}_2\text{O})_{0.34375} \cdot (\text{Al}_2\text{O}_3)_{0.15625} \cdot (\text{SiO}_2)_{1.1875} \cdot (\text{H}_2\text{O})_{1.3}$ $\leftrightarrow \text{Ca}^{2+} + 1.1875\text{SiO}_3^{2-} + 0.3125\text{AlO}_2^- + 0.6875\text{Na}^+ + 1.3125\text{H}_2\text{O}$	-10.00
INFCN	$(\text{CaO}) \cdot (\text{Na}_2\text{O})_{0.3125} \cdot (\text{SiO}_2)_{1.5} \cdot (\text{H}_2\text{O})_{1.1875} + 0.375\text{OH}^-$ $\leftrightarrow \text{Ca}^{2+} + 1.5\text{SiO}_3^{2-} + 0.625\text{Na}^+ + 1.375\text{H}_2\text{O}$	-10.70
T2C*	$(\text{CaO})_{1.5} \cdot (\text{SiO}_2) \cdot (\text{H}_2\text{O})_{2.5} \leftrightarrow 1.5\text{Ca}^{2+} + \text{SiO}_3^{2-} + \text{OH}^- + 2\text{H}_2\text{O}$	-11.60
T5C*	$(\text{CaO})_{1.25} \cdot (\text{SiO}_2)_{1.25} \cdot (\text{H}_2\text{O})_{2.5} \leftrightarrow 1.25\text{Ca}^{2+} + 1.25\text{SiO}_3^{2-} + 2.5\text{H}_2\text{O}$	-10.50
TobH*	$(\text{CaO}) \cdot (\text{SiO}_2)_{1.5} \cdot (\text{H}_2\text{O})_{2.5} + \text{OH}^- \leftrightarrow \text{Ca}^{2+} + 1.5\text{SiO}_3^{2-} + 3\text{H}_2\text{O}$	-7.90
<i>MA-OH-LDH<sub>ss</sub> model</i> [54]		
M <sub>4</sub> AH <sub>10</sub>	$(\text{MgO})_4 \cdot (\text{Al}_2\text{O}_3) \cdot (\text{H}_2\text{O})_{10} \leftrightarrow 4\text{Mg}^{2+} + 2\text{AlO}_2^- + 6\text{OH}^- + 7\text{H}_2\text{O}$	-49.70
M <sub>6</sub> AH <sub>12</sub>	$(\text{MgO})_6 \cdot (\text{Al}_2\text{O}_3) \cdot (\text{H}_2\text{O})_{12} \leftrightarrow 6\text{Mg}^{2+} + 2\text{AlO}_2^- + 10\text{OH}^- + 7\text{H}_2\text{O}$	-72.02
M <sub>8</sub> AH <sub>14</sub>	$(\text{MgO})_8 \cdot (\text{Al}_2\text{O}_3) \cdot (\text{H}_2\text{O})_{14} \leftrightarrow 8\text{Mg}^{2+} + 2\text{AlO}_2^- + 14\text{OH}^- + 7\text{H}_2\text{O}$	-94.34

### 8.2.3 Thermodynamic model for the N-A-S-H gel in alkali-activated fly ash

In this section a thermodynamic model for the N-A-S-H gel is proposed based on its structure and chemical composition. The thermodynamic data of this model are also obtained, such as heat capacity, entropy, Gibbs free energy, enthalpy, solubility product and density.

#### *Structure of the N-A-S-H gel*

The N-A-S-H (or K-A-S-H) gel is a structurally disordered and highly crosslinked aluminosilicate gel [182]. The gel framework mainly consists of Si and Al tetrahedras and the negative charge of Al tetrahedra is charge-balanced by alkalis (typically Na<sup>+</sup> and/or K<sup>+</sup>) as shown in Figure 2.6 in Chapter 2. Because the typical X-ray diffraction (XRD) patterns of the N-A-S-H (or K-A-S-H) gels show a “featureless hump” centered at about 27-29° 2θ [99, 183, 184], they are often described as “X-ray amorphous”. The local structure of this aluminosilicate gel was investigated and compared to leucite<sup>21</sup> using the X-ray atomic pair distribution function technique [186]. A similar local structure was found between the aluminosilicate gel and leucite within a length of 8 Å. Heating samples beyond 1060 °C led to transformation of the aluminosilicate gel into leucite. The effect of temperature on the local structure of aluminosilicate gel was also studied by White et al. using the neutron distribution function technique [60]. The aluminosilicate gel was predominantly converted to leucite by

<sup>21</sup> Leucite is a crystal with a tetragonal structure [185].

heating beyond 1000 °C. The rearrangement of the aluminosilicate gel structure was due to the dehydration and removal of the chemically bound water upon heating [186].

### *Chemical composition of the N-A-S-H gel*

The chemical composition of aluminosilicate gel can be approximated as  $M^+[AlO_2 \cdot nSiO_2]^- \cdot wH_2O$ , where M is a cation such as sodium and potassium. The Si/Al molar ratio, i.e. n, is a variable, depending on the raw materials and curing regime [57, 187]. Winnefeld reported this ratio to range from 3.4 to 4.6 for a sodium silicate activated fly ash [188]. The Si/Al ratio is also found between 1 and 4 for a sodium silicate activated metakaolin [57] and a sodium silicate activated fly ash [189]. It is found that aluminosilicate gels are best formed with Si/Al molar ratio values between 1 and 3 [99] or in the narrower range of 1.5~2 [190]. The water content of aluminosilicate gels have been found to be between 4 and 10 wt.%, which is also dependent on the raw materials and curing regime [191-193]. The ideal Na/Al molar ratio has been reported to be unity [57, 99].

### *Effect of calcium on the N-A-S-H gel*

Garcia-Lodeeiro et al. studied the interactions between the N-A-S-H gels with the aqueous calcium [52]. After adding calcium, FTIR spectra of samples showed no relevant changes in the positions of bands, indicating no significant modification on the gel structure. The chemical composition of the N-A-S-H gels, by contrast, was significantly modified. About 90 % of Na in the gel was replaced by Ca through the ion exchange processes.

### *A thermodynamic model for N-(C-)A-S-H gel: N(C)ASH<sub>ss</sub> model*

According to the structure and chemical composition of the N-A-S-H gel, a N-(C-)A-S-H solid solution model, i.e. N(C)ASH<sub>ss</sub> model, is proposed in this thesis to describe the solubility data for Na<sub>2</sub>O-(CaO)-Al<sub>2</sub>O<sub>3</sub>-SiO<sub>2</sub>-H<sub>2</sub>O systems and low-Ca-alkali-activated materials. The N(C)ASH<sub>ss</sub> model consists of eight solid solution members as listed in Table 8.2. Four Si/Al ratios are selected, i.e.  $n = 1, 2, 3$  and 4. As proposed by Davidovits [99], the Na/Al molar ratio is fixed at unity. This is also consistent with the values reported in [57, 99]. The molar ratio of H<sub>2</sub>O to Al<sub>2</sub>O<sub>3</sub> is fixed at unity. So the water content of these solid solution members can be calculated as between 5.29 and 11.44 wt.%, which is in line with the values in the literature [191-193]. In the following subsections the thermodynamic properties of these solid solution members are obtained. The results are presented in Appendix B (Table B.3).

#### (1) Estimation of the standard heat capacity ( $C_p^0$ ) and entropy ( $S^0$ )

Since the eight solid solution members (Table 8.2) are amorphous analogues to leucite, the standard heat capacity and entropy of these members can be estimated through the additivity method<sup>22</sup> based on the standard heat capacity and entropy of leucite and other structurally-relevant constituents, i.e. amorphous SiO<sub>2</sub>, Ca(OH)<sub>2</sub>, NaOH(s) and H<sub>2</sub>O, using the following equation:

<sup>22</sup> The additivity method is an approach that is used to estimate the thermodynamic properties of a phase from the thermodynamic properties of its constituents [194-196]. It usually has the following form:

$$\Phi^0 = \sum_j n_j \Delta\Phi_j^0 \quad (8.2)$$

where  $\Phi^0$  refers to thermodynamic property,  $n_j$  and  $\Delta\Phi_j^0$  are the number and thermodynamic property of the  $j$ th constituent. The additivity method has high accuracy of estimating the standard heat capacity and entropy if suitable constituents are selected [194].

$$\Phi_{0.5(1-x)Na_2O \cdot 0.5xCaO \cdot 0.5Al_2O_3 \cdot nSiO_2 \cdot H_2O}^0 = \Phi_{NaAlO_2 \cdot 2SiO_2}^0 + (n-2)\Phi_{amorphous SiO_2}^0 + 0.5x\Phi_{Ca(OH)_2}^0 - x\Phi_{NaOH(s)}^0 + \Phi_{H_2O}^0 \quad (8.3)$$

where  $\Phi^0$  denotes the standard heat capacity ( $C_p^0$ ) or entropy ( $S^0$ ).  $x$  represents the fraction of Na that is replaced by Ca through ion exchange processes and  $n$  is the Si/Al molar ratio. In this study,  $x = 0$  and  $0.9$ , i.e. 90% of substitution of Na by Ca.  $NaAlO_2 \cdot 2SiO_2$  is leucite with standard heat capacity and entropy of  $163.41 \text{ J/(mol}\cdot\text{K)}$  and  $165.74 \text{ J/(mol}\cdot\text{K)}$ , respectively [197]. The thermodynamic properties of amorphous  $SiO_2$ ,  $Ca(OH)_2$ ,  $NaOH(s)$  and  $H_2O$  can be found in Appendix B (Table B.2).

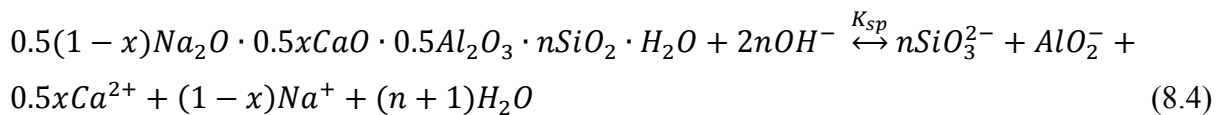
Table 8.2 Chemical reactions and solubility products ( $\log K_{sp}$ ) at  $25^\circ\text{C}$  and 1 bar for N-(C-)A-S-H

Solids	Dissociation reactions	$\log K_{sp}$
NASH_1-1 <sup>a</sup>	$(Na_2O)_{0.5} \cdot (Al_2O_3)_{0.5} \cdot (SiO_2)_1 \cdot (H_2O)_1 + 2OH^-$ $\leftrightarrow SiO_3^{2-} + AlO_2^- + Na^+ + 2H_2O$	-6.51
NASH_2-1	$(Na_2O)_{0.5} \cdot (Al_2O_3)_{0.5} \cdot (SiO_2)_2 \cdot (H_2O)_1 + 4OH^-$ $\leftrightarrow 2SiO_3^{2-} + AlO_2^- + Na^+ + 3H_2O$	-8.01
NASH_3-1	$(Na_2O)_{0.5} \cdot (Al_2O_3)_{0.5} \cdot (SiO_2)_3 \cdot (H_2O)_1 + 6OH^-$ $\leftrightarrow 3SiO_3^{2-} + AlO_2^- + Na^+ + 4H_2O$	-9.51
NASH_4-1	$(Na_2O)_{0.5} \cdot (Al_2O_3)_{0.5} \cdot (SiO_2)_4 \cdot (H_2O)_1 + 8OH^-$ $\leftrightarrow 4SiO_3^{2-} + AlO_2^- + Na^+ + 5H_2O$	-11.01
NCASH_1-0.1	$(Na_2O)_{0.05} \cdot (CaO)_{0.45} \cdot (Al_2O_3)_{0.5} \cdot (SiO_2)_1 \cdot (H_2O)_1 + 2OH^-$ $\leftrightarrow SiO_3^{2-} + AlO_2^- + 0.45Ca^{2+} + 0.1Na^+ + 2H_2O$	-8.51
NCASH_2-0.1	$(Na_2O)_{0.05} \cdot (CaO)_{0.45} \cdot (Al_2O_3)_{0.5} \cdot (SiO_2)_2 \cdot (H_2O)_1 + 4OH^-$ $\leftrightarrow 2SiO_3^{2-} + AlO_2^- + 0.45Ca^{2+} + 0.1Na^+ + 3H_2O$	-10.01
NCASH_3-0.1	$(Na_2O)_{0.05} \cdot (CaO)_{0.45} \cdot (Al_2O_3)_{0.5} \cdot (SiO_2)_3 \cdot (H_2O)_1 + 6OH^-$ $\leftrightarrow 3SiO_3^{2-} + AlO_2^- + 0.45Ca^{2+} + 0.1Na^+ + 4H_2O$	-11.51
NCASH_4-0.1	$(Na_2O)_{0.05} \cdot (CaO)_{0.45} \cdot (Al_2O_3)_{0.5} \cdot (SiO_2)_4 \cdot (H_2O)_1 + 8OH^-$ $\leftrightarrow 4SiO_3^{2-} + AlO_2^- + 0.45Ca^{2+} + 0.1Na^+ + 5H_2O$	-13.01

a. The first and second number after N(C)ASH represent the molar ratio of Si/Al and Na/Al in the solid solution member, respectively.

## (2) Estimation of the standard molar Gibbs free energy ( $\Delta_f G^0$ ) and enthalpy ( $\Delta_f H^0$ )

The dissociation reactions of the N-(C-)A-S-H solid solution members are represented by Equation 8.4.



where  $K_{sp}$  is the solubility product. The dissociation reactions and solubility products are listed in Table 8.2. The solubility products were determined by optimizing the fit of the thermodynamic model to the solubility data in this work and the solid phase chemistry data in the literature [58]. The ReacDC module in the GEM-Selektor was used to determine the standard molar Gibbs free energy and enthalpy of formation of the N-(C-)A-S-H members by

specifying the solubility products for the reaction shown in Equation 8.4, and the values of standard heat capacity ( $C_p^0$ ) and entropy ( $S^0$ ). The GEM-Selektor will be introduced in Section 8.2.5.

### (3) Determination of the standard molar volume

The standard molar volumes of the N(C)ASH<sub>ss</sub> members were determined from density calculations using the method by Thomas et al. [198], with the following equation:

$$\rho_{N(C)ASH}^{sc} = N_A \cdot \rho'_{N(C)ASH} \cdot \left[ \frac{\left(\frac{Na_2O}{SiO_2}\right) \cdot b_{Na_2O}^{sc} + \left(\frac{CaO}{SiO_2}\right) \cdot b_{CaO}^{sc} + \left(\frac{Al_2O_3}{SiO_2}\right) \cdot b_{Al_2O_3}^{sc} + b_{SiO_2}^{sc} + \left(\frac{H_2O}{SiO_2}\right) \cdot b_{H_2O}^{sc}}{MW_{N(C)ASH}} \right] \quad (8.5)$$

where  $\rho_{N(C)ASH}^{sc}$  and  $\rho'_{N(C)ASH}$  are the scattering length density and the predicted density of a N-(C-)A-S-H solid solution member, respectively. The scattering length density is taken as  $3.4 \times 10^{-14} \text{ m}^{-2}$  [199].  $N_A$  is Avogadro's number ( $6.02 \times 10^{23}$ ).  $b^{sc}$  are the neutron scattering lengths for  $Na_2O$ ,  $CaO$ ,  $Al_2O_3$ ,  $SiO_2$  and  $H_2O$ .  $MW_{N(C)ASH}$  is the molecular weight of a N-(C-)A-S-H solid solution member. The  $Na_2O/SiO_2$ ,  $CaO/SiO_2$ ,  $Al_2O_3/SiO_2$  and  $H_2O/SiO_2$  ratios are the molar composition ratios of a N-(C-)A-S-H solid solution member.

### 8.2.4 Other solid phases

As discussed in Chapter 2 (Section 2.2.3), some crystalline reaction products are also formed in AAMs besides the primary reaction products, i.e. the C-(N-)A-S-H gel and the N-A-S-H gel. The following subsections present the crystalline phases that will be included in the thermodynamic modelling of the reactions in alkali-activated slag systems and alkali-activated fly ash systems.

#### *For alkali-activated slag systems*

In the thermodynamic modelling by Myers et al. [54, 69], Fe was not considered due to its very low content in slag. Sulfur was represented as  $S^{2-}$ . According to Wolthers et al. [200], disordered mackinawite is the first iron sulfide to form in most ambient environments, and with time it reacts to form more stable iron sulfide phases such as ordered mackinawite ( $FeS$ ) and ultimately pyrite or pyrrhotite. It has been reported that mackinawite is more stable in the alkali-activated slag system than other phases like Fe-ettringite or microcrystalline  $Fe(OH)_3$  [94]. In this work, mackinawite is included to consider the reactions between aqueous  $Fe^{2+}$  and  $S^{2-}$  under ambient conditions.

Myers et al. [54] found that the solubility products of hydrotalcite reported in [201] and used in [175] are not consistent with the solubility data reported in [202]. In order to deal with this inconsistency a thermodynamic model, named MA-OH-LDH<sub>ss</sub>, was proposed to describe the hydrotalcite-like phase [54]. The MA-OH-LDH<sub>ss</sub> model is an ideal solid solution thermodynamic model, consisting of three solid phases ( $M_4AH_{10}$ ,  $M_6AH_{12}$  and  $M_8AH_{14}$ ). The dissociation reactions and solubility products of these three solids are presented in Table 8.1. The thermodynamic properties of these three solids are presented in Appendix B (Table B.1).

Besides mackinawite and the hydrotalcite-like phase, crystalline phases such as portlandite ( $CH$ ), katoite ( $C_3AH_6$ ), natrolite ( $NAS_3H_2$ ) and stratlingite ( $C_2ASH_8$ ) are also considered in the thermodynamic modelling of the reactions in alkali-activated slag systems. Thermodynamic properties of these phases are provided in Appendix B (Table B.5).



### *For alkali-activated fly ash systems*

In addition to the N-A-S-H gel, zeolites such as zeolite A ( $\text{NAS}_2\text{H}_5$ ), zeolite X ( $\text{NAS}_{2.5}\text{H}_{6.2}$ ), zeolite Y ( $\text{NAS}_4\text{H}_8$ ), zeolite P ( $\text{N}_3\text{A}_3\text{S}_{14}\text{H}_{15}$ ), Na-chabazite ( $\text{NAS}_4\text{H}_6$ ), hydroxysodalite ( $\text{N}_4\text{A}_3\text{S}_6\text{H}_3$ ), Na-analcime ( $\text{N}_{0.16}\text{A}_{0.16}\text{S}_{0.68}\text{H}_{0.333}$ ), Ca-chabazite ( $\text{C}_{0.111}\text{A}_{0.111}\text{S}_{0.778}\text{H}_{0.667}$ ), CaNa-heulandite ( $\text{C}_{0.111}\text{N}_{0.014}\text{A}_{0.125}\text{S}_{0.75}\text{H}_{0.667}$ ) and basic-sodalite ( $\text{N}_{0.325}\text{A}_{0.25}\text{S}_{0.5}\text{H}_{0.345}$ ), can also be formed in alkali-activated fly ash systems. Thermodynamic properties of these zeolites and the references are listed in Appendix B (Table B.5).

### **8.2.5 Modelling approach**

Thermodynamic simulation was carried out using GEM-Selektor V3 (<http://gems.web.psi.ch/>) [19, 20]. GEM-Selektor V3 is a widely used software tool for performing thermodynamic calculations [20, 54, 69, 70, 94, 175, 203, 204]. The CEMDATA07 thermodynamic database was used as the basis thermodynamic database [204]. This database contains thermodynamic data for various solid phases and aqueous species found in cement system. The detailed thermodynamic data of these solid phases and aqueous species can be found in [204]. The thermodynamic models for the C-(N-)A-S-H gel, N-A-S-H gel and hydrotalcite-like phase, and the thermodynamic data for zeolite phases are added to the basis thermodynamic database for thermodynamic modelling of the reactions in AAMs. The thermodynamic data for solids other than 25 °C are derived from the data at the reference temperature (25 °C). More details of the derivation can be found in [205]. In thermodynamic modelling, congruent dissolution of glass phases in aluminosilicate precursors was assumed.

As it is directly encoded in GEM-Selektor, the extended Debye-Huckel equation is used to calculate the ion activity coefficients [19, 20].

$$\text{Log}_{10}\gamma_j = \frac{-A_\gamma z_j^2 \sqrt{I}}{1 + \bar{a} B_\gamma \sqrt{I}} + b_\gamma I + \text{log}_{10} \frac{x_{jw}}{X_w} \quad (8.6)$$

where  $\gamma_j$  and  $z_j$  are the activity coefficient and charge of the aqueous species  $j$ , respectively.  $A_\gamma$  and  $B_\gamma$  are electrostatic parameters,  $I$  is the ionic strength of the aqueous electrolyte phase,  $x_{jw}$  is the mole quantity of water and  $X_w$  is the total mole amount of the aqueous phase.  $\bar{a}$  and  $b_\gamma$  are the average ion size and the parameter for common short-range interactions of the charged species.

The extended Debye-Huckel equation is accurate at moderate ionic strengths (up to ~1-2 molal) [206], which is lower than the ionic strength in the pore solutions of AAMs (~1-3 molal in sodium silicate activated slag [34]). The Pitzer model can be used to calculate the ion activity coefficients in solutions with high ionic strengths [207]. However, it is limited in the current version of GEM-Selektor. This is because the description of aqueous silicate species in the database of GEM-Selektor does not extend beyond dimeric silicate and aluminosilicate units [69]. On the other hand, the GEM-Selektor has been commonly used in thermodynamic modelling of the reactions in alkali-activated slag, and the simulation results agreed well with the experimental data [54, 70, 203]. Therefore, slight excess of ionic strengths (> 2 molal) would not impose a serious impact on the simulation results.

### **8.3 Thermodynamic modelling of the reactions in alkali-activated slag**

With the quantified reaction kinetics as a function of time in Chapter 4, the reaction of slag with different alkaline activators was thermodynamically simulated in a time domain. Figure

8.4 presents the simulated solid phase evolution of alkali-activated slag paste as a function of time. For all samples, the C-(N-)A-S-H gel was formed as the primary reaction product. Hydrotalcite-like phases (MA-OH-LDH), katoite ( $C_3AH_6$ ) and mackinawite (FeS) were formed in both sodium hydroxide activated slag and sodium silicate activated slag. Compared with the sodium hydroxide activated slag (Figures 8.4(A) and 8.4(B)), more crystalline phases were formed in sodium silicate activated slag (Figure 8.4(C)), such as stratlingite ( $C_2ASH_8$ ), brucite (MH) and natrolite ( $NAS_3H_2$ ). Figure 8.4(C) shows a more katoite and less stratlingite than the thermodynamic modelling results by Myers et al. [54] (a similar mixture composition was used). The reason is due to the different chemical composition of slag, particularly the MgO content (9.23 % in this work and 5.3 % in the literature). The comparison between the sample BFS\_N4S0 and the sample BFS\_N6S0 shows that an increase of  $Na_2O$  content did not influence the type and volume of solid phases in sodium hydroxide activated slag very much. As shown in the graphs, chemical shrinkage was predicted to increase as a function of reaction time for all alkali-activated slag samples. It is noted that chemical expansion occurred in the sodium silicate sample (Figure 8.4(C)) at the early age ( $\sim 1$  day). This is because of the formation of zeolite natrolite that has a porous structure.

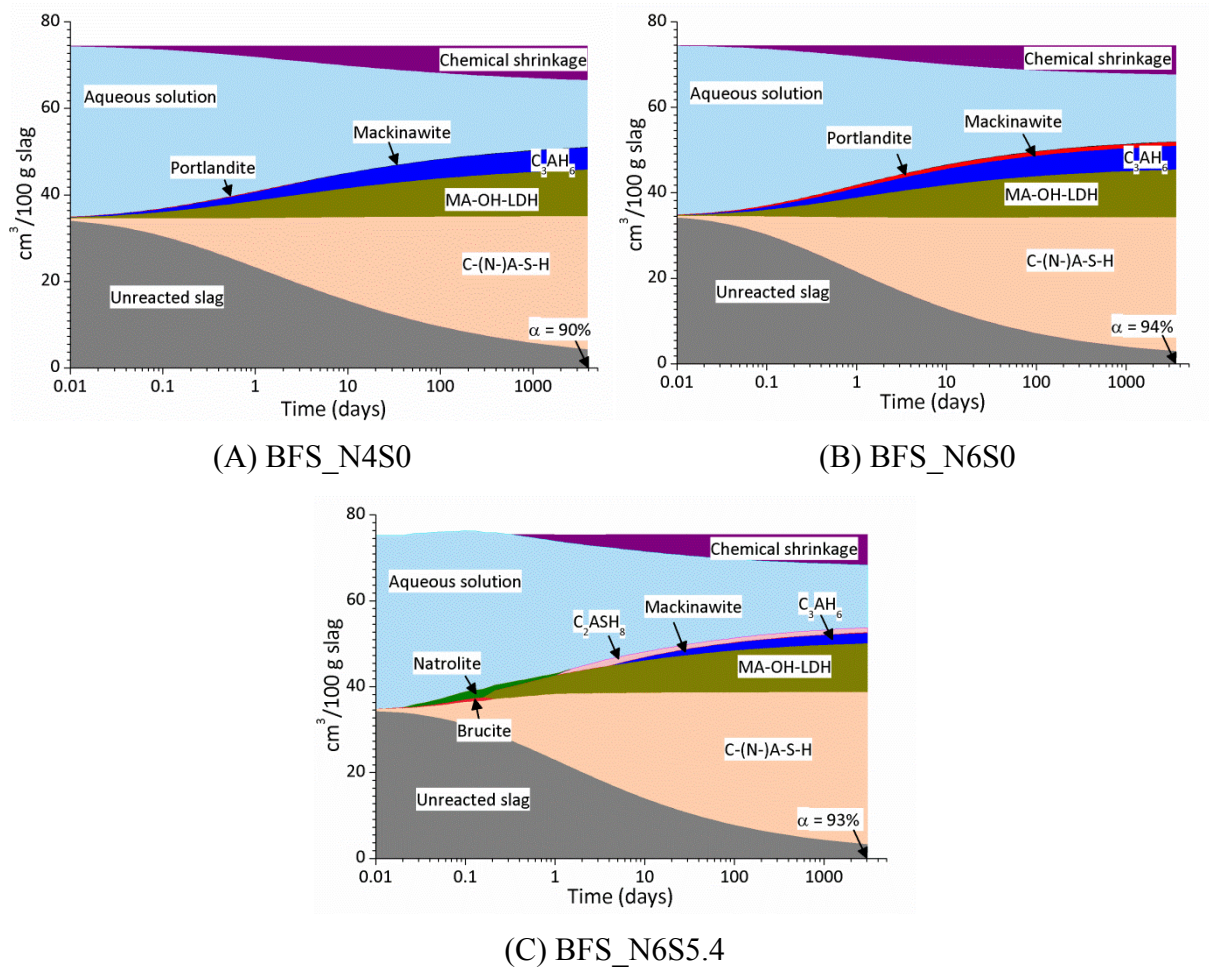


Figure 8.4 Thermodynamically simulated solid phase evolution of alkali-activated slag. In notations, BFS refers to alkali-activated slag, N and S represent the weight percentages of  $Na_2O$  and  $SiO_2$  with respect to slag. See more details of the mixtures in Table 3.2. The quantified reaction kinetics as a function of time was presented in Chapter 4.

Figure 8.5 displays the simulated element concentrations in comparison with the experimental results (presented in Chapter 3). The simulated concentrations of Na, OH<sup>-</sup> and Al were in good agreement with the measured data. In contrast the simulated concentrations of Si and Ca were smaller than the experimental results. This discrepancy between the simulation and experimental results will be explained below.

In thermodynamic modelling, thermodynamic equilibria are assumed between the aqueous ions in the aqueous solution and the solid reaction products. However, the pore solution of sodium hydroxide activated slag is actually oversaturated with respect to solid reaction products with time [33]. In the pore solution, the aqueous ions are presumed to be divided into two parts. The first part consists of the aqueous ions that are in thermodynamic equilibrium with the solid reaction products. The second part consists of the aqueous ions that result in oversaturation with respect to the solid reaction products. The assumption of thermodynamic equilibria in thermodynamic modelling causes the second part of aqueous ions to be completely consumed by reactions to form solid reaction products and only leaves the first part of aqueous ions in the solution. As a result, the results of thermodynamic modelling underestimate the element concentrations in the aqueous solution. Because C-(N-)A-S-H is the primary reaction product and it mainly consists of Si and Ca, the underestimation by thermodynamic modelling is strongly reflected on the concentrations of Si and Ca.

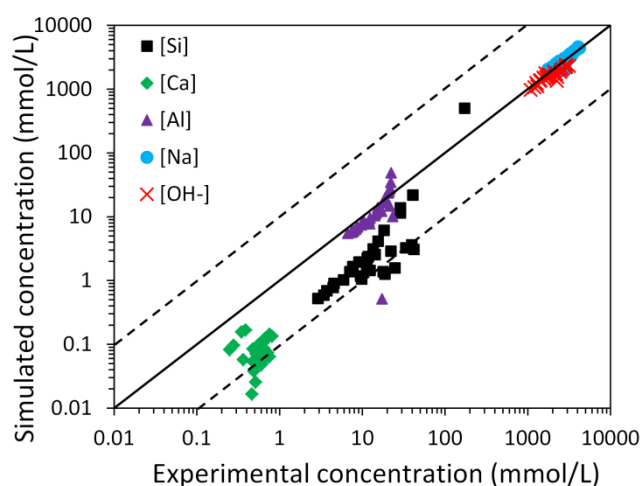


Figure 8.5 Simulated element concentration in comparison with the experimental results. The simulated data were obtained through thermodynamic modelling and the experimental results have been presented in Chapter 3.

## 8.4 Thermodynamic modelling of the reactions in alkali-activated fly ash

### 8.4.1 Element composition of the N-A-S-H gel

Fernández-Jiménez et al. studied the alkaline activation of three class F fly ashes with an 8 mol/L NaOH solution and cured at 85 °C [58]. These three fly ashes were denoted as FAP, FAL and FAM. The Si/Al ratio of the reactive SiO<sub>2</sub> and Al<sub>2</sub>O<sub>3</sub> in fly ash was 2.12, 1.60 and 3.04 for FAP, FAL and FAM, respectively. It was found that a N-A-S-H gel with a low Si/Al ratio was formed at the early curing time (2-5 hours). When the curing time increased (7 days) the gel changed into a more stable phase with a high Si/Al ratio.

The experimental results from the literature [58] were used to validate the thermodynamic model N(C)ASH<sub>ss</sub>. Figure 8.6 displays the simulated Si/Al ratio in the N-A-S-H gel as a function of the degree of reaction of fly ash. The experimental results by NMR and EDS are also shown in the graph. The relatively low Si/Al ratio measured for FAM resulted from the low content of reactive Al<sub>2</sub>O<sub>3</sub> in FAM, which slowed down the rate of reaction and thus retarded the incorporation of Si into the gel [58]. In thermodynamic modelling congruent dissolution of glass was assumed. The retardation of kinetics by low content of reactive Al<sub>2</sub>O<sub>3</sub> was not taken into account. So the simulated Si/Al ratio for FAM was larger than the measured one. Figure 8.6 shows that a higher degree of reaction of fly ash, i.e. a longer curing time, led to a larger Si/Al ratio in the N-A-S-H gel. This simulation result is in good agreement with the experimental result. The Si/Al ratio in the N-A-S-H gel increases with the degree of reaction of fly ash.

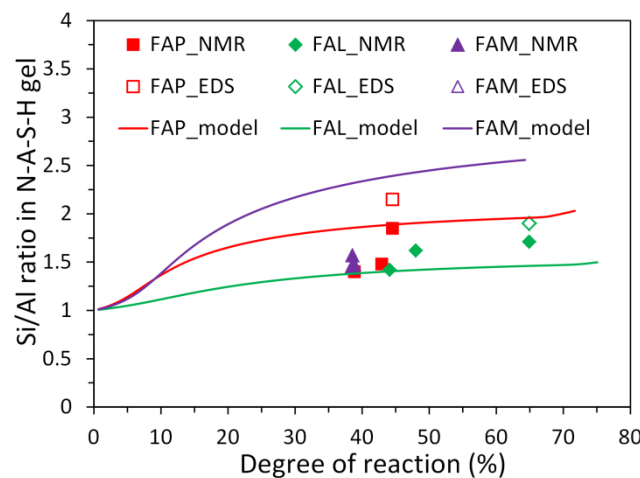


Figure 8.6 Si/Al ratio in N-A-S-H gel. FAP, FAL and FAM represent fly ash types of P, L and M, respectively. More information on these fly ashes and the experimental data can be found in [58].

The Si/Al ratio in N-A-S-H gel at complete reaction of reactive phases in fly ash was 1.99, 1.46 and 2.14 for FAP, FAL and FAM, respectively. The Si/Al ratio of the final N-A-S-H gel increased with the increase of the Si/Al ratio of the reactive phase in fly ash. This is in line with the experimental observation that an increase of the Si/Al ratio in the starting solution would lead to an increase of the Si/Al ratio in the synthetic N-A-S-H gel [208]. Therefore the Si/Al ratio of the reactive phase in fly ash exhibits a large influence on the element composition of the final N-A-S-H gel formed.

#### 8.4.2 Aqueous phase composition of alkali-activated fly ash

With the quantified reaction kinetics in Chapter 4, the reactions in samples FA\_N6.2S0T60, FA\_N9.3S0T60 and FA\_N9.3S9T60 were thermodynamically simulated in a time domain. The simulated concentrations of major elements are presented in comparison with the experimental results in Figure 8.7. The experimental data can be found in Chapter 3. The simulated concentrations of Na and OH<sup>-</sup> decreased with reaction time, in agreement with the experimental results. This phenomenon was also found for the concentration of Si by simulation and experiment for sample FA\_N9.3S9T60. For samples FA\_N6.2S0T60 and FA\_N9.3S0T60, by contrast, the simulated concentration of Si firstly increased and then

decreased with reaction time. This was not observed from the experimental results because the experimental data at the early curing time (first several hours) were not obtained. At the early curing time the alkali-activated fly ash paste was still in a fluid state. This made it infeasible to collect the pore solution using the steel-die method (see more information in Chapter 3). For this reason the maximum concentration of Si was not obtained and thus the increase of the concentration of Si was not observed from the experiment.

The simulated concentrations of Si, Na, Ca and  $\text{OH}^-$  matched the experimental results within  $\pm 1$  order of magnitude. This discrepancy is close to the uncertainty of experimental data [69]. However, the simulated concentration of Al was underestimated by several orders of magnitude. This may be due to the insufficient aqueous phase composition data for optimizing the solubility products of the  $\text{N(C)ASH}_{ss}$  solid solution members. More experimental data would be needed for improving the quality of the thermodynamic data.

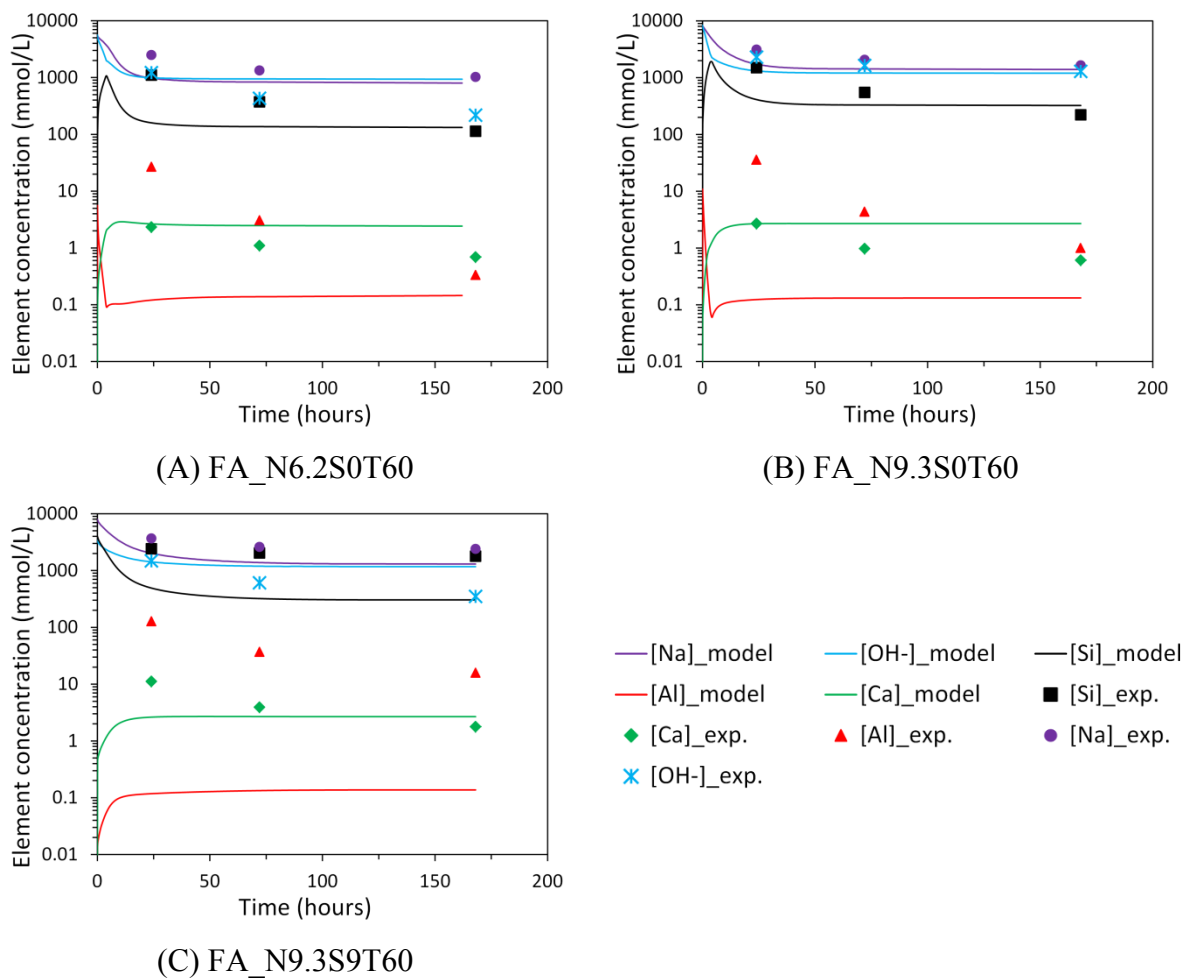


Figure 8.7 Simulated aqueous phase composition of alkali-activated fly ash. The experimental data can be found in Chapter 3. In notations, FA refers to alkali-activated fly ash, N and S represent the weight percentages of  $\text{Na}_2\text{O}$  and  $\text{SiO}_2$  with respect to fly ash, and T represents curing temperature in Celsius. See more details of the mixtures in Table 3.2.

#### 8.4.3 Simulated solid phase evolution of alkali-activated fly ash

Figure 8.8 shows the simulated solid phase evolution of alkali-activated fly ash for samples FA\_N6.2S0T60, FA\_N9.3S0T60 and FA\_N9.3S9T60. The N-(C)-A-S-H gel, natrolite,



goethite, portlandite and brucite were predicted to be formed in alkali-activated fly ash. With increase of the content of  $\text{Na}_2\text{O}$  in the alkaline activator, i.e. from 6.2 % to 9.3 %, the volume of the N-(C-)A-S-H gel decreased while the volume of zeolite natrolite increased. Comparing the sample FA\_N9.3S9T60 with the sample FA\_N9.3S0T60, the addition of  $\text{SiO}_2$  led to an increase of the volume of the N-(C-)A-S-H gel, while a decrease of the volume of natrolite. These simulation results are in line with the experimental results in the literature [37]. A higher alkalinity of the alkaline activator promotes polymerization and densification of the N-(C-)A-S-H gels, decreasing the volume of the N-(C-)A-S-H gel. An increase of  $\text{SiO}_2$  content in alkaline activator, by contrast, promotes the formation of the N-(C-)A-S-H gel.

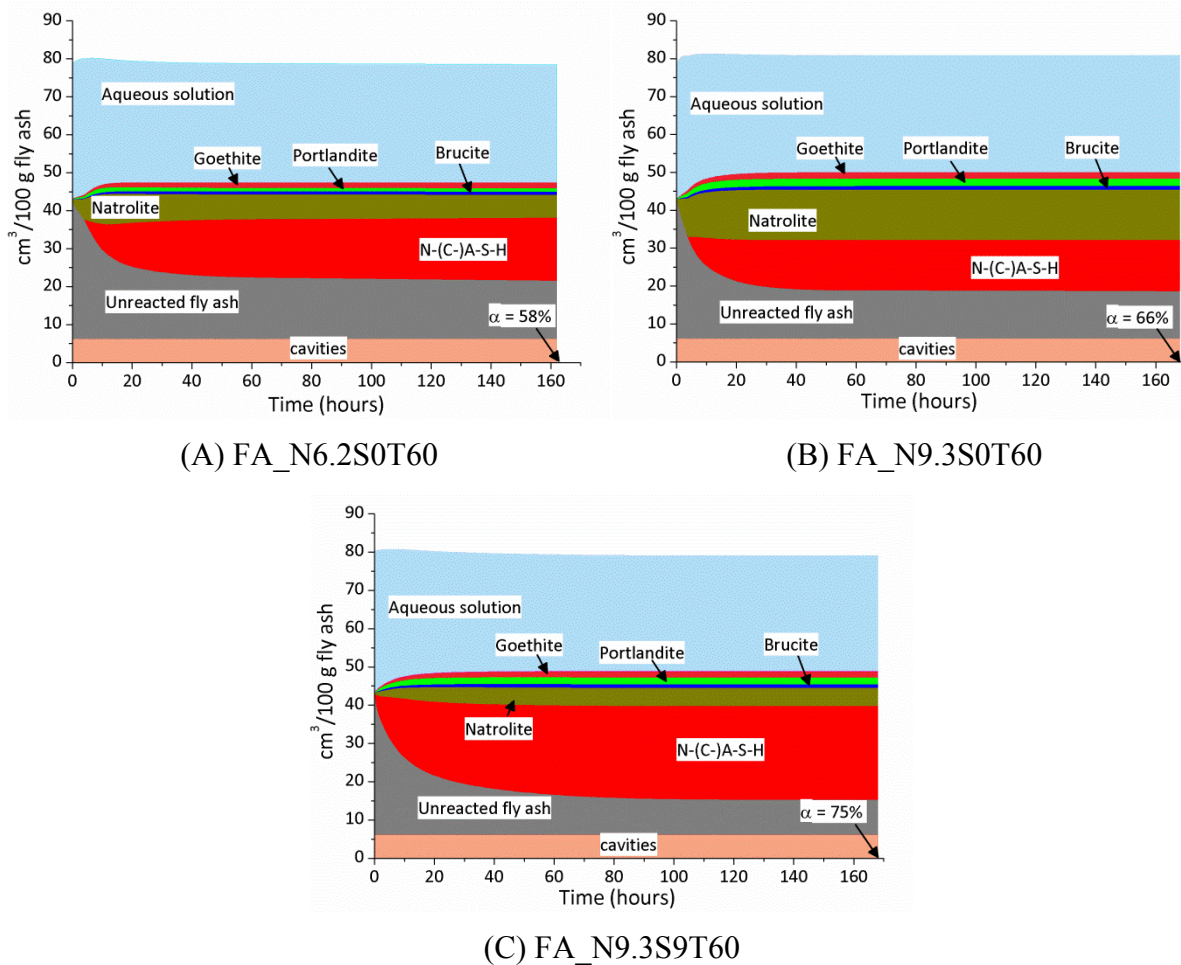


**Figure 8.8** Simulated solid phase evolution of alkali-activated fly ash. In the notations, FA refers to alkali-activated fly ash, N and S represent the weight percentages of  $\text{Na}_2\text{O}$  and  $\text{SiO}_2$  with respect to fly ash, and T represents curing temperature in Celsius. See more details of the mixtures in Table 3.2.

The minor phases, such as portlandite, goethite and brucite, did not show much variation over the different samples. It is noted that these crystals, however, have not been observed through experimental techniques in alkali-activated fly ash pastes. This discrepancy may result from the limitation of the model and the very small amount of those phases that makes it not easy to identify through experimental techniques. Different from the alkali-activated slag systems, alkali-activated fly ash systems did not exhibit significant chemical shrinkage. In contrast chemical expansion was predicted at the early reaction time in the alkali-activated fly ash system. This is because of the formation of zeolite natrolite and a relatively low content of chemically bound water in N-(C-)A-S-H gels. Natrolite has a relatively low density

(2.375 g/cm<sup>3</sup>) [209]. The water content of the N-(C-)A-S-H solid solution members is between 5.29 and 11.44 % for the N-A-S-H gel in alkali-activated fly ash. This is much smaller than the water content of the C-(N-)A-S-H solid solution members (12.56 – 23.81 %) for the C-(N-)A-S-H gel in alkali-activated slag.

## 8.5 Thermodynamic modelling of the reactions in alkali-activated slag/fly ash

By combining the thermodynamic databases for alkali-activated slag and alkali-activated fly ash, the reactions in alkali-activated slag/fly ash can be thermodynamically simulated. Figure 8.9 displays the simulated solid phase evolution of alkali-activated slag/fly ash (B\_N6S5.4 with slag/fly ash = 1, see more details in Table 3.2). Since 29 % of fly ash consisted of crystalline phases such as quartz, mullite and hematite (see Figure 3.3), fly ash was not completely reacted. The simulated results show the co-existence of the C-(N-)A-S-H gel and N-(C-)A-S-H gel in the sample. The C-(N-)A-S-H gel had a larger contribution to the volume of the solid phases of the sample than the N-(C-)A-S-H gel. This is in line with the observations presented in the literature [63, 64, 133]. In addition to the primary gels, crystalline phases, such as natrolite, goethite and brucite, were also formed in the sample. It is noted that natrolite was only formed within the first day. Afterwards natrolite was decomposed, and the species from the decomposition contributed to the formation of other solid phases.

A slight chemical volume expansion was identified at the early reaction time (up to 3 days). This may be attributed to the formation of zeolite natrolite. After the chemical expansion period chemical shrinkage was predicted. It increased as a function of reaction time.

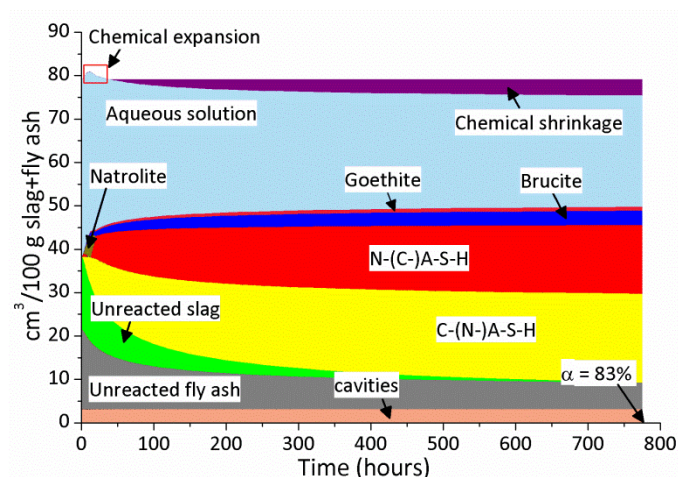


Figure 8.9 Simulated solid phase evolution of alkali-activated slag/fly ash (B\_N6S5.4). In the notations, B refers to alkali-activated slag blended with fly ash (slag/fly ash = 1), and N and S represent the weight percentages of Na<sub>2</sub>O and SiO<sub>2</sub> with respect to the precursor, respectively. See more details of the mixture in Table 3.2.

## 8.6 Conclusions

This chapter conducted a thermodynamic modelling investigation of the reactions in alkali-activated materials. From the presented results, the following conclusions can be drawn:

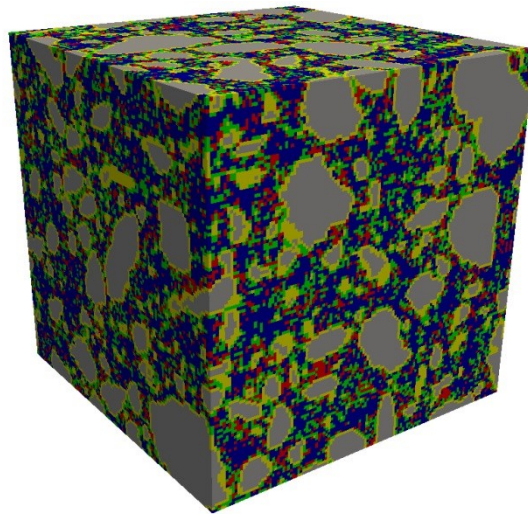
- (1) A thermodynamic model, i.e. N(C)ASH\_ss model, is developed to describe the N-A-S-H gel of alkali-activated fly ash. The simulation results showed that a higher degree of reaction of fly ash led to a larger Si/Al ratio in the N-A-S-H gel. This is in good agreement with the experimental results in the literature [58]. The simulated concentrations of Si, Na, Ca and OH<sup>-</sup> in the pore solution of alkali-activated fly ash paste matched the experimental results in this work within  $\pm 1$  order of magnitude.
- (2) For easy comparisons with experimental results, the reactions in the alkali-activated slag, alkali-activated fly ash and alkali-activated slag/fly ash were thermodynamically simulated in the time domain. The simulation results confirm that the C-(N-)A-S-H gel and N-A-S-H gel were the primary reaction products in alkali-activated slag and alkali-activated fly ash, respectively. In alkali-activated slag/fly ash, both the C-(N-)A-S-H gel and N-A-S-H gel were formed.
- (3) Besides the primary reaction products, crystalline reaction products were also formed. They were hydrotalcite, katoite, stratlingite, portlandite and mackinawite in alkali-activated slag, natrolite, brucite, portlandite and goethite in alkali-activated fly ash, natrolite, goethite and brucite in alkali-activated slag/fly ash.
- (4) With the simulated solid phase evolution the chemical deformation of alkali-activated materials can be obtained. It was found that chemical shrinkage mostly occurred in alkali-activated slag. In alkali-activated fly ash and alkali-activated slag/fly ash, by contrast, both chemical shrinkage and chemical expansion were predicted.



# Chapter 9

---

## Simulation of the reaction process and microstructure formation of alkali-activated materials<sup>23</sup>



Based on the modules presented in previous chapters a numerical model is developed in this chapter to simulate the reaction process and microstructure formation of alkali-activated materials (AAMs). This numerical model, i.e. GeoMicro3D, consists of four modules: the initial-particle-parking-structure module (Chapter 6), dissolution module (Chapter 7), thermodynamic modelling module (Chapter 8) and nucleation-growth module. The last module is presented in this chapter. After build-up of GeoMicro3D, it is used to simulate the reaction process and microstructure formation of alkali-activated slag systems and the simulation results are validated by the experimental results.

---

<sup>23</sup> This chapter is partially based on:

Yibing Zuo and Guang Ye. GeoMicro3D: A novel numerical framework for simulating the hydration and microstructure formation of alkali-activated materials. Proceeding of the Workshop on Concrete Modelling and Materials Behaviour in Honor of Professor Klaas van Breugel, RILEM Publications, Delft, The Netherlands, 2018, p. 30-41.

## 9.1 Introduction

With the thermodynamic modelling approach it is possible to simulate the reactions in alkali-activated materials (AAMs) and quantify the solid reaction products (Chapter 8). Based on the simulated solid phase evolution it is possible to predict the total porosity of the sample with time. But it is not possible to obtain other information on the microstructure development of the samples, such as the pore size distribution and connectivity of phases etc. This is because the distribution of reaction products is not taken into account in the thermodynamic simulations. In order to simulate the distribution of reaction products in AAMs, nucleation and growth of reaction products should be considered in the numerical models. Nucleation initiates the formation of reaction products in AAMs. If there are nuclei of the reaction products formed and the nuclei reach a critical size, the reaction products start to grow. The continuous growth of reaction products then leads to the microstructure formation of AAMs.

In this chapter the GeoMicro3D model is built up. As displayed in Figure 9.1 the GeoMicro3D model consists of four modules. The first module provides the particle structure of precursor particles in alkaline activator as the starting point for the simulation (Chapter 6). The second module simulates the dissolution of slag/fly ash (Chapter 7). The third module simulates the nucleation and growth of reaction products and a novel approach is proposed to speed up the nucleation simulations. This module will be given in this chapter. The fourth module simulates the chemical reactions and quantifies the reaction products (Chapter 8). The last three modules (2, 3 and 4) are assembled together by the lattice Boltzmann method (LBM). The LBM is used to simulate the transport of aqueous ions (Chapter 7).

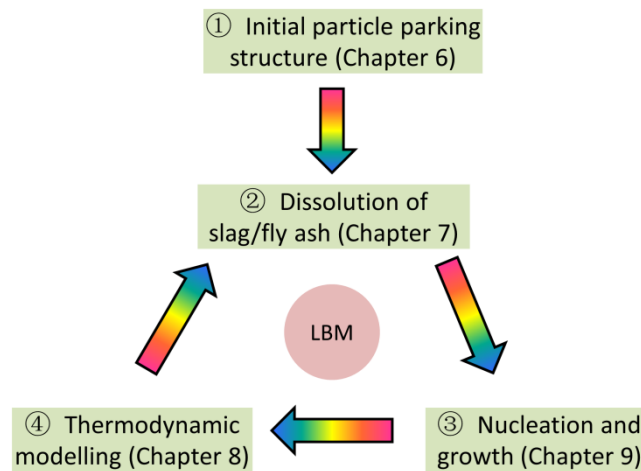


Figure 9.1 Modules of the GeoMicro3D model. LBM represent lattice Boltzmann method.

As a case study, the GeoMicro3D model is used to simulate the reaction process and microstructure formation of alkali-activated slag systems with three different alkaline activators. The simulation results by GeoMicro3D are discussed and the experimental results are used to validate GeoMicro3D. Figure 9.2 shows the position of Chapter 9 in structure of the study of the reaction process and microstructure formation of AAMs in this thesis.

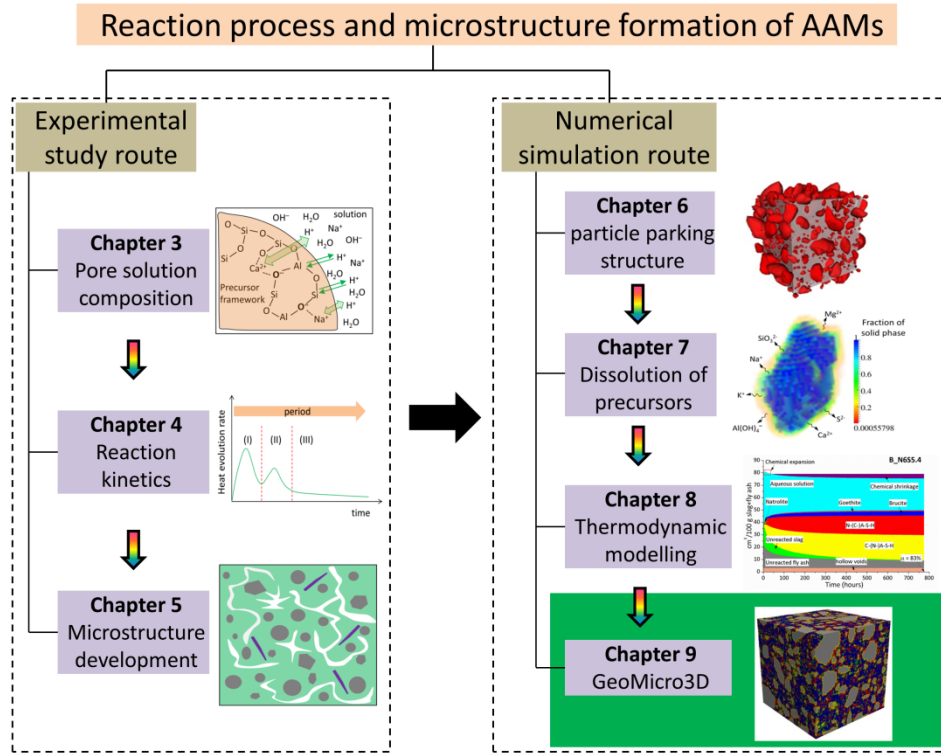


Figure 9.2 Position of Chapter 9 in structure of the study of the reaction process and microstructure formation of AAMs in this thesis.

## 9.2 Simulation of the nucleation and growth of reaction products

When the element concentrations in the pore solution of AAMs increase towards saturation or oversaturation with respect to reaction products, these elements are thermodynamically favored to form reaction products. If there are nuclei of the reaction products formed and the nuclei reach a critical size, the reaction products start to grow. The probability  $P(t)$  that at least one critical nucleus has formed in a time interval  $\Delta t$  (s) is expressed with Equation 9.1 [21]. The critical nucleus refers to the nucleus with a size larger than the critical size.

$$P(\Delta t) = 1 - \exp(-J \cdot V \cdot \Delta t) \quad (9.1)$$

where  $V$  ( $\text{m}^3$ ) is the solution volume within which the nucleus forms and  $J$  is the nucleation rate ( $\text{m}^{-3} \cdot \text{s}^{-1}$ ) that can be obtained with the following equation [21, 210]:

$$J(S) = A \cdot S \cdot \exp\left(-\frac{B}{\ln^2 S}\right) \quad (9.2)$$

where  $A$  ( $\text{m}^{-3} \cdot \text{s}^{-1}$ ) is the kinetic parameter,  $S$  is the supersaturation ratio and  $B$  is the thermodynamic parameter of nucleation. The thermodynamic parameter  $B$  for heterogeneous nucleation is expressed with the following equation:

$$B = \frac{4}{27} \frac{c^3 \cdot v^2 \cdot \gamma_{ef}^3}{k_B^3 \cdot T^3} \quad (9.3)$$

where  $c$  is a shape factor ( $(36\pi)^{1/3}$  for spheres and 6 for cubes),  $v$  is the molecular volume of the phase ( $\text{m}^3$ ),  $k_B$  ( $\text{J}\cdot\text{K}^{-1}$ ) is the Boltzmann constant and  $T$  (K) is the absolute temperature.  $\gamma_{ef}$  ( $\text{J}/\text{m}^2$ ) is the effective interfacial energy, where  $\gamma_{ef} = \psi\gamma$  with activity factor  $0 < \psi < 1$ . For homogeneous nucleation  $\psi = 1$ . The interfacial energy  $\gamma$  is calculated using the following equation [21, 210]:

$$\gamma = \beta_N \cdot k_B \cdot T \cdot \frac{1}{v^{2/3}} \cdot \ln\left(\frac{1}{N_a \cdot v \cdot c^*}\right) \quad (9.4)$$

where  $\beta_N$  is a numerical factor ( $\beta_N = 0.514$  for spherical nuclei),  $N_a$  is Avogadro's number and  $c^*$  (mol/L) is the molar solubility.

For a lattice cell that has no reaction products, each reaction product has a nucleation probability to precipitate according to Equation 9.1. In theory the reaction products should be dealt with individually and independently. This, however, would exponentially increase the computation efforts and decrease the computation efficiency. On the other hand, the observations from the SEM-micrographs (Figures 5.6, 5.8 and 5.9 in Chapter 5) show that the reaction products were intimately intermixed with each other at the micro level. It means that it is not plausible to separate the reaction products from each other at the micro level. In order to control the computation efforts within the capability of computing facility and comply with the experimental observations, this work innovatively proposed the following approach. The reaction products are divided into two groups, i.e. primary reaction products and secondary reaction products as discussed in Chapter 8. If at least one of primary gel end-members and at least one of secondary reaction products are predicted to nucleate, then the thermodynamic modelling module is called to simulate the chemical reactions and quantify the reaction products. The detailed procedures are provided in the following four steps and shown in Figure 9.3.

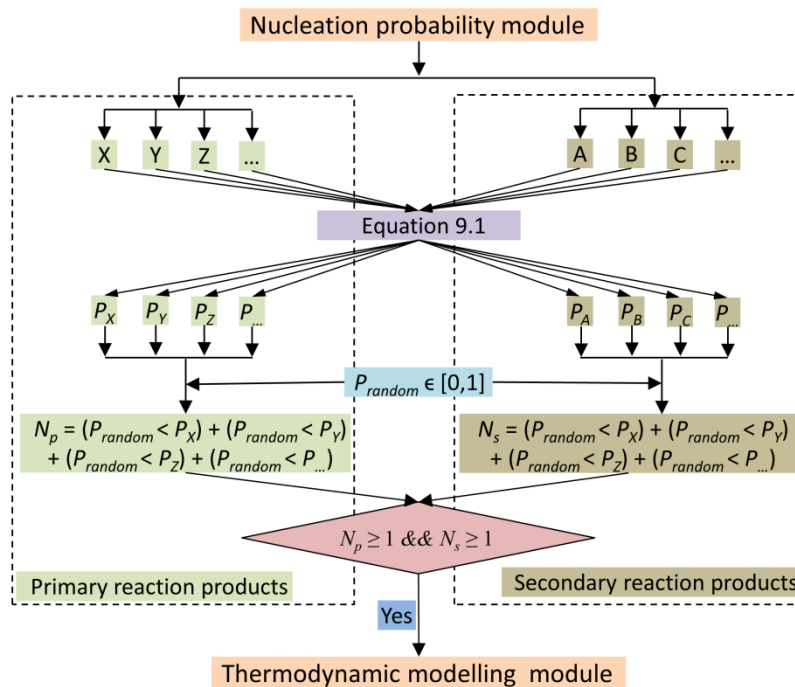


Figure 9.3 Flowchart of nucleation probability module.

- (1) Calculate the nucleation probabilities,  $P_X$ ,  $P_Y$  and  $P_Z$  for primary reaction products and  $P_A$ ,  $P_B$  and  $P_C$  for secondary reaction products, using Equation 9.1.

- (2) Generate a random probability  $0 \leq P_{\text{random}} \leq 1$ .
- (3) Calculate the numbers (i.e.  $N_p$  and  $N_s$ ) of primary reaction products and secondary reaction products that are predicted to nucleate, respectively.
- (4) If  $N_p \geq 1$  and  $N_s \geq 1$ , then the thermodynamic modelling module is called.

For a lattice cell that already has reaction products, the thermodynamic modelling module is called directly without calling the nucleation probability module. In GeoMicro3D the calculated amount of reaction products then fill the lattice cell until it is completely filled. In the meantime the solid phase and element concentrations of the lattice cell are updated.

### 9.3 Diffusivity of ions through lattice nodes

Figure 9.4 schematically represents the types of lattice cells through which ions may diffuse. The intact precursor cells (①) are non-diffusive cells. For simulating the diffusion of ions through these lattice cells, bounce back conditions are applied during the streaming process of particle distribution functions. Label ② represents solution cells. The diffusivities of ions in the solution cells are taken as those in water.

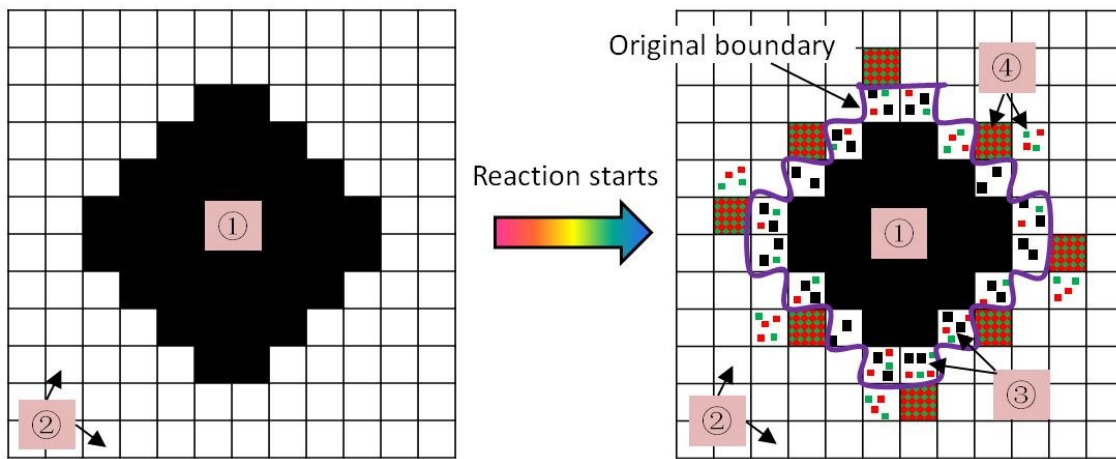


Figure 9.4 Schematic representation of the diffusion of ions through different lattice cells in 2D. In the graph black, white, red and green represent precursor, solution, primary reaction products and secondary reaction products, respectively. ① and ② represent precursor and solution cells, respectively. ③ represents cells where precursor may dissolve and reaction products may precipitate, and ④ represents cells that are completely or partially filled with reaction products.

The lattice cells represented by label ③ are within the original boundary of precursor. In these lattice cells precursor may dissolve and reaction products may also nucleate and grow. Label ④ represents the lattice cells filled partially or completely by the reaction products. Before determining the diffusivities through the lattice cells represented by labels ③ and ④, the following three models are introduced:

#### (1) Model-I

Figure 9.5 schematically shows a medium that consists of two phases – one phase is diffusive and the other phase is non-diffusive. By assuming the shapes of these inclusions (phase B) as fibrous the diffusivity of this medium is calculated with the following equation [169]:

$$D_{medium} = D_A(1 - \varphi_B)^{5/3} \quad (9.5)$$

where  $D_{medium}$  and  $D_A$  are diffusivities of this medium and phase A, respectively.  $\varphi_B$  is the volume fraction of phase B in the medium.

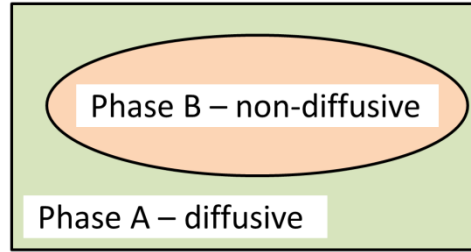


Figure 9.5 Schematic representation of a medium that consists of a diffusive phase and a non-diffusive phase.

## (2) Model-II

As shown in Figure 9.6 the medium is made up of two diffusive phases. For simulating the diffusion of ions through this kind of medium, the following equation is used to calculate the diffusivity of this medium [169, 211]. In this model phase B is considered as spherical inclusions in phase A.

$$\left( \frac{D_B - D_{medium}}{D_B - D_A} \right) \left( \frac{D_A}{D_{medium}} \right)^{1/3} = 1 - \varphi_B \quad (9.6)$$

where  $D_A$ ,  $D_B$  and  $D_{medium}$  are the diffusivities of ions in phase A, phase B and the medium, respectively.  $\varphi_B$  is the volume fraction of phase B in the medium.

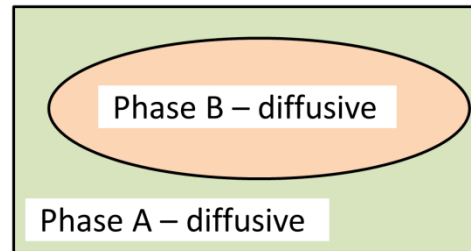


Figure 9.6 Schematic representation of a medium that consists of two diffusive phases.

## (3) Model-III

Figure 9.7 shows a medium which consists of three phases – two diffusive phases and one non-diffusive phase. In order to determine the diffusivity of this medium, two steps are followed. First the model-I is applied to determine the diffusivity of phase BC using Equation 9.7. Then the model-II is used to calculate the diffusivity of the medium with Equation 9.8.

$$D_{BC} = D_B(1 - \varphi_C)^{5/3} \quad (9.7)$$

$$\left( \frac{D_{BC} - D_{medium}}{D_{BC} - D_A} \right) \left( \frac{D_A}{D_{medium}} \right)^{1/3} = 1 - \varphi_{BC} \quad (9.8)$$

where  $D_A$ ,  $D_B$ ,  $D_{BC}$  and  $D_{medium}$  are the diffusivities of ions in phase A, phase B, phases BC and the medium, respectively.  $\varphi_C$  is the volume fraction of phase C in the phases B and C.  $\varphi_{BC}$  is the volume fraction of phases BC in the medium.

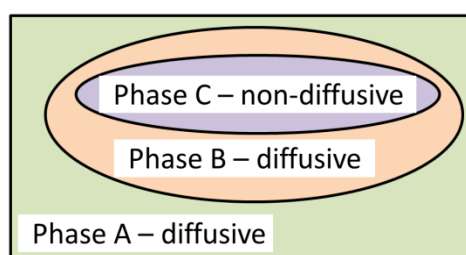


Figure 9.7 Schematic representation of a medium that consists of two diffusive phases and a non-diffusive phase.

The primary reaction products, i.e. the C-(N-)A-S-H gel and the N-A-S-H gel, are diffusive for ions. In contrast the secondary reaction products, i.e. crystalline phases, are non-diffusive for ions. Table 9.1 lists the relative diffusivity of ions through the C-S-H gel. The relative diffusivity of an ion in a medium is defined as the ratio of its diffusivity in this medium relative to that in water. The diffusivity of ions through the N-A-S-H gel, however, has not been reported in the literature.

Table 9.1 Relative diffusivity of ions through the C-S-H gel

Items	Relative diffusivity	Ref.
$\text{Cl}^-$	0.0025	[212]
$\text{H}_2\text{O}^a$	0.001	[213]
Aqueous ions <sup>b</sup>	0.00775	[214]

a. Some of the hydrogen atoms in  $\text{H}_2\text{O}$  have been replaced by tritium, a hydrogen isotope [215].

b. Based on the electric conductivity measurements [214].

In determining the diffusivities of the lattice cells represented by labels ③ and ④, the primary reaction products are regarded as a diffusive phase while the precursor and secondary reaction products are taken as non-diffusive phases. By applying the models discussed previously the diffusivity of the lattice cells represented by labels ③ and ④ are calculated accordingly as shown in Table 9.2.

Table 9.2 Type of lattice cell and the model used to obtain its diffusivity

Description of the lattice cell	Selection of the model
Contains one diffusive phase, i.e. solution, and one non-diffusive phase, i.e. slag or/and secondary reaction products	Model-I
Contains two diffusive phases, i.e. solution and primary reaction products	Model-II
Contains one non-diffusive phase, i.e. slag or/and secondary reaction products, and two diffusive phases, i.e. solution and primary reaction products	Model-III



#### 9.4 GeoMicro3D: the overall flowchart

Figure 9.8 shows the overall flowchart of the GeoMicro3D model. It consists of three parts. The first part describes the input data. The input data from the raw materials include the chemical composition, particle size distribution, amorphous content, reactivity index (NBO/T) and density of the precursor, and the chemical composition and density of the alkaline activator. The information about the mixture is also required, such as the liquid-to-precursor mass ratio, ratio of the volume of the alkaline activator to the surface area of the precursor, and curing temperature. Since the roughness of the precursor particles is not considered in the model, the geometry specific surface area of the precursor should be used to calculate the ratio of the volume of the alkaline activator to the surface area of the precursor.

In the second part the initial particle parking structure of precursor particles in alkaline activator is simulated using the extended Anm model (Chapter 6). The simulated initial particle parking structure is then digitized into a cube of voxels (lattice cells). The element constituents of each lattice cell is initialized according to the mixture composition. The liquid lattice cells have the same chemical composition as the alkaline activator. Since slag is totally amorphous, homogeneous distribution of elements is assumed. In other words, each slag lattice cell is assumed to have the same element composition as the chemical composition of the slag. For fly ash particles, one part of the fly ash lattice cells are randomly selected to represent the crystalline phases in fly ash. The remaining part of fly ash lattice cells are set as the reactive cells to represent the amorphous phases in fly ash. Only the reactive fly ash cells can be dissolved. For reactive fly ash cells, each of them is assumed to have the same element composition as the chemical composition of amorphous phases in fly ash.

The third part is the main part of the GeoMicro3D model. After the initialization step, the main loop starts from the *dissolution module*. Then the diffusion of the aqueous ions in the solution is simulated using the lattice Boltzmann method. The dissolved amounts of ions are considered as the source terms in the collision process. Following the diffusion step, the element concentrations of each lattice cell are updated. Before using the *thermodynamic modelling module* to simulate the chemical reactions, the places where nucleation and growth of reaction products will occur are determined using the *nucleation and growth module*. Given the nodes within which reaction products will precipitate, the reactions in these lattice cells are simulated and the reaction products are quantified with the *thermodynamic modelling module*. After the *thermodynamic modelling module*, the microstructure and pore solution composition are updated. The consumed ions will be added to the ones from the *dissolution module* as the source terms in the next iteration. Before going to the next iteration step one judgement is performed. If the current reaction time is *larger* than the target reaction time or the source terms ( $S$ ) are *zero*, then the main loop will stop and simulation results are output. *Otherwise* another iteration will start. The simulation results include the degree of reaction, pore solution composition, solid phase evolution and microstructure development with time. Since the dissolution of precursors and reactions of species are fundamentally described in the local lattice cell, the interactions between different precursors can be intrinsically dealt with.



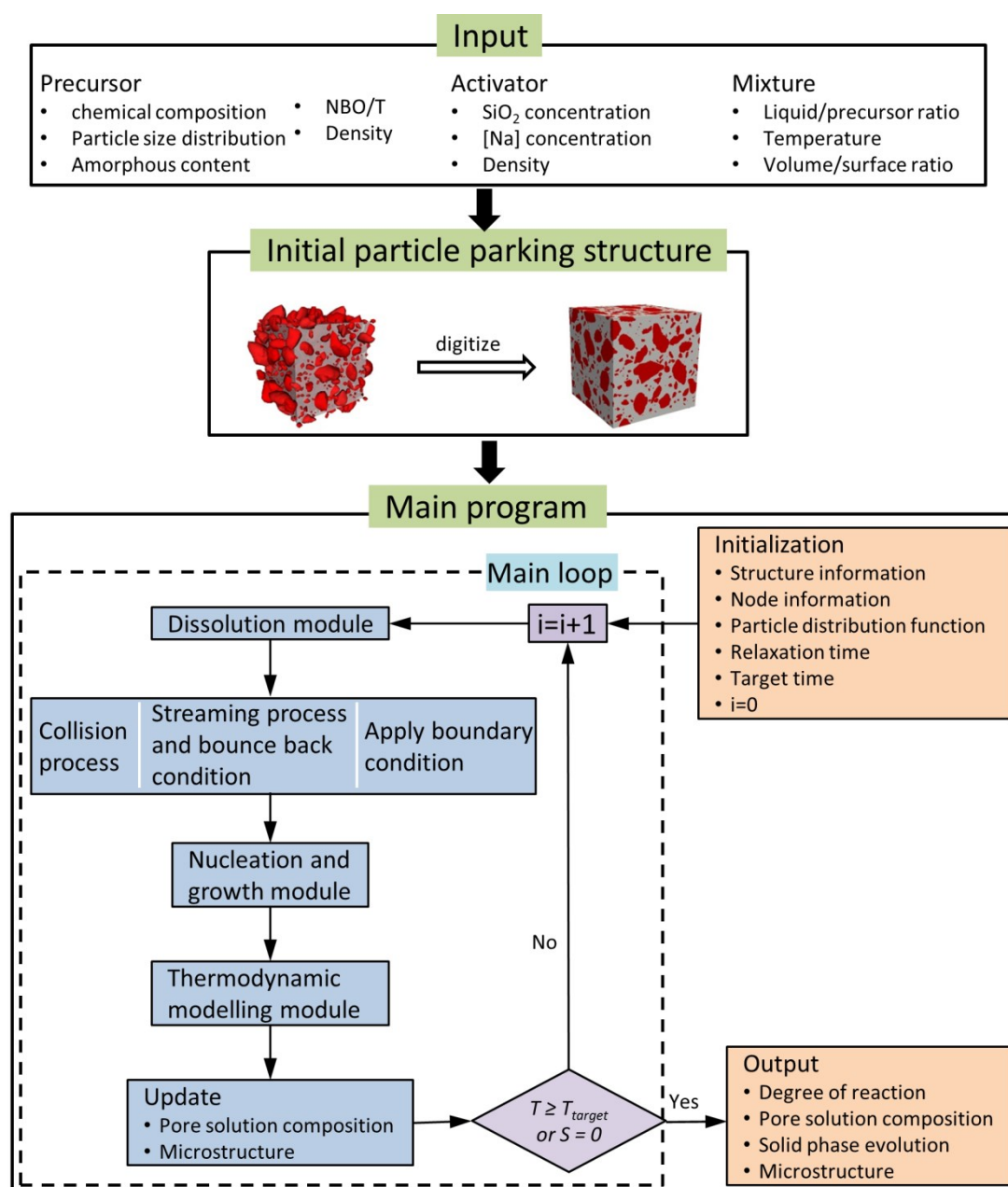


Figure 9.8 The overall flowchart of the GeoMicro3D model.

## 9.5 Implementation – a case study of the alkali-activated slag systems

### 9.5.1 Water retention of the C-(N-)A-S-H gel

For the eight C(N)ASH<sub>ss</sub> end-members proposed by Myers et al. [69] (see Table 8.1), the H<sub>2</sub>O/SiO<sub>2</sub> is defined as the water content of the solid nano-scale C-S-H. It includes hydroxyl groups and H<sub>2</sub>O held in the interlayer space but excludes any adsorbed or gel pore water (see Figure 9.9). In GeoMicro3D the adsorbed and gel pore water retained by the C-(N-)A-S-H gel are dealt with by following methods:

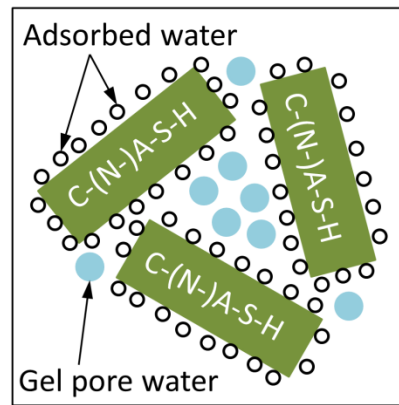


Figure 9.9 Schematic representation of the adsorbed water and gel pore water retained by C-(N-)A-S-H gel.

- (1) *Adsorbed water*: In GeoMicro3D each mole of C-(N-)A-S-H is assumed to have 0.3 moles of the adsorbed water with density of  $1.1 \text{ g/cm}^3$ . This is in accordance with the literature [198].
- (2) *Gel pore water*: For C-S-H in the hydration of  $\text{C}_3\text{S}$  or  $\text{C}_2\text{S}$ , Thomas et al used  $\text{H}_2\text{O}/\text{SiO}_2 = 4$  to include the water trapped in the gel pores [216]. As shown in Table 8.1, the  $\text{H}_2\text{O}/\text{SiO}_2$  ratio of the C(N)ASH<sub>ss</sub> end-members range from 0.792 to 2.5, which is much smaller than 4. In GeoMicro3D, extra water with density of  $1 \text{ g/cm}^3$  is added to meet  $\text{H}_2\text{O}/\text{SiO}_2 = 4$ . This amount of extra water is considered as the gel pore water in the C-(N-)A-S-H gel<sup>24</sup>.

### 9.5.2 Simulation parameters

The reaction process and microstructure formation of samples BFS\_N4S0, BFS\_N6S0 and BFS\_N6S5.4 will be simulated using GeoMicro3D. The mixture compositions of these samples are provided in Table 3.2. Since these three samples have the same water-to-slag ratio (0.40), they have very similar initial particle parking structure of slag in alkaline activator. Figure 9.10 shows the simulated initial particle parking structure of slag in alkaline activator using the extended Anm model in Chapter 6. The simulated initial particle parking structure is then used as the input for GeoMicro3D. It is noted that chemical shrinkage is not taken into account in the current GeoMicro3D. In other words the empty space resulting from chemical shrinkage is assumed to be replenished with water.

<sup>24</sup> Since the C-(N-)A-S-H gel is structurally similar to the C-S-H gel, a  $\text{H}_2\text{O}/\text{SiO}_2$  ratio of 4 used for considering the gel pore water in the C-S-H gel is also used in this work to consider the gel pore water in the C-(N-)A-S-H gel. Still more work is recommended to study the water retention of the C-(N-)A-S-H gel.

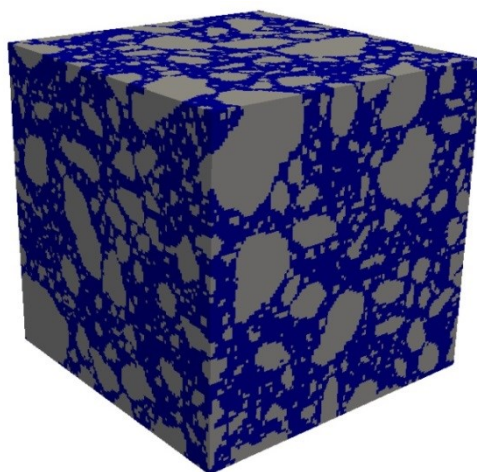


*Figure 9.10 Simulated initial particle parking structure of slag in alkaline activator using the extended Anm model in Chapter 6. In the graph, blue and gray represent activator and slag, respectively. The size of the cubic unit cell is  $125\ \mu\text{m} \times 125\ \mu\text{m} \times 125\ \mu\text{m}$ . The digitization resolution is  $1\ \mu\text{m} \times 1\ \mu\text{m} \times 1\ \mu\text{m}$  per voxel.*

The model parameters presented in Chapter 7 for the dissolution module are also used in GeoMicro3D, such as the diffusivities of ions in solution and activation energy of diffusion of ions (see Table 7.1). In order to account for the effect of precipitation of reaction products on the dissolution, the solubility products of  $\text{SiO}_2$ ,  $\text{Al}_2\text{O}_3$  and  $\text{CaO}$  for dissolution have to be adjusted and are taken as  $1.89 \times 10^{-3}$ ,  $2.47 \times 10^{-4}$  and  $5.31 \times 10^{-2}$ , respectively. The thermodynamic database presented in Chapter 8 for thermodynamic modelling of the reactions in alkali-activated slag is also used in GeoMicro3D. The kinetic parameter  $A$  for the nucleation of reaction products are determined through a parameter study and are listed in Table 9.3. The activity factor  $\psi$  is taken as 0.27 (see  $\psi$  in Section 9.2).

*Table 9.3 Kinetic parameter  $A$*

	C(N)ASH <sub>ss</sub>	M <sub>4</sub> AH <sub>10</sub>	M <sub>6</sub> AH <sub>12</sub>	M <sub>8</sub> AH <sub>14</sub>	C <sub>3</sub> AH <sub>6</sub>	C <sub>2</sub> ASH <sub>8</sub>	CH	Natrolite
$A\ (\text{m}^{-3} \cdot \text{s}^{-1})$	$4.24 \times 10^7$	$4.71 \times 10^{-26}$	$4.71 \times 10^{-51}$	$4.71 \times 10^{-71}$	27.6	0.101	$4.71 \times 10^9$	$9.62 \times 10^3$

In the following sections the simulation results obtained with GeoMicro3D are presented and discussed with respect to the degree of reaction of slag, pore solution chemistry, 3D microstructure, volume evolution of phases and pore structure. Along with the simulation results obtained with GeoMicro3D relevant experimental results and calculation results obtained from GEMS are also presented to validate the GeoMicro3D model.

### 9.5.3 Degree of reaction

Figure 9.11 shows the simulated degree of reaction of slag with GeoMicro3D in comparison with the experimental results (see Figure 4.14). It can be seen from the simulation results that the mixture with a higher  $\text{Na}_2\text{O}$  content had a higher degree of reaction of slag. In contrast, the mixture with an addition of  $\text{SiO}_2$  had a lower degree of reaction. These results are in good agreement with the observations from the experimental results. In comparison with the experimental results, the simulation results were within the errors of 5.8 %, 2.4 % and 7.0 % for samples BFS\_N4S0, BFS\_N6S0 and BFS\_N6S5.4, respectively.

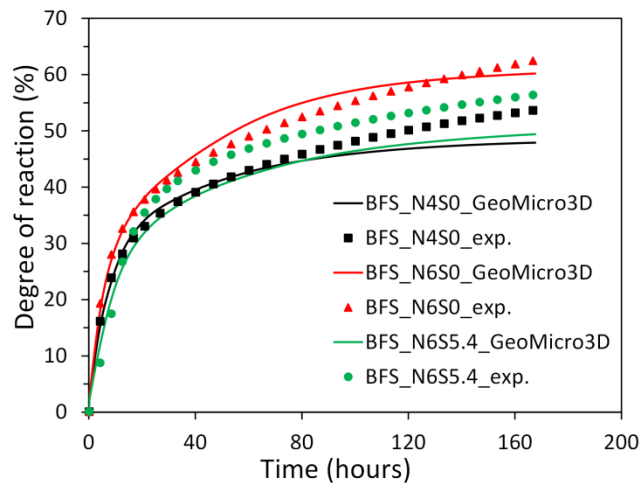


*Figure 9.11 Simulated degree of reaction of slag with GeoMicro3D in comparison with the experimental results. The experimental results are presented in Chapter 4 (see Figure 4.14). In the notations, BFS refers to alkali-activated slag, and N and S represent the weight percentage of  $\text{Na}_2\text{O}$  and  $\text{SiO}_2$  with respect to slag, respectively. See more details of mixtures in Table 3.2.*

### 9.5.4 Pore solution chemistry

Figure 9.12 displays the simulated element concentrations with GeoMicro3D in comparison with the experimental results (see Figure 3.5). The simulated element concentrations were calculated as the average of concentrations of elements in the solution cells. The simulated concentrations of Na, K and  $\text{OH}^-$  were in good agreement with the experimental results. For the concentrations of Si and Al, the simulated results matched the experimental results within  $\pm 1$  order of magnitude. This discrepancy is close to the uncertainty of experimental data [69]. For the concentration of Ca, the simulation results were about two orders of magnitude larger than the measured values. More work is recommended to look into this discrepancy.

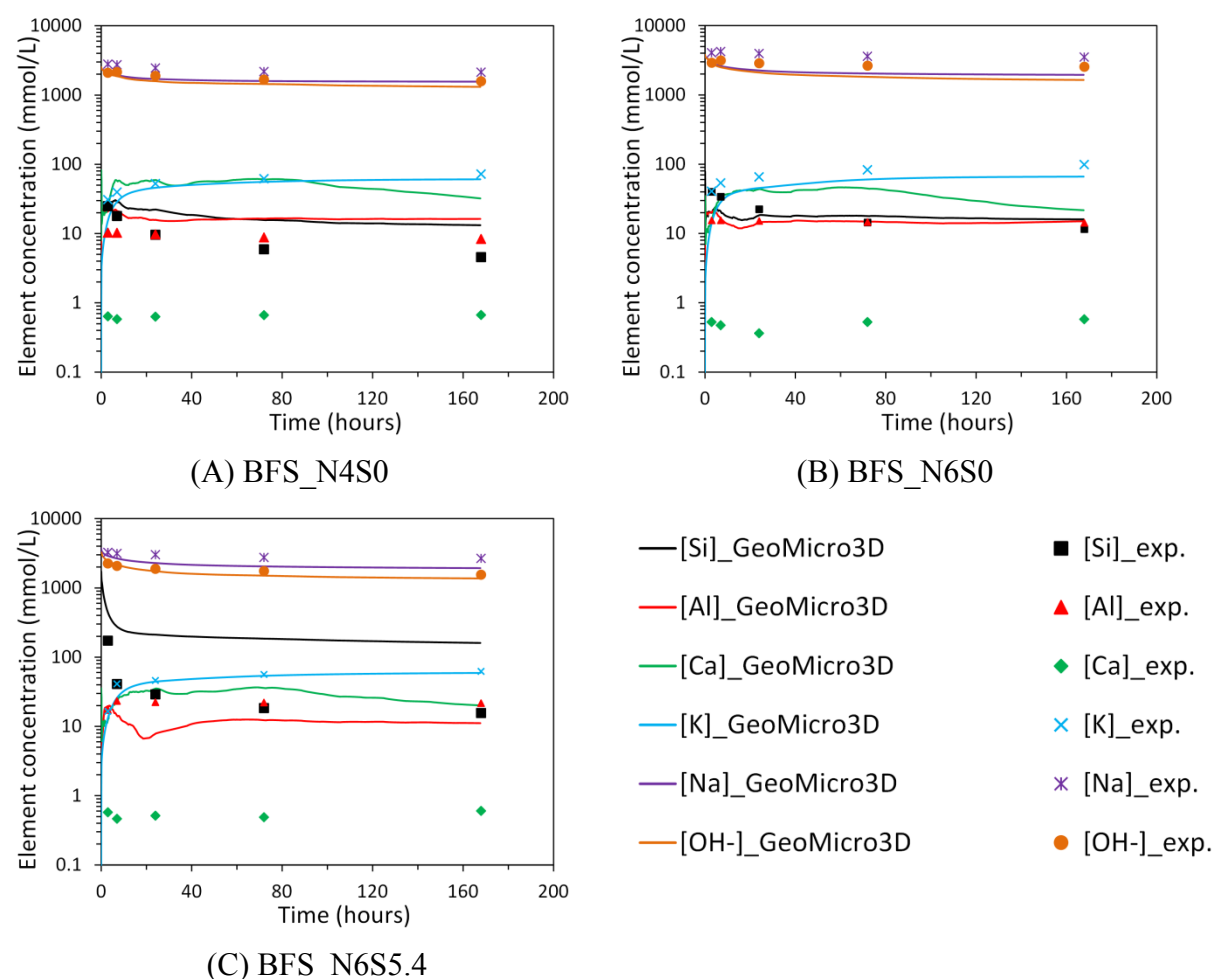
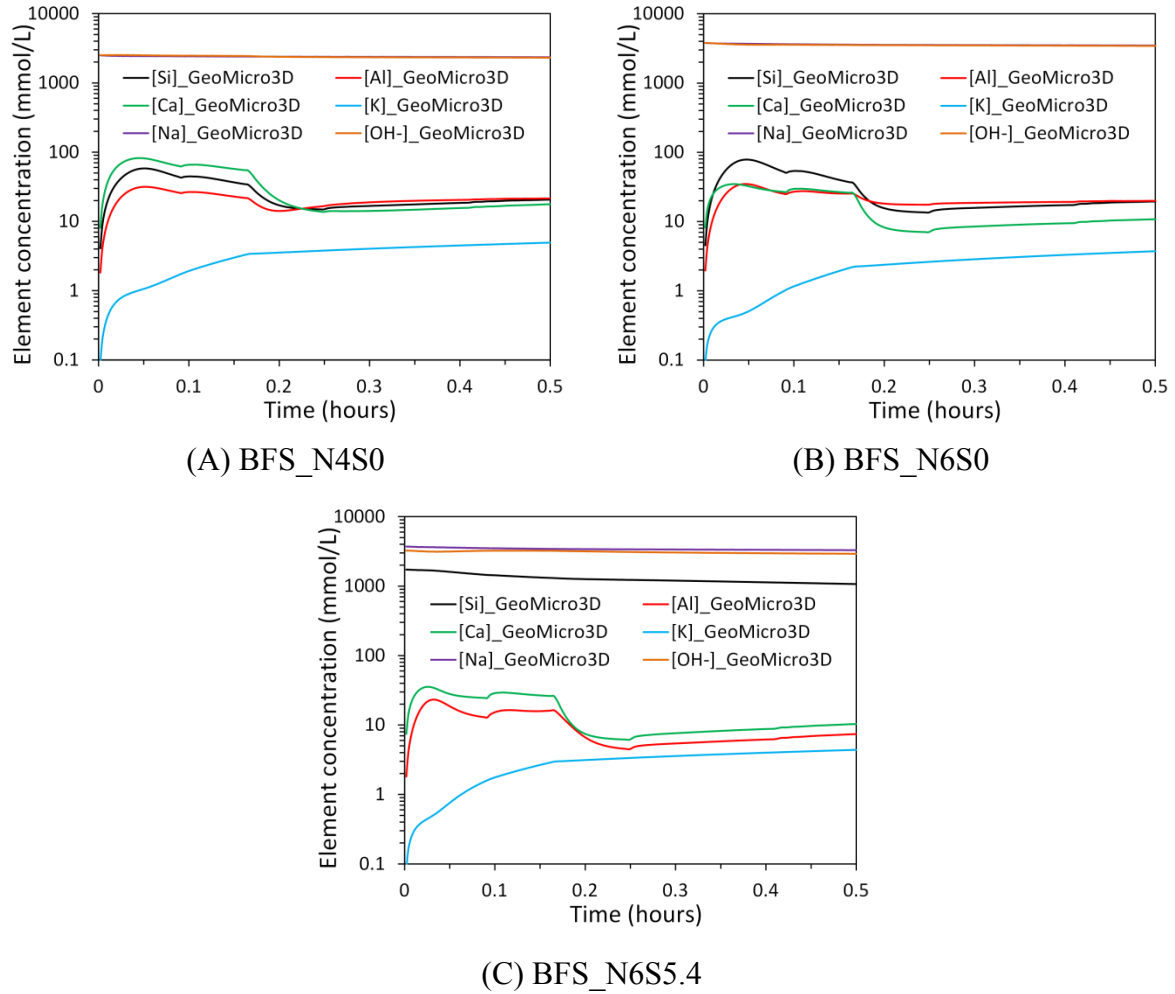


Figure 9.12 Simulated element concentrations with GeoMicro3D in comparison with the experimental results. The experimental results are presented in Chapter 3 (see Figure 3.5). In the notations, BFS refers to alkali-activated slag, N and S represent the weight percentage of Na<sub>2</sub>O and SiO<sub>2</sub> with respect to slag. See more details of mixtures in Table 3.2.

Figure 9.13 shows the simulated element concentrations in the first half hour with GeoMicro3D. The concentrations of Na and OH<sup>-</sup> had maximum values in the beginning and then decreased with time. This result is reasonable and expected, since these elements were mainly sourced from the alkaline activator and were consumed with time while forming reaction products. For samples BFS\_N4S0 and BFS\_N6S0, the concentrations of Si, Al and Ca started from zero and then increased with time. When the concentrations of these elements increased towards saturation or supersaturation with respect to solid reaction products, these elements were thermodynamically favored to precipitate. The precipitation of solid reaction products consumed these elements. When the rate at which these elements were consumed exceeded the release rates of these element by dissolution of slag, the concentrations of these elements started to decrease with time. For sample BFS\_N6S5.4, the concentration of Si had maximum value in the beginning and then decreased with time. This is because the alkaline activator for sample BFS\_N6S5.4 provided soluble Si in the beginning. The soluble Si reacted with the released Al and Ca from slag. So the concentration of Si decreased with time for sample BFS\_N6S5.4. For the concentration of K, it increased with time for all samples. This is because there was no K-containing reaction product that precipitated in the reaction of slag.



**Figure 9.13** Simulated element concentrations with GeoMicro3D in the beginning half hour. In the notations, BFS refers to alkali-activated slag, and N and S represent the weight percentage of  $\text{Na}_2\text{O}$  and  $\text{SiO}_2$  with respect to slag, respectively. See more details of mixtures in Table 3.2.

Besides the average element concentration in the pore solution, it is also possible to obtain the distribution of ions from the simulation with GeoMicro3D. As an example, Figure 9.14 shows the distribution of element concentration of Si for sample BFS\_N4S0 at 3 hours, 1 day and 7 days. The distribution of element concentration of Si for samples BFS\_N6S0 and BFS\_N6S5.4 can be found in Appendix C (Figures C.1 and C.2). It clearly shows that Si concentrated around the dissolving slag grains. The concentration of Si in the cells around the slag grains was much larger than the concentration in the pore solution.



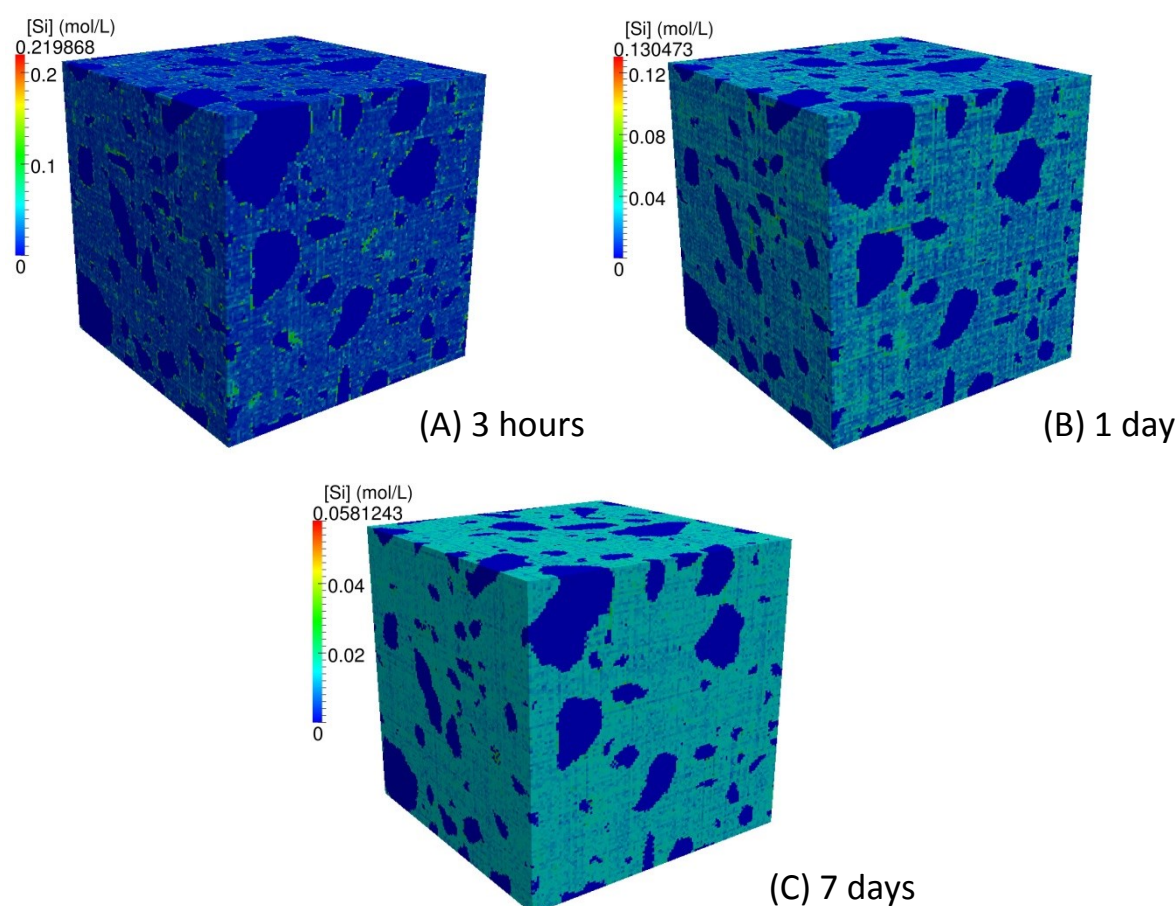
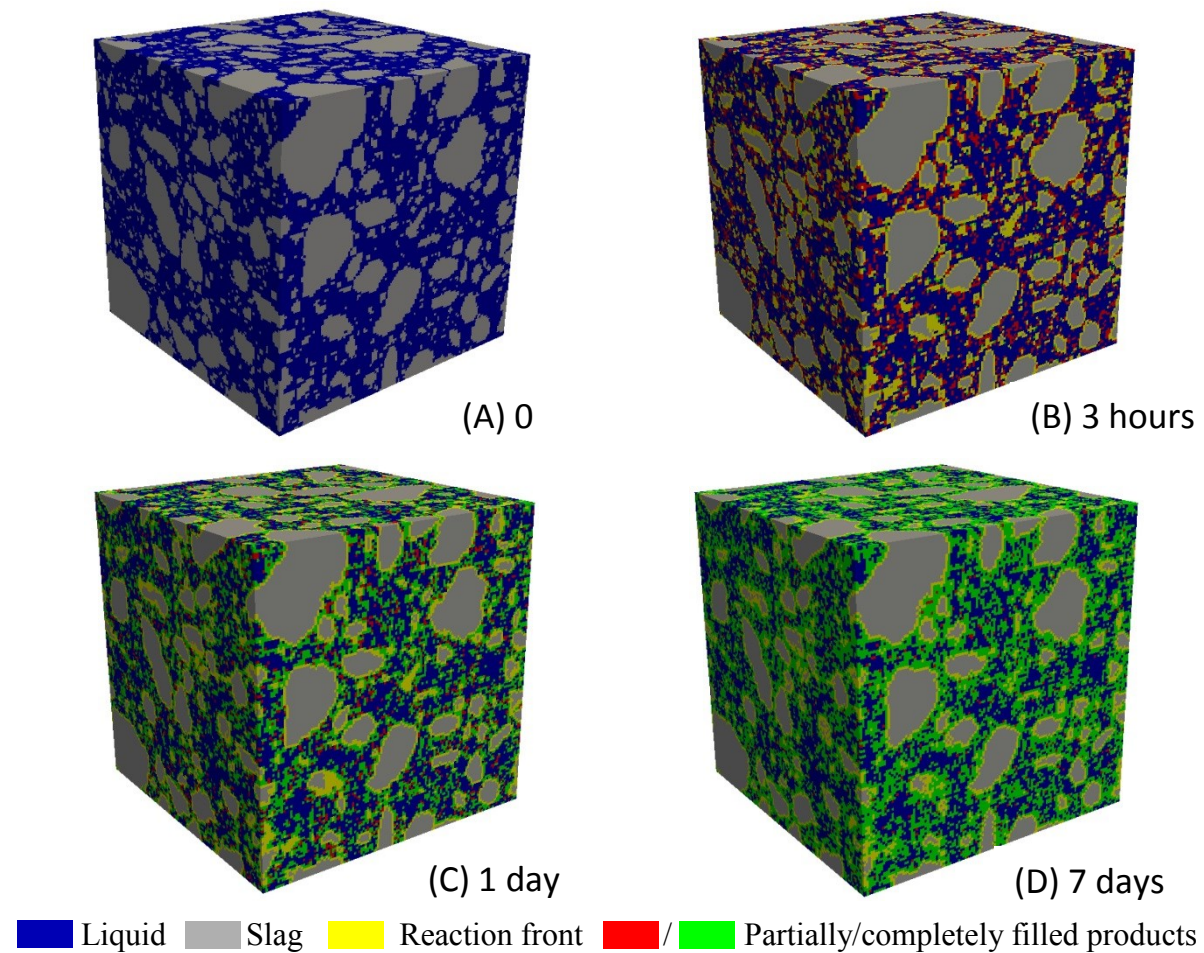


Figure 9.14 Distribution of element concentration of Si for sample BFS\_N4S0 at 3 hours, 1 day and 7 days. The size of the cubic unit cell is  $125\ \mu\text{m} \times 125\ \mu\text{m} \times 125\ \mu\text{m}$ . The digitization resolution is  $1\ \mu\text{m} \times 1\ \mu\text{m} \times 1\ \mu\text{m}$  per voxel. See more details of mixtures in Table 3.2.

### 9.5.5 Microstructure development

Figure 9.15 shows four stages of the simulated microstructures of sample BFS\_N4S0 at 0, 3 hours, 1 day and 7 days, respectively. The simulated microstructures of samples BFS\_N6S0 and BFS\_N6S5.4 are presented in Appendix C (Figures C.3 and C.4). The colors of blue and gray represent liquid and slag, respectively. The yellow color represents the reaction front cells within which slag may dissolve and reaction products may also precipitate. The colors of red and green represent the cells that are partially and completely filled with reaction products, respectively. The pictures in Figure 9.15 show the growth of reaction products.



*Figure 9.15 Simulated 3D microstructures of sample BFS\_N4S0 at 0, 3 hours, 1 day and 7 days. The size of the cubic unit cell is  $125\ \mu\text{m} \times 125\ \mu\text{m} \times 125\ \mu\text{m}$ . The digitization resolution is  $1\ \mu\text{m} \times 1\ \mu\text{m} \times 1\ \mu\text{m}$  per voxel. In the notations, BFS refers to alkali-activated slag, and N and S represent the weight percentage of  $\text{Na}_2\text{O}$  and  $\text{SiO}_2$  with respect to slag, respectively. See more details of mixtures in Table 3.2.*

As discussed in Chapter 5 (see Section 5.4.2), the presence of soluble silicate in the alkaline activator seriously affected the microstructure formation of alkali-activated slag. Figure 9.16 shows cross sections of the simulated 3D microstructures of the alkali-activated slag samples with and without addition of  $\text{SiO}_2$  at similar degrees of reaction of slag, i.e. BFS\_N6S5.4 ( $\alpha = 0.335$ ) and BFS\_N6S0 ( $\alpha = 0.317$ ). It clearly shows that the reaction products were more homogeneously distributed in the sample with soluble silicate (BFS\_N6S5.4) than those in the sample with no soluble silicate (BFS\_N6S0). These simulation results are well in line with previous discussions as shown in Figures 5.27 and 5.28.



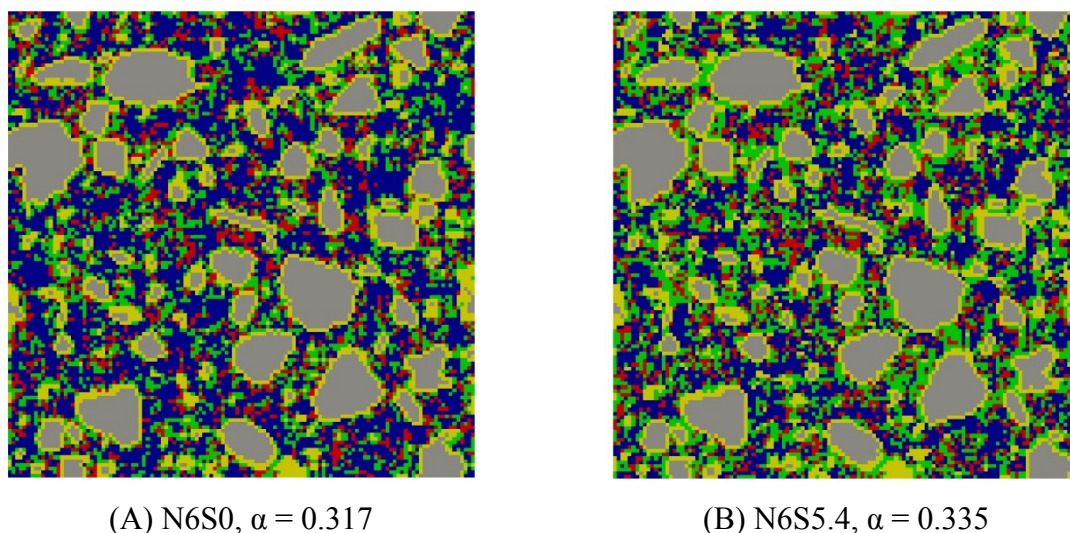


*Figure 9.16 Cross sections of samples BFS\_N6S0 and BFS\_N6S5.4 at similar degrees of reaction of slag. In the notations, BFS refers to alkali-activated slag, N and S represent the weight percentage of  $\text{Na}_2\text{O}$  and  $\text{SiO}_2$  with respect to slag. See more details of mixtures in Table 3.2.*

In the simulated 3D microstructures of sample BFS\_N4S0, some cells are completely filled with solids and some are partially filled with solids. Figure 9.17 shows the solid volume fraction of cells for sample BFS\_N4S0 at 3 hours, 1 day and 7 days. The solid volume fraction of cells for samples BFS\_N6S0 and BFS\_N6S5.4 are provided in Appendix C (Figures C.5 and C.6). It is clear that the solid volume fraction of cells for reaction products increased with time. This reflects the growth of reaction products.

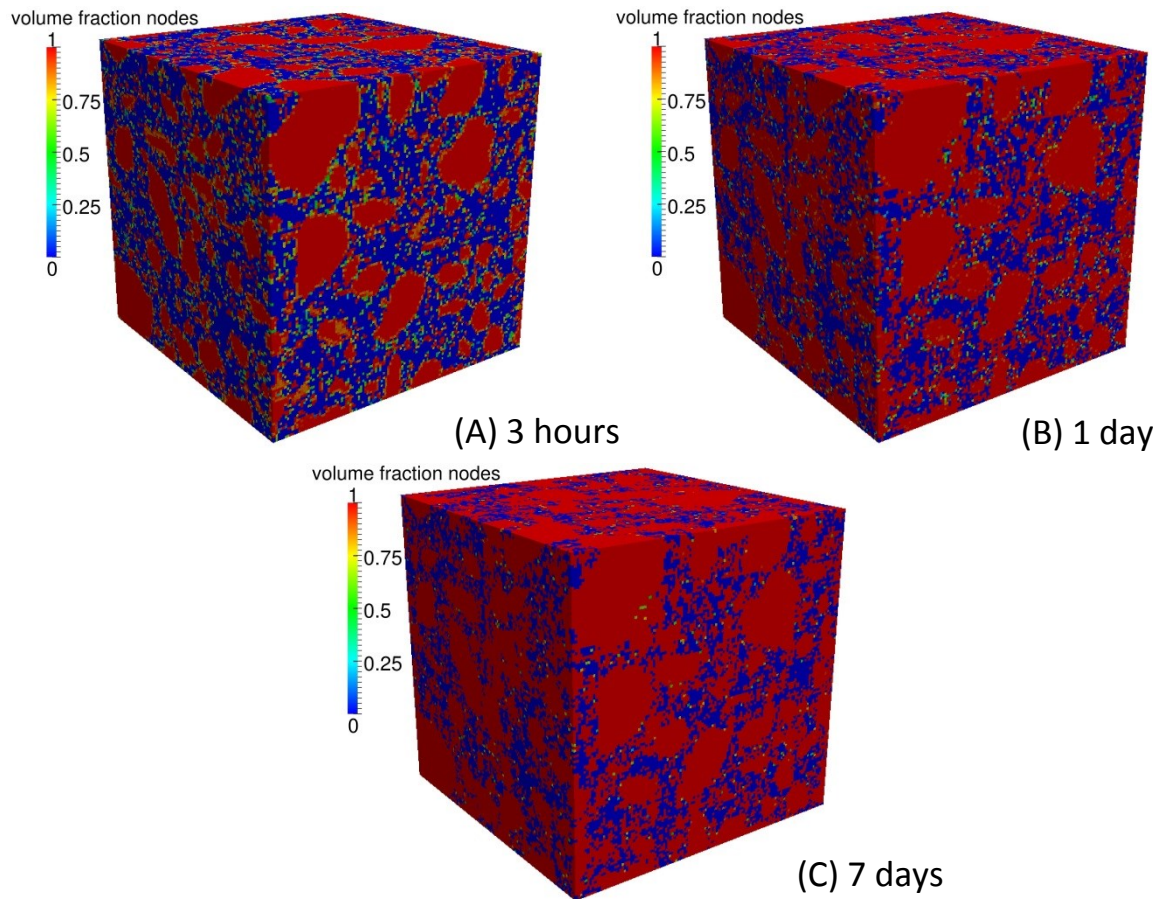


*Figure 9.17 Solid volume fraction of cells for sample BFS\_N4S0 at 3 hours, 1 day and 7 days. The size of the cubic unit cell is  $125\ \mu\text{m} \times 125\ \mu\text{m} \times 125\ \mu\text{m}$ . The digitization resolution is  $1\ \mu\text{m} \times 1\ \mu\text{m} \times 1\ \mu\text{m}$  per voxel. In the notations, BFS refers to alkali-activated slag, and N and S represent the weight percentage of  $\text{Na}_2\text{O}$  and  $\text{SiO}_2$  with respect to slag, respectively. See more details of mixtures in Table 3.2.*

With the growth of reaction products the microstructure of sample BFS\_N4S0 becomes denser with time. The density of the cells that were originally filled with liquid becomes larger with time as shown in Figure 9.18 for sample BFS\_N4S0. The density of cells for samples BFS\_N6S0 and BFS\_N6S5.4 are included in Appendix C (Figures C.7 and C.8).

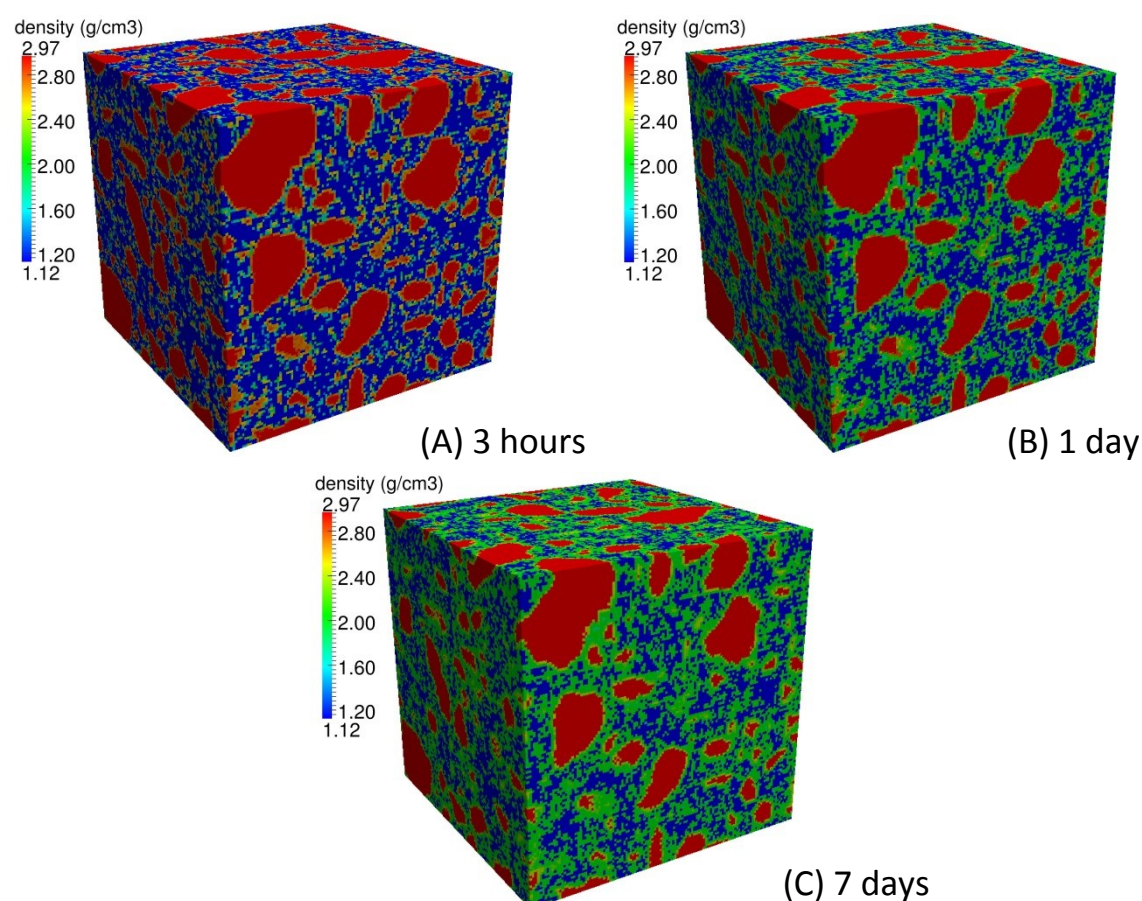


*Figure 9.18 Density of nodes for sample BFS\_N4S0 at 3 hours, 1 day and 7 days. The size of the cubic unit cell is  $125\ \mu\text{m} \times 125\ \mu\text{m} \times 125\ \mu\text{m}$ . The digitization resolution is  $1\ \mu\text{m} \times 1\ \mu\text{m} \times 1\ \mu\text{m}$  per voxel. In the notations, BFS refers to alkali-activated slag, and N and S represent the weight percentage of  $\text{Na}_2\text{O}$  and  $\text{SiO}_2$  with respect to slag, respectively. See more details of mixtures in Table 3.2.*

From GeoMicro3D it is also possible to obtain the distribution of reaction products in the sample. For example, Figure 9.19 presents the distribution of primary reaction products (C-(N-)A-S-H gel, including the adsorbed water and gel pore water) for sample BFS\_N4S0 at 3 hours, 1 day and 7 days. The distribution of the C-(N-)A-S-H gel (including the adsorbed water and gel pore water) for samples BFS\_N6S0 and BFS\_N6S5.4 are presented in Appendix C (Figures C.9 and C.10). It clearly shows that for sodium hydroxide activated slag systems the C-(N-)A-S-H gel mostly grew around the slag grains. In comparison with the distribution of primary reaction products for sodium hydroxide activated samples, i.e. BFS\_N4S0 and BFS\_N6S0, the distribution of primary reaction products for sodium silicate activated sample, i.e. BFS\_N6S5.4, was more homogeneous. These results are in good agreement with the observations from the SEM images presented in Chapter 5 (Figure 5.6).



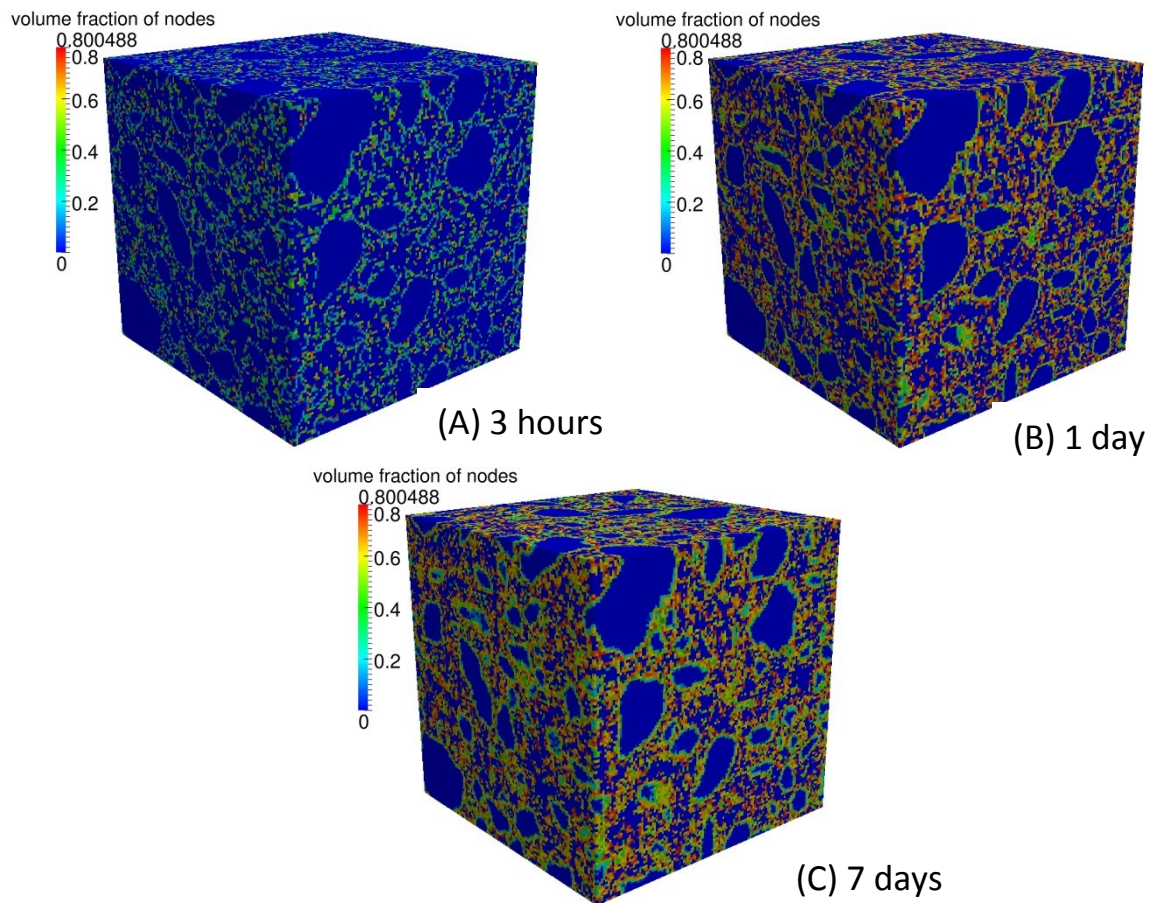


Figure 9.19 Distribution of the C-(N-)A-S-H gel (including adsorbed water and gel pore water) for sample BFS\_N4S0 at 3 hours, 1 day and 7 days. The size of the cubic unit cell is  $125\ \mu\text{m} \times 125\ \mu\text{m} \times 125\ \mu\text{m}$ . The digitization resolution is  $1\ \mu\text{m} \times 1\ \mu\text{m} \times 1\ \mu\text{m}$  per voxel. In the notations, BFS refers to alkali-activated slag, and N and S represent the weight percentage of  $\text{Na}_2\text{O}$  and  $\text{SiO}_2$  with respect to slag, respectively. See more details of mixtures in Table 3.2.

### 9.5.6 Volume evolution of phases

Figure 9.20 shows the simulated volume evolution of phases with GeoMicro3D in comparison with the calculated results using GEMS. More details of the calculated results using GEMS can be found in Chapter 8 (Figure 8.4). Since the amount of Fe in slag is very small (Table 3.1), Fe is not considered in GeoMicro3D. The thermodynamic modelling results (Figure 8.4) show that the amounts of mackinawite and brucite are very small in alkali-activated slag. So mackinawite and brucite are not considered in GeoMicro3D.

In general the simulated solid phases by GeoMicro3D were in line with the results calculated using GEMS. The C-(N-)A-S-H gel was the primary reaction product that consisted of more than 60 % of the volume of reaction products. The hydrotalcite-like phase (MA-OH-LDH) consisted of the second largest volume of reaction products. According to the simulation results by GeoMicro3D natrolite was formed in all samples and its amount increased with the increase of  $\text{Na}_2\text{O}$  content. In contrast natrolite was only formed in sample BFS\_N6S5.4 according to the calculated results by GEMS. The simulation results by GeoMicro3D also show that portlandite was formed in all samples. The amount of portlandite increased with the

increase of  $\text{Na}_2\text{O}$  content in the sample, while it decreased with the addition of  $\text{SiO}_2$  in the sample. This result is in good agreement with the calculated results using GEMS. Besides the solid phases, GeoMicro3D also provided the evolution of the adsorbed water and gel pore water retained by the C-(N-)A-S-H gel.

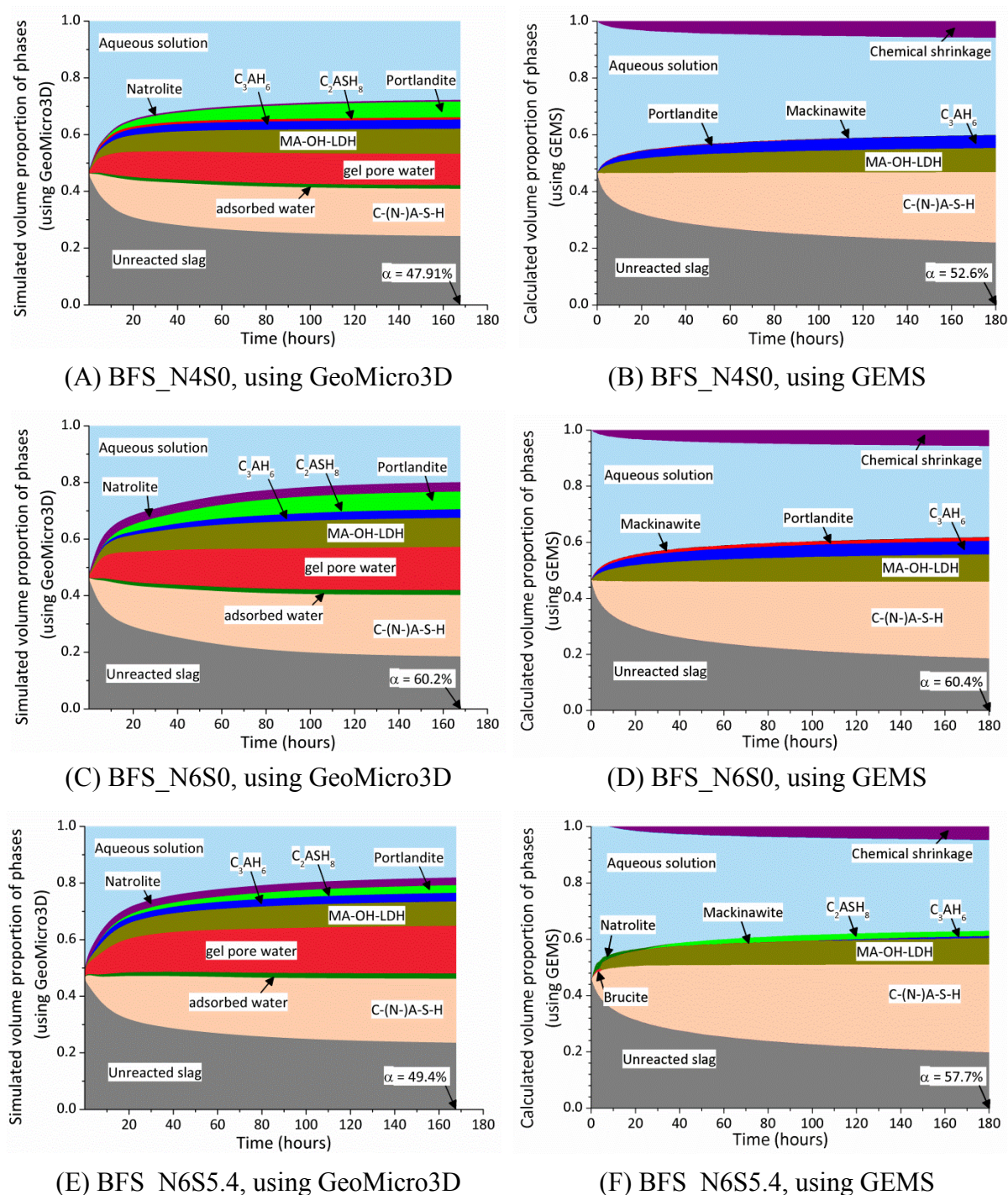


**Figure 9.20** Simulated volume proportion of phases with GeoMicro3D in comparison with the calculated results using GEMS. More details of the calculated results using GEMS can be found in Chapter 8 (Figure 8.4). In the notations, BFS refers to alkali-activated slag, and N and S represent the weight percentage of  $\text{Na}_2\text{O}$  and  $\text{SiO}_2$  with respect to slag. See more details of mixtures in Table 3.2.



### 9.5.7 Porosity and pore size distribution

Based on the simulated volume evolution of phases with GeoMicro3D the capillary porosity (i.e. the volume fraction of aqueous solution in Figure 9.20) was calculated and is presented in Figure 9.21. The sample with a higher content of  $\text{Na}_2\text{O}$  had a capillary lower porosity. For the samples with the same content of  $\text{Na}_2\text{O}$ , i.e. BFS\_N6S0 and BFS\_N6S5.4, an addition of  $\text{SiO}_2$  led to a lower capillary porosity. These results are in line with the observations from the experimental results in Chapter 5 (Figure 5.13).

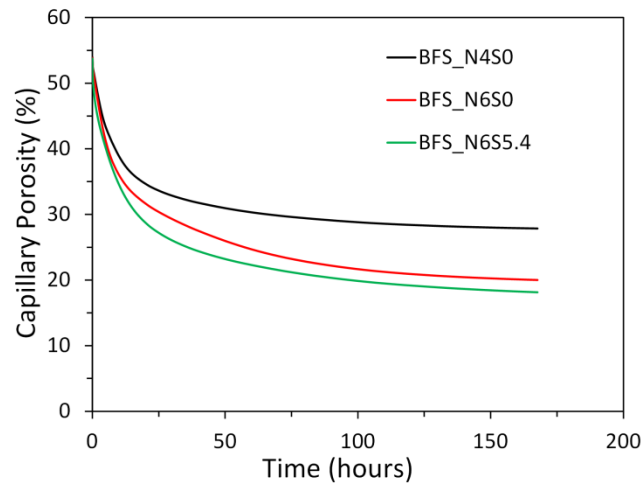


*Figure 9.21 Simulated capillary porosity with GeoMicro3D in comparison with the calculated results using GEMS. These results were obtained based on the volume evolution of phases (Figure 9.20). In the notations, BFS refers to alkali-activated slag, and N and S represent the weight percentage of  $\text{Na}_2\text{O}$  and  $\text{SiO}_2$  with respect to slag, respectively. See more details of mixtures in Table 3.2.*

Figure 9.22 displays the pore size distribution calculated from the simulated 3D microstructure with GeoMicro3D. With elapse of time the porosity decreased and the pore size distribution shifted to smaller pore sizes. The reduction of porosity and shift of pore size distribution to smaller pore sizes were also observed when the  $\text{Na}_2\text{O}$  content increased and the  $\text{SiO}_2$  was added into the sample. The reduction of porosity and shift of pore size distribution to smaller pore sizes indicate a denser microstructure. These simulation results are in line with the observations from the experimental results (Figures 5.15 and 5.16).

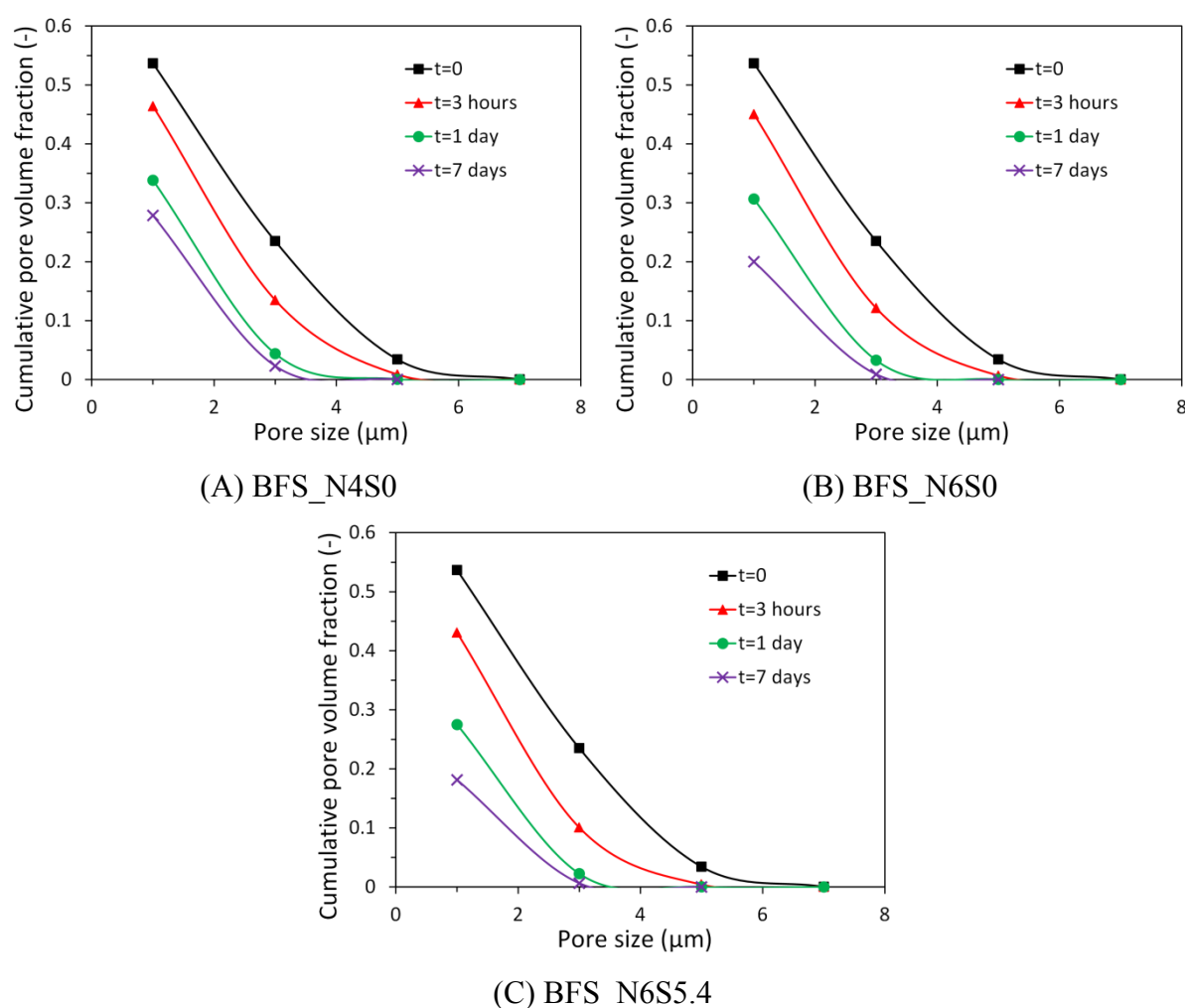


Figure 9.22 Calculated pore size distribution from the simulated 3D microstructure with GeoMicro3D. In the notations, BFS refers to alkali-activated slag, and N and S represent the weight percentage of  $\text{Na}_2\text{O}$  and  $\text{SiO}_2$  with respect to slag, respectively. See more details of mixtures in Table 3.2.

### 9.5.8 Simulation results of sample BFS\_N4S0 at an age of 28 days

As it will be discussed in more details in the following section, the computation efficiency of GeoMicro3D is not high. So the reaction of slag from the beginning to 28 days was only simulated for sample BFS\_N4S0. Table 9.4 present the simulation results of sample BFS\_N4S0 at an age of 28 days with GeoMicro3D. Along with the simulation results the experimental data are also presented for convenient comparisons. In general, the simulated results agreed with the experimental results with reasonable accuracy. The simulated degree of reaction and capillary porosity were a little smaller and larger, respectively, than the experimental results. This discrepancy may result from the ideal reaction condition that the empty space resulting from chemical shrinkage was always replenished with water. In this situation the concentration of  $\text{OH}^-$  around slag particles was underestimated, which slowed down the dissolution of slag. This then decreased the degree of reaction, reduced the amount of reaction products and thus underestimated the capillary porosity. The simulated element concentrations matched the experimental results within  $\pm 1$  order of magnitude. This discrepancy is close to the uncertainty of experimental data [69].

Table 9.4 Simulation results of sample BFS\_N4S0 at an age of 28 days

Item		GeoMicro3D	Experiment
Degree of reaction		0.485	0.573(0.051) <sup>a</sup>
Capillary porosity		0.274	0.194 <sup>b</sup>
Element concentration (mmol/L)	[Si]	11.6	3.73 <sup>c</sup>
	[Al]	16.3	7.46
	[Ca]	6.93	0.756
	[K]	61.8	81.2
	[Na]	$1.52 \times 10^3$	$1.75 \times 10^3$
	[OH <sup>-</sup> ]	$1.21 \times 10^3$	$1.29 \times 10^3$

a. Obtained by SEM-image analysis (see Figure 5.7). The number in the bracket is the deviation.

b. Obtained by MIP (see Figure 5.13).

c. The measured concentrations of Si, Al, Ca, K and Na were obtained by ICP-OES, while the measured concentration of OH<sup>-</sup> was obtained by titration against hydrochloride acid (0.1 mol/L). See more details in Figure 3.5.

## 9.6 Discussion

### 9.6.1 Computation efficiency

The computation efficiency largely depends on the digitization resolution. In the preliminary trials, the simulations were run at higher digitization resolutions, for instance 0.25 and 0.5  $\mu\text{m}$  per cubic voxel edge. It turned out that the computation efficiency of these trial simulations was rather low. A higher digitization resolution has two effects. On one hand it decreases the time interval in each lattice Boltzmann step. This, therefore, increases the number of iterations. On the other hand a higher digitization resolution leads to a huge increase of the computation load. These two effects decrease the computation efficiency. Besides the digitization resolution, the basic frequency and the number of cores that can be used during the computation also affect the computation efficiency. The codes of GeoMicro3D have been parallelized. GeoMicro3D can use cores as many as the computer has. The higher basic frequency and more cores that are used in the computation, the higher the computation efficiency is.

The simulations for samples BFS\_N4S0, BFS\_N6S0 and BFS\_N6S5.4 in this work were carried out in a computer server with the basic frequency of 3.6 GHz at the digitization resolution of 1  $\mu\text{m}$  per cubic voxel edge. The number of cores that were used was 16, 11 and 16 for samples BFS\_N4S0, BFS\_N6S0 and BFS\_N6S5.4, respectively. The time cost was 53.45, 98.15 and 57.48 hours, respectively, for the simulation of the reaction process and microstructure formation of samples for the first day. For implementation of GeoMicro3D, one should consider the digitization resolution and the capability of computation facilities.

### 9.6.2 Comparison of the simulation results from GeoMicro3D and the experimental results from MIP and SEM-image analysis

As an illustration for comparison Figure 9.23 shows the pore size distribution obtained from GeoMicro3D, MIP and SEM-image analysis for sample BFS\_N4S0 at 7 days. More details of the experimental results can be found in Chapter 5 (Figures 5.15 and 5.16). It is clear that the



pore size distributions obtained from GeoMicro3D, MIP and SEM-image analysis were quite different from each other. The comparison between the pore size distributions from MIP and those from SEM-image analysis has been presented and discussed in Chapter 5 (see Section 5.4.1).

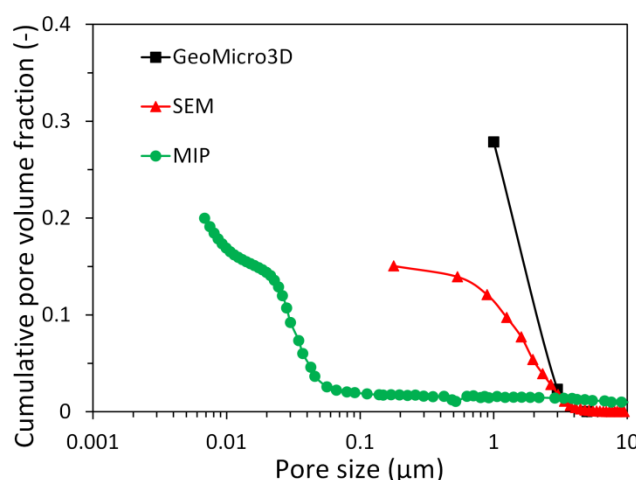


*Figure 9.23 Pore size distribution obtained from GeoMicro3D, MIP and SEM-image analysis for sample BFS\_N4S0 at 7 days. More details of the experimental results can be found in Chapter 5 (Figures 5.15 and 5.16).*

The pore size distribution obtained from GeoMicro3D had larger pore sizes than the experimental ones. This is because the pore size distribution from GeoMicro3D was affected by the digitization resolution. The minimum pore size simulated by GeoMicro3D is actually equal to the digitization resolution ( $1 \mu\text{m}^3/\text{voxel}$ ). Besides the pore size, the simulation results by GeoMicro3D also had a larger porosity than the results from MIP and SEM-image analysis. As discussed in Chapter 5, MIP cannot detect the isolated pores. As a result the porosity measured by MIP was underestimated. As for the porosity obtained from SEM-image analysis, it cannot reflect the real pore volume since it was obtained from the 2D images. Furthermore all the experimental results did not take into account the shrinkage of samples. Ignoring the shrinkage of samples also led to underestimation of the porosity. To sum up, each analysis technique has its own limitations. It is possible to use either of these techniques or combine them to investigate the effects of factors of interest on the microstructure development, such as contents of  $\text{Na}_2\text{O}$  and  $\text{SiO}_2$ . However, it is not recommended to use the results obtained by one technique to quantitatively validate the results by another.

## 9.7 Conclusions

From the results presented in this chapter, the following conclusions can be drawn:

- (1) GeoMicro3D is developed and used to simulate the reaction process and microstructure formation of alkali-activated slag with three different alkaline activators. The simulation results by GeoMicro3D are presented and discussed with respect to the degree of reaction of slag, element concentration, 3D microstructure, volume evolution of phases and pore structure. The simulated reaction kinetics (degree of reaction of slag) and pore solution chemistry (element concentration) were in agreement with the experimental results.

- (2) The simulated volume evolution of phases by GeoMicro3D was consistent with the results calculated by GEMS. The simulated pore structure shows a reduction of porosity and a shift of pore size distribution to small pores when the reaction time and contents of  $\text{Na}_2\text{O}$  and  $\text{SiO}_2$  increased. These results were in line with the experimental results.
- (3) The visualized distribution of the concentration of Si by GeoMicro3D show that Si concentrated around the dissolving slag grains. Thus the concentration of Si in the cells close to the slag grains was much larger than the concentration in the pore solution.
- (4) The computation efficiency of GeoMicro3D largely depends on the digitization resolution of the samples. Besides the digitization resolution, the basic frequency and the number of cores that are used during the computation also affect the computation efficiency.

## **PART IV**

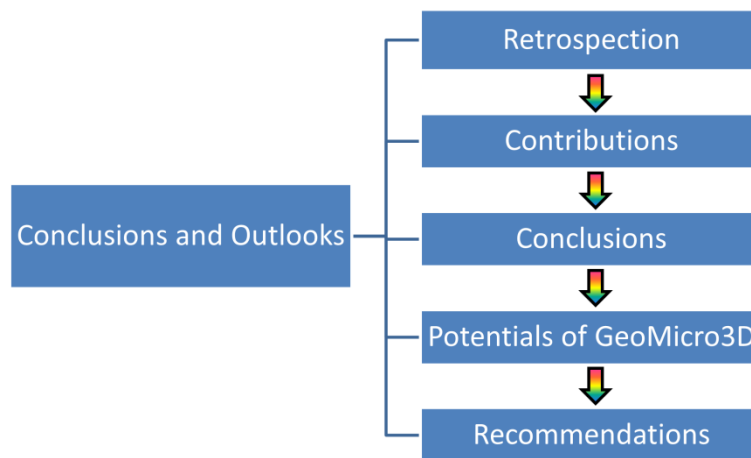
---

# **CONCLUSIONS**



# Chapter 10

## Retrospection, conclusions and outlooks



This chapter summarizes the work presented in this research. Contributions of this research, potentials of GeoMicro3D and recommendations for future research are given.

## 10.1 Retrospection

Alkali-activated materials (AAMs) show promising potentials for use as building materials. Before utilization, AAMs must satisfy the properties required from the application sector, such as good durability and long-term service life. The reaction process and microstructure formation of AAMs are two main factors that determine the properties of AAMs. As shown in Figure 10.1 this research adopts two routes to study the reaction process and microstructure formation of AAMs, i.e. the experimental study route and numerical simulation route. The experimental study route deals with the pore solution composition, reaction kinetics and microstructure development of AAMs. The numerical simulation route consists of the simulations of initial particle parking structure of precursor particles in alkaline activator, dissolution of precursors, chemical reactions and microstructure formation of AAMs. The observations and findings from the experimental study route provide insights for developing and validating the numerical model. With the developed numerical model, it is possible to numerically investigate the reaction process and microstructure formation of AAMs. Based on the numerical study in this thesis it is possible to investigate and predict many microstructure-related-physical-properties, such as tensile strength, permeability and diffusivity of chloride.

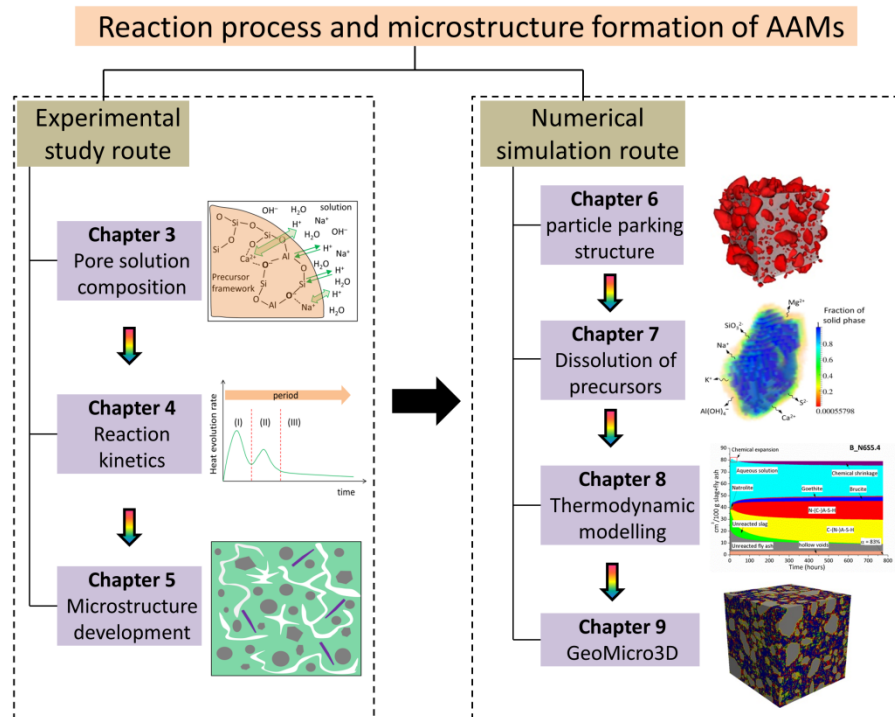


Figure 10.1 Two routes to study the reaction process and microstructure formation of AAMs.

Pore solution is an essential component of AAMs. It is in this medium where the aluminosilicate precursors dissolve and subsequently reactions take place to produce solid reaction products. In Chapter 3, the pore solutions of alkali-activated slag, alkali-activated fly ash and alkali-activated slag/fly ash pastes were studied by means of ICP-OES. The influences of type and concentration of alkaline activator and temperature on the pore solution composition were investigated. The experimental data obtained in Chapter 3 were used to validate the thermodynamic modelling results in Chapter 8 and the simulated pore solution composition by GeoMicro3D in Chapter 9.

In Chapter 4, the reaction kinetics of alkali-activated slag, alkali-activated fly ash and alkali-activated slag/fly ash were investigated by using isothermal calorimetry. According to the calorimetric responses, the reaction process of alkali-activated slag, fly ash and slag/fly ash was divided into different reaction stages. The reaction mechanism behind each reaction stage was discussed. Particularly the origin of the induction period was discussed. The obtained results of the reaction kinetics in Chapter 4 provided insights for developing GeoMicro3D in the subsequent chapters.

In Chapter 5, the microstructure development of alkali-activated slag paste, alkali-activated fly ash paste, and alkali-activated slag/fly ash paste was studied using SEM and MIP. The effects of alkaline activator and curing temperature on the microstructure formation were investigated. The studied parameters included the distribution of reaction products, total porosity, pore size distribution, and differential pore size distribution. The obtained results in Chapter 5 provided new insights into the microstructure formation of AAMs. All these results were used to develop GeoMicro3D in the next chapters.

The initial particle parking structure is the starting point to simulate the reactions and microstructure formation of AAMs. In Chapter 6, a geometry model, i.e. Anm material model, was extended to simulate the initial particle parking structure of precursor particles in alkaline activator using real-shape particles. The extended Anm material model in Chapter 6 was used to generate the initial particle parking structure for simulating the dissolution of precursors in alkaline solution in Chapter 7 and for simulating the reaction process and microstructure formation of AAMs in Chapter 9.

In Chapter 7, a numerical model was developed to simulate the dissolution of precursors in alkaline solution. The influences of temperature, reactivity of precursors, alkalinity of solution and inhibiting effect of aqueous Al etc. on the dissolution of precursors were taken into account in the model. The numerical model presented in Chapter 7 makes up the dissolution module of GeoMicro3D in Chapter 9.

In Chapter 8, a thermodynamic model was developed to describe the N-A-S-H gel and the associated thermodynamic data were obtained for the first time. By incorporating the thermodynamic data of this model into the thermodynamic database available in the literature (see Section 8.2.5), it is possible to simulate the reactions in alkali-activated slag, alkali-activated fly ash and alkali-activated slag/fly ash systems through thermodynamic modelling. The presented thermodynamic models in Chapter 8 make up the thermodynamic modelling module of GeoMyicro3D in Chapter 9.

In Chapter 9, the module of nucleation and growth of reaction products was presented. A nucleation probability theory was used to describe the nucleation and growth of reaction products and a novel approach was proposed to speed up the nucleation simulations. By assembling the modules of initial particle parking structure (Chapter 6), dissolution of precursors (Chapter 7), thermodynamic modelling (Chapter 8) and nucleation and growth (Chapter 9), the GeoMicro3D model was established. As a case study, the GeoMicro3D model was implemented to simulate the reaction process and microstructure formation of alkali-activated slag systems with different alkaline activators. The simulation results were discussed and validated by comparing to the experimental results.

## 10.2 Contributions of this research

This research contributes to a better understanding of the reaction process of AAMs and provides a numerical tool for the AAMs society. With this numerical tool it is possible to design, predict and validate the chemical and physical properties of AAMs. The main contributions of this research are as follows:

- (1) This research contains a systematic study on the pore solution composition of alkali-activated slag, alkali-activated fly ash and alkali-activated slag/fly ash pastes. The effects of type and concentration of alkaline activator and curing temperature on the pore solution composition were investigated. The obtained results provided new insights into the pore solution chemistry of AAMs.
- (2) The origin of the induction period during the reaction of AAMs was investigated. The presence of soluble silicate in the alkaline activator caused an induction period for alkali-activated slag systems, while it prevented the occurrence of the induction period during the reaction of alkali-activated fly ash systems. The fact that an induction period occurred in alkali-activated fly ash systems was mainly attributed to the passivation of the leached surface layer by the absorbed Al.
- (3) The effects of sodium and silica contents on the reaction kinetics and microstructure formation of AAMs were systematically studied. A higher sodium content accelerated the reactions of alkali-activated slag and alkali-activated fly ash, while the effect of silica content on the reaction kinetics of AAMs depended on the type of precursor. In comparison with the sodium content, the silica content had a larger effect on the microstructure formation of alkali-activated slag and alkali-activated fly ash.
- (4) In this research the Anm model was extended and applied to simulate the initial particle packing structure of AAMs using real-shape particles of slag and fly ash. This is different from the particle-based numerical models [136-139] that used regular shape particles (usually spherical particles) to represent the particles of cement, slag and fly ash.
- (5) A dissolution model was developed to simulate the dissolution of aluminosilicate precursors in alkaline solution. This dissolution model considered the influences of temperature, reactivity of aluminosilicate precursors, alkalinity of the solution and inhibiting effect of aqueous Al on the dissolution.
- (6) A thermodynamic model, i.e. N(C)ASH<sub>ss</sub>, was developed to describe the N-A-S-H gel. With this model it is possible to perform thermodynamic modelling of the reactions in low-calcium-alkali-activated-materials, for instance alkali-activated fly ash systems. Furthermore it is also possible to perform thermodynamic modelling of the reactions in alkali-activated slag/fly ash systems by coupling this model and the C(N)ASH<sub>ss</sub> model proposed by Myers et al. [69].
- (7) A numerical model, i.e. GeoMicro3D, for simulating the reaction process and the microstructure formation of AAMs was developed in this research. Based on this model many microstructure-related-physical-properties of AAMs can be studied numerically, such as tensile strength, permeability and diffusivity of chloride.



### 10.3 Conclusions and observations

The conclusions from the experimental study and numerical simulation of the reaction process and microstructure formation of AAMs are as follows:

*(1) The pore solution composition of AAMs depends on the activation conditions*

The curing temperature and silica content have pronounced effects on the pore solution composition of alkali-activated fly ash. An increase of the curing temperature, for instance from 40 °C to 60 °C, led to a decrease of the concentrations of Si, Al, Ca, K, Fe and Mg in the pore solution. In comparison with the sodium hydroxide activated fly ash pastes the concentrations of Si, Al, Ca, K, Fe and Mg were larger in the sodium silicate activated fly ash pastes.

The pore solution composition of alkali-activated slag also depends on the activation conditions. An increase of the sodium content led to an increase of the concentrations of Si, Al, K, Na and OH<sup>-</sup> in the pore solution. In contrast an increase of the silica content led to an decrease of the concentrations of K, Na and OH<sup>-</sup> in the pore solution.

*(2) The sodium content, silica content and curing temperature affect the reaction kinetics of AAMs*

Table 10.1 summarizes the observed number of calorimetric peaks and reaction periods of AAMs. An increase of Na<sub>2</sub>O content led to a higher calorimetric peak and accelerated the reaction of alkali-activated slag or fly ash. The effect of SiO<sub>2</sub> content on the reaction kinetics, however, varied with the type of aluminosilicate precursor. An addition of SiO<sub>2</sub> in the alkaline activator resulted in an induction period during the reaction of alkali-activated slag, while it prevented the occurrence of the induction period during the reaction of alkali-activated fly ash.

*Table 10.1 Observed number of calorimetric peaks and reaction periods of AAMs*

Precursor	Activator	Number of peaks	Reaction periods
slag	sodium hydroxide	2	
slag	sodium silicate	2	
fly ash	sodium hydroxide	2	
fly ash	sodium silicate	1	
slag + fly ash	sodium silicate	3	

Besides the alkalinity and type of alkaline activator, the number of reaction stages of alkali-activated fly ash also depended on the curing temperature. A higher curing temperature accelerated the reaction of alkali-activated fly ash and reduced the passivation of the leached surface layer. So, the induction period might not occur in sodium hydroxide activated fly ash at higher temperatures, for example the sample FA\_N9.3S0T60.

*(3) The origin of the induction period is different for alkali-activated slag systems and alkali-activated fly ash systems.*

For alkali-activated slag systems, the presence of soluble Si in the activator slowed down the dissolution of slag and caused an induction period. In contrast, the fact that an induction period occurred in alkali-activated fly ash was mainly attributed to the passivation of the leached surface layer by the absorbed Al.

*(4) The type and concentration of alkaline activator affect the microstructure formation of AAMs*

The effect of Na<sub>2</sub>O content on the microstructure development of AAMs varies with the type of aluminosilicate precursor. For alkali-activated slag systems, an increase of Na<sub>2</sub>O content led to a reduction of the total porosity and a refinement of the microstructure. For alkali-activated fly ash systems, however, an increase of Na<sub>2</sub>O content did not influence the total porosity very much. Instead, it altered the microstructure by increasing the amount of large pores and decreasing the amount of small pores.

The SiO<sub>2</sub> content seriously affects the microstructure formation of AAMs. In sodium hydroxide activated systems a relatively coarse microstructure was produced with connected capillary pores. In sodium silicate activated systems, by contrast, the soluble silicate in the activator led to a relatively dense microstructure with separated small capillary pores.

*(5) Using real-shape particles increases the total/bulk specific surface area and refines the pore structure of the simulated initial particle parking structure*

In comparison with the simulated initial particle parking structures using spherical particles, those using real-shape particles had larger *total* surface areas (up to 23 %) and larger bulk specific surface area (at least 12 %). For the investigated AAMs with high liquid/binder ratios (> 0.47), the pore size distribution of the simulated initial particle parking structures was not significantly affected by the particle shape. At low liquid/binder ratios, however, using real-shape particles led to a significant shift of the pore size distribution to small pores as compared to using the spherical particles in the initial particle parking structures.

*(6) The N(C)ASH<sub>ss</sub> model is able to describe the N-A-S-H gel with reasonable accuracy*

A thermodynamic model, i.e. the N(C)ASH<sub>ss</sub> model, is developed to describe the N-A-S-H gel in low-Ca-alkali-activated-materials, for instance the alkali-activated fly ash. The simulation results show that a higher degree of reaction of fly ash led to a larger Si/Al ratio in the N-A-S-H gel. This is in good agreement with the experimental results. The simulated concentrations of Si, Na, Ca and OH<sup>-</sup> in the pore solution of alkali-activated fly ash paste matched the experimental results within ± 1 order of magnitude.

*(7) The simulation results by GeoMicro3D are in line with the experimental results*

GeoMicro3D is developed for simulating the reaction process and microstructure formation of AAMs. The functionalities of GeoMicro3D are listed in Table 10.2. As a case study GeoMicro3D was used to simulate the reaction process and microstructure formation of alkali-activated slag with three different alkaline activators. The simulated reaction kinetics (degree of reaction of slag) and pore solution chemistry (element concentration) were in agreement with the experimental results. The simulated volume evolution of solid phases by GeoMicro3D was consistent with the results calculated by GEMS with regard to the primary

reaction products (C-(N-)A-S-H) and some crystalline reaction products, such as hydrotalcite-like phase and katoite. Besides the volume evolution of solid phases, GeoMicro3D also provided the volumes of adsorbed water and gel pore water that were retained by the C-(N-)A-S-H gel. Like the techniques of MIP and SEM-image analysis, GeoMicro3D was also able to obtain insights into the microstructure formation of AAMs.

*Table 10.2 Functionalities of GeoMicro3D*

Functionality	GeoMicro3D
Available systems	Mono system: AAS, AAFA Binary system: AA BFS/FA
Degree of reaction of precursor	Available
Pore solution chemistry	Available
Microstructure formation	Available
Volume evolution of solid phases	Available
Distribution of reaction products	Available
Distribution of ions	Available
Element composition of each cell	Available
Evolution of capillary porosity	Available
Evolution of gel porosity	Available
Parallelization of codes	Yes

*(8) The computation efficiency of GeoMicro3D depends on the digitization resolution of the samples, number of cores and basic frequency of the computer*

The effect of digitization resolution on the computation efficiency of GeoMicro3D is twofold: A higher digitization resolution decreases the time interval in each lattice Boltzmann step. This, therefore, increases the number of iterations. Furthermore a higher digitization resolution leads to a huge increase of the computation efforts. These two effects decrease the computation efficiency. Besides the digitization resolution, the basic frequency and number of cores that are used during the computation also affect the computation efficiency. The higher basic frequency and more cores that are used in the computation, the higher the computation efficiency is.

## 10.4 Outlooks

### 10.4.1 Potentials of GeoMicro3D

A novel numerical simulation framework was developed in this thesis to simulate the reaction process and microstructure formation of AAMs. Based on this framework GeoMicro3D was established. As a case study, GeoMicro3D has been implemented to simulate the reaction process and microstructure formation of alkali-activated slag systems. In addition to this case study GeoMicro3D has many other potentials, such as:

*(1) Simulation of the reaction process and microstructure formation of AAMs with different sources of aluminosilicate precursors*

GeoMicro3D was developed by strictly following the simulations of the initial particle parking structure, dissolution of precursors, diffusion of ions, chemical reactions of ions and

nucleation and growth of reaction products in AAMs. Each simulation process is carried out based on the individual lattice cell, as shown in Figure 10.2. Therefore, it is feasible to simulate the reaction process and microstructure formation of other alkali-activated materials by only changing the initial particle parking structure and some parameters appropriately, such as the solubility of  $\text{SiO}_2$ ,  $\text{Al}_2\text{O}_3$  and  $\text{CaO}$  in the precursor for dissolution.

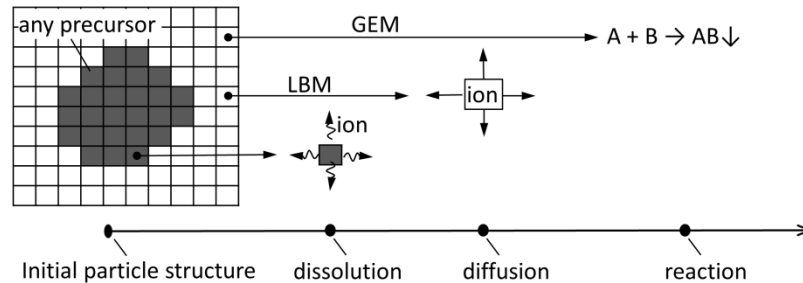


Figure 10.2 Schematic algorithm of GeoMicro3D to simulate the reaction process and microstructure formation of AAMs. LBM refers to lattice Boltzmann method and GEM refers to thermodynamic modelling with GEM code package. A and B represent ions and AB represents a solid reaction product.

## (2) Mixture design

Many sources of aluminosilicate materials can be used as precursors to produce AAMs. Alkali activation of aluminosilicate precursors depends on many factors, such as the alkaline activator, curing temperature and precursor itself. It is work and materials consuming for obtaining the desired mixtures through trial experiments. In this situation, therefore, GeoMicro3D can serve as a tool to design appropriate mixtures.

## (3) Prediction of mechanical properties

AAMs are porous materials. The pore structure determines the mechanical properties of AAMs, for instance the tensile strength. It has been demonstrated that the mechanical properties can be predicted by making use of a 3D lattice fracture model and the voxel-based microstructure of cement paste [217]. GeoMicro3D simulates the microstructure formation and provides the voxel-based microstructure of AAMs. Combining GeoMicro3D and the 3D lattice fracture model it is possible to investigate the mechanical properties of AAMs numerically.

## (4) Prediction of transport properties and evaluation of durability

Transport properties of AAMs, such as permeability and diffusivity, are significant factors that determine the durability and service life of AAMs. The permeability, diffusivity and other transport properties can be derived from the simulated microstructure by GeoMicro3D. Therefore, GeoMicro3D can provide the input to evaluate the durability of AAMs-based structures.

## (5) Simulation of carbonation of AAMs

Carbonation is one of the major practical issues that significantly affect the performance of AAMs [218]. Compared with OPC-based materials, AAMs have a very high alkali content in the pore solution. The carbonation of AAMs initiates from the carbonation of the pore

solution, forming alkali carbonates. Afterwards the reaction products such as the C-(N-)A-S-H gel may be subject to carbonation. GeoMicro3D provides the simulated pore solution composition and solid phase composition of AAMs. Using these results as the input, the carbonation of AAMs can be studied numerically.

#### 10.4.2 Recommendations for future research

In this thesis a numerical model, i.e. GeoMicro3D, is developed for simulating the reaction process and microstructure formation of AAMs. Although GeoMicro3D has been implemented to simulate the reaction process and microstructure formation of alkali-activated slag systems, there is still room to improve and extend GeoMicro3D for further research. The following aspects should be taken into account in future modelling studies:

##### *(1) Heterogeneous distribution of phases in aluminosilicate precursors*

In AAMs, the phase composition and distribution of aluminosilicate precursors depend on the type of the precursor. Ground granulated blast furnace slag contains more than 95 % amorphous phase. Therefore, the distribution of elements in slag can be regarded as homogeneous. In contrast, fly ash consists of crystalline phases and an amorphous phase. The amorphous phase in fly ash is much smaller than that in slag. As shown in Figure 10.3, the elements in fly ash are distributed heterogeneously. The heterogeneous distribution of elements exerts an effect on the dissolution kinetics of fly ash, which further affects the reaction process and microstructure formation of alkali-activated fly ash. Therefore, further work is needed to consider the heterogeneous distribution of elements in precursors, particularly like the fly ash type precursors.

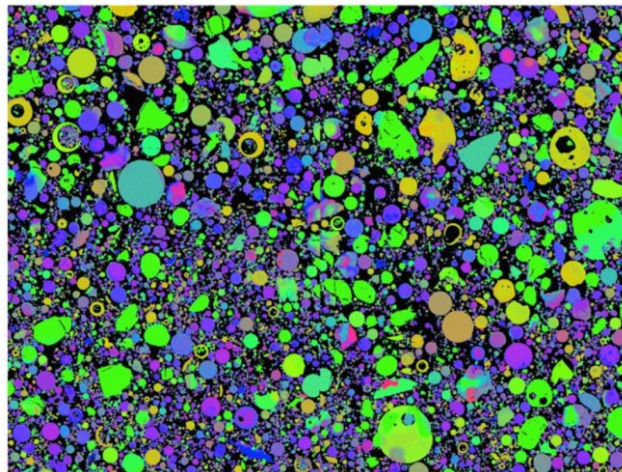


Figure 10.3 Visual representation of the distribution of elements in fly ash measured by EDS (cited from [219]). Red, green and blue represent Al, Si and Ca, respectively.

##### *(2) Forward dissolution rate*

The dissolution rate has a large dependence on the forward dissolution rate (see Equation 7.1). The forward dissolution rate depends on the reactivity of precursor and alkalinity of alkaline solution. In order to determine the forward dissolution rates of Si and Ca, a batch of tests were carried out in this thesis and a group of experimental data from the literature was used (see

Appendixes A.4 and A.5, respectively). But still more experimental data from the dissolution of precursors is needed to improve the established Equations 7.11 and 7.16.

### *(3) Thermodynamic model – N(C)ASH<sub>ss</sub>*

A thermodynamic model, i.e. N(C)ASH<sub>ss</sub>, was developed in this thesis for describing the N-A-S-H gel in low-calcium-alkali-activated-materials, for instance alkali-activated fly ash (see Chapter 8). This model consists of eight solid solution members as shown in Table 8.2. The solubility products of these eight solid solution members were determined by optimizing the fit of the modelling results to the pore solution composition data in this work and the solid phase data in the literature [58]. The simulated concentrations of Si, Na, Ca and OH<sup>-</sup> are in agreement with the experimental results within  $\pm 1$  order of magnitude, which is close to the uncertainty of experimental measurements. The simulated concentration of Al, however, was underestimated by several orders of magnitude. This indicates that more aqueous phase composition data and solid phase composition data are needed to improve the solubility products of the N(C)ASH<sub>ss</sub> solid solution members. Furthermore, the simulated solid phase evolution of alkali-activated fly ash was not validated by experiments yet in this research. So the experimental study of the solid phase evolution of alkali-activated fly ash is also needed in future research.

### *(4) Relaxation time scheme*

A single relaxation time scheme was used in the implementation of the lattice Boltzmann method in this thesis. Using the single relaxation time scheme, however, requires a large number of iterations to reach the steady state and thus it is computationally inefficient [169]. Multi relaxation time schemes, by contrast, reduce the number of iterations needed to reach the steady state. Therefore changing from a single relaxation time scheme to multi relaxation time schemes is probably one aspect that could increase the computation efficiency of GeoMicro3D.

### *(5) Model parameters and validation*

The values of many model parameters are not reported in the current literature, for example the kinetic parameter of nucleation for each reaction product (see Section 9.2.1 in Chapter 9). The number of these unknown parameters increases with the number of reaction products that are considered in the simulation. In the current GeoMicro3D these parameters are determined through the parameter study. In future modelling studies these parameters should be determined by other techniques, for example by experimental techniques [21], and their effects on the simulation results should be also evaluated. Furthermore, more mixtures with different mix compositions should be used to further validate GeoMicro3D with regard to reaction kinetics, pore solution chemistry and microstructure etc.

# Summary

---

Alkali-activated materials (AAMs) show promising potentials for use as building materials. Before the utilization, AAMs must satisfy the properties required from the construction sector, such as good durability and long-term service life. These properties mainly depend on the chemical and physical properties of the microstructure of AAMs. In the literature many studies have been presented about the reaction process and microstructure formation of AAMs, but still some aspects are not given due attention, such as the pore solution composition of AAMs and the origin of the induction period during the reaction of AAMs. Furthermore no computer-based simulation models have been developed so far for simulating the reaction process and microstructure formation of AAMs. It is still a big issue and challenge today to numerically obtain the microstructure of AAMs.

This research adopted two routes to study the reaction process and microstructure formation of AAMs, i.e. the experimental study route and numerical simulation route. Ground granulated blast furnace slag and fly ash were used as the aluminosilicate precursors and sodium hydroxide and sodium silicate were used as the alkaline activators. The experimental study route provided new results for better understanding the reaction process and microstructure formation of AAMs. Then the new insights from the experimental study route helped to develop the GeoMicro3D model for simulating the reaction process and microstructure formation of AAMs.

## **(1) Experimental study route**

Firstly, the pore solutions of alkali-activated slag, alkali-activated fly ash and alkali-activated slag/fly ash pastes with different activators and reaction conditions were studied by means of ICP-OES. It was found the pore solution composition of AAMs depended on the activation conditions, such as the type and concentration of alkaline activator and curing temperature.

Then, the reaction kinetics of alkali-activated slag, alkali-activated fly ash and alkali-activated slag/fly ash pastes were investigated by using isothermal calorimetry. The sodium content, silica content and curing temperature affected the reaction kinetics of AAMs. The origin of the induction period was different for alkali-activated slag systems and alkali-activated fly ash systems. For alkali-activated slag systems, the presence of soluble Si in the activator slowed down the dissolution of slag and caused an induction period. In contrast, the fact that an induction period occurred in alkali-activated fly ash systems was mainly attributed to the passivation of the leached surface layer caused by the absorbed Al.

Finally, the microstructure development of alkali-activated slag, alkali-activated fly ash and alkali-activated slag/fly ash pastes was studied using SEM and MIP. It was found that the type and concentration of alkaline activator affected the microstructure formation of AAMs. An increase of Na<sub>2</sub>O content led to a reduction of the total porosity and a refinement of the microstructure for alkali-activated slag systems. In contrast, an increase of Na<sub>2</sub>O content did not affect the total porosity of alkali-activated fly ash systems very much. Instead, it altered the microstructure by increasing the amount of large pores and decreasing the amount of small pores. The SiO<sub>2</sub> content seriously affected the microstructure formation of AAMs. In

sodium silicate activated systems, the soluble silicate in the activator led to a relatively dense microstructure with separated small capillary pores. This was different from the relatively coarse microstructure with connected capillary pores in sodium hydroxide activated systems.

## **(2) Numerical simulation route**

Firstly, the initial particle parking structure of AAMs, as the starting point for simulating the reactions and microstructure formation, was simulated using real-shape particles of slag and fly ash. In comparison with the spherical particles, using real-shape particles increased the total surface area (up to 23 %) and bulk specific surface area (at least 12 %) of the simulated initial particle parking structures. At low liquid/binder ratios ( $\leq 0.47$ ), using real-shape particles led to a significant shift of the pore size distribution to small pores as compared to using the spherical particles in the simulated initial particle parking structures.

Secondly, a dissolution model was developed for simulating the dissolution of aluminosilicate precursors in alkaline solution. The influences of temperature, reactivity of precursors, alkalinity of solution and inhibiting effect of aqueous Al etc. on the dissolution of precursors were taken into account in this model. The simulation results of the dissolution of slag and fly ash in alkaline solution were in agreement with the experimental data.

Then, the reactions in AAMs were thermodynamically simulated. A thermodynamic model, i.e. N(C)ASH<sub>ss</sub>, was developed to describe the N-A-S-H gel. With this model and the C(N)ASH<sub>ss</sub> model in the literature it is possible to perform thermodynamic modelling of the reactions in alkali-activated fly ash systems and alkali-activated slag/fly ash systems. The simulated pore solution compositions of AAMs were in line with the experimental results.

Finally, the GeoMicro3D model was built up based on the numerical modules of initial particle parking structure, dissolution of aluminosilicate precursor, thermodynamic modelling and nucleation & growth of reaction products. As a case study GeoMicro3D was implemented to simulate the reaction process and microstructure formation of alkali-activated slag with three different alkaline activators. The simulated reaction kinetics (degree of reaction of slag) and pore solution chemistry (element concentration) were in agreement with the experimental results. The simulated volume evolution of solid phases by GeoMicro3D was consistent with the results calculated by GEMS with regard to the primary reaction products (C-(N-)A-S-H) and some crystalline reaction products, such as the hydrotalcite-like phase and katoite. Besides the volume evolution of solid phases, GeoMicro3D also provided the volumes of adsorbed water and gel pore water that were retained by the C-(N-)A-S-H gel.

To sum up, the reaction process and microstructure formation of AAMs were studied experimentally and numerically. Based on the insights obtained from the experimental study numerical models were developed and validated. With these models it is possible to simulate the initial particle parking structure of slag/fly ash in alkaline activator, dissolution of slag/fly ash, chemical reactions and microstructure formation of AAMs with reasonable accuracy.



# Samenvatting

---

Alkali-geactiveerde materialen (AAM's) laten veelbelovende mogelijkheden zien voor gebruik als bouwmaterialen. Voor gebruik in de bouwsector moeten AAM's voldoen aan een aantal eigenschappen, zoals een goede duurzaamheid en een lange levensduur. Deze eigenschappen zijn hoofdzakelijk afhankelijk van de chemische en fysische eigenschappen van de microstructuur van AAM's. In de literatuur zijn veel studies uitgevoerd naar het reactieproces en de vorming van de microstructuur van AAM's, maar aan sommige aspecten is nog onvoldoende aandacht besteed, zoals de samenstelling van het poriënwater van AAM's en de oorzaak van de inductieperiode tijdens de reactie van AAM's. Verder zijn tot nu toe geen numerieke modellen ontwikkeld voor het simuleren van het reactieproces en van de microstructuurvorming van AAM's. Het is nog steeds een groot probleem en een uitdaging om numeriek de microstructuur van AAM's te verkrijgen.

Dit onderzoek behelst twee routes om het reactieproces en de microstructuurvorming van AAM's te bestuderen, te weten de experimentele route en die van numerieke simulatie. Gemalen hoogovenslakken en vliegasken zijn gebruikt als aluminosilicaat reactant en natriumhydroxide en natriumsilicaat zijn gebruikt als alkalische activators. De experimentele route leverde nieuwe resultaten op voor een beter begrip van het reactieproces en de vorming van microstructuren van AAM's. Deze nieuwe inzichten uit de experimentele studie zijn gebruikt om het GeoMicro3D-model te ontwikkelen voor het simuleren van het reactieproces en de vorming van microstructuren van AAM's.

## **(1) Experimentele studieroute**

Eerst is de samenstelling van het poriënwater van alkali-geactiveerde slakken, alkali-geactiveerde vliegasken en alkali-geactiveerde slak/vliegasken bestudeerd met behulp van verschillende activators en verschillende reactieomstandigheden, bestudeerd met behulp van ICP-OES. Het bleek dat de samenstelling van het poriënwater van AAM's afhing van de activeringsomstandigheden, zoals het type en de concentratie van alkalische activator en verhardingstemperatuur.

Vervolgens werden de reactiekinetiek van alkali-geactiveerde slakken, alkali-geactiveerde vliegasken en alkali-geactiveerde slak/vliegasken onderzocht met isotherme calorimetrie. Het natriumgehalte, het silicagehalte en de verhardingstemperatuur beïnvloedden de reactiekinetiek van AAM's. De oorzaak van de inductieperiode was verschillend voor alkali-geactiveerde slaksystemen en alkali-geactiveerde vliegassystemen. Voor alkali-geactiveerde slaksystemen vertraagde de aanwezigheid van oplosbaar Si in de activator het oplossen van slak en veroorzaakte een inductieperiode. Daarentegen werd de inductieperiode in alkali-geactiveerde vliegassystemen hoofdzakelijk toegeschreven aan de passivering van de uitgeloopte oppervlaktelaag door de geabsorbeerde Al.

Ten slotte werd de microstructuurontwikkeling van alkali-geactiveerde slakken, alkali-geactiveerde vliegasken en alkali-geactiveerde slak/vliegasken bestudeerd met behulp van SEM en MIP. Gevonden werd dat het type en de concentratie van alkalische activator de microstructuurvorming van AAM's beïnvloedden. Een toename van het Na<sub>2</sub>O-gehalte leidde

tot een vermindering van de totale porositeit en een verfijning van de microstructuur van alkali-geactiveerde slaksystemen. Daarentegen had een toename van het  $\text{Na}_2\text{O}$ -gehalte geen grote invloed op de totale porositeit van alkali-geactiveerde vliegassystemen. In plaats daarvan veranderde het de microstructuur door toename van het volume aan grote poriën en afname van het volume aan kleine poriën. Het  $\text{SiO}_2$ -gehalte had ernstige gevolgen voor de vorming van de microstructuren van AAM's. In met natriumsilicaat geactiveerde systemen leidde het oplosbare silicaat in de activator tot een relatief dichte microstructuur met gescheiden kleine capillaire poriën. Dit verschilde van de relatief grove microstructuur met verbonden capillaire poriën in natriumhydroxide-geactiveerde systemen.

## **(2) Numerieke simulatieroute**

Eerste werd de initiële korrelstapeling van AAMs, als startpunt voor het simuleren van de reacties en microstructuurvorming, gesimuleerd, rekening houdend met de werkelijk vorm van de slak- en vliegaskorrels. In vergelijking met bolvormige korrels namen het totale korreloppervlak en het bulk specifieke oppervlak toe met respectievelijk 23 % en ten minste 12 % wanneer de werkelijke korrelvorm werd aangehouden. Bij lage vloeistof/bindmiddel-verhoudingen ( $\leq 0.47$ ) leidden simulaties die uitgingen van de werkelijke korrelvorm tot een significante verschuiving van de poriëngrootteverdeling naar kleine poriën in vergelijking met simulaties uitgaande van bolvormige korrels.

Daarna is een model ontwikkeld voor het simuleren van het oplossen van aluminiumsilicaat in een alkalische oplossing. De invloeden van temperatuur, reactiviteit van de reactanten, alkaliteit van de oplossing en remmend effect van waterige Al enz., op het oplossen van de reactanten werden in dit model in aanmerking genomen. De simulatieresultaten betreffende het oplossen van slakken en vliegass in alkalische oplossing waren in overeenstemming met de experimentele resultaten.

Vervolgens werden de reacties in AAM's thermodynamisch gesimuleerd. Een thermodynamisch model, d.w.z. N(C)ASH<sub>ss</sub>, werd ontwikkeld om de N-A-S-H-gel te beschrijven. Met dit model en het in de literatuur beschreven C(N)ASH<sub>ss</sub>-model was het mogelijk om de reacties in alkali-geactiveerde vliegassystemen en alkali-geactiveerde slakken/vliegass systemen thermodynamisch te modelleren. De gesimuleerde samenstelling van het poriënwater van AAM's was in overeenstemming met experimentele resultaten.

Ten slotte werd het GeoMicro3D-model ontwikkeld op basis van de numerieke modules van de initiële korrelpakking, de oplossing van aluminosilicaat-reactant, de thermodynamische modellering en nucleatie en groei van reactieproducten. Als casestudy werd GeoMicro3D gebruikt om het reactieproces en de microstructuurvorming van alkali-geactiveerde slakken met drie verschillende alkalische activators te simuleren. De gesimuleerde reactiekinetiek (mate van reactie van de slak) en samenstelling van het poriënwater (elementconcentratie) waren in overeenstemming met experimentele resultaten. De met het GeoMicro3D model gesimuleerde ontwikkeling van het volume vaste stof was consistent met de resultaten berekend door GEMS met betrekking tot de primaire reactieproducten (C-(N)-A-S-H) en enkele kristallijne reactieproducten, zoals de hydrotalciet-achtige fase en katoiet. Naast de volumeontwikkeling van de vaste fasen leverde GeoMicro3D ook de volumes geadsorbeerd water en gelporiënwater die werden vastgehouden door de C-(N)-A-S-H-gel.

Samengevat: het reactieproces en de microstructuurvorming van AAM's werden experimenteel en numeriek bestudeerd. Op basis van de inzichten uit de experimentele studie werden numerieke modellen ontwikkeld en gevalideerd. Met deze modellen is het mogelijk

om de initiële korrelstapeling van slakken/vliegas in een alkalische activator, het oplossen van slakken/vliegas, de chemische reacties en microstructuurvorming van AAM's met redelijke nauwkeurigheid te simuleren.



# Appendix A

---

## Determination of the log forward dissolution rates of Ca and Si

### A.1 Methods

#### A.1.1 Solution analysis via ICP-OES

In the experimental program, 0.1 g of slag was dissolved in 200 mL of alkaline solution at 20 °C and with magnetic stirring at 250 rpm. The alkaline solution was the sodium hydroxide solution with six different alkali concentrations. These six alkali concentrations were 0.1, 0.5, 1.0, 1.5, 2.0 and 3.0 mol/L. During the dissolution process, the solution was sampled with a small volume of solution at set time intervals up to 2 hours. Then the sampled solutions were diluted using nitric acid (0.2 vol.%). The diluted solutions were analyzed using a PerkinElmer Optima 5300DV ICP-OES spectrometer. The concentrations of Si, Al and Ca were determined.

#### A.1.2 Thermodynamic analysis of solution

Thermodynamic analysis was carried out for the solution within which slag was dissolved. In thermodynamics, the saturation index,  $SI$ , is able to predict whether a solid phase can potentially form or not [85].

$$SI = \log(IAP/K_{sp}) \quad (A.1)$$

where  $IAP$  and  $K_{sp}$  are the ion activity product and solubility product of a solid phase, respectively. A positive  $SI$  indicates oversaturation and thus the possibility that this solid phase can precipitate. If  $SI$  is negative, it means undersaturation and implies that this solid phase is unstable in equilibrium within such a solution. A  $SI$  of zero indicates equilibrium between solution and solid. However,  $SI$  may be misleading when comparing phases which dissociate into a different number of ions ( $N$ ) [85]. For this reason, the effective saturation index ( $ESI$ ) was applied in this study for thermodynamic analysis.

$$ESI = SI/N \quad (A.2)$$

To perform the thermodynamic analysis, the Gibbs energy minimization software GEM-Selektor v.3 (<http://gems.web.psi.ch/>) [19, 20] and the thermodynamic database developed in [54, 69] for alkali-activated slag were used. The activities of ions were calculated using the element concentrations as the input.

#### A.1.3 Forward dissolution rates of Ca and Si

Based on the measured concentrations, the forward dissolution rates of Ca and Si can be calculated using the following equation:

$$r_{+,X} = \frac{d[X]}{\Delta t} \frac{V}{mSSA} \quad (\text{A.3})$$

where  $d[X]$  is the concentration change of X during the period  $\Delta t$ ,  $V$  is the solution volume,  $m$  is the slag mass and  $SSA$  is the specific surface area of slag. X represents Ca or Si.

## A.2 Experimental results

The measured concentrations of Si, Al and Ca are listed in Table A.1 for the dissolution of slag in sodium hydroxide solution with different alkali concentrations. The element concentrations increased with elapse of time. A higher alkali concentration of sodium hydroxide solution led to a higher element concentration.

*Table A.1 Measured element concentrations of Si, Al and Ca (mmol/L)*

NaOH	element	10 min	25 min	40 min	60 min	90 min	120 min
0.1 mol/L	[Si]	0.0786	0.0961	0.14	0.1929	0.2464	0.2857
	[Al]	0.0415	0.0459	0.0681	0.09	0.1111	0.1270
	[Ca]	0.13	0.165	0.1775	0.1975	0.25	0.27
0.5 mol/L	[Si]	0.0825	0.1168	0.1679	0.225	0.2821	0.3321
	[Al]	0.0463	0.0656	0.0896	0.1193	0.14	0.1630
	[Ca]	0.14	0.1525	0.19	0.24	0.2875	0.32
1.0 mol/L	[Si]	0.0889	0.15	0.2107	0.2607	0.3214	0.3536
	[Al]	0.0537	0.0896	0.1185	0.1370	0.1667	0.1778
	[Ca]	0.1575	0.2025	0.2625	0.285	0.3475	0.3725
1.5 mol/L	[Si]	0.1179	0.1643	0.2321	0.2929	0.325	0.3893
	[Al]	0.0696	0.0967	0.1259	0.1481	0.1667	0.1926
	[Ca]	0.19	0.215	0.26	0.3175	0.3425	0.41
2.0 mol/L	[Si]	0.1143	0.1964	0.2464	0.3	0.325	0.4
	[Al]	0.0630	0.1111	0.1407	0.1630	0.1630	0.2
	[Ca]	0.1775	0.2375	0.2925	0.3525	0.3675	0.435
3.0 mol/L	[Si]	0.3607	0.35	0.4286	0.5071	0.6214	0.6864
	[Al]	0.1481	0.1481	0.1741	0.2	0.2407	0.2667
	[Ca]	0.22	0.36	0.43	0.4825	0.525	0.34

## A.3 Thermodynamic analysis

In alkali-activated slag materials, the C-(N-)A-S-H type gel is the primary reaction product. Myers et al. used a set of eight end-members to describe the C-(N-)A-S-H gels in alkali-activated slag [69]. These eight end-members are 5CA, INFCA, 5CNA, INFCNA, INFCN, T2C\*, T5C\* and TobH\*. The details on these end-members are provided in chapter 8. The dissociation reactions and solubility products of the primary reaction products and the crystalline reaction products are also provided in chapter 8.

Figures A.1 and A.2 display the calculated effective saturation indexes for primary reaction products and crystalline reaction products, respectively. Most of the calculated *ESI* values were negative, indicating undersaturations for the solutions within which slag dissolved. This means that most of the solid reaction products are unstable in equilibrium within these

solutions and thus are not expected to form in the solutions. So all the dissolved elements were in the solutions and the element concentrations of Ca and Si can be used to determine the forward dissolution rates of Ca and Si.

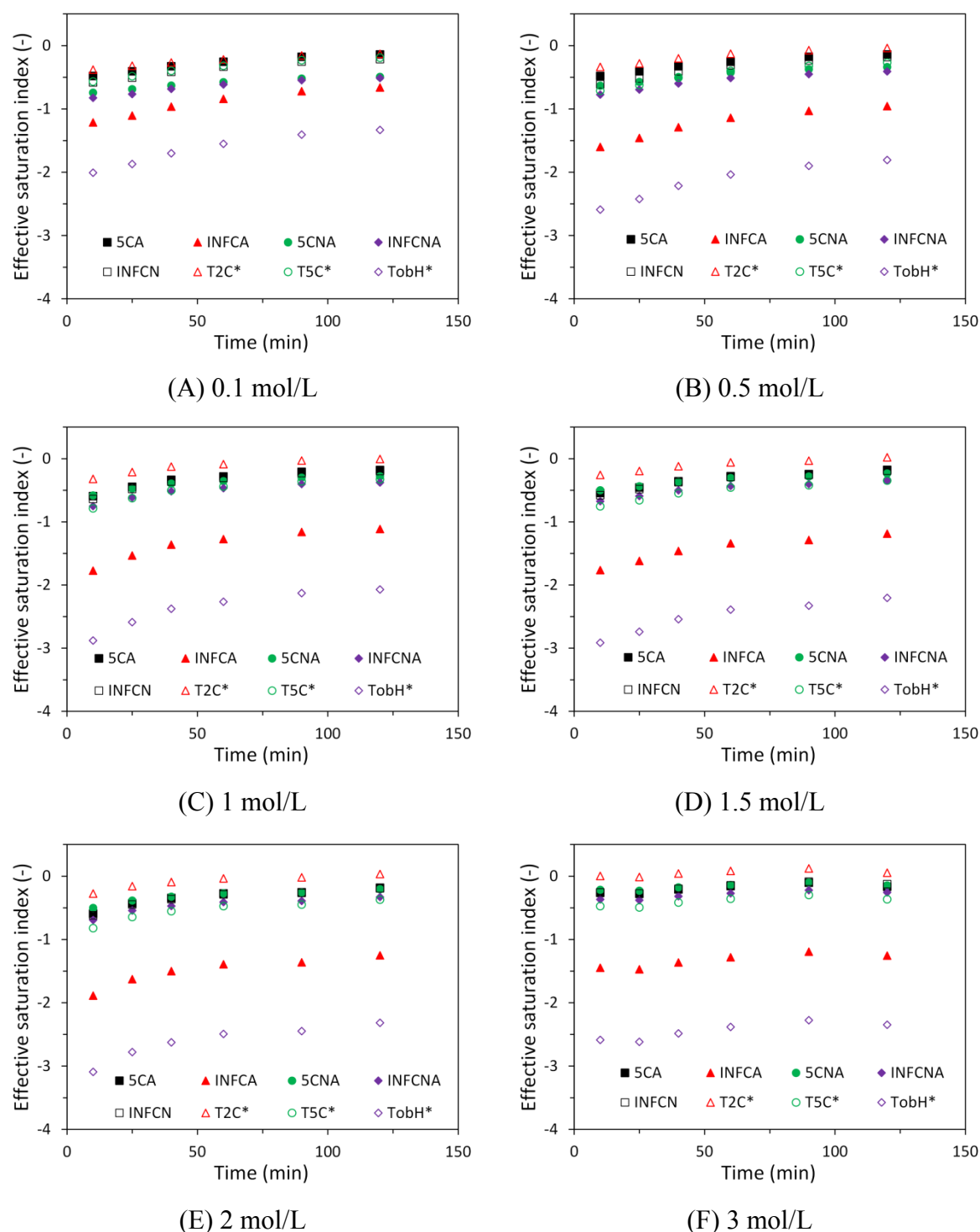


Figure A.1 Calculated effective saturation indexes (ESI) for primary reaction products for the dissolution of slag in sodium hydroxide solution with different alkali concentrations. In the graph, 5CA, INFCNA, 5CNA, INFCN, INFCA, T2C\*, T5C\* and TobH\* are eight end-members to describe the C-(N-)A-S-H gels in the alkali-activated slag system (see more details in Chapter 8).

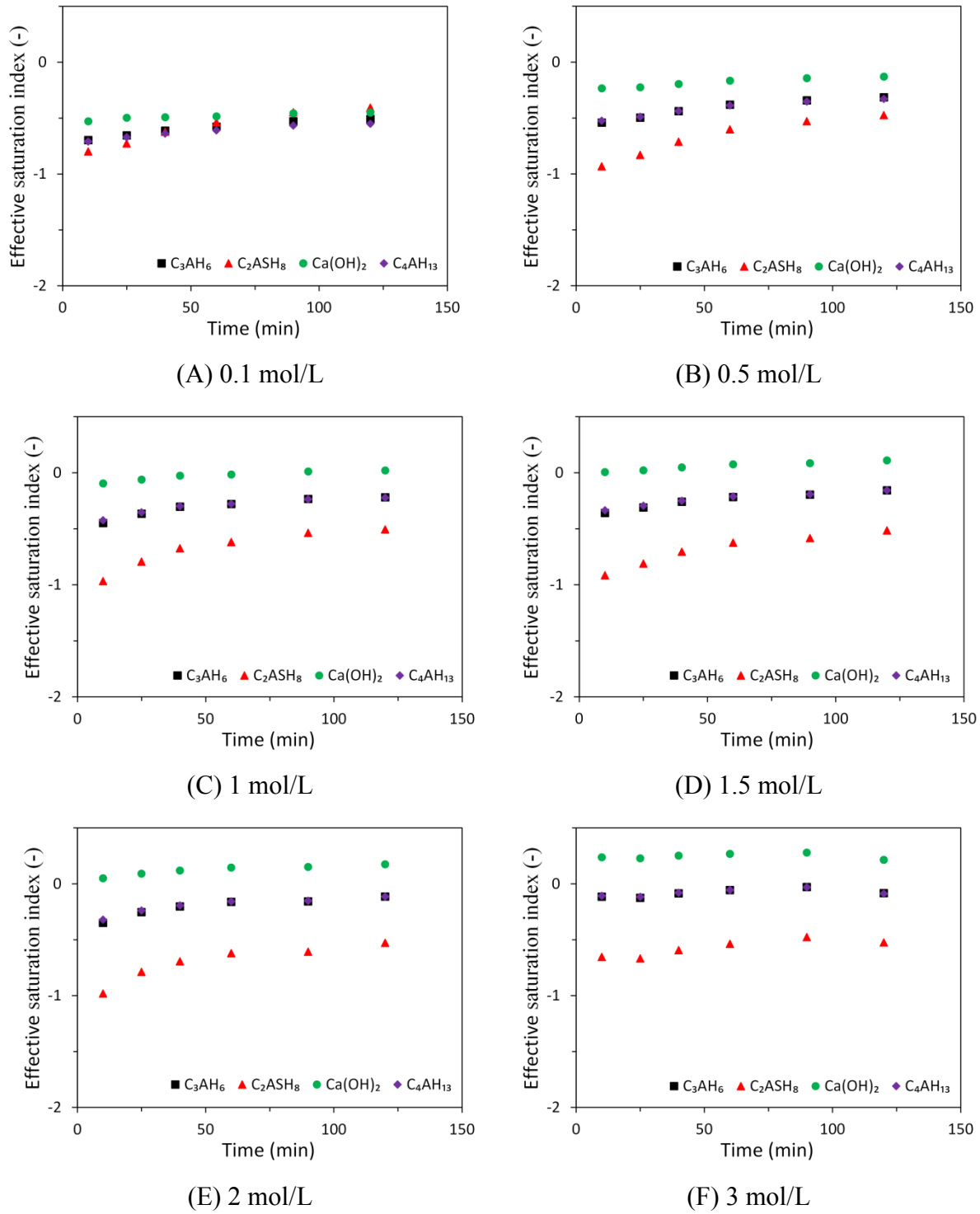


Figure A.2 Calculated effective saturation indexes (ESI) for crystalline reaction products for the dissolution of slag in sodium hydroxide solution with different alkali concentrations.

#### A.4 Determination of the log forward dissolution rate of Ca

Figure A.3 plots the measured concentration of Ca as a function of time. The concentration of Ca increased linearly with increase of time, indicating a steady-state dissolution. The slope of



the straight line was used to calculate the forward dissolution rate of Ca according to Equation A.3. The calculated forward dissolution rate of Ca was  $1.803 \times 10^{-7}$ ,  $2.357 \times 10^{-7}$ ,  $2.635 \times 10^{-7}$ ,  $2.773 \times 10^{-7}$ ,  $3.051 \times 10^{-7}$  and  $3.328 \times 10^{-7}$  mol/m<sup>2</sup>/s for the dissolution of slag in sodium hydroxide solution with alkali concentrations of 0.1, 0.5, 1.0, 1.5, 2.0 and 3.0 mol/L, respectively.

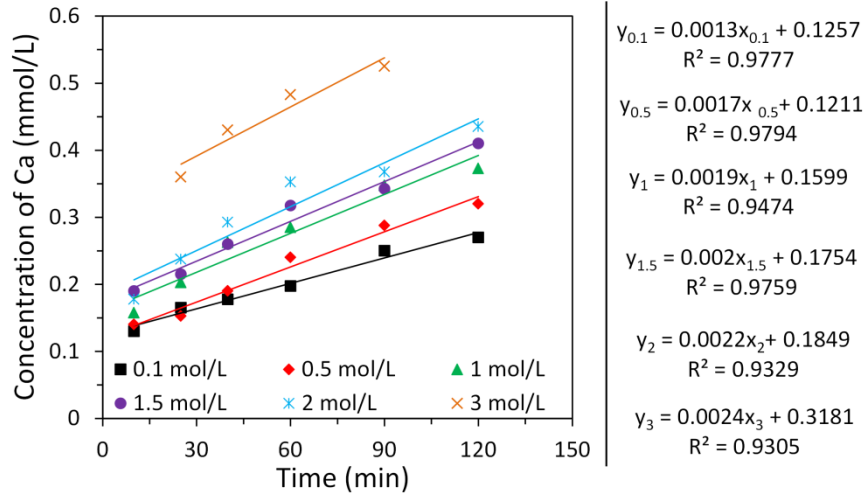


Figure A.3 Measured concentration of Ca plotted as a function of time.

The log forward dissolution rate of Ca was plotted as a function of the pH of the solution in Figure A.4. It shows a linear relationship between the log forward dissolution rate of Ca and the pH of solution. Then the log forward dissolution rate of Ca can be expressed as a function of pH:

$$\text{Log } r_{+,Ca} = 0.1868\text{pH} - 8.7729 \quad (\text{A.4})$$

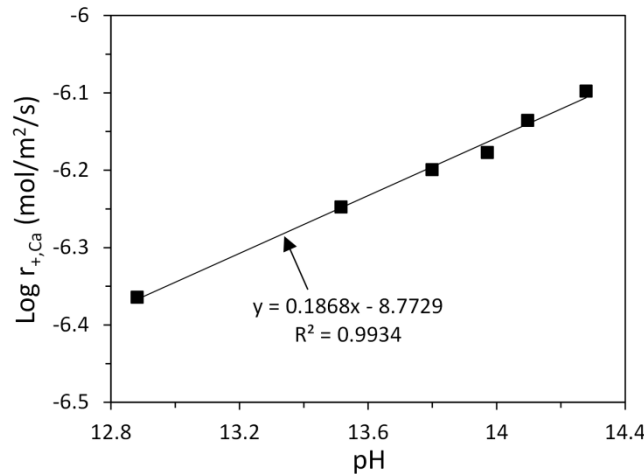


Figure A.4 Log forward dissolution of Ca plotted as a function of pH of the solution.

### A.5 Determination of the log forward dissolution rate of Si

The log forward dissolution rate of Si was determined and listed in Table A.2 for the dissolution of slag in sodium hydroxide solution with alkali concentrations of 0.1, 0.5, 1.0,

1.5, 2.0 and 3.0 mol/L. Table A.2 also listed the log forward dissolution rate of Si for the dissolution of synthetic glass in alkaline solution (pH = 13) [159]. It can be seen that the log forward dissolution rate of Si increases with the increase of the reactivity of aluminosilicate materials (NBO/T) and alkalinity of solution (pH).

Table A.2 Log forward dissolution rate of Si

sample	NBO/T	pH	Log $r_{+,Si}$ (mol/m <sup>2</sup> /s)	Remarks
0.1 mol/L	2.405	12.88	-6.20	From this study
0.5 mol/L	2.405	13.52	-6.12	
1.0 mol/L	2.405	13.80	-6.10	
1.5 mol/L	2.405	13.97	-6.08	
2.0 mol/L	2.405	14.10	-6.06	
3.0 mol/L	2.405	14.28	-5.99	
G1	1.460	13.0	-6.42	From Snellings [159]
G2	1.088	13.0	-6.99	
G3	0.318	13.0	-7.57	
G4	0.229	13.0	-7.85	
G5	0.091	13.0	-8.21	
G6	0.0	13.0	-8.45	

Note: G1 and G2 were used to represent the glasses encountered in slag, G3 and G4 were used to represent the glasses encountered in fly ash and, G5 and G6 were used to represent the glasses encountered in natural pozzolans and silica fume, respectively [159]. It is noted that the log forward dissolution rate of Si for the glasses was recalculated using Equation A.3, instead of Equation 1 in [159].

The following equation was used to describe the dependency of the log forward dissolution rate of Si on NBO/T and pH:

$$\text{Log } r_{+,Si} = 0.0155pH \cdot NBO/T + 0.0727pH + 0.6199 NBO/T - 9.0309 \quad (\text{A.5})$$

The predicted log forward dissolution rate of Si using Equation A.5 is plotted in comparison with the experimental results in Figure A.5. The predicted results matched the experimentally measured results within  $\pm 0.5$  order of magnitude.

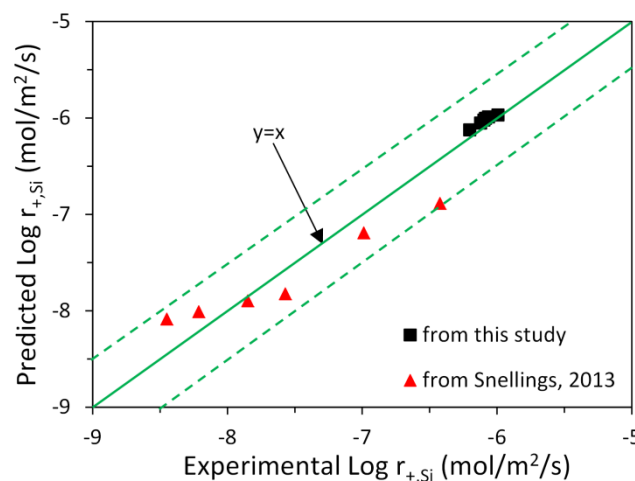


Figure A.5 Predicted log forward dissolution of Si compared to the experimental results.

### A.6 Coefficients for the determination of $b$ and $\theta_{Al,max}$ in Equation 7.31

According to Bickmore et al. [171],  $b$  and  $\theta_{max}$  in Equation 7.31 can be calculated as a function of the pH:

$$b = -3.00 \times 10^3 pH + 3.97 \times 10^4 \quad (A.6)$$

$$\theta_{Al,max} = -0.196pH + 2.94 \quad (A.7)$$

However, the coefficients in these equations were obtained by fitting the experimental results for the dissolution of quartz. These coefficients, however, are not suitable for use in simulating the inhibiting effect of aqueous Al species on the dissolution of aluminosilicate materials.

Snellings investigated the dissolution of synthetic glasses in alkaline solution (pH = 13) with different Al concentrations [159]. According to the reported values of the log forward dissolution rate of Si (Table A.3), the fraction of the glass surface passivated by aqueous Al species, i.e.  $\theta_{Al}$ , was calculated. The calculation results are listed in Table A.3. Since the variations of the log forward dissolution rate of Si remained within the error for G1 and G2,  $\theta_{Al}$  was not calculated for these two glasses.

*Table A.3 Log forward dissolution rate of Si for the dissolution of glasses in alkaline solution with different Al concentrations [159], and the calculated  $\theta_{Al}$*

samples	[Al] (mmol/L)	Log $r_{+,Si}$ (mol/m <sup>2</sup> /s)	$\theta_{Al}$
G3	0.25	-7.99	0.620
	1	-8.05	0.669
	5	-7.99	0.620
G4	0.25	-7.94	0.187
	1	-8.07	0.397
	5	-8.26	0.611
G5	0.25	-8.32	0.224
	1	-8.62	0.611
	5	-8.94	0.814
G6	0.25	-8.86	0.611
	1	-9.07	0.760
	5	-9.56	0.922

Note: the log forward dissolution rate of Si for the dissolution of glasses in alkaline solution with [Al] = 0, are listed in Table A.2.

By fitting the calculated  $\theta_{Al}$  in Table A.3, the coefficients for the determination of  $b$  and  $\theta_{Al,max}$  and the parameter  $k$  are obtained.  $k = 1.473$ . Equations A.6 and A.7 can be rewritten as:

$$b = -2.12 \times 10^3 pH + 3.18 \times 10^4 \quad (A.6)$$

$$\theta_{Al,max} = -0.177pH + 3.23 \quad (A.7)$$

Figure A.6 displays the predicted log forward dissolution rate of Si in comparison with the experimental results. The difference between the predicted results and experimental results was found within  $\pm 0.5$  order of magnitude, showing a good fit.

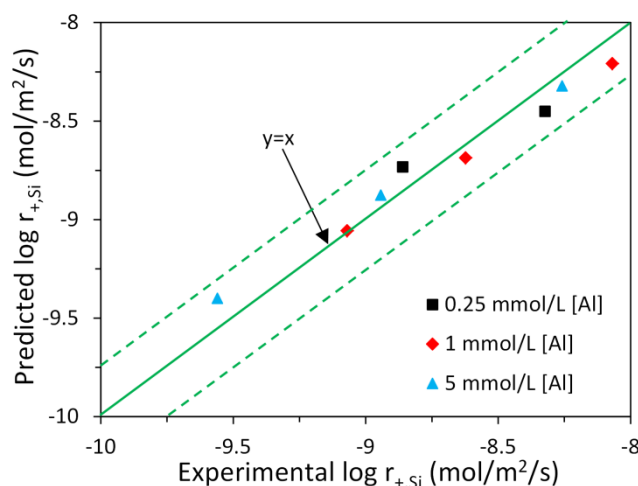


Figure A.6 Predicted log forward dissolution of Si compared to the experimental results for the dissolution of glasses in alkaline solution with different concentrations of Al.

#### A.7 Additional simulation results for the dissolution of slag and fly ash in alkaline solution

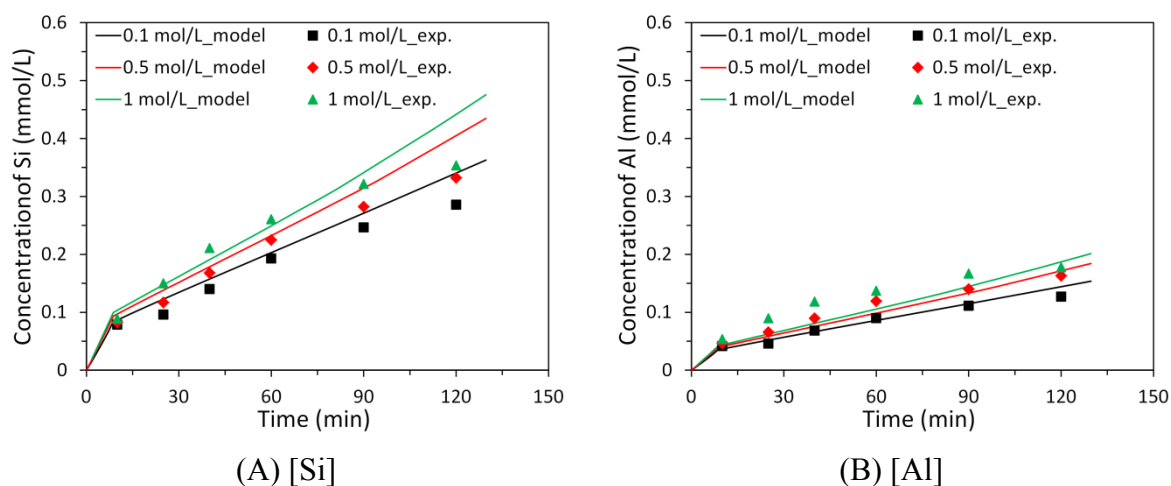


Figure A.7 Simulated concentrations of Si and Al in comparison with the experimental results for the dissolution of slag in sodium hydroxide solutions with different alkali concentrations.

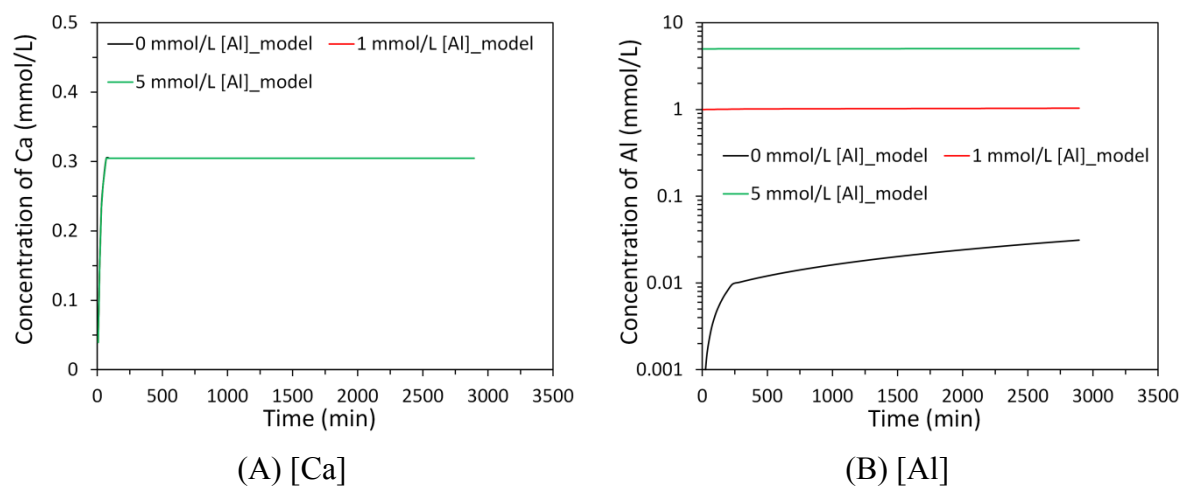


Figure A.8 Simulated concentrations of Ca and Al for the dissolution of fly ash (G4) in sodium hydroxide solutions with different Al concentrations. Since the concentrations of Ca and Al in experiment were not provided in [159], the experimental data are not shown in the graphs.



# Appendix B

## Thermodynamic properties of the phases used for thermodynamic modelling in this work

Table B.1 Thermodynamic properties of the C(N)ASH<sub>ss</sub> solid solution members and the MA-OH-LDH<sub>ss</sub> solid solution members. The reference state is 298.15 K and 1 bar.

Phase	$V^0$ (cm <sup>3</sup> /mol)	$\Delta_f H^0$ (kJ/mol)	$\Delta_f G^0$ (kJ/mol)	$S^0$ (J/mol.K)	$C_p^0$ (J/mol.K)	Ref.
5CA	57.3	-2491	-2293	163	177	[69]
INFCA	59.3	-2551	-2343	154	181	[69]
5CNA	64.5	-2569	-2382	195	176	[69]
INFCNA	69.3	-2667	-2474	198	180	[69]
INFCN	71.1	-2642	-2452	186	184	[69]
T2C*	80.6	-2721	-2465	167	237	[69]
T5C*	79.3	-2780	-2517	160	234	[69]
TobH*	85.0	-2831	-2560	153	231	[69]
M <sub>4</sub> AH <sub>10</sub>	219	-7160	-6358	549	648	[54]
M <sub>6</sub> AH <sub>12</sub>	305	-9007	-8023	675	803	[54]
M <sub>8</sub> AH <sub>14</sub>	392	-10853	-9687	801	958	[54]

Table B.2 Thermodynamic properties of the solid constituents used to calculate heat capacity ( $C_p^0$ ) and entropy ( $S^0$ ) of the N(C)ASH<sub>ss</sub> solid solution members. The reference state is 298.15 K and 1 bar.

Phase	$V^0$ (cm <sup>3</sup> /mol)	$\Delta_f H^0$ (kJ/mol)	$\Delta_f G^0$ (kJ/mol)	$S^0$ (J/mol.K)	$C_p^0$ (J/mol.K)	Ref.
Leucite	89.1	-3002.0	-2820.9 <sup>a</sup>	165.7	163.4	[197]
Amorphous SiO <sub>2</sub>	29.0	-903.3	-848.9	41.3	44.5	[220]
Portlandite	33.1	-984.7	-897.0	83.4	87.5	[69]
NaOH(s)	18.8	-425.8	-379.6	64.4	59.5	[69]

a. The standard Gibbs free energy of formation of leucite was calculated using the additivity method in this work.

Table B.3 Thermodynamic properties of the N(C)ASH<sub>ss</sub> solid solution members. The reference state is 298.15 K and 1 bar.

Phase	$V^0$ (cm <sup>3</sup> /mol)	$\Delta_f H^0$ (kJ/mol)	$\Delta_f G^0$ (kJ/mol)	$S^0$ (J/mol.K)	$C_p^0$ (J/mol.K)	Ref.
NASH_1-1 <sup>a</sup>	58.0	-2409.1	-2224.8	124.1	118.7	This work
NASH_2-1	86.0	-3333.3	-3094.5	165.4	163.2	This work
NASH_3-1	113.9	-4257.5	-3964.3	206.7	207.7	This work
NASH_4-1	141.8	-5181.7	-4834.0	248.0	252.2	This work
NCASH_1-0.1	56.0	-2431.5	-2249.3	103.7	104.5	This work
NCASH_2-0.1	83.9	-3355.7	-3119.0	145.0	149.0	This work
NCASH_3-0.1	111.8	-4279.9	-3988.7	186.3	193.5	This work
NCASH_4-0.1	139.8	-5204.1	-4858.4	227.6	238.0	This work

a. The first and second number after N(C)ASH represent the molar ratio of Si/Al and Na/Al in the solid solution member, respectively.

Table B.4 Thermodynamic properties of the major aqueous species<sup>a</sup>. The reference state is 298.15 K and 1 bar.

Phase	$V^0$ (cm <sup>3</sup> /mol)	$\Delta_f H^0$ (kJ/mol)	$\Delta_f G^0$ (kJ/mol)	$S^0$ (J/mol.K)	$C_p^0$ (J/mol.K)	Ref.
Al <sup>3+</sup>	-45.2	-530.6	-483.7	-352.1	-128.7	[221]
AO <sup>+</sup>	0.3	-713.6	-660.4	-113	-125.1	[221]
AlO <sub>2</sub> <sup>-</sup>	9.5	-925.6	-827.5	-30.2	-49	[221]
Ca <sup>2+</sup>	-18.4	-543.1	-552.8	-56.5	-30.9	[221]
CaOH <sup>+</sup>	5.8	-751.6	-717	28	6	[221]
K <sup>+</sup>	9.0	-252.1	-282.5	101	8.4	[221]
KOH(aq)	15	-474.1	-437.1	108.4	-85	[221]
Na <sup>+</sup>	-1.2	-240.3	-261.9	58.4	38.1	[221]
NaOH(aq)	3.5	-470.1	-418.1	44.8	-13.4	[221]
HSiO <sub>3</sub> <sup>-</sup>	4.5	-1145	-1014	20.9	-87.2	[222]
SiO <sub>2</sub> (aq)	16.1	-887.9	-833.4	41.3	44.5	[223]
SiO <sub>3</sub> <sup>2-</sup>	34.1	-1099	-938.5	-80.2	119.8	[224]
HS <sup>-</sup>	20.2	-16.2	12	68.2	-93.9	[221]
S <sup>2-</sup>	20.2	92.2	120.4	68.2	-93.9	[221]
Mg <sup>2+</sup>	-22	-465.9	-454	-138.1	-21.7	[221]
MgOH <sup>+</sup>	1.6	-690	-625.9	-79.9	129.2	[221]
Fe <sup>2+</sup>	-22.6	-92.24	-91.5	-105.9	-32.4	[225]
Fe <sup>3+</sup>	-37.8	-49.6	-17.2	-277.4	-76.7	[225]
OH <sup>-</sup>	-4.7	-230	-157.3	-10.7	-136.3	[221]
H <sup>+</sup>	0	0	0	0	0	[221]
H <sub>2</sub> O(aq)	18.1	-285.9	-237.2	69.9	75.4	[226]

a. The thermodynamic properties of other aqueous species can be found in [54, 69].



Table B.5 Thermodynamic properties of the crystalline phases. The reference state is 298.15 K and 1 bar

Phase	$V^0$ (cm <sup>3</sup> /mol)	$\Delta_f H^0$ (kJ/mol)	$\Delta_f G^0$ (kJ/mol)	$S^0$ (J/mol.K)	$C_p^0$ (J/mol.K)	Ref.
Katoite, C <sub>3</sub> AH <sub>6</sub>	150	-5537	-5008	422	446	[227]
Stratlingite, C <sub>2</sub> ASH <sub>8</sub>	216	-6360	-5705	546	603	[224]
Mackinawite, FeS	20.5	-92.0	-93.6	64.68	50.4	[228]
Brucite, MH	24.6	-923	-832	63.1	77.3	[54]
Goethite,	21	-568.2	-497.3	60	74.3	[225]
Natrolite, NAS <sub>3</sub> H <sub>2</sub>	169	-5728	-5325.7	360	359	[209]
Zeolite A, NAS <sub>2</sub> H <sub>5</sub>	187	-5559	-5133	441	420	calculated <sup>a</sup>
Zeolite P, N <sub>3</sub> A <sub>3</sub> S <sub>14</sub> H <sub>15</sub>	728.2	-24441	-22417	1588	1616	[229]
Zeolite X, NAS <sub>2.5</sub> H <sub>6.2</sub>	214	-6447	-5847.5	566	586	[209]
Zeolite Y, NAS <sub>4</sub> H <sub>8</sub>	283	-8327	-7552.5	734	739	[209]
Na-analcime, N <sub>0.16</sub> A <sub>0.16</sub> S <sub>0.68</sub> H <sub>0.333</sub>	32.5	-1099	-1026	75.6	70.5	[54]
Na-chabazite, NAS <sub>4</sub> H <sub>6</sub>	247.5	-7784	-7115	619.5	680.4	[230]
Ca-chabazite, C <sub>0.111</sub> A <sub>0.111</sub> S <sub>0.778</sub> H <sub>0.667</sub>	35.2	-1179	-1090	87.1	82.9	[54]
CaNa-heulandite, C <sub>0.111</sub> N <sub>0.014</sub> A <sub>0.125</sub> S <sub>0.75</sub> H <sub>0.667</sub>	35.2	-1185	-1094	84	82.9	[54]
Basic-sodalite, N <sub>0.325</sub> A <sub>0.25</sub> S <sub>0.5</sub> H <sub>0.345</sub>	35.0	-1190	-1106	67.8	66.7	[54]
Hydroxysodalite, N <sub>4</sub> A <sub>3</sub> S <sub>6</sub> H <sub>3</sub>	422.7	-14098	-13183	885.6	895	[231, 232]

a. The heat capacity and entropy were calculated using the additivity method in this work. The enthalpy and Gibbs free energy of formation were calculated from the solubility data in [233, 234]. The molar volume was obtained from [235].



# Appendix C

## Additional simulation results for samples BFS\_N6S0 and BFS\_N6S5.4

### C.1 Pore solution chemistry

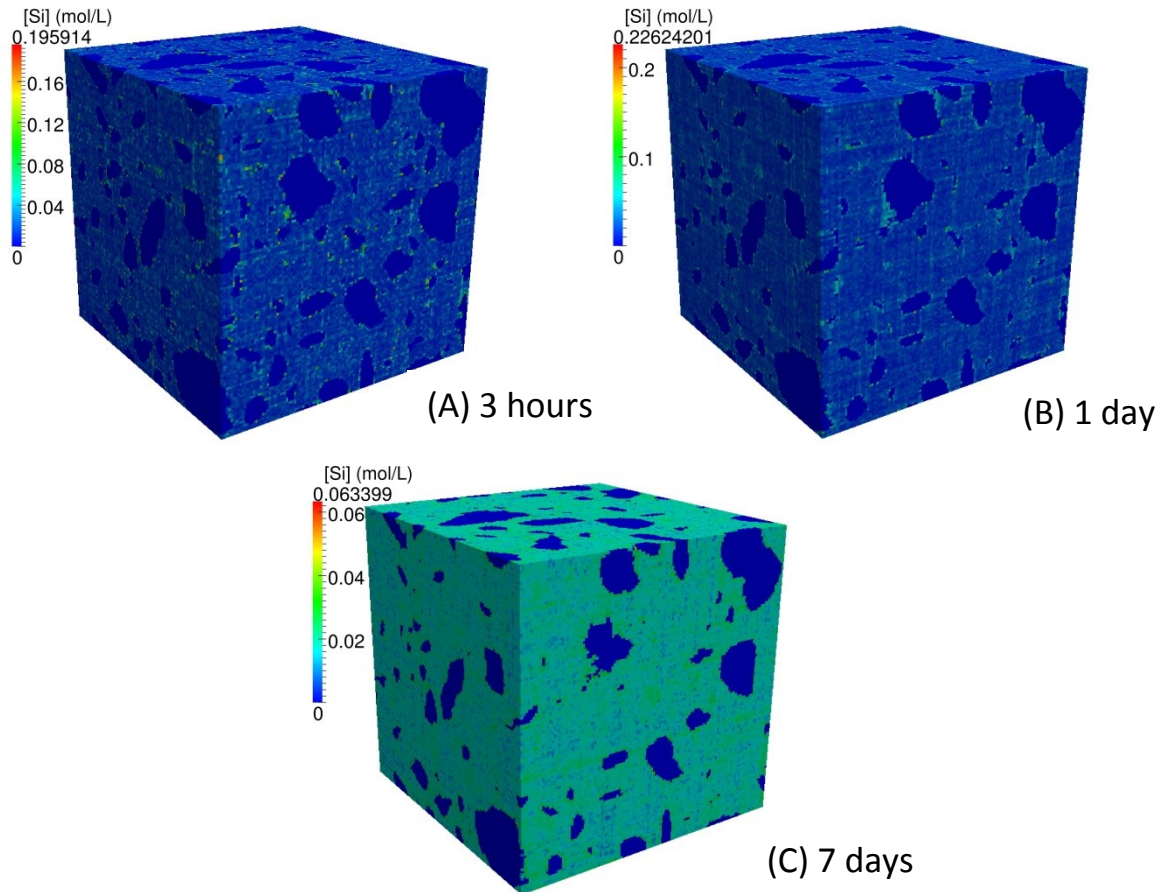
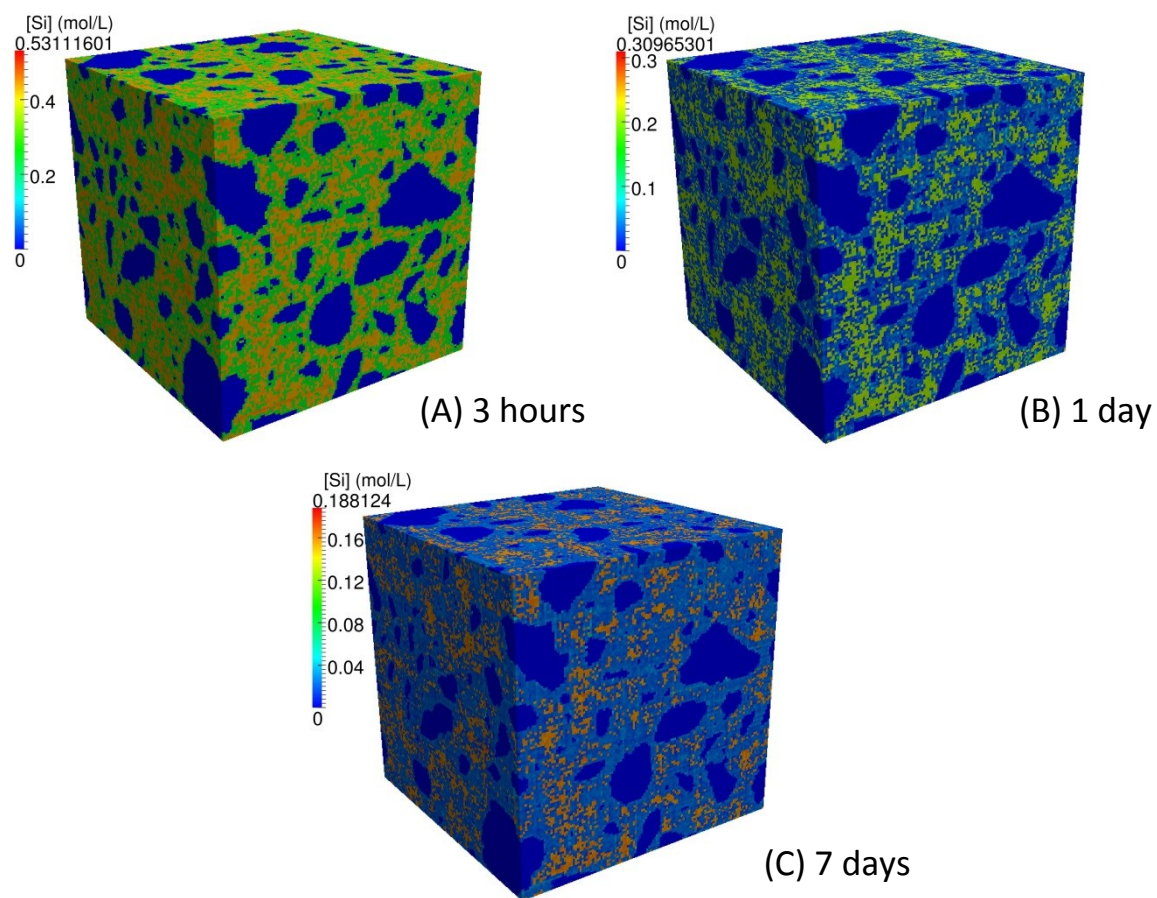


Figure C.1 Distribution of element concentration of Si for sample BFS\_N6S0 at 3 hours, 1 day and 7 days. The size of the cubic unit cell is  $125\ \mu\text{m} \times 125\ \mu\text{m} \times 125\ \mu\text{m}$ . The digitization resolution is  $1\ \mu\text{m} \times 1\ \mu\text{m} \times 1\ \mu\text{m}$  per voxel.



*Figure C.2 Distribution of element concentration of Si for sample BFS\_N6S5.4 at 3 hours, 1 day and 7 days. The size of the cubic unit cell is  $125\ \mu\text{m} \times 125\ \mu\text{m} \times 125\ \mu\text{m}$ . The digitization resolution is  $1\ \mu\text{m} \times 1\ \mu\text{m} \times 1\ \mu\text{m}$  per voxel.*

## C.2 3D visualization

### C.2.1 Microstructure evolution

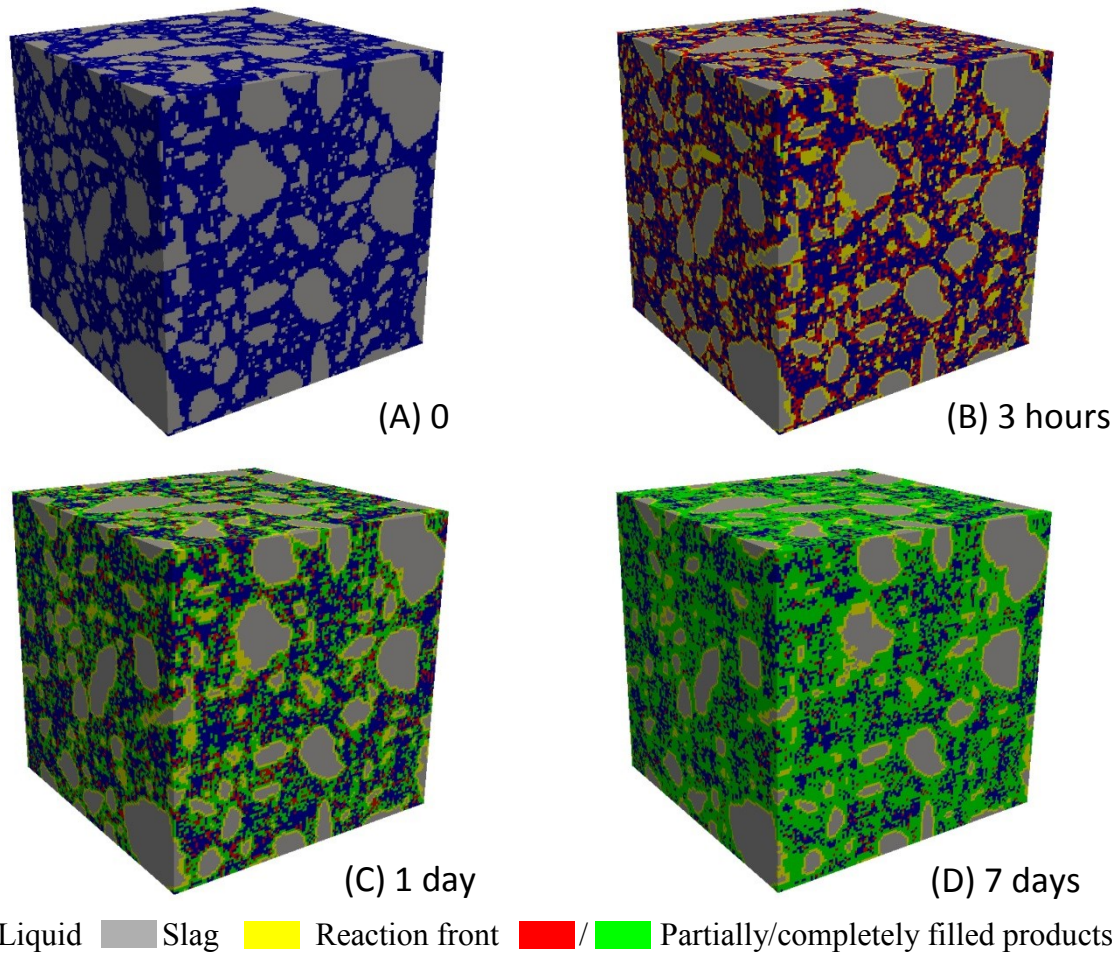


*Figure C.3 Simulated 3D microstructures of sample BFS\_N6S0 at 0, 3 hours, 1 day and 7 days. The size of the cubic unit cell is  $125\ \mu\text{m} \times 125\ \mu\text{m} \times 125\ \mu\text{m}$ . The digitization resolution is  $1\ \mu\text{m} \times 1\ \mu\text{m} \times 1\ \mu\text{m}$  per voxel.*



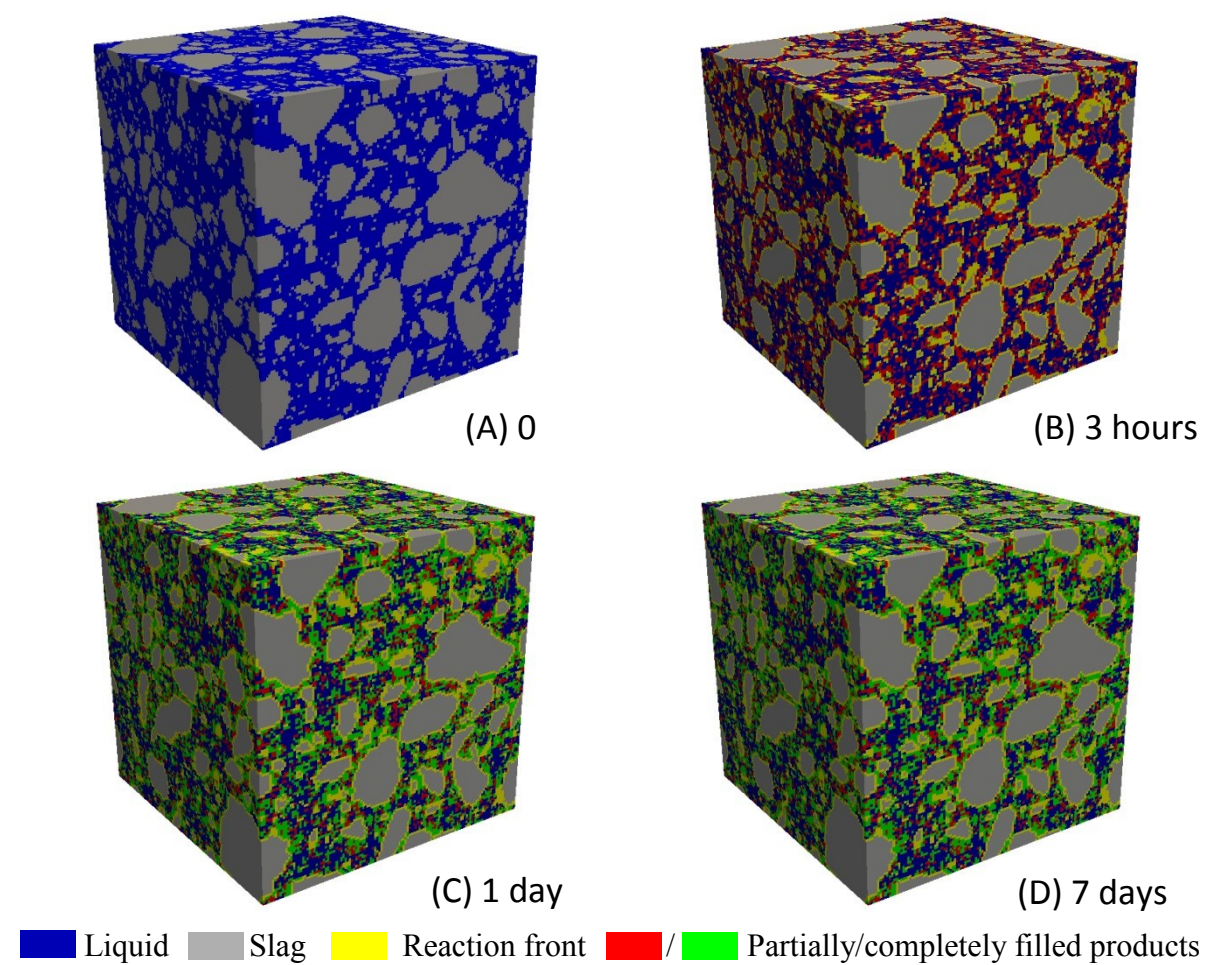


*Figure C.4 Simulated 3D microstructures of sample BFS\_N6S5.4 at 0, 3 hours, 1 day and 7 days. The size of the cubic unit cell is  $125\ \mu\text{m} \times 125\ \mu\text{m} \times 125\ \mu\text{m}$ . The digitization resolution is  $1\ \mu\text{m} \times 1\ \mu\text{m} \times 1\ \mu\text{m}$  per voxel.*

### C.2.2 Solid volume fraction of nodes

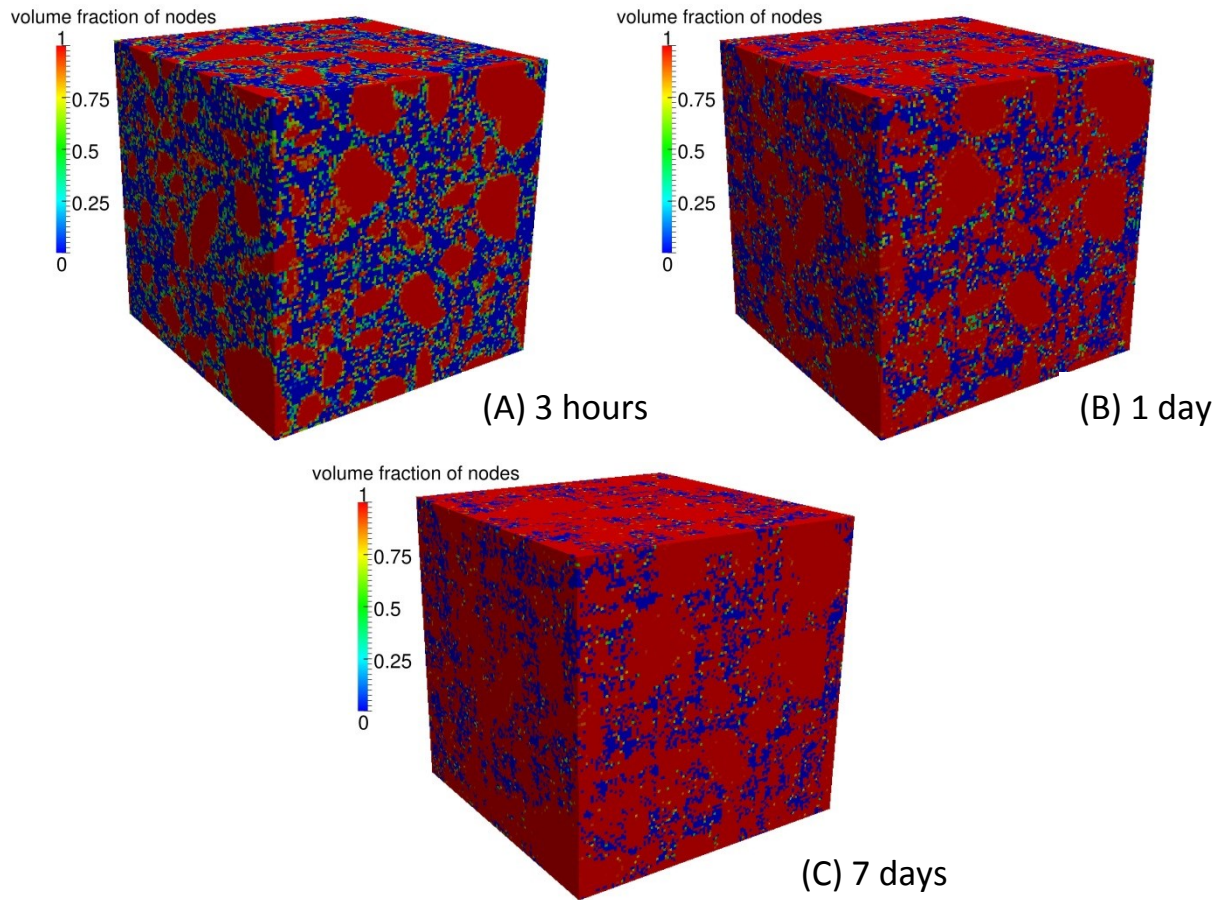


*Figure C.5 Solid volume fraction of nodes for sample BFS\_N6S0 at 3 hours, 1 day and 7 days. The size of the cubic unit cell is  $125\ \mu\text{m} \times 125\ \mu\text{m} \times 125\ \mu\text{m}$ . The digitization resolution is  $1\ \mu\text{m} \times 1\ \mu\text{m} \times 1\ \mu\text{m}$  per voxel.*

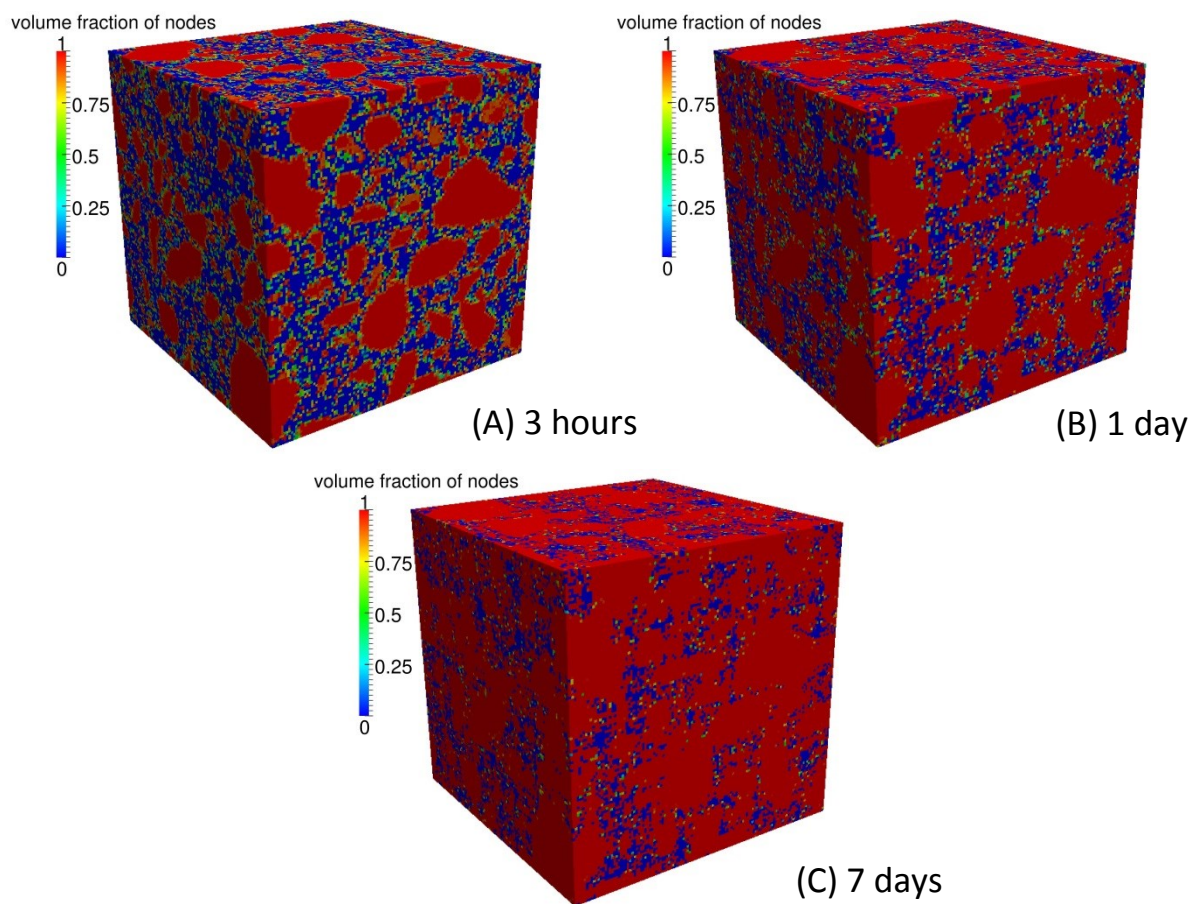


*Figure C.6* Solid volume fraction of nodes for sample BFS\_N6S5.4 at 3 hours, 1 day and 7 days. The size of the cubic unit cell is  $125\ \mu\text{m} \times 125\ \mu\text{m} \times 125\ \mu\text{m}$ . The digitization resolution is  $1\ \mu\text{m} \times 1\ \mu\text{m} \times 1\ \mu\text{m}$  per voxel.



### C.2.3 Density of nodes

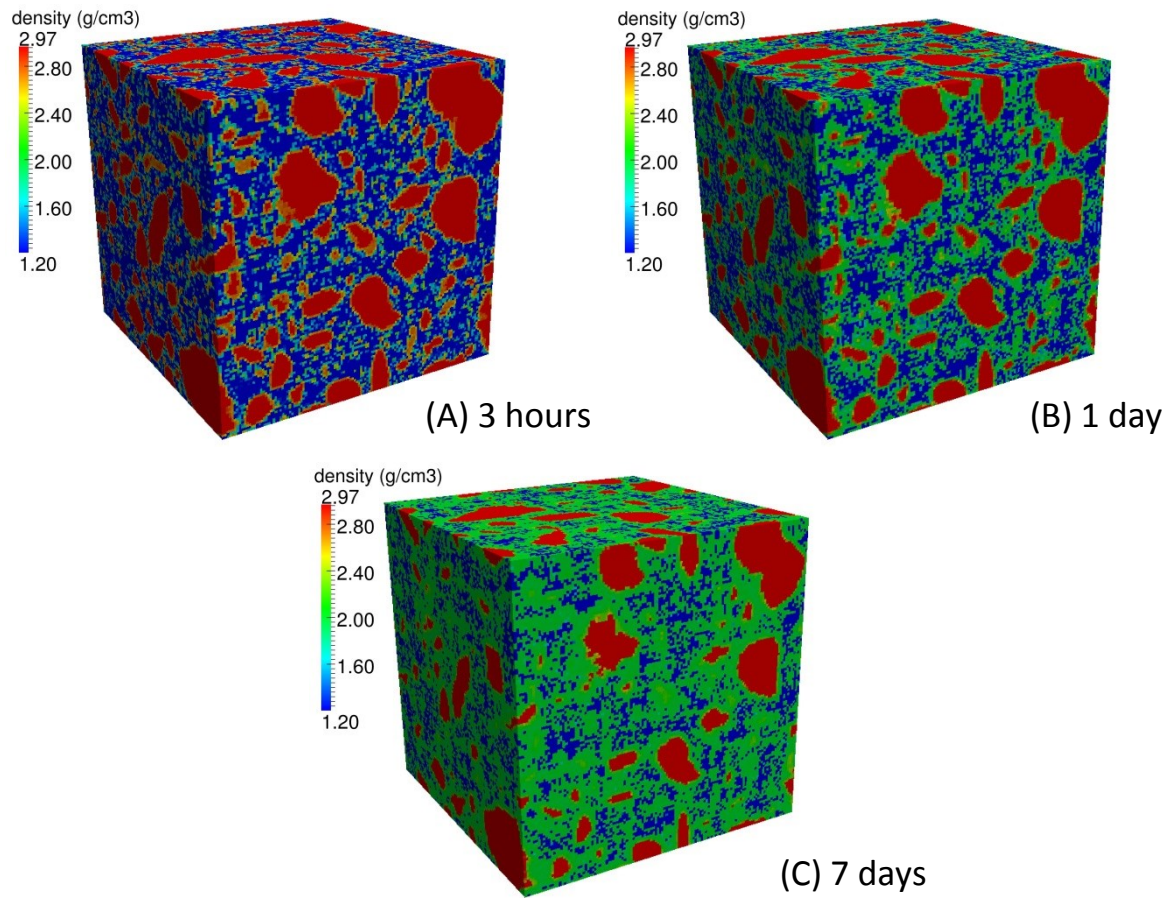


Figure C.7 Density of nodes for sample BFS\_N6S0 at 3 hours, 1 day and 7 days. The size of the cubic unit cell is  $125\ \mu\text{m} \times 125\ \mu\text{m} \times 125\ \mu\text{m}$ . The digitization resolution is  $1\ \mu\text{m} \times 1\ \mu\text{m} \times 1\ \mu\text{m}$  per voxel.

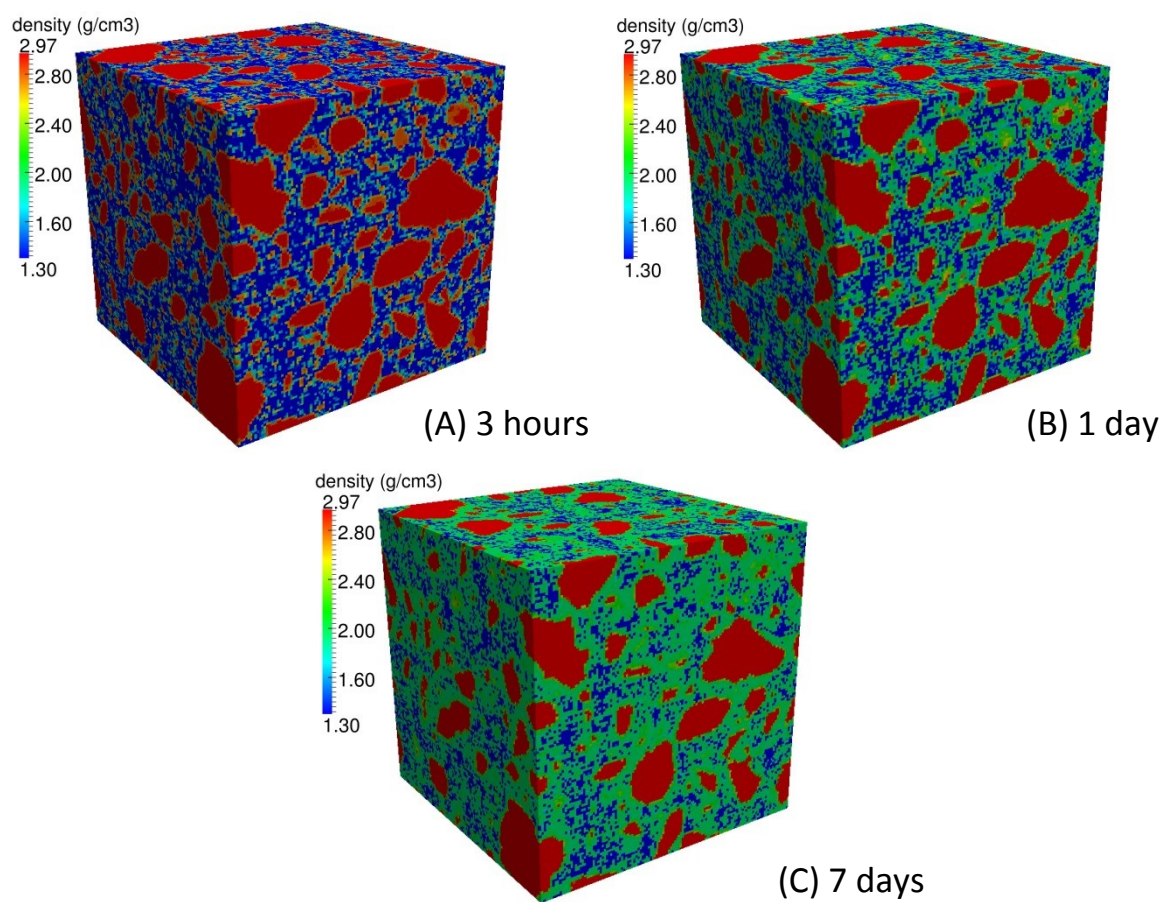
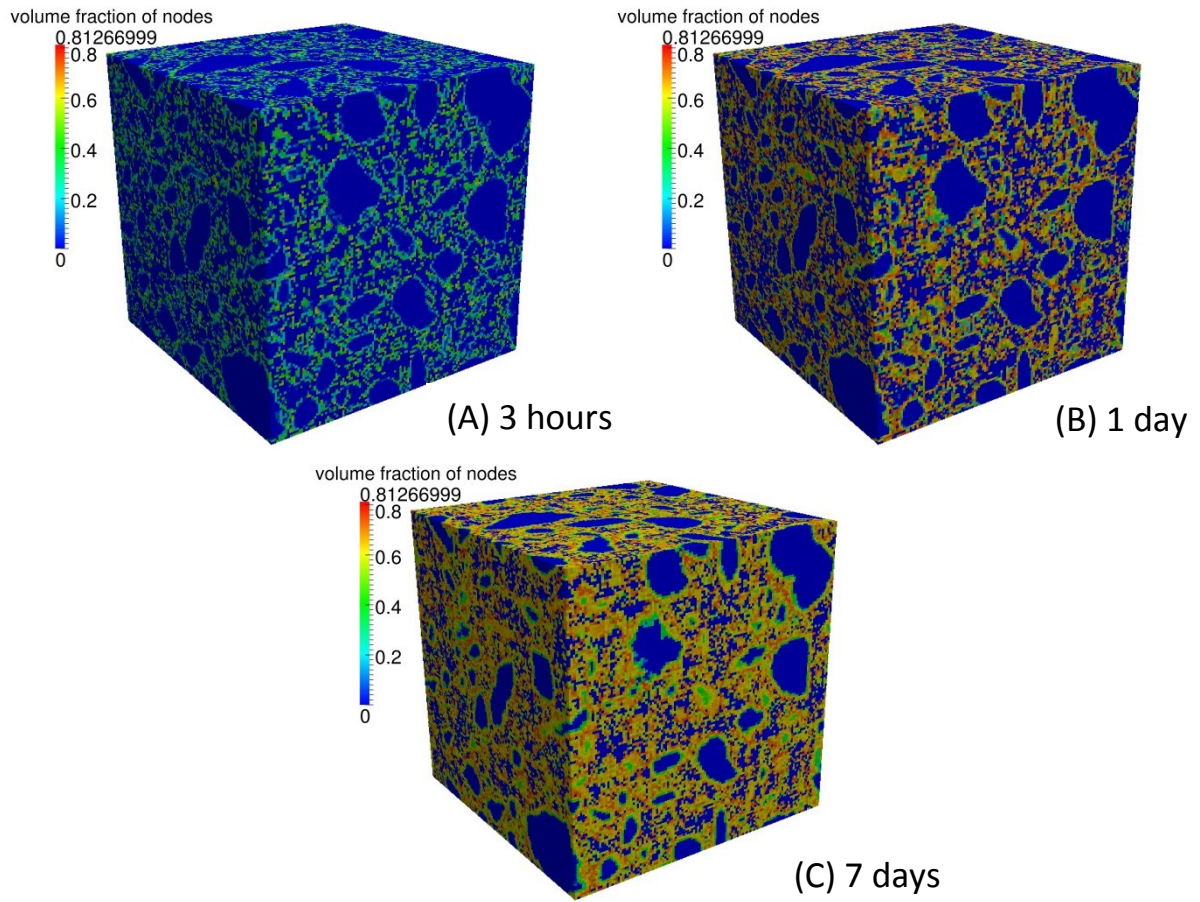


Figure C.8 Density of nodes for sample BFS\_N6S5.4 at 3 hours, 1 day and 7 days. The size of the cubic unit cell is  $125\ \mu\text{m} \times 125\ \mu\text{m} \times 125\ \mu\text{m}$ . The digitization resolution is  $1\ \mu\text{m} \times 1\ \mu\text{m} \times 1\ \mu\text{m}$  per voxel.

### C.2.4 Distribution of the C-(N-)A-S-H gel



*Figure C.9 Distribution of the C-(N-)A-S-H gel (including the adsorbed water and gel pore water) for sample BFS\_N6S0 at 3 hours, 1 day and 7 days. The size of the cubic unit cell is  $125 \mu\text{m} \times 125 \mu\text{m} \times 125 \mu\text{m}$ . The digitization resolution is  $1 \mu\text{m} \times 1 \mu\text{m} \times 1 \mu\text{m}$  per voxel.*



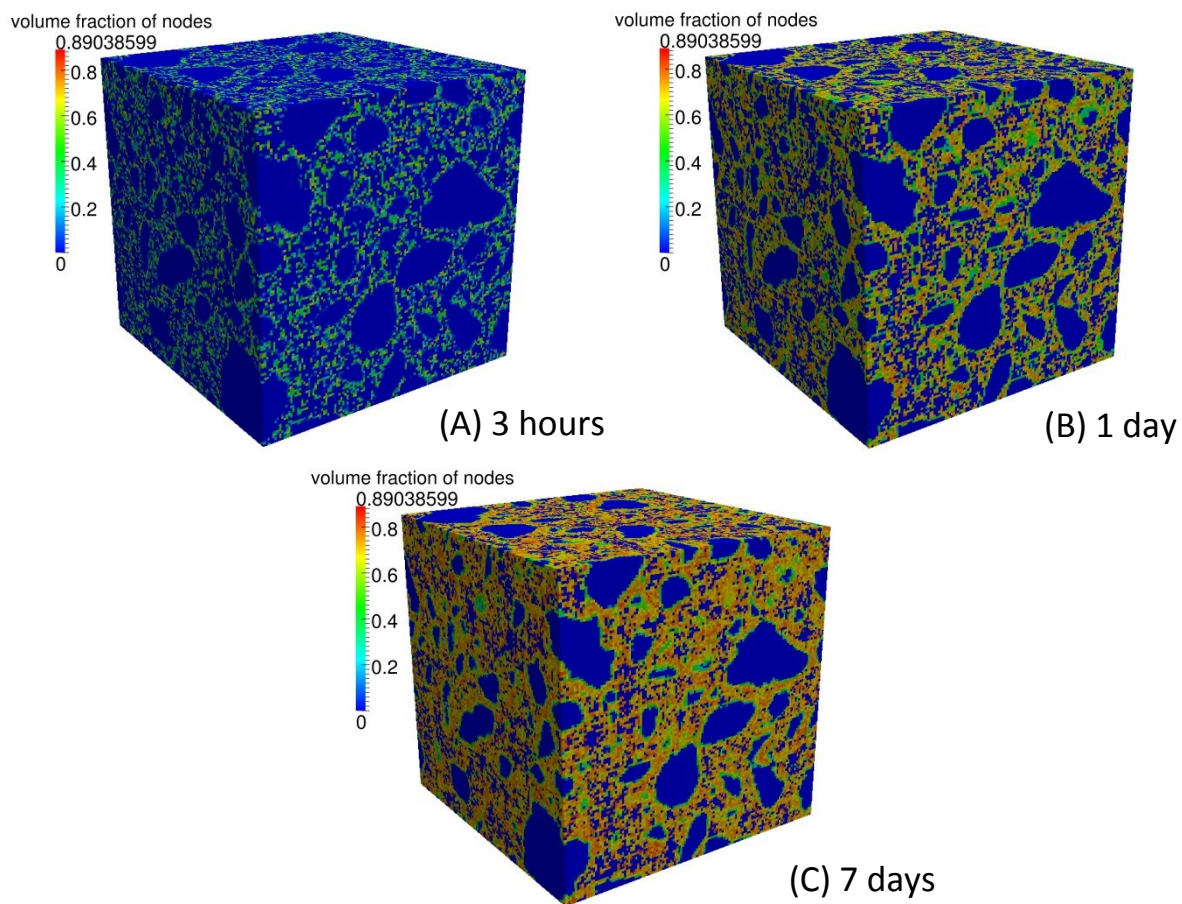


Figure C.10 Distribution of the C-(N-)A-S-H gel (including the adsorbed water and gel pore water) for sample BFS\_N6S5.4 at 3 hours, 1 day and 7 days. The size of the cubic unit cell is  $125 \mu\text{m} \times 125 \mu\text{m} \times 125 \mu\text{m}$ . The digitization resolution is  $1 \mu\text{m} \times 1 \mu\text{m} \times 1 \mu\text{m}$  per voxel.

# References

---

- [1] P. Duxson, J.L. Provis, G.C. Lukey, J.S. Van Deventer, The role of inorganic polymer technology in the development of 'green concrete', *Cem. Concr. Res.*, 37 (2007) 1590-1597.
- [2] J.S. van Deventer, J.L. Provis, P. Duxson, D.G. Brice, Chemical research and climate change as drivers in the commercial adoption of alkali activated materials, *Waste Biomass Valori.*, 1 (2010) 145-155.
- [3] J.S.J. van Deventer, J.L. Provis, P. Duxson, Technical and commercial progress in the adoption of geopolymer cement, *Miner Eng.*, 29 (2012) 89-104.
- [4] A. Fernández-Jiménez, J. Palomo, F. Puertas, Alkali-activated slag mortars: mechanical strength behaviour, *Cem. Concr. Res.*, 29 (1999) 1313-1321.
- [5] F. Pacheco-Torgal, Z. Abdollahnejad, A.F. Camões, M. Jamshidi, Y. Ding, Durability of alkali-activated binders: A clear advantage over Portland cement or an unproven issue?, *Constr. Build. Mater.*, 30 (2012) 400-405.
- [6] S.A. Bernal, J.L. Provis, Durability of alkali-activated materials: progress and perspectives, *J. Am. Ceram. Soc.*, 97 (2014) 997-1008.
- [7] J. Miranda, A. Fernández-Jiménez, J. González, A. Palomo, Corrosion resistance in activated fly ash mortars, *Cem. Concr. Res.*, 35 (2005) 1210-1217.
- [8] D. Cheema, N. Lloyd, B. Rangan, Durability of geopolymer concrete box culverts -- A green alternative, *Proceedings of the 34th Conference on Our World in Concrete and Structures*, , Singapore, 2009, pp. 16-18.
- [9] J. Gourley, G. Johnson, Developments in geopolymer precast concrete, *Proceedings of the International Workshop on Geopolymers and Geopolymer Concrete*, Perth, 2005, pp. 139-143.
- [10] N. Lloyd, V. Rangan, Geopolymer concrete with fly ash, *Proceedings of the 2nd International Conference on Sustainable Construction Materials and Technology*, Ancona, 2010, pp. 1493-1504.
- [11] R.R. Lloyd, J.L. Provis, J.S. Van Deventer, Pore solution composition and alkali diffusion in inorganic polymer cement, *Cem. Concr. Res.*, 40 (2010) 1386-1392.
- [12] B.S. Gebregziabihier, R.J. Thomas, S. Peethamparan, Temperature and activator effect on early-age reaction kinetics of alkali-activated slag binders, *Constr. Build. Mater.*, 113 (2016) 783-793.
- [13] B. Lothenbach, D. Damidot, T. Matschei, J. Marchand, Thermodynamic modelling: State of knowledge and challenges, *Adv. Cem. Res.*, 22 (2010) 211-223.
- [14] D. Damidot, B. Lothenbach, D. Herfort, F.P. Glasser, Thermodynamics and cement science, *Cem. Concr. Res.*, 41 (2011) 679-695.
- [15] M. Ben Haha, G. Le Saout, F. Winnefeld, B. Lothenbach, Influence of activator type on hydration kinetics, hydrate assemblage and microstructural development of alkali activated blast-furnace slags, *Cem. Concr. Res.*, 41 (2011) 301-310.
- [16] Y. Ma, J. Hu, G. Ye, The pore structure and permeability of alkali activated fly ash, *Fuel*, 104 (2013) 771-780.
- [17] R.R. Lloyd, J.L. Provis, J.S.J. van Deventer, Microscopy and microanalysis of inorganic polymer cements. 2: the gel binder, *J. Mater. Sci.*, 44 (2009) 620-631.
- [18] Z. Qian, E. Garboczi, G. Ye, E. Schlangen, Anm: a geometrical model for the composite structure of mortar and concrete using real-shape particles, *Mater. Struct.*, 49 (2016) 149-158.
- [19] D.A. Kulik, T. Wagner, S.V. Dmytrieva, G. Kosakowski, F.F. Hingerl, K.V. Chudnenko, U.R. Berner, GEM-Selektor geochemical modeling package: revised algorithm and GEMS3K numerical kernel for coupled simulation codes, *Comput. Geosci.*, 17 (2013) 1-24.
- [20] T. Wagner, D.A. Kulik, F.F. Hingerl, S.V. Dmytrieva, GEM-Selektor geochemical modeling package: TSolMod library and data interface for multicomponent phase models, *Can. Mineral.*, 50 (2012) 1173-1195.

- [21] S. Jiang, J.H. ter Horst, Crystal nucleation rates from probability distributions of induction times, *Cryst. Growth Des.*, 11 (2010) 256-261.
- [22] E.H. Oelkers, S.R. Gislason, The mechanism, rates and consequences of basaltic glass dissolution: I. An experimental study of the dissolution rates of basaltic glass as a function of aqueous Al, Si and oxalic acid concentration at 25 C and pH= 3 and 11, *Geochim. Cosmochim. Acta*, 65 (2001) 3671-3681.
- [23] E.H. Oelkers, General kinetic description of multioxide silicate mineral and glass dissolution, *Geochim. Cosmochim. Acta*, 65 (2001) 3703-3719.
- [24] S.R. Gislason, E.H. Oelkers, Mechanism, rates, and consequences of basaltic glass dissolution: II. An experimental study of the dissolution rates of basaltic glass as a function of pH and temperature, *Geochim. Cosmochim. Acta*, 67 (2003) 3817-3832.
- [25] E.H. Oelkers, J. Schott, J.-L. Devidal, The effect of aluminum, pH, and chemical affinity on the rates of aluminosilicate dissolution reactions, *Geochim. Cosmochim. Acta*, 58 (1994) 2011-2024.
- [26] P. Duxson, J.L. Provis, Designing precursors for geopolymer cements, *J. Am. Ceram. Soc.*, 91 (2008) 3864-3869.
- [27] W.H. Casey, H.R. Westrich, G.R. Holdren, Dissolution rates of plagioclase at pH= 2 and 3, *Am. Mineral.*, 76 (1991) 211-217.
- [28] C.A. Rees, J.L. Provis, G.C. Lukey, J.S. van Deventer, The mechanism of geopolymer gel formation investigated through seeded nucleation, *Colloids Surf. A Physicochem. Eng. Asp.*, 318 (2008) 97-105.
- [29] L. Weng, K. Sagoe-Crentsil, Dissolution processes, hydrolysis and condensation reactions during geopolymer synthesis: Part I—Low Si/Al ratio systems, *J. Mater. Sci.*, 42 (2007) 2997-3006.
- [30] K. Sagoe-Crentsil, L. Weng, Dissolution processes, hydrolysis and condensation reactions during geopolymer synthesis: Part II. High Si/Al ratio systems, *J. Mater. Sci.*, 42 (2007) 3007-3014.
- [31] C. Shi, Early hydration and microstructure development of alkali-activated slag cement pastes, *Proceedings of the 10th International Congress on the Chemistry of Cement*, Gothenburg, Sweden, 1997, pp. 3ii099.
- [32] S. Song, H.M. Jennings, Pore solution chemistry of alkali-activated ground granulated blast-furnace slag<sup>1</sup>, *Cem. Concr. Res.*, 29 (1999) 159-170.
- [33] F. Puertas, A. Fernández-Jiménez, M.T. Blanco-Varela, Pore solution in alkali-activated slag cement pastes. Relation to the composition and structure of calcium silicate hydrate, *Cem. Concr. Res.*, 34 (2004) 139-148.
- [34] A. Gruskovnjak, B. Lothenbach, L. Holzer, R. Figi, F. Winnefeld, Hydration of alkali-activated slag: comparison with ordinary Portland cement, *Adv. Cem. Res.*, (2006) 119-128.
- [35] S. Mundra, M. Criado, S.A. Bernal, J.L. Provis, Chloride-induced corrosion of steel rebars in simulated pore solutions of alkali-activated concretes, *Cem. Concr. Res.*, 100 (2017) 385-397.
- [36] T.W. Swaddle, Silicate complexes of aluminum (III) in aqueous systems, *Coord. Chem. Rev.*, 219 (2001) 665-686.
- [37] P. Duxson, J.L. Provis, G.C. Lukey, S.W. Mallicoat, W.M. Kriven, J.S. Van Deventer, Understanding the relationship between geopolymer composition, microstructure and mechanical properties, *Colloids Surf. A Physicochem. Eng. Asp.*, 269 (2005) 47-58.
- [38] D. Ravikumar, N. Neithalath, Reaction kinetics in sodium silicate powder and liquid activated slag binders evaluated using isothermal calorimetry, *Thermochim Acta*, 546 (2012) 32-43.
- [39] B.S. Gebregziabiher, R. Thomas, S. Peethamparan, Very early-age reaction kinetics and microstructural development in alkali-activated slag, *Cem. Concr. Comp.*, 55 (2015) 91-102.
- [40] X. Gao, Q. Yu, H. Brouwers, Reaction kinetics, gel character and strength of ambient temperature cured alkali activated slag–fly ash blends, *Constr. Build. Mater.*, 80 (2015) 105-115.
- [41] S.A. Bernal, J.L. Provis, V. Rose, R.M. De Gutierrez, Evolution of binder structure in sodium silicate-activated slag-metakaolin blends, *Cem. Concr. Comp.*, 33 (2011) 46-54.
- [42] C.J. Shi, R.L. Day, A calorimetric study of early hydration of alkali-slag cements, *Cem. Concr. Res.*, 25 (1995) 1333-1346.

- [43] E. Deir, B.S. Gebregziabher, S. Peethamparan, Influence of starting material on the early age hydration kinetics, microstructure and composition of binding gel in alkali activated binder systems, *Cem. Concr. Comp.*, 48 (2014) 108-117.
- [44] S. Chithiraputhiran, N. Neithalath, Isothermal reaction kinetics and temperature dependence of alkali activation of slag, fly ash and their blends, *Constr. Build. Mater.*, 45 (2013) 233-242.
- [45] F. Pacheco-Torgal, J. Labrincha, C. Leonelli, A. Palomo, P. Chindaprasit, *Handbook of alkali-activated cements, mortars and concretes*, Elsevier, 2014.
- [46] J.L. Provis, S.A. Bernal, Geopolymers and related alkali-activated materials, *Annu. Rev. Mater. Res.*, 44 (2014) 299-327.
- [47] C. Li, H.H. Sun, L.T. Li, A review: The comparison between alkali-activated slag (Si plus Ca) and metakaolin (Si plus Al) cements, *Cem. Concr. Res.*, 40 (2010) 1341-1349.
- [48] R.J. Myers, S.A. Bernal, R. San Nicolas, J.L. Provis, Generalized structural description of calcium-sodium aluminosilicate hydrate gels: the cross-linked substituted tobermorite model, *Langmuir*, 29 (2013) 5294-5306.
- [49] S.-D. Wang, K.L. Scrivener, Hydration products of alkali activated slag cement, *Cem. Concr. Res.*, 25 (1995) 561-571.
- [50] F. Puertas, M. Palacios, H. Manzano, J.S. Dolado, A. Rico, J. Rodríguez, A model for the C-A-S-H gel formed in alkali-activated slag cements, *J. Eur. Ceram. Soc.*, 31 (2011) 2043-2056.
- [51] A. Fernández-Jiménez, F. Puertas, I. Sobrados, J. Sanz, Structure of calcium silicate hydrates formed in alkaline-activated slag: influence of the type of alkaline activator, *J. Am. Ceram. Soc.*, 86 (2003) 1389-1394.
- [52] I. García-Lodeiro, A. Fernández-Jiménez, A. Palomo, D.E. Macphee, Effect of calcium additions on N-A-S-H cementitious gels, *J. Am. Ceram. Soc.*, 93 (2010) 1934-1940.
- [53] M.B. Haha, B. Lothenbach, G. Le Saout, F. Winnefeld, Influence of slag chemistry on the hydration of alkali-activated blast-furnace slag — Part II: Effect of Al<sub>2</sub>O<sub>3</sub>, *Cem. Concr. Res.*, 42 (2012) 74-83.
- [54] R.J. Myers, B. Lothenbach, S.A. Bernal, J.L. Provis, Thermodynamic modelling of alkali-activated slag cements, *Appl. Geochem.*, 61 (2015) 233-247.
- [55] I.G. Richardson, A.R. Brough, G.W. Groves, C.M. Dobson, The characterization of hardened alkali-activated blast-furnace slag pastes and the nature of the calcium silicate hydrate (C-S-H) phase, *Cem. Concr. Res.*, 24 (1994) 813-829.
- [56] A. Fernández-Jiménez, A. Palomo, Composition and microstructure of alkali activated fly ash binder: effect of the activator, *Cem. Concr. Res.*, 35 (2005) 1984-1992.
- [57] M.R. Rowles, B.H. O'Connor, Chemical and structural microanalysis of aluminosilicate geopolymers synthesized by sodium silicate activation of metakaolinite, *J. Am. Ceram. Soc.*, 92 (2009) 2354-2361.
- [58] A. Fernandez-Jimenez, A. Palomo, I. Sobrados, J. Sanz, The role played by the reactive alumina content in the alkaline activation of fly ashes, *Micropor Mesopor Mat*, 91 (2006) 111-119.
- [59] P. Duxson, A. Fernández-Jiménez, J. Provis, G. Lukey, A. Palomo, J. Van Deventer, Geopolymer technology: the current state of the art, *J. Mater. Sci.*, 42 (2007) 2917-2933.
- [60] C.E. White, J.L. Provis, T. Proffen, J.S. Van Deventer, The effects of temperature on the local structure of metakaolin-based geopolymer binder: A neutron pair distribution function investigation, *J. Am. Ceram. Soc.*, 93 (2010) 3486-3492.
- [61] A. Palomo, M.W. Grutzeck, M.T. Blanco, Alkali-activated fly ashes - A cement for the future, *Cem. Concr. Res.*, 29 (1999) 1323-1329.
- [62] M. Criado, A. Fernández-Jiménez, A. Palomo, I. Sobrados, J. Sanz, Effect of the SiO<sub>2</sub>/Na<sub>2</sub>O ratio on the alkali activation of fly ash. Part II: 29Si MAS-NMR Survey, *Micropor Mesopor Mat*, 109 (2008) 525-534.
- [63] S. Puligilla, P. Mondal, Co-existence of aluminosilicate and calcium silicate gel characterized through selective dissolution and FTIR spectral subtraction, *Cem. Concr. Res.*, 70 (2015) 39-49.
- [64] I. Ismail, S.A. Bernal, J.L. Provis, R.S. Nicolas, S. Hamdan, J.S.J. van Deventer, Modification of phase evolution in alkali-activated blast furnace slag by the incorporation of fly ash, *Cem. Concr. Comp.*, 45 (2014) 125-135.

- [65] M.B. Haha, B. Lothenbach, G. Le Saout, F. Winnefeld, Influence of slag chemistry on the hydration of alkali-activated blast-furnace slag — Part I: Effect of MgO, *Cem. Concr. Res.*, 41 (2011) 955-963.
- [66] H. Ye, A. Radlińska, Quantitative analysis of phase assemblage and chemical shrinkage of alkali-activated slag, *J. Adv. Concr. Technol.*, 14 (2016) 245-260.
- [67] Y. Ma, Microstructure and engineering properties of alkali activated fly ash -as an environment friendly alternative to Portland cement, Tu Delft, Delft University of Technology, 2013.
- [68] Y. Ma, J. Hu, G. Ye, The effect of activating solution on the mechanical strength, reaction rate, mineralogy, and microstructure of alkali-activated fly ash, *J. Mater. Sci.*, 47 (2012) 4568-4578.
- [69] R.J. Myers, S.A. Bernal, J.L. Provis, A thermodynamic model for C-(N-)A-S-H gel: CNASH<sub>ss</sub>. Derivation and validation, *Cem. Concr. Res.*, 66 (2014) 27-47.
- [70] R.J. Myers, S.A. Bernal, J.L. Provis, Phase diagrams for alkali-activated slag binders, *Cem. Concr. Res.*, 95 (2017) 30-38.
- [71] I.G. Richardson, G.W. Groves, The incorporation of minor and trace elements into calcium silicate hydrate (C-S-H) gel in hardened cement pastes, *Cem. Concr. Res.*, 23 (1993) 131-138.
- [72] R.J. Myers, S.A. Bernal, J.D. Gehman, J.S.J. van Deventer, J.L. Provis, The role of Al in cross-linking of alkali-activated slag cements, *J. Am. Ceram. Soc.*, 98 (2015) 996-1004.
- [73] W. Chen, H. Brouwers, The hydration of slag, part 1: reaction models for alkali-activated slag, *J. Mater. Sci.*, 42 (2007) 428-443.
- [74] C. Catlow, A. George, C. Freeman, Ab initio and molecular-mechanics studies of aluminosilicate fragments, and the origin of Lowenstein's rule, *Chem. Commun.*, (1996) 1311-1312.
- [75] F. Lolli, H. Manzano, J.L. Provis, M.C. Bignozzi, E. Masoero, Atomistic simulations of geopolymer models: the impact of disorder on structure and mechanics, *ACS Appl. Mater. Interfaces*, (2018).
- [76] J. Faimon, Oscillatory silicon and aluminum aqueous concentrations during experimental aluminosilicate weathering, *Geochim. Cosmochim. Acta*, 60 (1996) 2901-2907.
- [77] J. Provis, P. Duxson, J. Van Deventer, G. Lukey, The role of mathematical modelling and gel chemistry in advancing geopolymer technology, *Chemical Engineering Research and Design*, 83 (2005) 853-860.
- [78] J.L. Provis, J.S.J. van Deventer, Geopolymerisation kinetics. 2. Reaction kinetic modelling, *Chem Eng Sci*, 62 (2007) 2318-2329.
- [79] C.E. White, J.L. Provis, T. Proffen, J.S.J. van Deventer, Quantitative Mechanistic Modeling of Silica Solubility and Precipitation during the Initial Period of Zeolite Synthesis, *J Phys Chem C*, 115 (2011) 9879-9888.
- [80] C.E. White, J.L. Provis, T. Proffen, J.S.J. van Deventer, Molecular mechanisms responsible for the structural changes occurring during geopolymerization: Multiscale simulation, *Aiche J*, 58 (2012) 2241-2253.
- [81] K. Kupwade-Patil, F. Soto, A. Kunjumon, E.N. Allouche, D.S. Mainardi, Multi-scale modeling and experimental investigations of geopolymeric gels at elevated temperatures, *Comput. Struct.*, 122 (2013) 164-177.
- [82] J.L. Provis, Alkali-activated materials, *Cem. Concr. Res.*, 114 (2018) 40-48.
- [83] J.H. Espenson, Chemical kinetics and reaction mechanisms, McGraw-Hill, New York, 1995.
- [84] Z. Huanhai, W. Xuequan, X. Zhongzi, T. Mingshu, Kinetic study on hydration of alkali-activated slag, *Cem. Concr. Res.*, 23 (1993) 1253-1258.
- [85] B. Lothenbach, Thermodynamic equilibrium calculations in cementitious systems, *Mater. Struct.*, 43 (2010) 1413-1433.
- [86] V.O. Özçelik, C.E. White, Nanoscale charge-balancing mechanism in alkali-substituted calcium-silicate-hydrate gels, *J. Phys. Chem. Lett.*, 7 (2016) 5266-5272.
- [87] M. Criado, A. Fernández-Jiménez, A.G. de la Torre, M.A.G. Aranda, A. Palomo, An XRD study of the effect of the SiO<sub>2</sub>/Na<sub>2</sub>O ratio on the alkali activation of fly ash, *Cem. Concr. Res.*, 37 (2007) 671-679.
- [88] D. Hobbs, Concrete deterioration: causes, diagnosis, and minimising risk, *Int. Mater. Rev.*, 46 (2001) 117-144.



- [89] S. Mundra, S.A. Bernal, J.L. Provis, Chloride Induced Corrosion of Steel in Alkali-activated Cements: A review, *Proceedings of the Advances in Construction Materials and Systems*, Chennai, India, 2017, pp. 147.
- [90] S. Diamond, Particle morphologies in fly ash, *Cem. Concr. Res.*, 16 (1986) 569-579.
- [91] S. Ahmad, Reinforcement corrosion in concrete structures, its monitoring and service life prediction—a review, *Cem. Concr. Comp.*, 25 (2003) 459-471.
- [92] K. Scrivener, T. Füllmann, E. Gallucci, G. Walenta, E. Bermejo, Quantitative study of Portland cement hydration by X-ray diffraction/Rietveld analysis and independent methods, *Cem. Concr. Res.*, 34 (2004) 1541-1547.
- [93] R.S. Barneyback Jr, S. Diamond, Expression and analysis of pore fluids from hardened cement pastes and mortars, *Cem. Concr. Res.*, 11 (1981) 279-285.
- [94] B. Lothenbach, A. Gruskovnjak, Hydration of alkali-activated slag: thermodynamic modelling, *Adv. Cem. Res.*, 19 (2007) 81-92.
- [95] A. Fernández-Jiménez, F. Puertas, Effect of activator mix on the hydration and strength behaviour of alkali-activated slag cements, *Adv. Cem. Res.*, 15 (2003) 129-136.
- [96] C. Shi, R. Day, Selectivity of alkaline activators for the activation of slags, *Cem. Concr. Aggre.*, 18 (1996) 8-14.
- [97] D. Rothstein, J.J. Thomas, B.J. Christensen, H.M. Jennings, Solubility behavior of Ca-, S-, Al-, and Si-bearing solid phases in Portland cement pore solutions as a function of hydration time, *Cem. Concr. Res.*, 32 (2002) 1663-1671.
- [98] A. Fernández-Jiménez, A. Palomo, M. Criado, Alkali activated fly ash binders. A comparative study between sodium and potassium activators, *Mater Construcc*, 56 (2006) 51-65.
- [99] J. Davidovits, Geopolymers, *J. Therm. Anal.*, 37 (1991) 1633-1656.
- [100] C.B. Cheah, W.K. Part, M. Ramli, The hybridizations of coal fly ash and wood ash for the fabrication of low alkalinity geopolymer load bearing block cured at ambient temperature, *Constr. Build. Mater.*, 88 (2015) 41-55.
- [101] W.K.W. Lee, J.S.J. van Deventer, Structural reorganisation of class F fly ash in alkaline silicate solutions, *Colloids Surf. A Physicochem. Eng. Asp.*, 211 (2002) 49-66.
- [102] J.L. Provis, J.S.J. Van Deventer, *Geopolymers: structures, processing, properties and industrial applications*, Elsevier 2009.
- [103] D. Hardjito, B.V. Rangan, *Development and properties of low-calcium fly ash-based geopolymer concrete*, Curtin University of Technology, 2005.
- [104] A. C1679-14, *Standard Practice for Measuring Hydration Kinetics of Hydraulic Cementitious Mixtures Using Isothermal Calorimetry*, ASTM International, PA, West Conshohocken, 2014.
- [105] R. Barrer, D. Mainwaring, Chemistry of soil minerals. Part XIII. Reactions of metakaolinite with single and mixed bases, *J. Chem. Soc., Dalton Trans.*, (1972) 2534-2546.
- [106] E. Altan, S.T. Erdoğan, Alkali activation of a slag at ambient and elevated temperatures, *Cem. Concr. Comp.*, 34 (2012) 131-139.
- [107] A. Fernández-Jiménez, F. Puertas, Alkali-activated slag cements: kinetic studies, *Cem. Concr. Res.*, 27 (1997) 359-368.
- [108] C. Chen, W. Gong, W. Lutze, I.L. Pegg, Kinetics of fly ash geopolymerization, *J. Mater. Sci.*, 46 (2011) 3073-3083.
- [109] N. Neithalath, Quantifying the effects of hydration enhancement and dilution in cement pastes containing coarse glass powder, *J. Adv. Concr. Technol.*, 6 (2008) 397-408.
- [110] H.F. Taylor, *Cement chemistry*, Thomas Telford 1997.
- [111] P. Juilland, E. Gallucci, R. Flatt, K. Scrivener, Dissolution theory applied to the induction period in alite hydration, *Cem. Concr. Res.*, 40 (2010) 831-844.
- [112] C. Shi, Strength, pore structure and permeability of alkali-activated slag mortars, *Cem. Concr. Res.*, 26 (1996) 1789-1799.

- [113] F. Collins, J. Sanjayan, Effect of pore size distribution on drying shrinking of alkali-activated slag concrete, *Cem. Concr. Res.*, 30 (2000) 1401-1406.
- [114] G. Ye, Experimental Study and Numerical Simulation of the Development of the Microstructure and Permeability of Cementitious Materials, Delft University of Technology, Delft, 2003.
- [115] E.W. Washburn, The dynamics of capillary flow, *Phys. Rev.*, 17 (1921) 273.
- [116] D.R. Lide, CRC Handbook of Chemistry and Physics, 84 ed., CRC Press, Boca Raton, 2003.
- [117] J. Zhou, G. Ye, K. van Breugel, Characterization of pore structure in cement-based materials using pressurization–depressurization cycling mercury intrusion porosimetry (PDC-MIP), *Cem. Concr. Res.*, 40 (2010) 1120-1128.
- [118] K. Scrivener, R. Snellings, B. Lothenbach, A practical guide to microstructural analysis of cementitious materials, Crc Press, 2016.
- [119] I. Arganda-Carreras, V. Kaynig, C. Rueden, K.W. Eliceiri, J. Schindelin, A. Cardona, H. Sebastian Seung, Trainable Weka Segmentation: a machine learning tool for microscopy pixel classification, *Bioinformatics*, 33 (2017) 2424-2426.
- [120] F. Deschner, B. Münch, F. Winnefeld, B. Lothenbach, Quantification of fly ash in hydrated, blended Portland cement pastes by backscattered electron imaging, *J. Microsc.*, 251 (2013) 188-204.
- [121] F. Chayes, Petrographic modal analysis: an elementary statistical appraisal, Wiley 1956.
- [122] S. Roels, J. Elsen, J. Carmeliet, H. Hens, Characterisation of pore structure by combining mercury porosimetry and micrography, *Mater. Struct.*, 34 (2001) 76-82.
- [123] Z. Yang, X.-F. Peng, D.-J. Lee, M.-Y. Chen, An image-based method for obtaining pore-size distribution of porous media, *Environ. Sci. Technol.*, 43 (2009) 3248-3253.
- [124] R.J. Myers, S.A. Bernal, J.D. Gehman, J.S. Deventer, J.L. Provis, The role of Al in cross-linking of alkali-activated slag cements, *J. Am. Ceram. Soc.*, (2015) 996-1004.
- [125] J. Van Deventer, J. Provis, P. Duxson, G. Lukey, Reaction mechanisms in the geopolymeric conversion of inorganic waste to useful products, *J. Hazard. Mater.*, 139 (2007) 506-513.
- [126] R.R. Lloyd, J.L. Provis, K.J. Smeaton, J.S. van Deventer, Spatial distribution of pores in fly ash-based inorganic polymer gels visualised by Wood's metal intrusion, *Micropor Mesopor Mat*, 126 (2009) 32-39.
- [127] E.J. Garboczi, Permeability, diffusivity, and microstructural parameters: a critical review, *Cem. Concr. Res.*, 20 (1990) 591-601.
- [128] R.A. Cook, K.C. Hover, Mercury porosimetry of hardened cement pastes, *Cem. Concr. Res.*, 29 (1999) 933-943.
- [129] L. Cui, J.H. Cahyadi, Permeability and pore structure of OPC paste, *Cem. Concr. Res.*, 31 (2001) 277-282.
- [130] R.A. Olson, C.M. Neubauer, H.M. Jennings, Damage to the pore structure of hardened Portland cement paste by mercury intrusion, *J. Am. Ceram. Soc.*, 80 (1997) 2454-2458.
- [131] Z. Yu, Microstructure development and transport properties of Portland cement-fly ash binary systems: In view of service life predictions, Delft University of Technology, Delft, 2015.
- [132] J.L. Provis, R.J. Myers, C.E. White, V. Rose, J.S.J. van Deventer, X-ray microtomography shows pore structure and tortuosity in alkali-activated binders, *Cem. Concr. Res.*, 42 (2012) 855-864.
- [133] S.A. Bernal, J.L. Provis, B. Walkley, R. San Nicolas, J.D. Gehman, D.G. Brice, A.R. Kilcullen, P. Duxson, J.S. van Deventer, Gel nanostructure in alkali-activated binders based on slag and fly ash, and effects of accelerated carbonation, *Cem. Concr. Res.*, 53 (2013) 127-144.
- [134] D.A. Lange, H.M. Jennings, S.P. Shah, Image analysis techniques for characterization of pore structure of cement-based materials, *Cem. Concr. Res.*, 24 (1994) 841-853.
- [135] J. Kaufmann, R. Loser, A. Leemann, Analysis of cement-bonded materials by multi-cycle mercury intrusion and nitrogen sorption, *J. Colloid Interface Sci.*, 336 (2009) 730-737.
- [136] H.M. Jennings, S.K. Johnson, Simulation of microstructure development during the hydration of a cement compound, *J. Am. Ceram. Soc.*, 69 (1986) 790-795.

- [137] P. Navi, C. Pignat, Three-dimensional characterization of the pore structure of a simulated cement paste, *Cem. Concr. Res.*, 29 (1999) 507-514.
- [138] K. Maekawa, R. Chaube, T. Kishi, Modeling of concrete performance: hydration, microstructure formation and mass transport, E and FN SPON, London, (1999).
- [139] K.v. Breugel, Simulation of hydration and formation of structure in hardening cement-based materials, Delft University of Technology, Delft, 1991.
- [140] P. Gao, G. Ye, J. Wei, Q. Yu, Simulation of the development of pH in the pore solution of slag cement paste at early age, Proceedings of the RILEM International Symposium on Concrete Modelling, , Beijing, China, 2014, pp. 273-280.
- [141] Z. Qian, E. Schlangen, G. Ye, K. van Breugel, Modeling Framework for Fracture in Multiscale Cement-Based Material Structures, *Materials*, 10 (2017) 587.
- [142] Z. Qian, Multiscale modeling of fracture processes in cementitious materials, Delft University of Technology, Delft, 2012.
- [143] G. Arfken, Mathematical Methods for Physicists, 2nd ed., Academic Press, New York, 1970.
- [144] E.J. Garboczi, Three-dimensional mathematical analysis of particle shape using X-ray tomography and spherical harmonics: Application to aggregates used in concrete, *Cem. Concr. Res.*, 32 (2002) 1621-1638.
- [145] M.A. Taylor, E.J. Garboczi, S. Erdogan, D. Fowler, Some properties of irregular 3-D particles, *Powder Technol.*, 162 (2006) 1-15.
- [146] S. Erdoğan, E.J. Garboczi, D. Fowler, Shape and size of microfine aggregates: X-ray microcomputed tomography vs. laser diffraction, *Powder Technol.*, 177 (2007) 53-63.
- [147] J.M. Fernlund, The effect of particle form on sieve analysis: a test by image analysis, *Engineering Geology*, 50 (1998) 111-124.
- [148] S. Thomas, Y. Lu, E. Garboczi, Improved model for three-dimensional virtual concrete: Anm model, *J. Comput. Civil Eng.*, 30 (2015) 04015027.
- [149] P. Gao, Simulation of hydration and microstructure development of blended cements, Delft University of Technology, Delft, 2018.
- [150] J.W. Bullard, E.J. Garboczi, A model investigation of the influence of particle shape on portland cement hydration, *Cem. Concr. Res.*, 36 (2006) 1007-1015.
- [151] S. Li, D.M. Roy, Investigation of relations between porosity, pore structure, and C1- diffusion of fly ash and blended cement pastes, *Cem. Concr. Res.*, 16 (1986) 749-759.
- [152] V. Ngala, C. Page, Effects of carbonation on pore structure and diffusional properties of hydrated cement pastes, *Cem. Concr. Res.*, 27 (1997) 995-1007.
- [153] S. Erdogan, P. Quiroga, D. Fowler, H. Saleh, R.A. Livingston, E.J. Garboczi, P.M. Ketcham, J.G. Hagedorn, S.G. Satterfield, Three-dimensional shape analysis of coarse aggregates: New techniques for and preliminary results on several different coarse aggregates and reference rocks, *Cem. Concr. Res.*, 36 (2006) 1619-1627.
- [154] T. Vuk, V. Tinta, R. Gabrovšek, V. Kaučič, The effects of limestone addition, clinker type and fineness on properties of Portland cement, *Cem. Concr. Res.*, 31 (2001) 135-139.
- [155] D.P. Bentz, G. Sant, J. Weiss, Early-age properties of cement-based materials. I: Influence of cement fineness, *J. Mater. Civ. Eng.*, 20 (2008) 502-508.
- [156] S. Song, D. Sohn, H. Jennings, T. Mason, Hydration of alkali-activated ground granulated blast furnace slag, *J. Mater. Sci.*, 35 (2000) 249-257.
- [157] A. Kashani, J.L. Provis, G.G. Qiao, J.S. van Deventer, The interrelationship between surface chemistry and rheology in alkali activated slag paste, *Constr. Build. Mater.*, 65 (2014) 583-591.
- [158] C. Panagiotopoulou, E. Kontori, T. Perraki, G. Kakali, Dissolution of aluminosilicate minerals and by-products in alkaline media, *J. Mater. Sci.*, 42 (2007) 2967-2973.
- [159] R. Snellings, Solution-controlled dissolution of supplementary cementitious material glasses at pH 13: The Effect of Solution Composition on Glass Dissolution Rates, *J. Am. Ceram. Soc.*, 96 (2013) 2467-2475.

- [160] A. Schöler, F. Winnefeld, M.B. Haha, B. Lothenbach, The effect of glass composition on the reactivity of synthetic glasses, *J. Am. Ceram. Soc.*, (2017) 1-15.
- [161] D. Wolff-Boenisch, S.R. Gislason, E.H. Oelkers, C.V. Putnis, The dissolution rates of natural glasses as a function of their composition at pH 4 and 10.6, and temperatures from 25 to 74 degrees C, *Geochim. Cosmochim. Acta*, 68 (2004) 4843-4858.
- [162] G. Berger, C. Claparols, C. Guy, V. Daux, Dissolution rate of a basalt glass in silica-rich solutions: implications for long-term alteration, *Geochim. Cosmochim. Acta*, 58 (1994) 4875-4886.
- [163] V. Daux, C. Guy, T. Advocat, J.-L. Crovisier, P. Stille, Kinetic aspects of basaltic glass dissolution at 90°C: role of aqueous silicon and aluminium, *Chem. Geol.*, 142 (1997) 109-126.
- [164] C. Guy, J. Schott, Multisite surface reaction versus transport control during the hydrolysis of a complex oxide, *Chem. Geol.*, 78 (1989) 181-204.
- [165] B.O. Mysen, Structure and properties of silicate melts, *Devel. Geochem.*, (1988).
- [166] Y.-H. Qian, D. d'Humières, P. Lallemand, Lattice BGK models for Navier-Stokes equation, *EPL*, 17 (1992) 479.
- [167] N. Jeong, D.H. Choi, C.-L. Lin, Estimation of thermal and mass diffusivity in a porous medium of complex structure using a lattice Boltzmann method, *Int. J. Heat Mass Transfer*, 51 (2008) 3913-3923.
- [168] A.A. Mohamad, Lattice Boltzmann method: fundamentals and engineering applications with computer codes, Springer Science & Business Media, 2011.
- [169] R. Patel, Lattice Boltzmann method based framework for simulating physico-chemical processes in heterogeneous porous media and its application to cement paste, Ghent University, Ghent, 2016.
- [170] B. Sedgewick, K. Wayne, Percolation, <https://coursera.cs.princeton.edu/algs4/assignments/percolation/specification.php>, 2008.
- [171] B.R. Bickmore, K.L. Nagy, A.K. Gray, A.R. Brinkerhoff, The effect of  $\text{Al}(\text{OH})_4^-$  on the dissolution rate of quartz, *Geochim. Cosmochim. Acta*, 70 (2006) 290-305.
- [172] Y. Niibori, M. Kunita, O. Tochiyama, T. Chida, Dissolution rates of amorphous silica in highly alkaline solution, *J. Nucl. Sci. Technol.*, 37 (2000) 349-357.
- [173] A. Packter, H. Dhillon, Studies on recrystallised aluminium hydroxide precipitates, *Colloid. Polym. Sci.*, 252 (1974) 249-256.
- [174] T. Stamatis, M. Aggeliki, Hydration of CaO present in fly ashes, in: F. Edition (Ed.), 2015, pp. 1-74.
- [175] B. Lothenbach, F. Winnefeld, Thermodynamic modelling of the hydration of Portland cement, *Cem. Concr. Res.*, 36 (2006) 209-226.
- [176] C. database, <http://thermoddem.brgm.fr/spip.php/rubrique9>, 2014.
- [177] H. Huang, Thermodynamics of autogenous self-healing in cementitious materials, Delft University of Technology, Delft, 2014.
- [178] E.L. Cussler, Diffusion: mass transfer in fluid systems, Cambridge university press, 2009.
- [179] C.J. Fell, H.P. Hutchison, Diffusion coefficients for sodium and potassium chlorides in water at elevated temperatures, *Journal of Chemical & Engineering Data*, 16 (1971) 427-429.
- [180] S.A. Socolofsky, G.H. Jirka, Environmental Fluid Mechanics Part I: Mass Transfer and Diffusion, Karlsruhe Institute of Technology, 2002.
- [181] E. Goli, T. Hiemstra, W.H. Van Riemsdijk, R. Rahnemaie, M.J. Malakouti, Diffusion of neutral and ionic species in charged membranes: boric acid, arsenite, and water, *Anal. Chem.*, 82 (2010) 8438-8445.
- [182] J.L. Provis, G.C. Lukey, J.S.J. van Deventer, Do geopolymers actually contain nanocrystalline zeolites? A reexamination of existing results, *Chem Mater*, 17 (2005) 3075-3085.
- [183] S. Alonso, A. Palomo, Calorimetric study of alkaline activation of calcium hydroxide–metakaolin solid mixtures, *Cem. Concr. Res.*, 31 (2001) 25-30.
- [184] M.L. Granizo, S. Alonso, M.T. Blanco-Varela, A. Palomo, Alkaline activation of metakaolin: effect of calcium hydroxide in the products of reaction, *J. Am. Ceram. Soc.*, 85 (2002) 225-231.

- [185] A. Alberti, T. Armbruster, G. Artioli, C. Colella, E. Galli, J.D. Grice, F. Liebau, H. Minato, E.H. Nickel, E. Passaglia, Recommended nomenclature for zeolite minerals: Report of the subcommittee on zeolites of the International Mineralogical Association, Commission on New Minerals and Mineral Names, *Can. Mineral.*, 35 (1997) 1571-1606.
- [186] J.L. Bell, P. Sarin, P.E. Driemeyer, R.P. Haggerty, P.J. Chupas, W.M. Kriven, X-ray pair distribution function analysis of a metakaolin-based,  $\text{KAlSi}_2\text{O}_6 \cdot 5.5\text{H}_2\text{O}$  inorganic polymer (geopolymer), *J Mater Chem*, 18 (2008) 5974-5981.
- [187] T. Bakharev, Geopolymeric materials prepared using Class F fly ash and elevated temperature curing, *Cem. Concr. Res.*, 35 (2005) 1224-1232.
- [188] F. Winnefeld, A. Leemann, M. Lucuk, P. Svoboda, M. Neuroth, Assessment of phase formation in alkali activated low and high calcium fly ashes in building materials, *Constr. Build. Mater.*, 24 (2010) 1086-1093.
- [189] F. Škvára, L. Kopecký, J. Nemecek, Z. Bittnar, Microstructure of geopolymer materials based on fly ash, *Ceramics-Silikaty*, 50 (2006) 208-215.
- [190] I. Garcia-Lodeiro, E. Aparicio-Rebollo, A. Fernández-Jimenez, A. Palomo, Effect of calcium on the alkaline activation of aluminosilicate glass, *Ceram. Int.*, 42 (2016) 7697-7707.
- [191] D. Dimas, I. Giannopoulou, D. Panias, Polymerization in sodium silicate solutions: a fundamental process in geopolymerization technology, *J. Mater. Sci.*, 44 (2009) 3719-3730.
- [192] Z. Zuhua, Y. Xiao, Z. Huajun, C. Yue, Role of water in the synthesis of calcined kaolin-based geopolymer, *Appl. Clay Sci.*, 43 (2009) 218-223.
- [193] D.L. Kong, J.G. Sanjayan, K. Sagoe-Crentsil, Factors affecting the performance of metakaolin geopolymers exposed to elevated temperatures, *J. Mater. Sci.*, 43 (2008) 824-831.
- [194] G.M. Anderson, D.A. Crerar, *Thermodynamics in geochemistry: the equilibrium model*, Oxford University Press on Demand 1993.
- [195] A.G. Mostafa, J.M. Eakman, S.L. Yarbrow, Prediction of standard heats and Gibbs free energies of formation of solid inorganic salts from group contributions, *Ind Eng Chem Res*, 34 (1995) 4577-4582.
- [196] A.G. Mostafa, J.M. Eakman, M.M. Montoya, S.L. Yarbrow, Prediction of heat capacities of solid inorganic salts from group contributions, *Ind Eng Chem Res*, 35 (1996) 343-348.
- [197] R.O. Sack, M.S. Ghiorso, Thermodynamics of feldspathoid solutions, *Contrib. Mineral. Petrol.*, 130 (1998) 256-274.
- [198] J.J. Thomas, A.J. Allen, H.M. Jennings, Density and water content of nanoscale solid C-S-H formed in alkali-activated slag (AAS) paste and implications for chemical shrinkage, *Cem. Concr. Res.*, 42 (2012) 377-383.
- [199] C. Maitland, C. Buckley, B. O'Connor, P. Butler, R. Hart, Characterization of the pore structure of metakaolin-derived geopolymers by neutron scattering and electron microscopy, *J. Appl. Crystallogr.*, 44 (2011) 697-707.
- [200] M. Wolthers, L. Charlet, P.R. van Der Linde, D. Rickard, C.H. van Der Weijden, Surface chemistry of disordered mackinawite (FeS), *Geochim. Cosmochim. Acta*, 69 (2005) 3469-3481.
- [201] D. Bennett, D. Read, M. Atkins, F. Glasser, A thermodynamic model for blended cements. II: Cement hydrate phases; thermodynamic values and modelling studies, *J. Nucl. Mater.*, 190 (1992) 315-325.
- [202] W. Gao, Z. Li, Solubility and KSP of  $\text{Mg}_4\text{Al}_2(\text{OH})_{14} \cdot 3\text{H}_2\text{O}$  at the various ionic strengths, *Hydrometallurgy*, 117 (2012) 36-46.
- [203] R.J. Myers, *Thermodynamic Modelling of CaO-Al<sub>2</sub>O<sub>3</sub>-SiO<sub>2</sub>-H<sub>2</sub>O-Based Cements*, University of Sheffield, Sheffield, 2015.
- [204] B. Lothenbach, T. Matschei, G. Möschner, F.P. Glasser, Thermodynamic modelling of the effect of temperature on the hydration and porosity of Portland cement, *Cem. Concr. Res.*, 38 (2008) 1-18.
- [205] D.A. Kulik, Minimising uncertainty induced by temperature extrapolations of thermodynamic data: a pragmatic view on the integration of thermodynamic databases into geochemical computer codes, in: F. Monpean (Ed.) *Proceedings of the The use of thermodynamic databases in performance assessment*, Barcelona, Spain, 2002, pp. 125-137.

- [206] H.C. Helgeson, D.H. Kirkham, G.C. Flowers, Theoretical prediction of the thermodynamic behavior of aqueous electrolytes by high pressures and temperatures; IV, Calculation of activity coefficients, osmotic coefficients, and apparent molal and standard and relative partial molal properties to 600 degrees C and 5kb, *American journal of science*, 281 (1981) 1249-1516.
- [207] K.S. Pitzer, Ion interaction approach: theory and data correlation, *Activity coefficients in electrolyte solutions*, 1991, pp. 75-153.
- [208] A. Buchwald, H.-D. Zellmann, C. Kaps, Condensation of aluminosilicate gels—model system for geopolymer binders, *J. Non-Cryst. Solids*, 357 (2011) 1376-1382.
- [209] B. Lothenbach, E. Bernard, U. Mäder, Zeolite formation in the presence of cement hydrates and albite, *Physics and Chemistry of the Earth, Parts A/B/C*, 99 (2017) 77-94.
- [210] D. Kashchiev, G. Van Rosmalen, Nucleation in solutions revisited, *Cryst. Res. Technol.*, 38 (2003) 555-574.
- [211] N. Phan-Thien, D. Pham, Differential multiphase models for polydispersed spheroidal inclusions: thermal conductivity and effective viscosity, *Int. J. Eng. Sci.*, 38 (2000) 73-88.
- [212] E. Garboczi, D. Bentz, Computer simulation of the diffusivity of cement-based materials, *J. Mater. Sci.*, 27 (1992) 2083-2092.
- [213] S. Kamali-Bernard, F. Bernard, W. Prince, Computer modelling of tritiated water diffusion test for cement based materials, *Comput. Mater. Sci.*, 45 (2009) 528-535.
- [214] H. Ma, D. Hou, J. Liu, Z. Li, Estimate the relative electrical conductivity of C–S–H gel from experimental results, *Constr. Build. Mater.*, 71 (2014) 392-396.
- [215] F. Nogue, M.-P. Yssorche-Cubaynes, J. Ollivier, Innovative study of non-steady-state tritiated water diffusion test, *Cem. Concr. Res.*, 37 (2007) 1145-1151.
- [216] J.J. Thomas, H.M. Jennings, A.J. Allen, Relationships between composition and density of tobermorite, jennite, and nanoscale CaO– SiO<sub>2</sub>– H<sub>2</sub>O, *J. Phys. Chem. C*, 114 (2010) 7594-7601.
- [217] Z. Qian, E. Schlangen, G. Ye, K. Van Breugel, Prediction of mechanical properties of cement paste at microscale, *Mater Construcc*, 60 (2010) 7-18.
- [218] K. Arbi, M. Nedeljković, Y. Zuo, G. Ye, A Review on the Durability of Alkali-Activated Fly Ash/Slag Systems: Advances, Issues, and Perspectives, *Ind Eng Chem Res*, 55 (2016) 5439-5453.
- [219] P.T. Durdziński, C.F. Dunant, M.B. Haha, K.L. Scrivener, A new quantification method based on SEM-EDS to assess fly ash composition and study the reaction of its individual components in hydrating cement paste, *Cem. Concr. Res.*, 73 (2015) 111-122.
- [220] D.A. Kulik, M. Kersten, Aqueous Solubility Diagrams for Cementitious Waste Stabilization Systems: II, End-Member Stoichiometries of Ideal Calcium Silicate Hydrate Solid Solutions, *J. Am. Ceram. Soc.*, 84 (2001) 3017-3026.
- [221] E.L. Shock, D.C. Sassani, M. Willis, D.A. Sverjensky, Inorganic species in geologic fluids: Correlations among standard molal thermodynamic properties of aqueous ions and hydroxide complexes, *Geochim. Cosmochim. Acta*, 61 (1997) 907-950.
- [222] D. Sverjensky, E. Shock, H. Helgeson, Prediction of the thermodynamic properties of aqueous metal complexes to 1000 C and 5 kb, *Geochim. Cosmochim. Acta*, 61 (1997) 1359-1412.
- [223] E.L. Shock, H.C. Helgeson, D.A. Sverjensky, Calculation of the thermodynamic and transport properties of aqueous species at high pressures and temperatures: Standard partial molal properties of inorganic neutral species, *Geochim. Cosmochim. Acta*, 53 (1989) 2157-2183.
- [224] T. Matschei, B. Lothenbach, F.P. Glasser, Thermodynamic properties of Portland cement hydrates in the system CaO–Al<sub>2</sub>O<sub>3</sub>–SiO<sub>2</sub>–CaSO<sub>4</sub>–CaCO<sub>3</sub>–H<sub>2</sub>O, *Cem. Concr. Res.*, 37 (2007) 1379-1410.
- [225] B. Lothenbach, D.A. Kulik, T. Matschei, M. Balonis, L. Baquerizo, B. Dilnesa, G.D. Miron, R.J. Myers, Cemdata18: A chemical thermodynamic database for hydrated Portland cements and alkali-activated materials, *Cem. Concr. Res.*, 115 (2019) 472-506.
- [226] J.W. Johnson, E.H. Oelkers, H.C. Helgeson, SUPCRT92: A software package for calculating the standard molal thermodynamic properties of minerals, gases, aqueous species, and reactions from 1 to 5000 bar and 0 to 1000 C, *Comput. Geosci.*, 18 (1992) 899-947.

- [227] B. Lothenbach, L. Pelletier-Chaignat, F. Winnefeld, Stability in the system  $\text{CaO}-\text{Al}_2\text{O}_3-\text{H}_2\text{O}$ , *Cem. Concr. Res.*, 42 (2012) 1621-1634.
- [228] A. Anderko, P.J. Shuler, A computational approach to predicting the formation of iron sulfide species using stability diagrams, *Comput. Geosci.*, 23 (1997) 647-658.
- [229] R. Glaccum, K. Boström, (Na, K)-phillipsite: its stability conditions and geochemical role in the deep sea, *Mar. Geol.*, 21 (1976) 47-58.
- [230] E.S.P. Aradóttir, E.L. Sonnenthal, H. Jónsson, Development and evaluation of a thermodynamic dataset for phases of interest in  $\text{CO}_2$  mineral sequestration in basaltic rocks, *Chem. Geol.*, 304–305 (2012) 26-38.
- [231] L. Zeng, Z. Li, Solubility and modeling of sodium aluminosilicate in  $\text{NaOH}-\text{NaAl}(\text{OH})_4$  solutions and its application to desilication, *Ind Eng Chem Res*, 51 (2012) 15193-15206.
- [232] H. Park, P. Englezos, Thermodynamic modeling of sodium aluminosilicate formation in aqueous alkaline solutions, *Ind Eng Chem Res*, 38 (1999) 4959-4965.
- [233] J. Šefčík, A. McCormick, What is the solubility of zeolite A?, *Microporous Mater.*, 10 (1997) 173-179.
- [234] L. Valentini, Modeling Dissolution–Precipitation Kinetics of Alkali-Activated Metakaolin, *ACS Omega*, 3 (2018) 18100-18108.
- [235] A. Palčić, B. Subotić, V. Valtchev, J. Bronić, Nucleation and crystal growth of zeolite A synthesised from hydrogels of different density, *CrystEngComm*, 15 (2013) 5784-5791.





# Propositions

---

1. It is possible to use either of MIP, SEM-image analysis and GeoMicro3D, or combine them, to gain insights into the microstructure formation of alkali-activated materials (AAMs). However, the pore size distribution obtained by one technique is not recommended to quantitatively validate the pore size distribution obtained by another technique.
2. Code debug is more time consuming than code writing.
3. “The purpose of computing is insight, not numbers.” (Richard Wesley Hamming)
4. Among the methods to determine model parameters, parameter studies should not be the first option. Instead experimental techniques should be considered as the first option.
5. A PhD candidate is often very ambitious on the research in the beginning. Afterwards he/she has to set up realistic goals.
6. For a PhD candidate self-motivation is more important than the other qualities like intelligence, hardworking and perseverance etc.
7. Literature is the best “supervisor” for doing a PhD research.
8. Thinking while running sparks new ideas.
9. “I am what I am.” (Leslie Cheung).
10.  $(1 - 0.01)^{365} \approx 0.0255$  and  $(1 + 0.01)^{365} \approx 37.78$ . A little difference a day makes a big difference a year.

*These proporsitions are regarded as opposable and defendable, and have been approved as such by the promotors Prof. dr. ir. K. van Breugel and Dr. G. Ye.*



# List of Publications

---

## Journal papers

1. **Yibing Zuo**, Marija Nedeljkovic, Guang Ye. Pore solution composition of alkali-activated slag/fly ash pastes. *Cement and Concrete Research*, 115(2019) 230-250.
2. **Yibing Zuo**, Marija Nedeljkovic, Guang Ye. Coupled thermodynamic modelling and experimental study of sodium hydroxide activated slag. *Construction and Building Materials*. 188(2018) 262-279.
3. **Yibing Zuo**, Zhiwei Qian, Edward J Garboczi, Guang Ye. Numerical simulation of the initial particle packing structure of cement/geopolymer paste and the dissolution of amorphous silica using real-shape particles. *Construction and Building Materials*. 185(2018) 206-219.
4. **Yibing Zuo**, Guang Ye. Pore structure characterization of sodium hydroxide activated slag using mercury intrusion porosimetry, nitrogen adsorption, and image analysis. *Materials*, 11(2018) 1035.
5. **Yibing Zuo**, Marija Nedeljkovic, Guang Ye. Pore solution composition and solubility of alkali-activated fly ash. *Key Engineering Materials*, 761(2018) 65-68.
6. Zhenming Li, Shizhe Zhang, **Yibing Zuo**, Wei Chen, Guang Ye. Chemical deformation of metakaolin based geopolymer. *Cement and Concrete Research*, 120(2019) 108-118.
7. Marija Nedeljkovic, Branko Savja, **Yibing Zuo**, Mladena Lukovic, Guang Ye. Effect of natural carbonation on the pore structure and elastic modulus of the alkali-activated fly ash and slag pastes. *Construction and Building Materials*, 161(2018) 687-704.
8. Marija Nedeljkovic, **Yibing Zuo**, Kamel Arbi, Guang Ye. Carbonation resistance of alkali-activated slag under natural and accelerated conditions. *Journal of Sustainable Metallurgy*, 4(2018) 33-49.
9. Hua Dong, Hongzhi Zhang, **Yibing Zuo**, Peng Gao, Guang Ye. Relationship between the size of the samples and the interpretation of the mercury intrusion results of an artificial sandstone. *Materials*, 161(2018) 201.

10. Marija Nedeljkovic, **Yibing Zuo**, Kamel Arbi, Guang Ye. Natural carbonation of alkali-activated fly ash and slag pastes. *High Tech Concrete: Where Technology and Engineering Meet*, (2018) 2213-2223.
11. Marija Nedeljkovic, **Yibing Zuo**, Guang Ye. New test method for assessing the carbonation front in alkali-activated fly ash/slag pastes. *Key Engineering Materials*, 761(2018) 148-151.
12. Kamel Arbi, Marija Nedeljkovic, **Yibing Zuo**, Guang Ye. A review on the durability of alkali-activated fly ash/slag systems: advance, issues, and perspectives. *Industrial & Engineering Chemistry Research*, 55(2016) 5439-5453.

### Conference Papers

1. **Yibing Zuo**, Guang Ye. GeoMicro3D: A novel numerical framework for simulating the hydration and microstructure formation of alkali-activated materials. *In Concrete Modelling Symposium*, Delft, The Netherlands, August 26-29, 2018.
2. **Yibing Zuo**, Guang Ye. Experimental study and numerical simulation of the dissolution of blast furnace slag in alkaline solution. *In Alkali Activated Materials and Geopolymers: Versatile Materials Offering High Performance and Low Emissions*, Tomar, Portugal, May 27 – June 1, 2018.
3. **Yibing Zuo**, Zhiwei Qian, Edward J Garboczi and Guang Ye. Numerical study of the initial particle parking structure of cement/geopolymer pastes and dissolution of amorphous silica using real-shape particles. *The 9<sup>th</sup> International Symposium on Cement and Concrete*, Wuhan, China, November 1-3, 2017.
4. **Yibing Zuo**, Marija Nedelkovic, Guang Ye. Pore solution composition and solubility of alkali-activated fly ash. *In the 6<sup>th</sup> International Conference, Non-traditional Cement and Concrete*, Brno, Czech Republic, June 19-22, 2017.
5. **Yibing Zuo**, Marija Nedelkovic, Guang Ye. Pore structure characterization of sodium hydroxide activated slag paste. *In the 5<sup>th</sup> International Slag Valorisation Symposium*, Leuven, Belgium, April 3-5, 2017.
6. **Yibing Zuo**, Marija Nedeljkovic, Kamel Arbi, Guang Ye. Aqueous phase composition of alkali-activated blast furnace slag pastes. *In the 2<sup>nd</sup> International Conference on the*

- Chemistry of Construction Materials*, Technical University of Munich, Munich, German, October 10-12, 2016.
7. **Yibing Zuo**, Marija Nedeljkovic, Kamel Arbi, Guang Ye. Thermodynamic modelling and experimental study of alkali-activated slag pastes. *In the 4<sup>th</sup> International Symposium on Ultra-High Performance Concrete and High Performance Construction Materials*, Kassel University, Kassel, German, March 11-13, 2016.
  8. **Yibing Zuo**, Marija Nedeljkovic, Guang Ye. Reaction kinetics and thermodynamic modelling of sodium hydroxide activated slag paste. *In the 3<sup>rd</sup> International RILEM Conference on Microstructure Related Durability of Cementitious Composites*, Nanjing, China, October 24-26, 2016.
  9. Shizhe Zhang, **Yibing Zuo**, Zhenming Li, Guang Ye. Isothermal calorimetric study on heat evolution and of apparent activation energy of alkali-activated slag/fly ash pastes. *In 2<sup>nd</sup> International Conference on Sustainable Building Materials*, Eindhoven, The Netherlands, August 12-15, 2019.
  10. Zhenming Li, Marija Nedeljkovic, **Yibing Zuo**, Guang Ye. Autogenous shrinkage of alkali-activated slag-fly ash pastes. *In the 5<sup>th</sup> International Slag Valorisation Symposium*, Leuven, Belgium, April 3-5, 2017.
  11. Kamel Arbi, Marija Nedeljkovic, **Yibing Zuo**, Steffen Grunewald, Arno Keulen, Guang Ye. Experimental study on workability of alkali-activated fly ash and slag-based geopolymer concretes. *Geopolymers: The route to eliminate waste and emissions in ceramic and cement manufacturing*, Austria, May 24-29, 2015.
  12. Kamel Arbi, Marija Nedeljkovic, **Yibing Zuo**, Steffen Grunewald, Arno Keulen, Guang Ye. Durability of alkali-activated fly ash and slag concrete. *In the 9<sup>th</sup> International Concrete Conference at Dundee*, Scotland, July 4-6, 2016.
  13. Marija Nedeljkovic, Kamel Arbi, **Yibing Zuo**, Guang Ye. Physical properties and pore solution analysis of alkali-activated fly ash-slag pastes. *International RILEM Conference on Materials, Systems and Structures in Civil Engineering Conference segment on Concrete with Supplementary Cementitious Materials*, Technical University of Denmark, Lyngby, Denmark, August 22-24, 2016.
  14. Marija Nedeljkovic, **Yibing Zuo**, Guang Ye. Microstructural and mineralogical analysis of alkali-activated fly ash-slag pastes. *In the 3<sup>rd</sup> International RILEM Conference on*

*Microstructure Related Durability of Cementitious Composites*, Nanjing, China, October 24-26, 2016.

# Curriculum Vitae

---

## Personal information

Name: Yibing Zuo (左义兵)

Date of birth: 1 December 1986

Place of birth: Xiaogan, Hubei Province, P.R. China

Email: [crickzuo@qq.com](mailto:crickzuo@qq.com)



## Education background

September 2014 – September 2019

PhD candidate, Microlab, Section of Materials and Environment

Faculty of Civil Engineering and Geosciences

Delft University of Technology, The Netherlands

September 2011 – June 2014

Master of science, Structure Engineering

School of Civil Engineering and Mechanics

Huazhong University of Science and Technology, P.R. China

September 2007 – June 2011

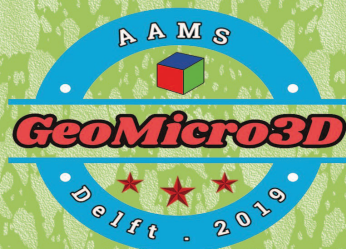
Bachelor, Safety Engineering and English (Dual)

School of Resource and Environmental Engineering

Wuhan University of Science and Technology, P.R. China







  
**TU**Delft

ISBN 978-94-6384-062-0



9 789463 840620